Characterization of human ribs under dynamic impact loads: Finite Element simulations and experimental validation

Aravind Rajan Ayagara

To cite this version:

Aravind Rajan Ayagara. Characterization of human ribs under dynamic impact loads: Finite Element simulations and experimental validation. Biomechanics [physics.med-ph]. Université d'Orléans, 2019. English. NNT : . tel-02568503

HAL Id: tel-02568503
https://hal.science/tel-02568503

Submitted on 9 May 2020

UNIVERSITÉ D'ORLÉANS

ÉCOLE DOCTORALE ÉNERGIE, MATÉRIAUX, SCIENCES DE LA TERRE ET DE L'UNIVERS

LABORATOIRE DE MÉCANIQUE GABRIEL LAMÉ

THÈSE

présentée par :

Aravind Rajan AYAGARA

soutenue le : **14 Novembre 2019**
pour obtenir le grade de : **Docteur de l'Université d'Orléans**
Discipline/ Spécialité : Génie Mécanique

Caractérisation de la fracturation dynamique des os de la cage thoracique : simulations numériques et validation expérimentale

---

Thèse dirigée par :

André LANGLET	HDR, LaMé, Université d'Orléans
Ridha HAMBLI	Professeur, LaMé, Université d'Orléans

JURY :

Patrick CHABRAND	Professeur, ISM, Université Aix-Marseille	Rapporteur
Jean-François GANGHOFFER	Professeur, LEM3, Université de Lorraine	Président du jury
Sébastien LAPORTE	Professeur, IBHGC, ENSAM Paris	Rapporteur
Salah NAILI	Professeur, MSME, Université de Paris-Est Créteil	Examinateur
Julien PAVIER	Docteur, Nexter Munitions, Bourges	Invité
Nicolas PRAT	Docteur en Médecine, HDR, Institut de Recherche Biomédicale des Armées (IRBA),	Examinateur

I dedicate this thesis to
my parents,
and
to his excellency, late. Dr A.P.J. Abdhul Kalam
11th president of the Republic of India (2002-2007)

"Sometimes it is the people who no one imagines anything of
who do the things that no one can imagine"

- *Alan Turing*

ACKNOWLEDGEMENTS

I would like to sincerely thank my PhD supervisors Dr. André LANGLET and Pr. Ridha HAMBLI for their valuable suggestions, insights and for having supported me during the time period of my thesis.

I would also like to express my sincere gratitude to Pr. Patrick CHABRAND of l'Institut des Sciences du Mouvement from the Aix-Marseille Université and to Pr. Sébastien LAPORTE of l'Institut de Biomécanique Humaine Georges Charpak from the École National Supérieur d'Arts et Métiers for having accepted and granted their valuable time to review my PhD thesis.

I would equally like to express my sincere gratitude to the members of the jury Pr. Jean-François GANGHOFFER of Laboratoire d'étide des Microstructures et de Mécanique des Matériaux (LEM3) from the École Nationale Supérieur d'Electricité et de Mécanique (ENSEM), to Pr. Salah NAILI of Laboratoire Modélisation et Simulation Multi Echelle (MSME) from the Université Paris Est Créteil (UPEC), to Dr. Julien PAVIER of Nexter Munitions and to Dr. Nicolas PRAT of Institut de Recherche Biomécanique des Armées (IRBA) for having granted their time to exterminate my thesis and for having participated in the jury.

I would like to than the French Région Centre Val de Loire for having provided the funding required for this thesis. Meanwhile, I would like to express my sincere gratitude to Dr. Eric LESPESSAILLE (MD,PhD,PAST) of the Centre Hospitalier Régional Orléans for his valuable assistance in the High Resolution peripheral

Quantitative Computer Tomography (HR-pQCT) procedure.

I would also like to express my sincere gratitude to former head of the M2RI research masters program at polytech Tours, retired Pr. Narayanaswami Mohan Ranganathan , to Pr. Mame Williams-Louis of Université d'Orléans from Laboratoire Pluridisciplinaire de Recherche Ingénierie des systèmes, Mécanique, Énergétique, to Pr. S.H. Venkatasubramanian and to Pr. Ramesh D. Kandadai of SRM University, India for having encouraged me to pursue my career in research and to do my PhD.

I am grateful to my parents, siblings, friends and acquaintances who wished me the ultimate success. I consider myself nothing without them. They gave me enough moral support, encouragement and motivation to accomplish the personal goals. Most importantly for their help to learn french. Without their help, I could never imagine that I would speak french as fluent as I do today.

Préambule

Le thorax contient le cœur et les poumons qui sont les éléments principaux des systèmes respiratoire et circulatoire. Les fractures costales sont de fréquentes lésions causées par les accidents de la route ou des impacts balistiques à grande vitesse. Les fragments osseux créés par les impacts thoraciques peuvent blesser le cœur, les poumons, la plèvre, et conduire à des pneumothorax ou des hémothorax. Il est donc intéressant de développer une méthode de prédiction des fractures thoraciques sous des chargements de type impact dynamiques. De nos jours, les modèles biomécaniques humains basés sur la méthode des éléments finis (EF) sont de plus en plus employés pour analyser les mécanismes lésionnels. De tels modèles peuvent être utilisés comme substituts aux expérimentations réelles couteuses en temps et en ressources. En particulier, les modèles EF sont devenus des outils intéressants pour étudier la réponses des organes du thorax en conditions tant statiques que dynamiques et cela jusqu'aux impacts balistiques.

Un certain nombres d'études ont été réalisées pour étudier la réponse du thorax dans les crashs automobiles. Cependant, ces travaux ne permettent pas de connaître précisément la localisation de la fracture et le faciès de rupture, malgré les progrès réalisés. En effet, les modèles thoraciques restent simplifiés, car ils ne prennent pas en compte, d'une part, la progressivité de la fracture (propagation) couplée à l'endommagement du matériau, et d'autre part, la géométrie et l'hétérogénéité de la structure et du matériau. Il subsiste donc toujours un besoin de caractériser expérimentalement le comportement osseux en dynamique rapide pour identifier le mécanisme de la rupture et pour élaborer une loi de comportement réaliste implémentée dans un modèle EF innovant.

Objectifs

Dans cette thèse, nous nous intéresserons uniquement aux impacts non pénétrants. Afin de minimiser les risques d'apparition de lésions létales, il est nécessaire de :

1. Développer une méthodologie expérimentale spécifique pour caractériser la fracture en dynamique rapide sous impact non pénétrant.

2. Développer un modèle numérique tri-dimensionnel réaliste de la structure.

Verrous de la thèse

Pour atteindre les objectifs fixés pour la thèse, nous avons identifié que : (i) les propriétés mécaniques des constituants de la côte, (ii) la loi de comportement et la loi de l'endommagement, (iii) les effets de la vitesse de déformation, doivent être considérées avec une égale importance pour parvenir a une modélisation pertinente de la réponse de la structure osseuse.

Les verrous à lever sont les suivants :

- Propriétés mécaniques
  - Corrélation de la masse volumique apparente avec l'échelle des niveaux de gris ;
  - Définition des relations entre les propriétés (module d'Young, limite élastique, etc.) et la masse volumique ;
- Formuler la loi de comportement et de l'endommagement couplés.
- Implémenter cette formulation dans un code numérique adapté à la dynamique rapide.

Structure du mémoire de thèse

Le présent mémoire s'organise en cinq parties articulées en sept chapitres.

La **partie 1** présente l'état de l'art et l'étude bibliographique.

Dans le *chapitre 1,* nous présentons d'abord une description anatomique de la cage thoracique humaine, les conséquences cliniques des fractures des côtes et différentes échelles empiriques d'évaluation de la gravité des lésions thoraciques. Puis, certains éléments de biologie osseuse sont présentés.

La côte appartient à la catégorie des os plats. Elle a la forme d'un arc dont la ligne moyenne présente une certaine torsion entre ses deux extrémités. Les côtes les plus fréquemment sujettes aux fractures lors d'impacts rapides sont les troisièmes, quatrièmes, cinquièmes et sixièmes côtes. L'évaluation du la sévérité des lésions par les modèles présentés dans ce chapitre ne peuvent pas être utilisés dans cette thèse, car ils s'appliquent au thorax entier.

Concernant la composition biologique des tissus osseux, il existe neuf niveaux hiérarchiques. Parmi ceux-ci, nous n'en considérerons que deux : *l'os cortical* et *l'os trabéculaire* (niveau VIII) et la structure côte entière (niveau IX). Nous allons supposer que le “cortical” et le “trabéculaire” sont composés d’un matériau de même type. Ainsi, le comportement mécanique sera dû à la variation de l’architecture entre le cortical et le trabéculaire. Les propriétés de ce matériau (en particulier les propriétés élastiques) sont fondamentalement corrélées à la densité apparente. De plus, nous introduirons la dépendance de certaines propriétés (par exemple la déformation à la rupture) vis-à-vis de la vitesse de déformation.

L’influence de la géométrie de la côte sur sa réponse statique ou dynamique a conduit à des travaux de caractérisation sur la structure entière ou sur des segments isolés. Il a été montré que l’évolution des aires de section, des moments d’inertie, en fonction de la position, sont des paramètres importants pour analyser la réponse. Selon une étude largement citée (Granik and Stein, 1973) portant sur la réponse quasi-statique en flexion trois points de côtes humaine, la partie trabéculaire n’a pas d’influence sur la capacité de résistance à l’effort (chargement) de la côte. pourtant d’autres études soutiennent le contraire. Nous pensons donc que les modèles existants doivent être améliorés tant dans leurs représentation géométrique de la structure que dans leur formulation du comportement du matériau et de leur prédiction de la fracture. Ce triple objectif conduit au développement de modèles de *la structure isolée.* De plus, il n’existe quasiment pas de modèles permettant d’aborder le régime des vitesses de déformation $(\dot{\varepsilon})$[1] aux valeurs intermédiaires ($150\ \text{s}^{-1} \leq \dot{\varepsilon} \leq 1200\ \text{s}^{-1}$) ou élevées ($\dot{\varepsilon} > 1200\ \text{s}^{-1}$). Enfin, il nous paraît nécessaire de tenir compte simultanément de l’effet de l’accumulation de l’endommagement.

Dans la **partie II,** nous présentons l’exploitation d’un ensemble de résultats expérimentaux obtenus antérieurement au laboratoire. Ces données ont été obtenues lors d’une campagne d’essais de flexion trois points avec le montage des barres de Hopkinson. Tous les essais n’avaient pas été dépouillés et leur analyse n’avait été que partielle. Un début d’analyse avait été fait avec un modèle simplifié de géométrie et de comportement. Nous approfondirons l’analyse au moyen du modèle développé dans notre thèse. Parmi les côtes testées, 27 côtes on été considérées pour l’exploitation. Nous avons noté trois réponses différentes (pas de rupture, rupture pendant l’équilibre entre la force entrante et les forces sortantes, et rupture avant l’équilibre), qui sont liées à la vitesse relative des interfaces. Nous présenterons les résultats expérimentaux sous forme de 3 couloirs ou gabarits. Gabarit 1 : pas de fracture ; gabarit 2 : fracture pendant la phase d’équilibre de l’essai aux barres de Hopkinson ; gabarit 3 : fracture avant la phase d’équilibre (ou “hors équilibre”). A l’intérieur de chaque couloir, on note une variation des réponses due aux variations de la géométrie et des propriétés entre les échantillons réels.

Grâce à ces gabarits, nous constatons que le comportement de la côte apparaît comme élastique-viscoplastique, car la vitesse de déformation n’a pas d’influence

---

[1] également appelé taux de déformation

sur la partie linéaire de la réponse. De plus, le pic de force maximale n'influence pas la rupture. La rupture de la côte a toujours comme point de départ une fissure de la face inférieure (sollicitée en tension). Cette fissure se propage ensuite jusqu'au point d'impact.

La **partie III** concerne les simulations numériques. Elle se compose des chapitres 3 et 4.

Dans le chapitre 3, nous présentons la méthodologie suivie pour construire la structure numérique. Pour construire le maillage 3D, nous avons utilisé le module ScanIP du logiciel Simpleware pour traiter les images obtenues par imagerie à haute résolution (HR-pQCT). Ensuite, la masse volumique apparente ρ_{app} a été corrélée aux niveaux de gris (exprimée en Houndsfiled Units [HU]). Grâce a la masse volumique apparente, nous pouvons relier chaque niveau de gris à la la porosité Po. Les valeurs de porosité, nous permettent de distinguer le type de tissu osseux, puis de déterminer les propriétés mécaniques par des lois puissances. Les propriétés mécaniques des constituants de la côte de porc obtenues par cette méthodologie sont dans le même ordre de grandeur que celles utilisées pour les côtes humaines dans les études publiées antérieurement.

Le chapitre 4 présente la mise en place du modèle numérique du comportement et de l'endommagement. Nous avons constaté dans le chapitre 2 que la côte possède un comportement élastique-viscoplastique. Du point de vue numérique, l'effet de la vitesse de déformation au-delà de la limite élastique est décrit par le modèle de Cowper-Symmonds. Cependant, l'écrousissage peut être soit isotrope soit cinématique, et la loi d'endommagement peut être soit formulée de manière intrinsèque au comportement, soit externe à la loi de comportement. Dans le chapitre 4, nous présentons l'étude de trois formulations. Parmi celles-ci, deux utilisent un endommagement externe dépendant de l'état de contrainte et prenant en compte la vitesse de déformation. Ces deux formulations sont capables de prendre en compte l'évolution non-linéaire de l'endommagement (et donc la diminution de la rigidité de l'échantillon). Ensuite, nous présentons aussi l'algorithme de contact utilisé aux interfaces entre l'échantillon et les barres. De plus, l'échantillon contenant des parties ayant des propriétés mécaniques différentes, nous avons utilisé un autre algorithme de contact, grâce auquel, le solveur est capable de tenir compte de l'hétérogénéité de l'échantillon. *Au terme de notre étude,* nous avons choisi un comportement élastique-viscoplastique avec écrouissage isotrope pour l'os cortical et un comportement élastique-viscoplastique avec écrouissage cinématique pour l'os trabéculaire.

Le chapitre 5 de la **partie IV**, présente l'application du modèle numérique pré-

senté dans le chapitre 4 aux cas expérimentaux.

Nous nous intéresserons aux cas expérimentaux où la fracture se produit pendant la phase hors équilibre de l'essai aux barres de Hopkinson. Pour mettre en évidence l'influence de l'os trabéculaire sur la réponse dynamique, nous avons testé deux échantillons numériques différents (i) sans os trabéculaire et (ii) avec os trabéculaire. L'échantillon (i) montre une réponse bien plus rigide que l'échantillon (ii) pour la même vitesse donnée à l'impacteur. Cela prouve que l'os trabéculaire joue un rôle très important en participant à l'absorption des forces d'impacts.

La réponse numérique de l'échantillon numérique complet (os cortical et trabéculaire) a été calculée pour deux vitesses d'impacts différentes. Dans tous les cas, le modèle numérique est capable de reproduire la forme et l'amplitude moyenne des cas expérimentaux du gabarit 3. Une des réponses expérimentales est particulièrement proche du calcul numérique.

Enfin, les conclusions et les perspectives de ce travail sont présentées dans la **partie V**.

Mots Clefs : Impacts dynamiques, Côtes, Fracture, Barres de Hopkinson, Flexion trois points, Éléments-Finis, HR-pQCT, Élastique-viscoplastique, Endommagement, LS-Dyna.

french

Prologue

The thorax contains the primary elements of respiratory and circulatory systems. Rib fractures are frequent thoracic injuries that are caused by Road Traffic Accidents (RTA's) or High Speed Ballistic Impacts (HSBI's). The bone fragments or fractured ribs originating from chest injuries, may injure the heart or lung plural surface or the lung parenchyma, leading to pneumothorax or hemothorax. Therefore, it is important to develop a modeling method to predict the occurrence of thoracic fracture under impact situations. Nowadays, biomechanical human body Finite Element (FE) models play an increasingly important role in modeling injury mechanisms. Such models can be used as a substitute for time consuming and expensive experimental measurements. In particular, FE models of human thorax are becoming an important tool in the investigation of the structural responses of the thorax and the ribs under various static, dynamic and ballistic loading conditions.

A number of studies were performed to investigate the injury mechanisms of the ribs and the entire rib cage under dynamic loading for automotive crash simulation and injury analyses in the past. Nevertheless, they have failed to properly predict the fracture location and fracture profile. Despite the progress performed in this field, finite element models of the thorax and ribs are simplified and don't take into account the damage, the complete progressive nature of fracture, the precise geometrical representation of the ribs considering the cortical bone and trabecular bone regions and the heterogeneity of the material properties. Therefore, there is still need to characterize the dynamic fracture behaviour of the bone, to identify the fracture mechanisms of bone and to develop bone behaviour law and novel validated finite element model to predict the fracture conditions of ribs and thoraxes under high speed dynamic impacts.

Objectives

In order to reduce the risks of lethal injuries, it is necessary to:

1. Develop a specific experimental methodology in order to characterize accurately the bone fracture process (and the possible injury mechanisms) induced by dynamic blunt impacts on the chest at high velocities.
2. Develop a three dimensional numerical model of the bone tissue and structure able to simulate the fracture and to predict its occurrence in specific impact conditions (car accidents, falling of the person, ballistic impact). Such a numerical model will be used to guide the experimental studies and to reduce the costs of the experiments.

Problem Constraints

In order to address the objectives of this thesis, we had identified that the mechanical properties of bone constituents of rib, the parameters influencing the mechanical properties, constitutive and damage law, the effects of strain rate have to be given equal importance in such a way that the realistic behavior of rib is simulated as efficient as possible. The constrains addressed in this thesis are:

- Mechanical properties
    - Calibration of apparent density ρ_{app} with grey scale intensity CT_{bone}
    - Respective mathematical models to interpolate the mechanical properties with grey scale intensity CT_{bone}
- Simulation of wave propagation in bars.
- A realistic constitutive law coupled with a damage law.
- Contact algorithm.

Thesis structure

This thesis articulates around five main parts, divided into 7 chapters.

Chapter 1, presents an introduction to the human thorax, the clinical consequences of rib fractures and the existing evaluation methods for chest trauma, followed by the biological and mechanical aspects of rib, existing studies on human ribs and imaging methods used in this field of research.

A rib belongs to the flat bone category of the human skeletal system. It is curved and twisted structure that comprises a head, a body, and a tail. A rib articulates with the thoracic vertebrae with its head and a part of its neck at the anterior end and with the sternum through costal cartilage at the posterior end. Most common ribs prone to fracture under dynamic environment are the 3rd, 4th, 5th, and 6th. The injury severity evaluation models presented in this chapter could not be used in this thesis as they consider the whole thorax for a good prediction.

Regarding biological composition of bone tissues, a bone in general is a hierarchical structure with nine different levels of hierarchy. The concerns of this thesis are restricted to the level VIII (cortical and trabecular bone tissues) and level IX (whole structure) only. Several hypothesis have been put forth regarding the differences in the mechanical behavior of cortical and trabecular bone tissues. We embark with an assumption that these tissues are made of same morphological material *i.e.* same composition, thus the difference in their corresponding mechanical behavior is due to the difference in architectural arrangement. Therefore, the variables influencing the mechanical properties in this thesis are primarily the apparent density and the mechanical environment *i.e.* strain rate. Yet the variables regarding bone composition are considered to compare and verify the mechanical properties.

The geometrical constraints posed by bone samples have led to studies on characterization of whole bone structures or segments of bone structures. It has been proved that the anatomical location of the segments, the geometrical variables such as area moment of inertia or the cross sectional area of the geometry influence the mechanical behavior of these structures. The most cited study (Granik and Stein, 1973) on quasi-static three point bending of human rib segments concluded that the trabecular bone in the rib does not play an important role in load carrying capacity. Yet, recent studies have proved the contrary. The existing numerical models of human thorax do need developments in geometrical representation, mechanical behavior and fracture prediction. These constraints have led to the development of isolated rib models. Despite the existence of different numerical models, there are almost no numerical models in dynamic loading at intermediate ($150\ \mathrm{s}^{-1} \leq \dot{\varepsilon} \leq 1200\ \mathrm{s}^{-1}$) and high strain rate ($\dot{\varepsilon} > 1200\ \mathrm{s}^{-1}$). Moreover, there is a need for the development of models that consider the effects on strain rate in both mechanical behavior and damage accumulation as well.

Part II presents the processing of existing experimental data base obtained earlier at our laboratory during the master of Aubert (2012) and PhD thesis of Pavier (2013). This data was obtained from dynamic three point bending (3PB) experiments using the Split Hopkinson Pressure Bar apparatus for dynamic bending at our lab. Due to a lack of time, not every experimental data were processed, yet an initial analysis of the geometry and its approximation is presented. We present a deep analysis of this existing database in this thesis.

Among the porcine ribs tested, only 27 were considered to be worthy for post-processing. The experimental results of these ribs are classified into three different categories of response (no fracture, fracture during equilibrium between input and output forces and fracture before equilibrium), which are influenced by the relative interface velocity. All these results are presented in form of corresponding experimental corridors. Thanks, to this way of presentation, we identify that the rib shows an elasticviscoplastic behavior. Moreover, the rupture of the sample is due to a crack originating from the inferior surface (subjected to tension) and its propagation towards the point of impact. We do notice that the peak of the input force does not have an effect of the type of rupture observed, rather it is influenced by the local displacement and velocity of the sample at the interfaces.

The methodology adapted for numerical simulations is presented in **Part III** in two chapters.

Firstly, the generation of numerical rib sample is presented in *Chapter 3*. The 3D geometry of porcine rib is obtained High Resolution peripheral Computer Tomography (HR-pQCT) imaging technique. The geometry was reconstructed using the ScanIP module of the Simpleware software for the sake of FE mesh. Once the mesh is done, the apparent density ρ_{app} was correlated to the different greyscale values in (expressed in HU). Assuming that both, cortical and trabecular bones are made of same morphological material, we can calculate the porosity Po values corresponding to each grey scale. The Po values were the deciding factor for choosing power law equations for mechanical properties. The properties obtained from apparent density are in the same order of magnitude to that used be previous authors for human ribs. This thereby proves that the porcine rib a reliable biological surrogate and apparent density is a good measure of mechanical properties.

Secondly, the numerical considerations for the developments of the FE porcine rib model are presented in *Chapter 4*. This speaks about the constitutive law and damage law required for our rib and other aspects such as mesh size and contact algorithm.

The experimental results have shown that the rib shows elasticviscoplastic behavior. Therefore, we had tested three different constitutive laws, capable of considering the effects of strain rate on the post yield behavior through Cowper-

Symmonds model. Out the three laws tested, two necessitates coupling an external damage law for progressive fracture simulation. The so called external damage law is incremental and is dependent on the stress state in the sample. In addition to this, the damage law is also capable of considering non-linear damage accumulation, reduction in stiffness with increase in damage and the effects of strain rate on the fracture behavior of the sample.

The contact algorithm between sample and bar elements is presented at the end of this chapter. Apart for this, another contact algorithm is defined so that the solver considers the heterogeneity of the sample.

In fact, we have chosen elastiviscoplastic behavior with isotropic hardening for cortical bone whilst the trabecular bone is assigned with an elastiviscoplastic behavior with kinematic hardening.

The *Chapter 5* of **Part IV**, presents the application of numerical model put forth in *Chapter 4* to experimental cases.

The experimental case 3 is peculiar, since the experimental conditions do not permit the sample to establish an equilibrium. Therefore, we show keen interest in simulating this behavior. In order to understand the role of trabecular bone, we have tested two different samples (i) with no trabecular bone and (ii) with trabecular bone ("Composite sample"). The sample with no trabecular bone is too rigid compared to its counterpart when subjected to sample impact velocities. This proves that the trabecular bone in fact plays an important role in absorbing the impact forces and energies.

The composite sample was then tested at different impact velocities. In all cases, the numerical model is capable of producing results similar to corresponding experimental cases, but with little difference. This difference is in fact due to the difference in the geometry of experimental and numerical sample.

The conclusions and perspectives presented in **Part V**, conclude this PhD thesis.

Keywords: Dynamic Impacts, Ribs, Fracture, Split Hopkinson Pressure Bar, Three point bending, Finite Element simulations, HR-pQCT, Elastic-viscoplastic, Damage, LS-Dyna.

Contents

List of Figures

List of Tables

Nomenclature

Acronyms

3PB	Three Point Bending
BTT	Blunt Thoracic Trauma
CAP	Collagen - Apatite Porosity
ChT	Chest Trauma
CT	Computed Tomography
DAX	Dual-energy X-Ray Absorptiometry
HeT	Head Trauma
HR-pQCT	High Resolution - peripheral Quantitative Computed Tomography
HSBI	High Speed Ballistic Impacts
IA	Industrial Accidents
ITP	Inter Trabecular Porosity
LCP	Lacunar-Canalicular Porosity
MIL	Mean Intercept Length
MRI	Magnetic Resonance Imaging
pQCT	peripheral Quantitative Computed Tomography
PTT	Penetrating Thoracic Trauma
RTA	Road Traffic Accidents
VP	Vascular Porosity

Greek symbols

α	Ash fraction	%
α_{ij}	Center of the yield surface	
β_h	Hardening parameter	
$\boldsymbol{\sigma_I}$	Maximum Principal Stress tensor	Pa

$\boldsymbol{\sigma}^*_{ij}$	Trial stress tensor	Pa
$\boldsymbol{\sigma}^n_{ij}$	stress tensor from previous iteration	Pa
$\tilde{\boldsymbol{\sigma}}$	Effective stress of damaging material	Pa
Δx	Mesh size	m
$\Delta\varepsilon_{kl}$	Strain increment	
δ_{max}	Displacement at F_{max} of human rib segment	mm
$\dot{\varepsilon}$	Strain rate	s^{-1}
η	Stress triaxiality	
$\frac{1}{3}\mathrm{tr}\,\boldsymbol{\sigma}$	Hydrostatic stress	Pa
Γ	Mesh density	
λ	Desired wave length in FE mesh	m
ν	Poisson's coefficient	
ϕ	Yield function	
ρ_α	Apparent ash density	$\mathrm{kg.m^{-3}}$
ρ_{app}	Apparent density	$\mathrm{kg.m^{-3}}$
ρ_{bone}	Density of bone sample	$\mathrm{kg.m^{-3}}$
ρ_{dry}	Apparent dry density	$\mathrm{kg.m^{-3}}$
ρ_{rel}	Relative bone density	$\mathrm{kg.m^{-3}}$
ρ_{solid}, ρ_{tissue}	Density of mineralized bone tissue	$\mathrm{kg.m^{-3}}$
ρ_{wet}	Wet apparent density	$\mathrm{kg.m^{-3}}$
σ_{fRS}	Flexural strength of human rib segment	psi
σ_{ult}	Ultimate Strength	Pa
σ_{vm}	von-Mises Stress	Pa
σ_{y_0}	Initial yield stress	Pa
σ_y	Dynamic yield stress	Pa
Υ	Strain energy density release rate	
$\varepsilon(x,t)$	Strain in a section of bar	
ε^P_{eff}	Effective plastic strain	
ε_{fd}	Strain rate sensitive fracture strain	

ε_{fs}	Static fracture strain	
ε_f	Strain at failure	%
$\varepsilon_{inc}(t)$	Shifted incident wave in input bar	
$\varepsilon_{ref}(t)$	Shifted reflected wave in input bar	
$\varepsilon_{tr1}(t)$	Shifted transmitted wave in output bar	
$\varepsilon_{tr2}(t)$	Shifted transmitted wave in output bar 2	
ς	Strain energy release rate	
ξ_{ij}	Invariant of deviatoric stress components	Pa
ξ_{ij}^*	Trial invariant of deviatoric stress tensor	Pa
$f_h(\varepsilon_{eff}^P)$	Hardening function	

Injury Scoring Systems

AIS	Abbreviated Injury Scale
APACHE	Acute Physiology and Chronic Health Evaluation
GS	Glasgow Coma Score
ISS	Injury Severity Score
NISS	New Injury Severity Score
RTS	Revised Trauma Score
TRISS	Trauma and Injury Severity Score
TTSS	Thoracic Trauma Severity Score

Latin symbols

$2a$	Major axis at the cross-section	mm
$2b$	Minor axis at the cross-section	mm
α	Angle of the porcine rib sample	deg
CR	The ratio of numerical celerity to theoretical celerity	
C	1st Cowper-Symmonds parameter	Pa
c_b	Celerity of 1D longitudinal waves in nylon bar	m.s^{-1}
c_{FEM}	Celerity of longitudinal wave in FE mesh	m.s^{-1}
C_{ijkl}	Isotropic elastic tangent modulus matrix	Pa
c_{th}	Theoretical longitudinal wave celerity	m.s^{-1}

Ca	Calcium content	$\mathrm{mg.g^{-1}}$
D	Damage scalar	
E	Young's Modulus	Pa
e_c	Energy absorption capacity	$\mathrm{J.m^{-3}}$
E_{fRS}	Flexural modulus of human rib segment	psi
E_P	Plastic hardening modulus	Pa
E_{TAN}	Tangent modulus	Pa
F_{in}	Input force at the input bar sample interface	N
F_{max}	Maximum force observed	N
F_{out1}	Output force at the output bar 1 sample interface	N
F_{out2}	Output force at the output bar 2 sample interface	N
h_s	Cross-sectional thickness of the superior cortical bone	mm
h_i	Cross-sectional thickness of the inferior cortical bone	mm
I,I_b,I_c	Quadratic moments of inertia of human rib segment	$\mathrm{inches^4}$
K	Slope of the linear part of the force displacement response	$\mathrm{N.mm^{-1}}$
L	Length of human rib segment	inches
l	Anterior-Posterior length of the porcine rib sample	mm
m	Mass of the porcine rib sample	g
p	2^{nd} Cowper-Symmonds parameter	
P_{can}	Pressure in air canon	bar
R	Coefficient of reflection	
r	Damage effective plastic strain for MAT-105	
r	Radius of the porcine rib sample	mm
r_D	Damage threshold	
$R_v(\eta)$	Triaxiality function	
S_{ij}	Deviatoric stress components	Pa
S_{ij}^*	Trial deviatoric stress tensor	Pa
T	Coefficient of transmission	
t_{end}	Time corresponding to rapid decrease in force	s

t_{frac}	Shifted time corresponding to rupture	s
t_{max}	Time corresponding to maximum value of force	s
U	Relative interface displacement	mm
U_r	Relative interface displacement corresponding to rupture	m
V	Relative interface velocity	m.s^{-1}
v_c	Critical velocity	m.s^{-1}
V_f	Volume fraction	%
v_{in}	Input velocity at the input bar sample interface	m.s^{-1}
v_{out1}	Output velocity at the output bar 1 sample interface	m.s^{-1}
v_{out2}	Output velocity at the output bar 2 sample interface	m.s^{-1}
v_{str}	Striker velocity	m.s^{-1}
W_f	Energy absorbed at failure	J or N m
W_r	Energy absorbed by rib sample till rupture	J
Z_b	Mechanical impedance of bar material	
Z_s	Mechanical impedance of sample material	
Po	Porosity	%

Part I

Bibliographical Research

Chapter 1

State of the art

Résumé

Ce chapitre présente l'état de l'art et l'étude bibliographique. Nous présenterons d'abord l'anatomie de la cage thoracique, les conséquences médicales des fractures de côtes, les aspects biologiques et le comportement mécanique de l'os. Puis, nous présenterons les études existantes sur les côtes humaines et leurs substituts biologiques, les modèles numériques de la cage thoracique. Enfin, nous rappelons les différentes techniques d'imagerie à notre disposition dans le cadre de cette thèse.

En cas de fracture des côtes, il y a un risque important de pénétration des fragments osseux et de lésions complexes du cœur et du poumon. Plusieurs auteurs ont établi des méthodes d'évaluation de la gravité des traumatismes (échelle AIS par exemple) basées sur l'analyse clinique des blessures. Cette thèse se concentre sur le développement du modèle pour les côtes isolées. Comme, les méthodes d'évaluation de la gravité de traumatismes, l'appliquent au thorax entier, ces systèmes de notations ne peuvent pas être utilisés dans cette thèse.

Une côte humaine est composée de deux tissus osseux différents : le tissu cortical, qui entoure le tissu spongieux. La différence de comportement mécanique est due à l'agencement architectural de ces tissus. Les propriétés mécaniques de ces tissus sont influencées par l'âge, la composition, l'architecture et les sollicitations mécaniques de l'environnement.

Les études sur les côtes humaines traitent soient de côtes entières, soient de segments représentatifs de la variation géométrique des côtes. Aujourd'hui il existe

un nombre limité de travaux sur le comportement mécanique des côtes sous charge dynamique aux vitesses de déformation intermédiaires (1 [s^{-1}] $\leq$ $\dot{\varepsilon}$ $\leq$ 100 [s^{-1}]). *Cela entraîne un manque de compréhension des phénomènes se produisant en régime dynamique, en particulier de la fracture. De plus, les modèles numériques de thorax humain sont limités par les contraintes liées à la représentation géométrique et la description fiable du comportement jusqu'à la rupture complète.*

Parmi les techniques disponible aujourd'hui (IRM, DAX, CT, pQCT, HR-pQCT, etc.), le HR-pQCT convient à cette thèse car il donne une distribution volumique de la densité, des paramètres osseux spécifiques aux niveaux de la macro-structure et de la micro-structure.
french

Abstract:

This chapter presents the literature study concerning this thesis. First of all, we present the anatomy of thoracic cage, the consequences of rib fractures, the biological and mechanical characteristics of bones. This is followed by a detailed introduction to existing studies on human rib and its biological surrogates and also the existing numerical models on human thorax and ribs. We finish this chapter with an introduction to different imaging techniques used in the field of biomechanics.

There is a huge risk of penetration of the bone fragments and injuries to heart and lungs in the case of rib fractures. Several authors have established different evaluation methods for thoracic injuries (for example the AIS thoracic injury scale). These methods require to take the whole thorax into account. As this thesis deals with isolated ribs, unfortunately, these evaluation methods could not be used.

A human rib is composed of two different bone tissues: cortical and trabecular. These two tissues show different mechanical behavior, that arises due to the different in architectural arrangement. Moreover, the mechanical properties of bone tissues depend on age of the subject, the mineral composition, and the mechanical environment.

Very few studies could be found today concerning the fracture and behavior of human ribs. These studies concern either whole ribs or segments of ribs representing the geometrical variation of a rib. Yet, there is a void in studies concerning the behavior of human ribs under dynamic loads in the intermediate strain rate regime (1 [s^{-1}] $\leq$ $\dot{\varepsilon}$ $\leq$ 100 [s^{-1}])*, proving the lack of human knowledge in this regime.*

Several numerical models of human thorax and ribs were developed in recent years. These numerical models do come with their respective constraints. These so called constraints could be narrowed down to lack of geometrical representation and the use of reliable constitutive and damage law.

Among the imaging techniques used in the biomechanical field today (MRI, DAX, CT, pQCT, etc.), the HR-pQCT imaging technique is the most feasible for this thesis as it provides information on volumetric distribution of density and specific architectural parameters at both macro and micro scale.

1.1 Introduction to human thorax

The trunk of a human body is divided by the diaphragm into two parts, the upper part is called the thorax and the lower part is called the abdomen. The human thorax is supported by a skeletal framework called thoracic cage and contains vital respiratory and circulatory organs such as Lungs and Heart (Chaurasia, 2006). The thoracic cage is an osseocartilaginous elastic cage (see Fig. 1.1a), which is designed for increasing and decreasing intrathoracic pressure during inspiration and expiration of breathing process. It is formed by:

1. Sternum at the anterior end (Fig. 1.1b)

2. 12 Thoracic vertebrae and intervening intervertebral discs at the posterior end

3. 12 ribs on either sides, that articulate with the thoracic vertebrae of vertebral column (Fig. 1.1a).

    (a) Whilst, only 7 rib pairs articulate with the sternum at the anterior end, known as true ribs or vertebrosternal ribs (Fig. 1.1b).

    (b) The 8^{th},9^{th} and 10^{th} ribs articulate with vertebral column at posterior end and with sternum at anterior end through costal cartilages. Thus they are known as false ribs or vertebrochondral ribs (Fig. 1.1b).

    (c) The 11^{th} and 12^{th} ribs are known as floating ribs or vertebral ribs since they are free at the anterior end (Fig. 1.1b).

An interesting fact is that, the thoracic wall of infants is highly elastic hence, the rib fracture is rare. On the other hand, the rib fractures in adult may occur at its weakest point. The upper two ribs and the lower two ribs (floating ribs) are the least commonly fractured.

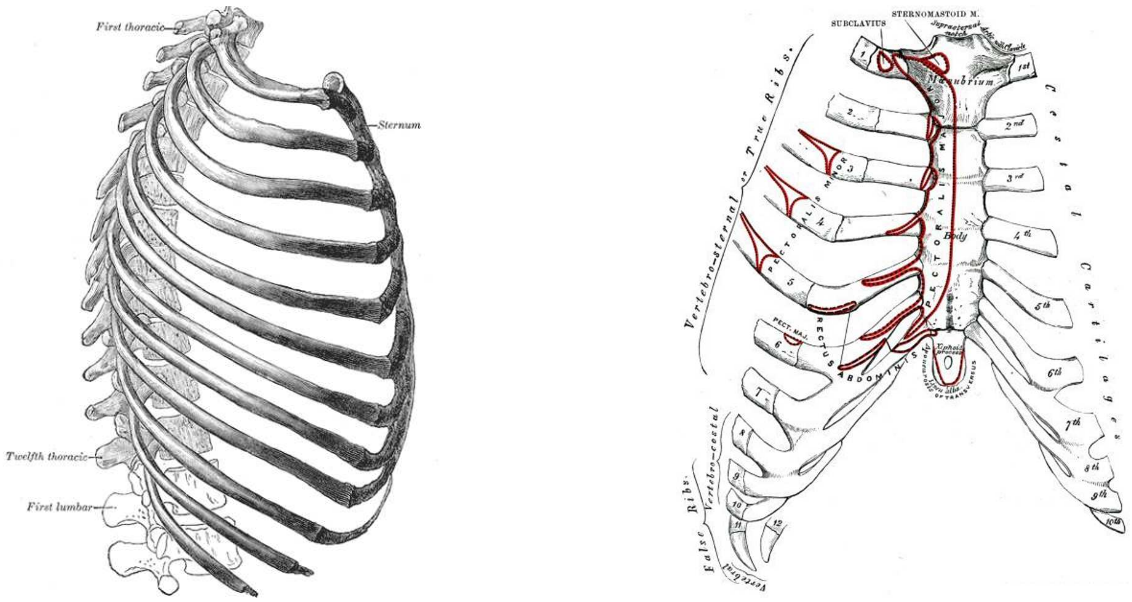

(a) Lateral perspective of the thoracic cage

(b) Anterior perspective of thoracic cage

Figure 1.1 – Lateral and anterior perspectives of thoracic cage
Gray and Lewis (1918)

1.1.1 Bones of the Thorax

Sternum

The sternum is a flat bone, forming the anterior-median part of the thoracic cage as in Fig. 1.2a. It supports the clavicle and articulates with first 7 pairs of ribs. It consists of *Manubrium*, *Gladiolus* and *Xiphoid Process* (Gray and Lewis, 1918)

1. *Manubrium*, is quadrilateral in shape. It is thick and broad above, narrow and thin at the junction with the Gladiolus. The Manubrium has an articular facet for the clavicle bone and a depression for the 1^{st} costal cartilage.

2. *Gladiolus*, is narrow, long and thin than the manubrium. It is the broadest close to its lower end (at facet for 5^{th} costal cartilage).

3. *Xiphoid Process*, is the smallest and thinnest of all the three components. It is less oscified when compared to other sternum components in adults, whilst it is a cartilaginous structure amongst the youth.

Thoracic Vertebrae

The thoracic vertebrae are intermediate in size, placed in between the cervical and lumbar regions. These vertebrae are distinguished by the demi-facets on the sides of body for articulation with the ribs of thoracic cages. They are thinner at the upper extremity and increase in size downwards (see Fig. 1.2b).

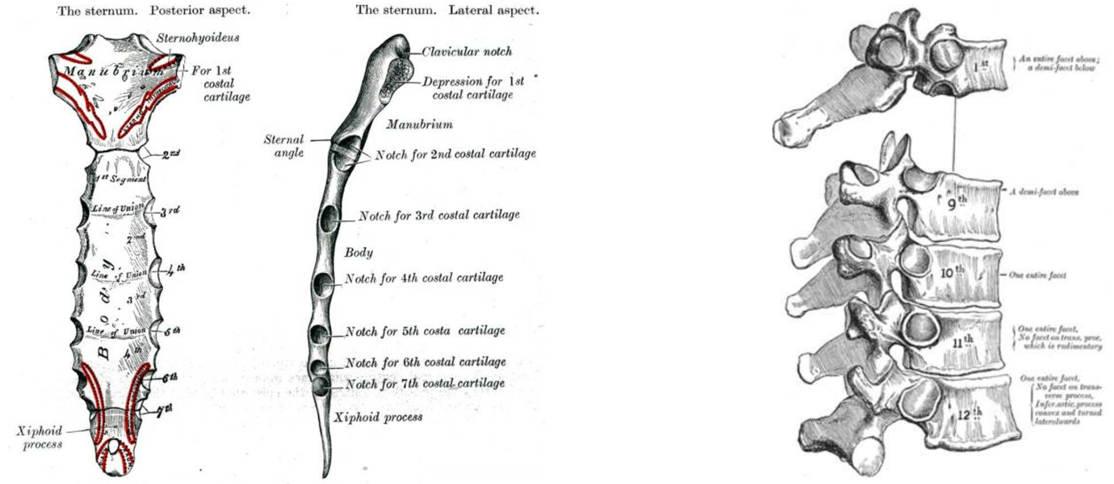

(a) Posterior and anterior views of human sternum

(b) A typical thoracic vertebrae

Figure 1.2 – Sternum and Thoracic Vertebrae
Gray and Lewis (1918)

Ribs

Rib are bony arches placed one below the other to form a thoracic cage. They can be classified as flat bones. An adult thoracic cage, consists of 12 pairs of ribs (as in Fig. 1.1a) that are classified into three categories:

- True ribs (1 to 7), are those which articulate with the sternum through corresponding coastal cartilage.
- False ribs (8 to 10), are those which articulate with the sternum but with only one single cartilage.
- Floating ribs (11 and 12), are those which do not articulate with the sternum. They a free to move, therefore to “float".

Each rib is supposed to consist three anatomical regions as in Fig. 1.3 (Gray and Lewis, 1918).

1. *Head*, is at the anterior side of the rib. It has two articular facets separated by a wedge. These articular facets help the rib to articulate with corresponding thoracic vertebrae and the one above it.

2. *Neck*, in particular has no biological importance. It just connects the head with rib body a point called the "*Tubercle*". This tubercle has one articular facet, that articulates with the corresponding thoracic vertebrae.

3. *Body* or *Shaft* of the rib is flat and curved with external and internal surfaces. The internal surface has a groove called "*Costal Groove*", which protects the intercostal vein, artery and nerve from external damage.

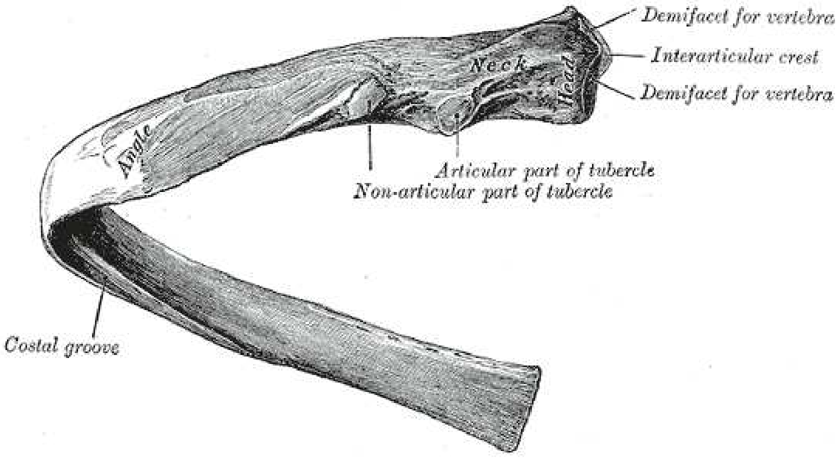

Figure 1.3 – Structure of a typical human rib
Gray and Lewis (1918)

As seen in Fig. 1.1a, ribs are oriented at a certain angle to the horizontal reference plane. The first rib has peculiar characteristics when compared to its counterparts in terms of orientation as it has a higher angle. In morphological terms, each rib is considered to be different since, the lengths and angle of orientation are not the same. Another common feature of human ribs is the transition of cross-sectional geometry, which is of circular cross-section from the head of the rib to the neck and seems to undergo a transition to elliptical cross-section at the neck and maintain it throughout the body.

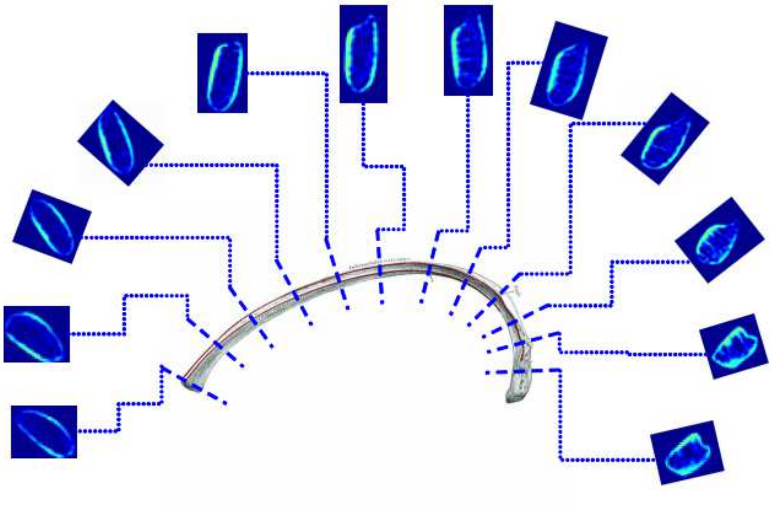

Figure 1.4 – Evolution of rib cross-section

The Fig. 1.4 shows that a rib is made of two different bone tissues. A quite porous tissue know as *trabecular bone*, surrounded by a thin layer of less porous tissue know as *cortical bone*.

1.1.2 Clinical relevance of rib fractures

Rib fractures are most common thoracic injuries, which are principal causative factors in Road Traffic Accidents (RTAs) (Cavanaugh et al., 1993) and in High Speed Ballistic Impacts (HSBIs) (Shen et al., 2006). The Chest Trauma (ChT) is one of the main contributors to the development of complications and mortality amongst poly-trauma patients (Horst et al., 2017). Among the organs of human thorax, lungs represent the target organ for secondary damage by post traumatic inflammation (Mommsen et al., 2011). Moreover, in some cases, lung injuries contribute to Multiple Organ Failure (MOF) and represents around 24% of late deaths after trauma (Dewar et al., 2013). For these reasons, ChT is considered to be the second most lethal right next to Head Trauma (HeT) (Ludwig and Koryllos, 2017).

One of the most recent case studies on ChT due to impacts, states that a ChT may arise either from a penetrating injury or a blunt injury (Arunan and Roodenburg, 2017). They have also investigated and put forth the evolution of critical condition of the victim with respect to time of accident. Evidences show that Blunt Thoracic Trauma (BTT) out ranks Penetrating Thoracic Trauma (PTT) since, it needs more attention and time for recovery Dewar et al. (2013), Arunan and Roodenburg (2017). Thus, in this thesis, we concentrate on BTTs only.

Several authors have investigated BTT through case studies, most of them state that RTAs is the common causative factor for BTTs Roux and Fisher (1992), Hamid and McManus (2011) and Blau et al. (2018). Apart from RTAs, Industrial Accidents (IAs) and Falls are other causative factors. In fact, the injury mechanism plays an important role in the severity of injury and critical condition of victim Burnside and McManus (2014) and Fallouh et al. (2017).

Assessment of an injury can be done using a scoring system, and there are a variety of scoring systems available today. These so called scoring systems can be classified on the basis of their predicting nature (*i.e.*) systems based on anatomical description of injury, systems based on physiological parameters and systems combining both anatomical and physiological factors. The later being the most commonly used in predicting of outcome after trauma (Chawda et al., 2004). The Tab. 1.1 presents the different trauma scoring systems available such as

- Anatomical scoring systems
    (a) Abbreviated Injury Scale (**AIS**)
    (b) Injury Severity Score (**ISS**)
    (c) New Injury Severity Score (**NISS**).
- Physiological scoring systems
    (a) Revised Trauma Score (**RTS**)
    (b) Acute Physiology And Chronic Health Evaluation (**APACHE**).
- Combined scoring systems
    (a) Trauma and Injury Severity Score (**TRISS**).
- Other scoring systems
    (a) Glasgow Coma Score (**GCS**)
    (b) Thoracic Trauma Severity Score (**TTSS**.)

Type	Scoring system	Variables used	References
Anatomical	AIS (general) AIS for thorax	dissipated energy threat to life permanent impairment treatment period incidence	Petrucelli et al. (1981) Chawda et al. (2004) Gennarelli and Wodzin (2006)
	ISS	3 most severe AIS body regions	Baker et al. (1974) Bull (1975) Moylan et al. (1976) Chawda et al. (2004)
	NISS	3 most severe AIS irrespective of body regions	Osler et al. (1997) Chawda et al. (2004)
Physiological	RTS	GCS Systolic blood pressure Respiratory rate	Champion et al. (1981) Champion et al. (1989)
	APACHE	12 variables	Knaus et al. (1981) Wagner and Draper (1984) Knaus et al. (1991)
Combined	TRISS	ISS RTS age	Chawda et al. (2004)
Other	GCS	values for response to motor response verbal response eye opening	Teasdale and Jennett (1974) Barlow (2012)
	TTSS	age, PF ratio chest wall injuries interthoracic injuries injuries to pleura	Pape et al. (2000) Aukema et al. (2011) Rai et al. (2018)

Table 1.1 – Different scoring systems

1.2 Bone biology

Bone is one of the building block of the human musculoskeletal system, that takes part in several roles such as protection, transmission of mechanical forces and serves as a mineral reservoir. Moreover, it is a determinant of the global structural stiffness.

Bone tissue is composed of organic materials, inorganic materials and water. The following minerals are the subcategories of above mentioned materials:

1. Organic materials
    (a) Type I collagen molecules in high concentrations
    (b) Type III, VI and V collagen molecules in less amounts (Keaveny et al., 2003; Reznikov et al., 2014)
    (c) Noncollagenous proteins such as osteocalcin, osteonectin, osteopontin and sialopretein.
2. Inorganic materials
    (a) Ceramic crystalline material in impure form, known as hydroxyapetite ($Ca_{10}(PO_4)_6(OH)_2$). It is considered to be impure because of the existence of potassium, magnesium, strontium, carbonate and chloride/fluoride. (Lowenstam and Weiner, 1989)
3. Water in different forms. It is bound to crystal surface at microscopic levels, in between the triple helix collagen molecules and also in fluid form. Water present in these three forms is known as bound water. Moreover, water can also be found in unbound form in canaliculi, lacunae and blood vessels.

The interesting properties of bone is due to its hierarchical structure, which is of nine levels according to Reznikov et al. (2014) as in Tab. 1.2. The materials and tissue array at each level is responsible for forming different tissues. For example, the lamellar packets of ordered and disordered units form the trabeculae, which is the structural element of the trabecular bone. Whereas, the osteon and fibrolamellar units form the cortical bone (Reznikov et al., 2014). Thereby, forming a composite structure seen at IX hierarchical level, referred as '*bone*' . Thus, at a macroscopic level, bone is non-homogeneous anisotropic and porous with two different tissues namely, cortical and trabecular.

It is clearly seen in Fig. 1.4 that a rib is composed by two different tissues: cortical and trabecular bone. Therefore, we are interested in biological and mechanical characteristics of the level VIII tissues (Tab. 1.2) in this thesis.

During their lifetime, cortical and cacellous bones are formed two different building blocks, namely *woven* and *lamellar* bone (see level VI of tab. 1.2 and Fig. 1.5). Both bones are composed only of woven bone during the embryo stage and initial stages of development (age $<$ 5 yrs) as well as during the fracture healing process. Later, the pockets of woven bones are replaced by lamellar bone. A woven bone is formed rapidly, poorly organized with random arrangement of collagen fibers and mineral crystals and is considered to be a transient tissue. Lamellar bone on the other hand, forms at a slow pace, is highly organized with parallel layers of lamellae, making it more stronger than its counterpart at level VI.

Level	Components			
I	Collagens, Hydroxyapetite, Non-Collagenous proteins			
II	Mineralized Collagen Fibrils			Interfibular Matrix
III	Ordered arrays of Fibrils			Mineralized fibrils
IV	Unidirectional array	Fanning arrays	Transverse isotropic arrays	Disordered Phase
V	Bundles			Cellular Network
VI	Lamellar Bone		Woven Bone	Parallel fiber bone
VII	Trabecula	Osteons		Fibrolamellar Matrix
VIII	Trabecular Bone	Cortical Bone		
IX	Whole Bone			

Table 1.2 – Hierarchical Organization of Bone
(Reznikov et al., 2014)

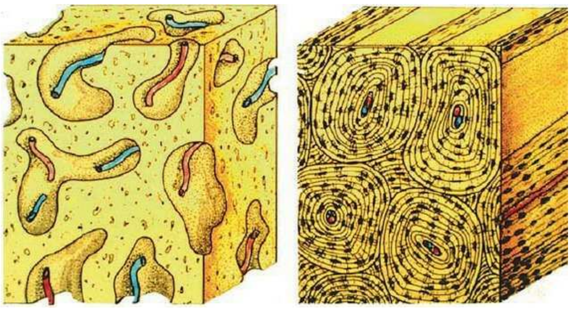

Figure 1.5 – Woven (to the left) and Lamellar (to the right) bone

Another aspect of bone is its self repairing through a process called remodeling. Bone remodeling occurs on surface of trabeculae of cancellous bone and at haversian system of cortical bone. The modeling and remodeling process of bones is carried out by a group of bone cells (*osteoblasts, osteoclasts, bone lining cells and osteocytes*), known as “Basic Multicellular Units” (BMU’s).

1.2.1 Level VIII tissues: cortical and trabecular

Cortical bone is in general more mineralized and less porous structure ($5\% \leq Po \leq 30\%$) . In the case of an healthy adult human, cortical bone exists in form of osteonal or Haversian bone *i.e.* an arrangement of 10-15 lamellae in concentric cylinders around the Haversian canal. These canals carry several blood vessels, nerves and blood cells which aide in communication with bone cells (see Fig. 1.6a). Since the bone tissue has the capacity of self repair through bone remodeling, the newly formed osteons are separated from the interstitial bone by a thin layer, known as cement line. This cement line forms a weak interface and is known to improve fatigue properties of cortical bone through microcraks, which server as reserves for energy dissipation during crack propagation (Keaveny et al., 2003).

The porosity associated with cortical bone are Vascular Porosity (VP) formed from the canals carrying bone fluids, nerves (osteon canals and Volkmann canals), Lacunar-Canalicular Porosity (LCP) arising from the spaces in canals such as lacunae and canaliculi and Collagen-Apatite Porosity (CAP) associated with the spaces between collagen and hydroxyapetite (S.C.Cowin, 1999) (see Fig.1.6b). Cortical bone exists at the shafts of long bone such as femur or as an external shell around the trabecular bone in flat or short bones such as ribs or vertebrae.

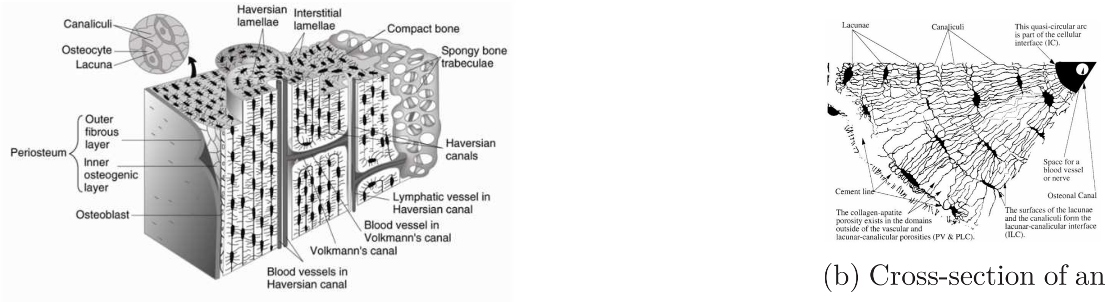

(a) Haversian canals in human cortical bone (Tortora and Nielsen, 1983)

(b) Cross-section of an osteon (S.C.Cowin, 1999)

Figure 1.6 – Cortical bone

Trabecular bone is less mineralized and more porous as opposed to cortical bone. It is a structure formed by interconnecting trabeculae with ($45\% \leq Po \leq 90\%$). The most distinguished characteristic of trabecular bone is its porosity resulting from voids external to mineralized trabeculae, known as Inter-Trabecular space porosity (ITP), represented by voids in Fig.1.7. These so called 'trabeculae' exist either in forms of rods or plates, depending on the need for force absorption. For example, the trabecuale in the human femoral neck (as in Fig. 1.7c) are in form of plates where as they exist in form of both rods and plates in the human vertebrae (as in Fig. 1.7d).

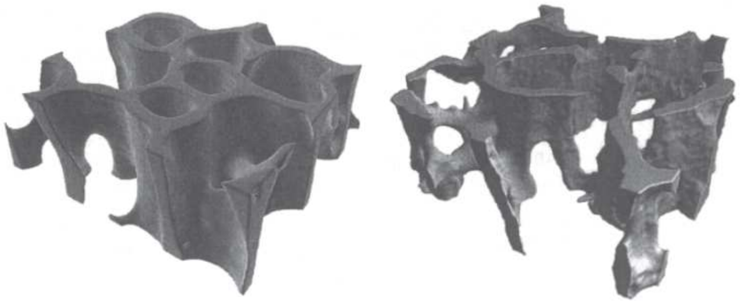

(a) Bovine proximal tibia (b) Human proximal tibia

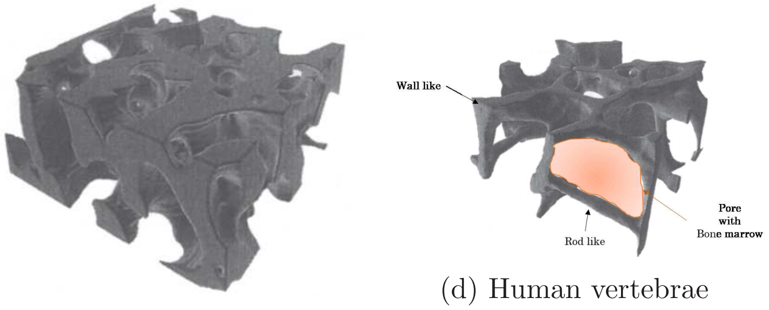

(d) Human vertebrae

(c) Human femoral neck

Figure 1.7 – Trabecular bone at different anatomical sites
(Keaveny et al., 2003)

1.3 Mechanical insights on bone

Mechanical behavior of cortical and trabecular bone

We had seen the variables influencing mechanical properties of bone in Sec. 1.3. Most of the research data presented were either on isolated cortical or on trabecular bone samples. These data suggests that there is an essential difference between the mechanical behavior of these two tissues. Quite a few authors suggest that these are two different tissues and thus the difference in mechanical behavior. On the other hand, these two tissues are based on the same morphological tissue, but the difference in mechanical behavior is due to the difference in architectural arrangement.

For example, cortical bone shows a behavior corresponding to elastic-plastic where as the trabecular bone shows behavior similar to that of polymeric foams.

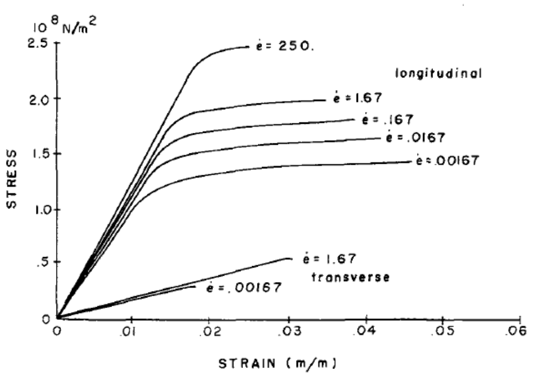

(a) Cortical bone
(Crowninshield and Pope, 1974)

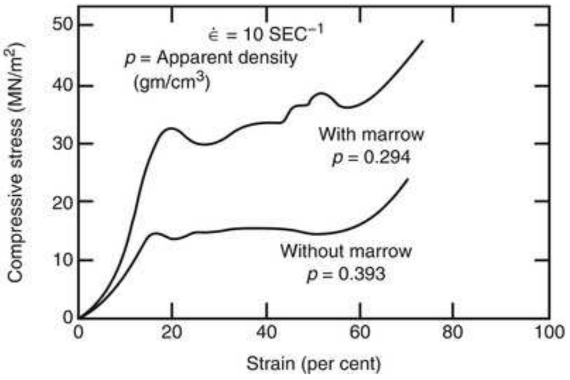

(b) Trabecular bone
(Carter and Hayes, 1977)

Figure 1.8 – Mechanical behavior of cortical and trabecular bone

Another main difference between the mechanical behavior of cortical and trabecular bone is in their post yield response to loading-reloading tests.

Cortical bone

1. It exhibits mechanical properties degradation due to damage accumulation, thus it's post yield response is damage related.
2. It has a relatively low yield offset point and can be determined by standard yield offset technique (0.2%).
3. When reloaded beyond yield point, the initial modulus is not the same as its intact modulus (see Fig. 1.9a) .
4. According to Keaveny et al. (2003), the microdamage patterns include microcracks in longitudinal and transversal directions, cross-hatched shear band patterns and damage diffusion.

Trabecular bone

1. It exhibits loss of stiffness and permanent strains.
2. It starts to yield at ≈ 1% and can sustain large deformations upto 50%.
3. It reloading modulus is close to intact modulus but loses its stiffness rapidly (see Fig. 1.9b) .
4. This does not depend on volume fraction since similar response can be seen in bovine trabecular bone (as in Fig. 1.7a (Keaveny et al., 2003).
5. Therefore, there is an evidence of residual strain and back stress.

These data suggest that cortical bone can be modeled as transverse isotropic material with isotropic hardening and trabecular bone can be modeled as an anisotropic material with kinematic hardening.

In either cases simple yield criteria such as von-Mises yield cannot be applied for cortical and trabecular bone materials, since they show evidences of more strength in compression with respect to tension. Moreover, damage seems to play an important role in post yield behavior, thereby suggesting the use of damage dependent yield and progressive failure criteria.

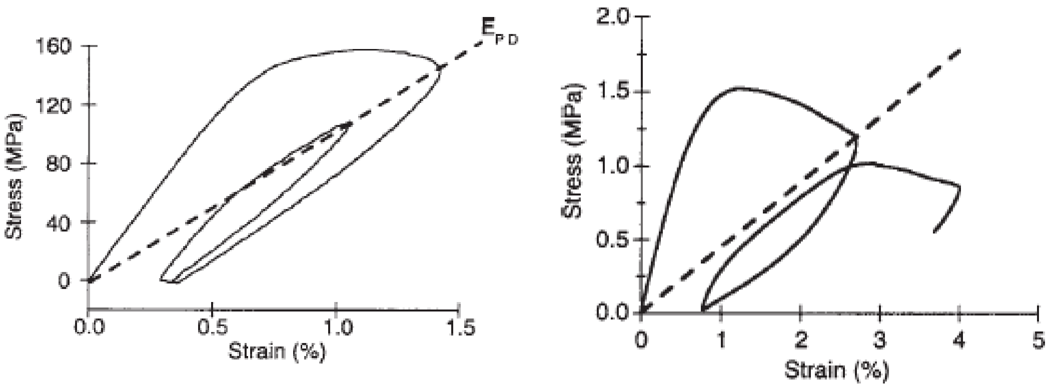

(a) cortical bone

(b) trabecular bone

Figure 1.9 – Loading-reloading response of cortical and trabecular bone (Keaveny et al., 2003)

Variables influencing mechanical properties of bone

In order to understand the behavior of bone under certain mechanical conditions, it is important to quantify its mechanical properties and corresponding variables influencing it. Since bone can adapt it self by remodeling, its properties change with respect to age, diseases and the mechanical environment it is subjected to. Therefore, it is important to quantify the mechanical properties before understanding its mechanical behavior.

Age

As said above, certain authors have investigated the influence of age on the variation of mechanical properties (Young's modulus (E) , ultimate strength (σ_{ult}) , energy absorbed at failure (W_f) and strain at failure (ε_f)). For example, Currey (1979) had postulated that the energy absorbed at failure decrease with increase in age. This is since the ash content of bone increases with increase in age. Later, Currey et al. (1996) had stated that "*there is a strong decrease in properties with increase in ash content of bone, but other factors such as age are probably also responsible for deterioration of bone properties*". In contrast, Leng et al. (2013) have shown that E and σ_{ult} (tensile) are age and orientation dependent *i.e.* there was a decrease in these properties in longitudinal and transversal directions with ageing as opposed to McCalden et al. (1993) and Wang et al. (2002). This peculiar behavior was correlated to the collagen matrix in cortical bone. However, the effects of ageing on mechanical properties of bone are still ambiguous.

Bone composition

The next parameter supposed to influence the mechanical properties of bone is its composition. A question often posed is *which density is the appropriate independent variable characterizing mechanical properties of bone ?*. There are different measures of densities, which are either measured directly or indirectly correlated with QCT images.

1. Apparent dry density (ρ_{dry})[1], is the ratio of dry specimen mass to specimen volume
$$\rho_{dry} = \frac{\text{Dry specimen mass}}{\text{specimen volume}} \tag{1.1}$$

2. Apparent wet density (ρ_{wet}), is the ratio of hydrated specimen mass to specimen volume
$$\rho_{wet} = \frac{\text{hydrated specimen mass}}{\text{specimen volume}} \tag{1.2}$$

---

[1] represented as ρ_{app} in this thesis.

3. Apparent ash density (ρ_α), is expressed in terms of ash fraction and apparent dry density as

$$\rho_\alpha = \alpha\rho_{dry} \tag{1.3}$$

where α is the ash content of a bone, defined as the ratio of ash weight to dry specimen weight.

The studies concerning the influence of bone composition on it mechanical properties could be grouped as per the variables used.

Group 1: ash fraction (α)

Two most cited studies in this group are Vose and Kubala (1959) and Currey J.D (1969). The equations put forth by them are presented in Tab. 1.3.

Author	Origin	variable	E	σ_{ult}
Vose and Kubala (1959)	human	α	-	$1.304e^{0.202\alpha}$
Currey J.D (1969)	wild rabbit	α	$197.32\alpha - 11.85$	$1.75\alpha - 100.47$

Table 1.3 – α based equations

Group 2: ash density (ρ_α)

Quite a few other authors have had investigated the influence of apparent ash density ρ_α on E and σ_{ult}. Among the authors of this group, Keller (1994) and Keyak et al. (1994). The Tab. 1.4.

Author	Origin	variable	E	σ_{ult}
Keller (1994)	human	ρ_α	$10500{\rho_\alpha}^{2.37}$	$117{\rho_\alpha}^{1.93}$
Keyak et al. (1994)	wild rabbit	ρ_α	$33900{\rho_\alpha}^{2.2}$	$137{\rho_\alpha}^{1.88}$

Table 1.4 – ρ_α based equations

Note: Keller (1994) used pooled data of cortical and trabecular bone samples from human vertebrae and femur, leading to a conclusion that ρ_α explained over 96% of variations in mechanical behavior. Whereas Keyak et al. (1994) used trabecular bone samples from human proximal tibia, leading to the conclusion that ρ_α had the strongest correlation.

Group 3: apparent density (ρ_{app})

Apart from mineral content, apparent density was also considered as control variable by several authors. Galante et al. (1970), had investigated the effect of apparent density ρ_{wet} on compressive strength σ_{ult} of cancellous bone sample extracted from human vertebrae. They concluded that "*porosity Po is a major factor in determining* ρ_{wet}*, which in turn influences* σ_{ult}". Moreover, their tests proved that σ_{ult} showed a positive linear correlation with ρ_{wet}. This was backed up by Carter.D.R and Hayes.W.C (1977), who had proved that $E \propto {\rho_{wet}}^3$ and $\sigma_{ult} \propto {\rho_{wet}}^2$.

Rice et al. (1988) put forth a pooled data in concern of the dependence of Elastic Modulii and strength on the apparent density. For their Young's Modulus estimates, the authors had used a pooled data from (Carter.D.R and Hayes.W.C, 1977; Bensusan.J.S and Verdin.D.J, 1983; Williams and Lewis, 1982). They came to a conclusion that the Young's Modulus of Human Cancellous bone depends on square of apparent density (see table:1.5)

Species	Orientation	Axial Stress Direction	Young's modulus
Human	Longitudinal	Tension	$0.07\ +\ 1.65\,{\rho_{app}}^2$
	Medial/Lateral	Compression	$0.07\ -\ 0.70\,{\rho_{app}}^2$
		Tension	$0.07\ +\ 0.13\,{\rho_{app}}^2$
	Anterior/Posterior	Compression	$0.07\ +\ 0.10\,{\rho_{app}}^2$
		Tension	$0.07\ +\ 0.93\,{\rho_{app}}^2$

Table 1.5 – Young's modulus E [GPa] as a function of apparent density as put forth by Rice et al. (1988)

In the case of compressive strength, the data were taken from Galante et al. (1970), Behrens et al. (1974), Carter and Hayes (1977), Williams and Lewis (1982) and (Bensusan.J.S and Verdin.D.J, 1983). Similar to Young's Modulus estimations, the axial compressive strength (σ_{ult}) too depends on square of apparent density.

Species	Orientation	Method	Equation σ_{ult}(MPa)
Human	Longitudinal	Confined	$2.45\ +\ 32.66{\rho_{app}}^2$
		Unconfined	$2.45\ -\ 3.04{\rho_{app}}^2$
	Transverse	Confined	$2.45\ +\ 15.40{\rho_{app}}^2$
		Unconfined	$2.45\ -\ 20.30{\rho_{app}}^2$

Table 1.6 – Compressive strength as a function of apparent density, put forth by (Rice et al., 1988)

As both Young's Modulus and Strength (Compressive & Tensile) are dependent on the square of apparent density, they are proportional to each other. This proportionality was also substantiated by Currey et al. (1996), Brown.T.D and Ferguson.A.B (1980) and Bensusan.J.S and Verdin.D.J (1983).

Apart from this, they also proposed extrapolated equations of dependence of mechanical properties of Compact bone on apparent density in contradiction to Wolff's statement:

"*Compact bone is simply more dense than Cancellous Bone*"

Whilst Galante et al. (1970), Carter.D.R and Hayes.W.C (1977), Gibson (1985) and Rice et al. (1988) have investigated the isotropic behavior of cortical and cacellous bones, some authors have also presented evidences of transverse isotropic behavior of bone. For example, Lotz et al. (1991) have carried out three point bending tests on rectangle sample extracted from metaphyseal shell of proximal femur and femoral diaphysis. They had considered ρ_{app} as a control variable to study its influence on longitudinal, transversal Young's modulus (E_{long}, E_{trans}) and longitudinal, transversal compressive strength ($\sigma_{ult,l}$, $\sigma_{ult,t}$).

Property	Orientation	Equation
E, MPa	Longitudinal	$2065{\rho_{app}}^{3.09}$
$\sigma_{ult,l}$, MPa		$72.4{\rho_{app}}^{1.88}$
E, MPa	Transverse	$2314{\rho_{app}}^{1.57}$
$\sigma_{ult,t}$, MPa		$37.0{\rho_{app}}^{1.51}$

Table 1.7 – Mechanical properties as a function of apparent density as put forth by (Lotz et al., 1991)

They had concluded that "*The difference between global average values of longitudinal and transverse properties is due to the difference in density and decrease in transverse anisotropy.*"

Similar to Lotz et al. (1991), Keaveny (2001) had presented the variation of properties in longitudinal and transverse directions for trabecular bone as follows:

Property	Orientation	Equation
E, MPa	Longitudinal	$1904{\rho_{app}}^{1.64}$
$\sigma_{ult,l}$, MPa		$40.8{\rho_{app}}^{1.89}$
E, MPa	Transverse	$1157{\rho_{app}}^{1.78}$
$\sigma_{ult,t}$, MPa		$21.4{\rho_{app}}^{1.37}$

Table 1.8 – Mechanical properties of trabecular bone, poposed by Keaveny (2001)

On the other hand, Gibson (1985) stated that cancellous bone is a cellular structure connected with a network of rods or plates. She had quantified the dependence of mechanical properties to relative density ρ_{rel}, expressed as follows:

$$\rho_{rel} \ = \rho_{bone}/\rho_{solid} \tag{1.4}$$

where ρ_{bone} is the density of the cancellous bone sample and ρ_{solid} is the density of solid bone in the cell wall. Based on ρ_{rel}, she had classified the type of cellular structure exhibited by cancellous bone.

$$\text{Cellular structure} \begin{cases} \text{Open cell (rod like)} & \text{if } \rho_{rel} \ < \ 0.2 \\ \text{Closed cell (plate like)} & \text{if } \rho_{rel} \ > \ 0.2 \end{cases}$$

Each cellular structure appears to exhibit either symmetry or no symmetry, therefore, resulting in 4 structures (asymmetric cells with open cell structure, asymmetric cells with closed cell structure, columnar cells with open cell structure and columnar cells with closed cell structure).

She had then performed compression tests on samples in order to correlate mechanical property, mechanism of deformation with ρ_{rel}.

- Asymmetric cells:
    - with open cell structure showed that the young's modulus E and ultimate stress in compression σ_{ult} are proportional to the square of relative density ($\propto \ \rho_{rel}{}^2$).
    - with closed cell structure showed that the young's modulus E and ultimate stress in compression σ_{ult} are proportional to the cube of relative density ($\propto \ \rho_{rel}{}^3$).
- Columnar cells:.
    - For both open and closed cells, the young's modulus and ultimate stress in compression along longitudinal direction were proportional to relative density ($\propto \ \rho_{rel}$).

Group 4: Two variables

The models presented above are single parameter models *i.e.* they consider either mineral composition (α) or apparent density (ρ_{app}) as control variables. On the other hand, several authors have proposed two parameter models. For example, Currey (1988) had proposed both power law and linear regression models to explain the variation of Young's modulus (E) with respect to calcium content (Ca mg.g^{-1}) and volume fraction (V_f %) of cortical bone samples extracted from various mammals and birds. The volume fraction (V_f) is expressed in terms of ρ_{app} and ρ_{tissue} as

$$V_f = \frac{\rho_{app}}{\rho_{tissue}} \tag{1.5}$$

He had concluded that "*Young's modulus shows a positive correlation with both calcium content and volume fraction*" and "*power law regression seems to fit the data better than linear equations*". His results are given in Tab. 1.9

Model	Tension	Bending
Linear	$E = -71.2 + 0.197Ca + 42.5V_f$	$E = -52.3 + 0.143Ca + 35.3V_f$
Power law	$\log_{10}E = -6.30 + 3.17\log_{10}Ca + 3.52\log_{10}V_f$	$\log_{10}E = -4.84 + 2.55\log_{10}Ca + 3.13\log_{10}V_f$

Table 1.9 – Two variable models for variation of E Currey (1988)

Although the models presented by Currey (1988), Keller (1994) and Keyak et al. (1994) were capable of explaining the fact that the mechanical properties of bone depend both on ρ_α and ρ_{app}, their models did not separate the effects of each individual variable. This so called drawback was brought into light by Hernandez et al. (2001), who had formed an equation for true tissue density ρ_{tissue} based on data of Keller (1994) as follows

$$\rho_{tissue} \approx 1.41 + 1.29\alpha \tag{1.6}$$

V_f can be expressed in terms of α as

$$V_f = \frac{\rho_{app}}{1.41 + 1.29\alpha} \tag{1.7}$$

Based on α and v_f from Eq. (1.7), they had proposed a two variable power law regression models for E and σ_{ult}

$$E\,[\mathrm{GPa}] = 84.37{V_f}^{2.58}\alpha^{2.74} \tag{1.8}$$

$$\sigma_{ult}\,[\mathrm{MPa}] = 794.33{V_f}^{1.92}\alpha^{2.79} \tag{1.9}$$

We can notice that most of the regression models presented above are either based on uniaxial compression or three point bending, as the tensile properties are usually expressed in percentages of compressional properties. Several authors have investigated and presented different values for the ratio of tensile to compressive properties. In fact, this ratio depends on the origin of the sample, test direction and type of bone tissue tested (Reilly and Burstein, 1975). A list of studies in concern with the ratio between tensile and compressive properties is given in Tab. 1.10. Even though this ratio seems to vary between 0.33 and 1.27 depending on the anatomical location, type of bone tissue and origin of test sample, Keyak and Rossi (2000) had considered this ratio to be a constant and is best when considered between 0.7 and 1.0.

Author	Origin	Anatomical location	Bone type	Load direction	Ratio[2]
Reilly and Burstein (1975)	human	cortex	cortical	longitudinal transverse	≈ 0.7 ≈ 0.5
Carter et al. (1980)	human	proximal femur	trabecular	longitudinal	1.0
Stone et al. (1983)	bovine	humerus	trabecular	longitudinal	≈ 0.33
Neil et al. (1983)	human	lumbar spine	trabecular	longitudinal	1.0
Kaplan et al. (1985)	bovine	proximal humerus	trabecular	longitudinal	≈ 0.62
Røhl et al. (1991)	human	proximal tibia	trabecular	longitudinal	≈ 1.27
Keaveny et al. (1994)	bovine	tibia	trabecular	-	≈ 0.72

Table 1.10 – Ratio of tensile to compressive properties of bone

Bone Organization

Bone samples have same bone composition *i.e.* similar density or porosity and mineralization can show different material properties, this difference can be backed up by a difference in organization of bone tissues at different levels of Tab. 1.2. These organizational factors contribute to the anisotropic behavior of bone.

Cortical bone architecture

Cortical bone in general, is a solid structure with osteons and canals immersed in its matrix. The orientation of these osteons describes the anisotropic nature of cortical bone. Since the principle direction of these osteons is along the longitudinal axis, cortical bone is more strong along longitudinal direction than transverse direction. Apart from osteons, the circumferential lamallae (as in Fig. 1.5) do exhibit different material properties in radial and tangential directions. According to Reilly and Burstein (1975), this structure is influenced by secondary osteons, therefore cortical bone has transverse isotropic nature.

Trabecular bone architecture

In contradiction to cortical bone, trabecular bone is dominated by voids with little space occupied by trabeculae. The anisotropic nature of trabecular bone is better described by the orientation of these trabeculae. Several authors have presented different hypothesis regarding the influence of trabecular orientation on its mechanical properties. Whitehouse (1974) was the first to propose a methodology to measure the microscopic anisotropic structure of trabecular bone in terms of distance between bone marrow and trabeculae, known as 'Mean Intercept Length (MIL)' . Later, Cowin (1985) proposed a relation between the elastic tensor and a second order tensor called fabric tensor. The Fabric tensor is expressed as the inverse square root of the MIL tensor. The major assumption considered by Cowin (1985) is the matrix material is isotropic in order to calculate the anistropic nature arising from different orientations of the matrix materials (trabeculae). This hypothesis was used to put forth an anisotropic strength criterion depending on the fabric tensor by Cowin (1986). The fabric dependence anisotropic nature of trabecular bone was then validated by Turner et al. (1990).

Mechanical environment

Other parameters influencing the mechanical properties of bone is the mechanical environment in which it is supposed to function. For example, bone behaves differently in static, quasi-static and dynamic environments, therefore, there is an influence of strain rate ($\dot{\varepsilon}$).

McElhaney (1966) was probably the first and the most cited article in this concern. He had studied these effects through compression test on bone samples form a 3 year old bovine femur and a 24 years old male femur using an air gun under $\dot{\varepsilon} \in [0.001\,s^{-1}, 1500\,s^{-1}]$. Properties like ultimate stress (σ_{ult}), energy absorption capacity (e_c) , Young's modulus (E), strain at failure (ε_f) were studied. The variation in these properties were studied in terms of a critical velocity (v_c) [3]. In case of bone, v_c occurred when $\dot{\varepsilon} \in [0.1\,s^{-1}, 1\,s^{-1}]$. He had also pointed out that $\dot{\varepsilon}$ also had an influence on fracture mechanism. The average values of these properties are given in Tab. 1.11. It can be noticed that as $\dot{\varepsilon}$ increased, e_c begins to increase in the begining and shows a drastic decrease for $\dot{\varepsilon} \in [0.1\,s^{-1}, 1\,s^{-1}]$. On the other hand, ε_f tends to decrease but shows a drastic decrease for $\dot{\varepsilon} \in [0.1\,s^{-1}, 1\,s^{-1}]$. This shows that the critical velocity v_c for bovine femur bone exists for $\dot{\varepsilon} \in [0.1\,s^{-1}, 1\,s^{-1}]$.

---

[3] critical velocity occurs when a material property exhibits large variations over a small range of $\dot{\varepsilon}$, McElhaney (1966)

Another peculiar results to be noted from the results of McElhaney (1966) is that both σ_{ult} and E continued to increase with increasing $\dot{\varepsilon}$. Moreover, McElhaney (1966) had stated that stress at a particular strain level, can be related to the corresponding strain rate with an exponential as in Eq. 1.10.

$$\sigma = A\mathrm{Ln}(\dot{\varepsilon}) + B \tag{1.10}$$

where, A and B are constants determined from experimental data. $A = 2.96 \times 10^7\,\mathrm{Pa.s^{-1}}$ and $A = 2.68 \times 10^8\,\mathrm{Pa}$ for bovine femur bone. [4]

Strain rate $\dot{\varepsilon}$, [s^{-1}]	σ_{ult}, [MPa]	e_c, [J.m^{-3}]	E, [GPa]	ε_f, [%]
0.001	175.81	9.68×10^6	18.61	1.88
0.01	206.84	1.15×10^7	19.99	1.82
0.1	230.97	1.16×10^7	24.13	1.75
1	251.65	7.20×10^6	27.57	1.25
300	282.68	6.36×10^6	33.09	1.00
1500	365.42	6.09×10^6	42.05	0.90

Table 1.11 – Average data for bovine femur bone
(McElhaney, 1966)

Increase in young's modulus with increasing strain rate was also reported by Crowninshield and Pope (1974), Currey (1975), Wright and Hayes (1976) and Hansen et al. (2008). On the other hand, a decreasing effect was reported by Ferreira et al. (2006) whilst Pithioux et al. (2004) had reported no correlation.

Similar to Young's modulus, several authors have reported the effect of strain rate on post yield behavior (yield stress and yield strain). For example, Crowninshield and Pope (1974) and Currey (1975) have reported an increasing correlation with increasing strain rate as opposed to Hansen et al. (2008), who had observed a decreasing correlation.

McElhaney (1966), Crowninshield and Pope (1974), Pithioux et al. (2004) have reported a decreasing trend in fracture strain with respect to increasing strain rate for cortical bone. Guedes et al. (2006) had reported an increasing trend in fracture strain with respect to increasing strain rate for trabecular bone.

Whilst the authors mentioned above have reported the effects of strain rate on isolated cortical and trabecular sample, Wood (1971) had investigated the behavior of human cranial bone samples extracted from male subjects with age between 25

---

[4] note: Ln denotes natural logarithm

yrs to 95 yrs (with bith cortical and trabecular). These samples were subjected to a tensile load for $\dot{\varepsilon} \in [0.005\,s^{-1}, 150\,s^{-1}]$. Properties like ultimate stress (σ_{ult}), energy absorption capacity (e_c), Young's modulus (E), strain at failure (ε_f) were studied. The regression models proposed by Wood (1971) are given in Tab. 1.12

Property	regression equation
E, GPa	$15.99 + 1.93\text{Ln}\dot{\varepsilon}$
σ_{ult}, MPa	$0.0826 + 6.94\text{Ln}\dot{\varepsilon}$
ε_f, %	$0.63 - 0.04\text{Ln}\dot{\varepsilon}$
e_c, kg.m^{-3}	1.179×10^6

Table 1.12 – Variation of tensile properties of cranial bone with $\dot{\varepsilon}$, [s^{-1}] (Wood, 1971)

He concludes that:

1. human cranial bone exhibits transverse isotropic behavior.
2. young's modulus E and ultimate tensile strength σ_{ult} tend to increase with increasing strain rate.
3. failure strain ε_f decreases with increasing strain rate.
4. energy absorbed at failure e_c, on the other hand seems not to be influenced by strain rate.

Numerous studies were presented in Sec. 1.3 concerning the mechanical behavior of bones. It is noted that these studies were based on small sized bone samples extracted from bone organs. The reason for samples of such sizes is the nature and aim of research studies mentioned above *i.e.* to characterize and to apprehend the mechanical behavior under specific mechanical environments.

Despite these studies, quite a few authors have also studied the behavior of whole bone organs to characterize the response of the structure. In such cases, small sized samples do not give good insights. Therefore, we are obliged to use samples of decent size and different materials. This chapter, presents existing studies on ribs at Level IX of Tab. 1.2 or samples with both cortical and trabecular bone.

1.4 Experimental studies on structural response of ribs

In case of structural response characterization, it is logical to use either whole rib samples or an anatomical segment. Therefore, the tests on structural response can be categorized as:

1. Three point bending tests on whole or partial rib samples
2. compression or tensile tests on mutli-material cylindrical samples of decent size.

1.4.1 Quasi-Static tests

Three point bending

Granik and Stein (1973) is one of the most cited articles regarding the fracture of ribs and their response in static three point bending. They had tested segments from 6^{th} and 7^{th} human ribs (see Fig. 1.10a). The segments of ribs with least apparent curvature were selected (4 in long). Their data suggest that the thickness distribution of cortical bone is non-uniform and the average dimensions of the cross section at point of loading were 0.650inches × 0.290inches as in Fig. 1.10b.

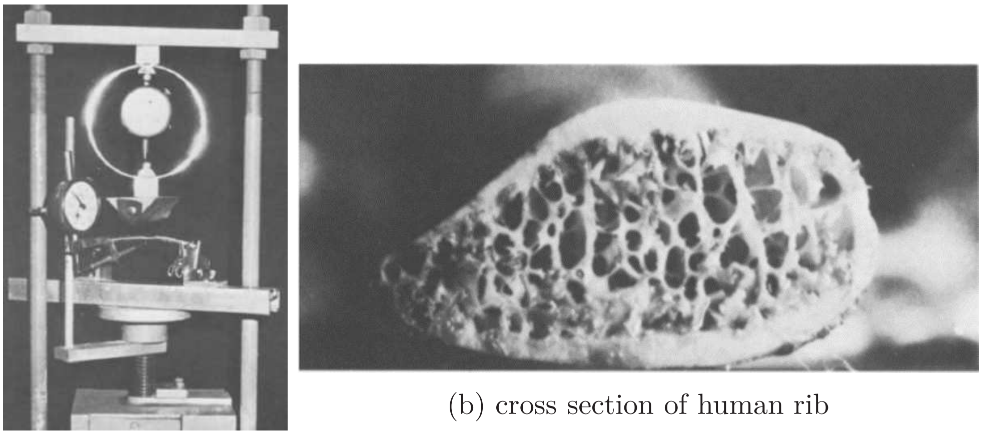

(b) cross section of human rib

(a) test setup

Figure 1.10 – Data from Granik and Stein (1973)

They have concluded that the skew and taper are not important and did not influence the mechanical properties of the rib segment. Moreover, the trabecular bone of a rib shows negligible contribution to the mechanical properties of rib, since its stiffness and strength are much less when compared to that of whole structure.

The stiffness (eq. 1.11) and strength (eq. 1.12) of rib sections were calculated as follows

$$E_{fRS} = \frac{\Delta P L^3}{\Delta \delta 48 I} \tag{1.11}$$

$$\sigma_{fRS} = \frac{P_{max} L c}{4I} \tag{1.12}$$

$$E^{'}_{fRS} = \frac{\Delta P L^3}{\Delta \delta 768} \left(\frac{10}{I} + \frac{3}{I_b} + \frac{3}{I_c} \right) \tag{1.13}$$

where, ΔP is the change in load (expressed in pounds lbs), $\Delta\delta$ is the change in deflection (expressed in inches), L is the segment length (expressed in inches), I, I_b and I_c are area moments of inertia at point of loading, L/4 and 3L/4 respectively (inches^4).

Got et al. (1975) have tested 80mm long straight bone segments from 4^{th},5^{th} and 6^{th} human ribs. They have presented correlations between ash fraction per unit mass of the segment (A_s/M_s), ash content per unit length of the segment (A_s/L_s), age and sex.

- Their results shows that the slope of elastic region in quasi-static regime is strongly correlated with the ash content per unit length (A_s/L_s), thickness of cortical bone and cortical bone surface area.
- Where as the dynamic three point bending tests prove that the maximum force in force-displacement response is strongly correlated to (A_s/L_s)

In contrast to Granik and Stein (1973) and Got et al. (1975), Stein and Granik (1976) have studied the response of human rib segments from 79 male cadavers with respect to age and possible disease. They concluded that "*apart from myeloma and arthritis, none of the other diseases had an effect on the response.*"

Another commonly cited work on quasistatic three point bending behavior of human ribs is Charpail (2006), who had studied the behavior of 6^{th},7^{th} and 8^{th} human ribs. The experimental setup used is shown in Fig. 1.11. The behavior of rib was characterized through the following variables

- t_{max}, is the time corresponding to maximum force observed
- t_{end}, is the time at which a rapid decrease in force is observed, indicating rupture

- F_{max}, is the maximum force observed
- δ_{max}, is the rib displacement corresponding to maximum force observed
- K, is the slope of linear part of the force displacement curve

Figure 1.11 – Experimental setup
(Charpail, 2006)

According to Charpail (2006), the mechanism of rupture under quasi-static three point bending can be explained in 5 stages:

Stage 1 the striker comes into contact with the external cortical bone in rib and an equilibrium is established with supports (Fig. 1.12a)

Stage 2 the cortical bone under the striker, caves in due to local damage (Fig. 1.12b)

Stage 3 due to further displacement, the caved in cortical bone clamps itself with the striker (Fig. 1.12c)

Stage 4 further buckling occurs (Fig. 1.12d)

Stage 5 rupture occurs from the interior cortical bone end (Fig. 1.12e).

(a) stage 1 (b) stage 2 (c) stage 3

(d) stage 4 (e) stage 5

Figure 1.12 – Different stages of response
(Charpail, 2006)

The tests carried out by Charpail (2006) have led to the following conclusions :

- There is a difference between the response of female and male ribs. This difference is due to the variation in geometry of corresponding rib. A similar conclusion was also put forth by Kimpara et al. (2003).
- The modulus and ultimate strength found by three point bending tests are ≈ 1.5 times greater than those found in compression tests. This can be explained by the difference in the behavior of bone subjected to uniaxial compression and tension respectively.
- The thickness of cortical bone at a particular cross-section plays an important role in bending stiffness and strength. "*more the thickness, less are bending stiffness and strength*".

The data for modulus and ultimate strength subjected to three point bending tests found in literature are presented in Fig. 1.13a and Fig. 1.13b respectively. This data is grouped with respect to the loading direction, LM Dy signifies Dynamic loading in Lateral Medial direction, LM QS signifies Quasi Static loading in Lateral Medial direction, ML QS signifies Quasi Static loading in Medial Lateral direction and NR signifies Not Reported by the author or ambiguous.

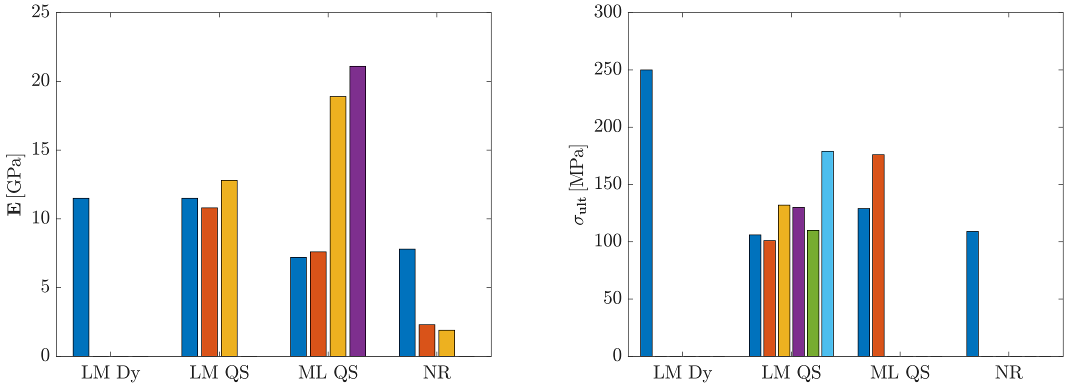

(a) Young modulus

(b) Ultimate strength

Figure 1.13 – Characteristics of human rib in three point bending

Author	Rib #	Loading type	direction	E, GPa	σ_{ult}, MPa
Granik and Stein (1973)	6,7	Manual	Lateral Medial	11.5 ± 2.1	106 ± 31
Got et al. (1975)	5,6	Quasi Static	NR	7.8 ± 4.1	109 ± 61
		Dynamic	NR	NR	NR
Stein and Granik (1976)	6,7	Quasi static	Lateral Medial	NR	101 ± 4
Kallieris et al. (1981)	6	Quasi Static	Lateral medial	NR	132 ± 66
	7			NR	130 ± 45
Yoganandan and Pintar (1998)	7	Quasi Static	NR	2.3 ± 0.4	NR
	8			1.9 ± 0.3	NR
Kallieris and Reidl (2000)	6,7	Quasi Static	Lateral medial	10.8 ± 4.0	110 ± 59
		Dynamic		11.5 ± 3.7	250 ± 84
Kimpara et al. (2003)	6,7 M	Quasi Static	Medial lateral	7.2 ± 5.9	NR
	F			7.6 ± 5.4	NR
Charpail (2006)	6-9	Quasi static	Lateral medial	12.8 ± 5.0	179 ± 59
Kemper et al. (2007)	6,7	Quasi Static	Medial lateral	18.9 ± 3.6	129 ± 43
				21.1 ± 2.1	176 ± 31

Table 1.13 – Existing data on human ribs under three point bending (Mayeur, 2013)

The studies presented above have used human ribs for experimental characterization. In case of constraints to obtain human ribs, biological surrogates can be used. One of the recent studies concerning quasi static three point bending had used porcine ribs as substitute Aubert (2012).

The porcine rib was represented as a curve beam with an uniform circular cross section in order to calculate the Young's modulus through a curved beam subjected to small displacements hypothesis. They found that the average Young's modulus of 6 porcine rib sample was around 14 GPa, though the Eq. 1.14

$$K_{pr} = \frac{2EI}{R^3\delta(\alpha)} \tag{1.14}$$

The results states that on loading the same rib beyond a displacement of 4 mm, the initial elastic modulus is not the same. For example, the Fig. 1.14, shows the response of porcine rib to loading-unloading and reloading response for the case $\delta = 3.5$mm in red and $\delta = 4$mm in green respectively. It is clear that once the same rib is loaded at different displacements, the initial elastic response is almost the same since the curves overlap.

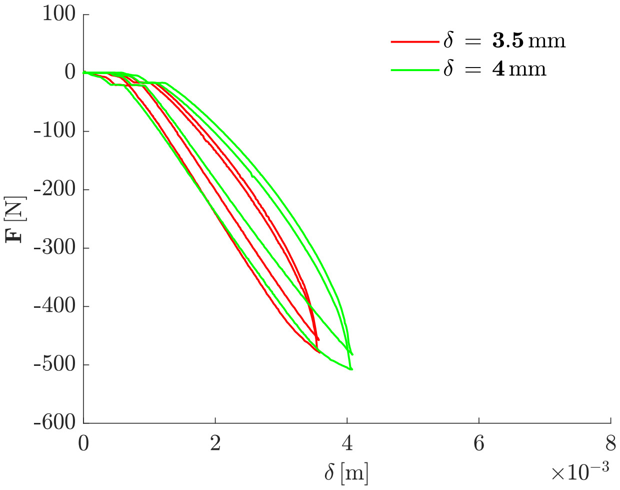

Figure 1.14 – $\delta \leq$ 4mm (Aubert, 2012)

On the other hand, if the displacement is greater than 4 mm, there is a shift in the initial elastic response as in Fig. 1.15.

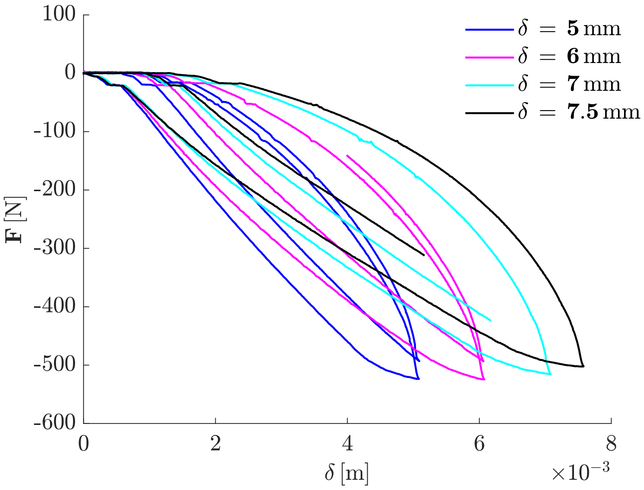

Figure 1.15 – $\delta >$ 4mm Aubert (2012)

This change in response with respect to displacement is due to the accumulation of damage and plastification of the rib. In contradiction to Granik and Stein (1973), the response in Fig. 1.15 proves that there is an influence of trabecular bone on the response of whole rib.

Multimaterial cylindrical samples

The three point bending data presented above lead to a conclusion that the geometry of the rib and the segment has an influence on the structural response of a rib. Since it is difficult to obtain a straight and uniform sample to study the compressive and tensile behavior of rib. Thus, quite a few authors have suggested to conduct tests on cylindrical segments of ribs containing both cortical and trabecular bone. Quite a few studies can be found in the literature regarding uniaxial tests on human rib samples are shown in Fig. 1.16a and Fig. 1.16b

Yet this proves that the sample location does play an important role for the response of human ribs. One of the studies concerning the dispersion of properties with respect to anatomical location of the sample was proposed by Charpail (2006). She concludes that the sample extracted from posterior end were more stronger than that from the anterior end. Therefore, showing the influence of porosity.

1.4.2 Dynamic tests

Most of the studies presented above, were based on quasi static test or dynamic tests using pendulum. In order to characterize the structural response of a rib under similar dynamic environments similar to automotive impacts, it is necessary to subject the rib to a three point bending load at high strain rates. This can be possible through the Split Hopkinson Pressure bar method.

The inconvenience in split hopkinson pressure bar is the choice of material for the bars so that the strain signals can be treatable for results. This depends on the mechanical impedance of the bar and sample materials. As we know that bone has very low mechanical impedance compared to metals, polymeric materials must be considered. The use of polymeric materials for testing low impedance materials in dynamic environment is not new, it was used by Zhao and Gary (1996) and most recently by Pavier et al. (2015) for low dense polymers. Unfortunately, there are only a few studies concerning three point bending tests on whole ribs using SHPB (Aubert et al., 2012; Pavier, 2013).

The experimental setup used by Pavier (2013) is considered as reference for this thesis and is presented in the next chapter.

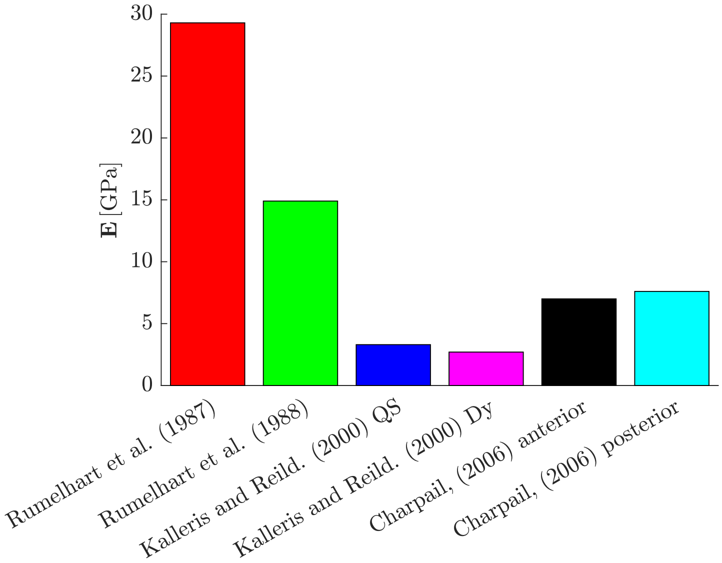

(a) Young modulus

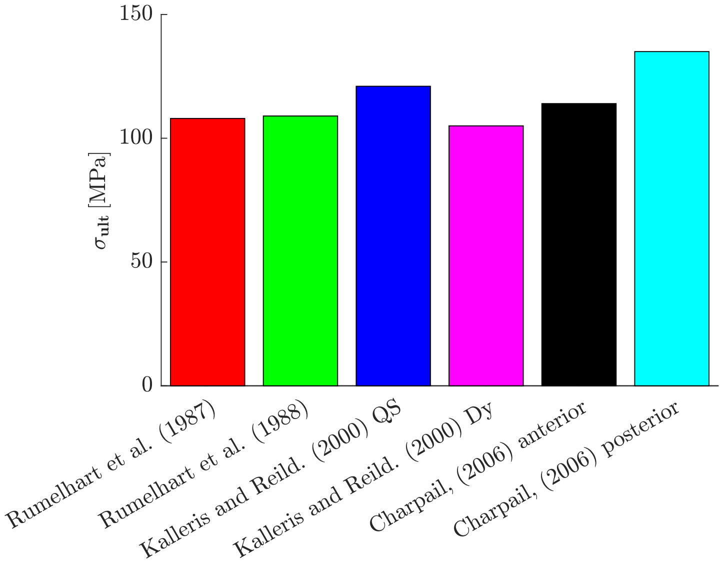

(b) Ultimate strength

Figure 1.16 – Compressive properties of cylindrical human rib samples

1.5 Numerical models of human thorax and ribs

Several models and proposals were put forth for the human thorax. These models can be classified as either Isolated Thorax models or Full body human models. On the other hand, quite a few authors have also presented isolated rib models with both cortical and trabecular bones.

1.5.1 Human Thorax Models

The first finite element model of the human thorax was proposed by Roberts and Chen (1971), Roberts and Chen (1972) and Sundaram and Feng (1977). In these models, the ribs were represented as beam elements. Roberts and Chen (1971) is one of the most commonly cited models, which was based on postmortem studies on first 8 ribs from one female cadaver. Even though this model was a break through for its time in terms of numerical representation of a human thorax, there was no correlation with cadaver experimental database. Another drawback of this model is that it did not consist the intercostal muscle tissues and spine.

This loophole was filled by Andriacchi et al. (1974), who added the tissues and spine. The bones were modeled as rigid bodies and tissues of the thoracic cage as deformable beams. Later, Sundaram and Feng (1977) proposed a FE model for the thorax by considering the entire thoracic cage as deformable body. The thorax model proposed by Sundaram and Feng (1977), consisted of almost all the crucial components of the thoracic cage including lungs and heart. A major draw back of this model was that, it was not capable of simulating large displacements, non-linear behavior and elements were not fine enough.

Later with the improvement of computer graphics and competencies, several well refined models were proposed. Some of the most commonly used models in the industry are the HUman MOdel for Safety, HUMOS (Robin, 2001), the Total HUman Model for Safety THUMS (Maeno and Hasegawa, 2001), the RADIOSS human model (Arnoux et al., 2003), the H-model (Haug et al., 2004) and the Isolated thorax model (Schoell et al., 2015).

Mayeur (2013), had pointed out a few drawbacks and simplifications of most frequently used human models concerning the human ribs of these models as follows:

1. there is need for accurate geometrical representation of ribs
2. need for integrity between bones and other tissue
3. different properties are to be allocated to different ribs

1.5.2 Isolated Rib Models

Isolated rib models are the ones aimed in improving either the geometrical representation or mechanical behavior of the ribs in the human body models. Some of the most recent isolated human rib models are Charpail (2006), Li et al. (2010), Yates and Untaroiu (2018) and Lundin and Storm (2018).

Author	Bone	$\rho, \text{kg.m}^{-3}$	E, GPa	σ_y, MPa	$\varepsilon_f, \%$
Charpail (2006)	Cortical	2000	13	150	10
	Trabecular	1000	2.4	2	10
Li et al. (2010)	Cortical	2000	11.5	88	2
	Trabecular	1000	0.04	2.2	3
Lundin and Storm (2018)	Cortical	2000	11.5	88	2
	Trabecular	-	-	-	-
Yates and Untaroiu (2018) a	Cortical	2000	11.03	98.98	2.635
	Trabecular	1000	0.04	1.8	2.0
Yates and Untaroiu (2018) b	Cortical	2000	12.38	82.36	1.367
	Trabecular	1000	0.04	1.8	2.0

Table 1.14 – Data of existing isolated human rib FE model

The mechanical properties of trabecular bone used by Lundin and Storm (2018) were adapted by a homogenization method proposed by Amine (2017), which was not reported in their document. The authors presented above, have tested the mesh sensitivity and have proposed all-hex / hex-shell models for ribs. The most feasible model was supposed to be the shell-solid model *i.e.* the cortical bone was represented by shell elements and trabecular with solid elements.

Among them, Charpail (2006) tested the human rib with no trabecular bone under lateral medial loads (Fig. 1.17a). These results were used to optimize the properties of cortical bone in anterior-posterior loads with trabecular bone (Fig. 1.17b) in Radioss solver.

(a) Lateral Medial bending

(b) Anterior-Posterior bending

Figure 1.17 – Three point bending models
(Charpail, 2006)

Whilst Li et al. (2010), Lundin and Storm (2018) and Yates and Untaroiu (2018) tested human ribs in Anterior-Posterior loading using LS-Dyna solver for numerical calculations. The models used by these authors are presented in Fig. 1.18.

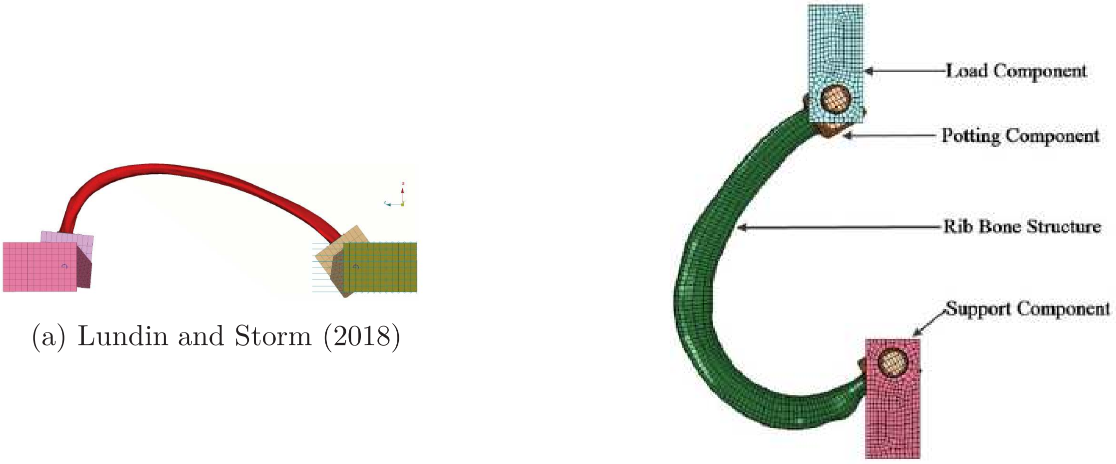

(a) Lundin and Storm (2018)

(b) Li et al. (2010)

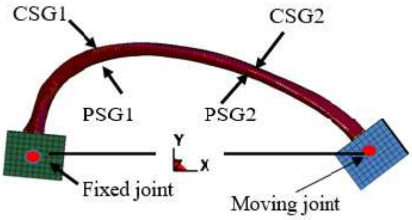

(c) Yates and Untaroiu (2018)

Figure 1.18 – Other Anterior-Posterior bending models

The constitutive law used by these authors is presented in Tab. 1.15

Bone	Li et al. (2010)	Lundin and Storm (2018)	Yates and Untaroiu (2018)
Cortical	Elastic-Plastic Isotropic hardening Strain rates effects failure strain	Elastic-Plastic Isotropic hardening - failure strain	Elastic-Plastic Isotropic hardening - failure strain
Trabecular	Elastic-Plastic Kinematic hardening Strain rates effects failure strain	NR - - NR	Elastic-Plastic Isotropic hardening - failure strain

Table 1.15 – Existing numerical models details for human rib in LS Dyna

On the other hand, Pavier (2013) had presented a numerical model of porcine rib in dynamic three point bending to lateral medial load. The porcine rib was represented by a circular arc with no trabecular bone. He had used an elastic-plastic constitutive law with no strain rate effects but with an external damage law. The properties of the numerical rib are given in Tab 1.16.

Property	value
ρ, kg.m^{-3}	6000
E, GPa	14
σ_y, MPa	70
σ_{ult}, MPa	70
ν	0.3
ε_f, %	7.6

Table 1.16 – Mechanical properties of numerical porcine rib (Pavier, 2013)

1.6 Image acquisition techniques and densitometry

Bone density alone is not sufficient for a detailed description of bone strength. It needs several other parameters such as architectural parameters. These architectural parameters are of two categories, (i) Macro-architectural parameters such as bone size and geometry and (ii) Micro-architectural parameters such as cortical and trabecular bone thickness or structural detail.

Several imaging techniques are available and in use in the filed of clinical densitometry for analysis of bone strength and the parameters influencing it. Speaking of which, the type of technique differs with the requirements of different applications. For example, techniques such as radiography, dual-energy X-ray absorptiometry (DXA), peripheral quantitative computed tomography (pQCT), computed tomography (CT) and the magnetic resonance imaging (MRI) are sufficient enough for analysis of macro-architectural properties. Micro-architectural properties in contrast to their counter part, require imaging techniques with more resolution such as multidetector CT, MRI, and high-resolution peripheral quantitative computed tomography (HR-pQCT). The above mentioned points were adapted from Griffith and Genant (2008).

However, as said by Wong (2016), the pQCT, the HR-pQCT and MRI techniques excel in depiction of bone architecture. He had also pointed out the limitation of MRI technique used for bone architecture that "*one must be cautioned as to the accuracy of MRI measures of bone structure, especially when the in-plane pixel size is larger than 0.2 mm*". The effects of different imaging techniques and their dosage levels on age of the subject were brought into light by Irogi et al. (2018) in their article concerning the use of these techniques for children and adolescents.

All together, we can narrow down to HR-pQCT imaging technique for its reliable and efficient depiction of both bone mineral density and its architecture. To understand the working principle of HR-pQCT, we shall first consider QCT. A typical QCT technique works on the principles of photoelectric absorption. AS said by Wong (2016), thicker and denser the object, fewer the photons are detected. In fact the intensities of incident (I_{in}) and transmitted (I_{out}) photons are related to the thickness (th) and linear attenuation coefficient (μ) of the object examined as follows

$$\frac{I_{out}}{I_{in}} = e^{\mu th} \tag{1.15}$$

As we know that the bone has the capacity to attenuate more photons than its surrounding tissues (muscles and fat for example), QCT scans are capable of quantifying theses materials separately. The HR-pQCT on the other hand, is capable of providing high resolution images of both trabecular and cortical bone architecture, whilst capable of given volumetric density distributions separately.

1.7 Summary

In a nutshell, despite the existence of huge research in concern to thoracic trauma assessment tools, the most common conclusion encountered is

"*None of the existing trauma scoring systems considers all the parameters such as variation in population, age , physiological variability,., etc and continuous validation is needed. Therefore, we must be cautious in the use of currently existing trauma scoring systems*".

All these studies show that rib fractures due to impact are often associated with serious morbidity and mortality, which tend to increase with number of ribs fractured. Key medical complications associated with rib fractures are hemothorax, pneumothorax, pulmonary laceration, pulmonary contusion and vascular injury. The complication endangering a victim is fail chest, that arises due to multiple ribs / adjacent ribs fractured leading to free-floating and individual movements of ribs. Therefore it is important to either improve thoracic trauma prediction or at least to mitigate the effects in case of blunt chest trauma. A good understanding on the fracture of ribs under these specific mechanical loading conditions can lead us to address the aforementioned improvements. In order to have a good apprehension of rib fractures, it is necessary to give equal importance to the geometry of rib, the mechanical properties of its tissues (cortical and trabecular) and the mechanism of fracture and the variables influencing it. The following chapters address these constraints from bio-medical as well as mechanical point of view.

Bone is a self repairing and evolving tissue. The complicated mechanical properties and behavior is due to the constant erosion of under developed tissues by mature tissues during initial stages of development that occurs at microscopic scale and lower levels of hierarchy.

A human rib consists of two different tissues, namely cortical and trabecular bone. The difference in mechanical behavior of these tissues is essentially due to the difference in their architecture and structure. Since both bone tissues are strong in compression when compared to tension, common yield criteria such as von-Mises yield criterion is not suitable for numerical models. Moreover, the behavior reported by Keaveny et al. (2003), suggests that damage accumulation has an important role in the determination of post yield behavior of these tissues.

Another interesting fact is that the mechanical properties are influenced by many variables such as age, bone composition (density and mineral content), architectural arrangement and also the mechanical environment. These data suggest that corresponding variables of each category must be given equal importance for a valid simulation. Since this thesis deals with high speed dynamic loading, the strain rate plays a key role in the behavior of numerical rib sample.

Therefore, we propose that elastic-viscoplastic behavior with isotropic hardening is suitable for cortical bone and an elastic-viscoplastic behavior with kinematic hardening for trabecular bone. Moreover, as damage accumulation is also involved in the post yield behavior, a strain rate sensitive external damage law based on the continuum damage mechanics is the one and only suitable law for a progressive fracture propagation is suggested.

The response of human rib as a structure is done through three point bending tests on either whole human ribs or segments of certain length. These tests prove that the geometry of the rib had a strong influence on the mechanical response. It was initially concluded that the trabecular bone did not change the response of a rib, since its rigidity and stiffness is low when compared to that of whole rib. Moreover, the thickness of the cortical bone played a key role in characterizing the response. The results of quasi static bending tests on porcine ribs show that the trabecular bone has an influence if the displacement of the rib exceeds a certain amount.

In order to make sure that the geometry had an influence, studies on mutli-material cylindrical samples were carried out by certain authors. Their results prove that the anatomical location of the sample in a rib did influence the rigidity and stiffness of the sample. The fact that there is a huge dispersion in the properties of ribs is due to the difference in load direction, sample size and location and sex. Very few studies can be found regarding the response of human rib or its biological surrogates to dynamic three point lateral medial bending.

When it comes to numerical modes of human thorax, there is always a question regarding the resolution and representation of its constituents. Even though these models are used quite often in the industry, there are still improvements to be made notably in

1. the geometrical representation
2. the mechanical constitutive law
3. the consideration of mechanical environment *i.e.* strain rate effects

To confront the problems of geometrical representation and mechanical behavior, quite a few authors have presented isolated rib models. Their results have proved that use of elastic plastic constitutive law for bone is feasible. Yet unfortunately, no studies can be found to consider the strain rate effects on damage accumulation and progressive crack propagation.

Therefore, the numerical model of a human rib or its surrogate must have a good geometrical representation, a constitutive law with strain rate effects and most importantly a damage law that is capable of considering the rate effects and progressive damage accumulation and crack propagation.

Part II

Analysis of experimental data obtained previously at the laboratory

Chapter 2

Processing of experimental data

Résumé :

Ce chapitre présente la caractérisation expérimentale des côtes de porc en flexion dynamique "trois points". La base de données expérimentale brute a été obtenue par Aubert (2012). Les données ont été analysées pendant cette thèse.

Le banc expérimental est constitué par des barres de Hopkinson permettant l'étude de la réponse en flexion. Il se compose de trois barres : une barre dite "entrante" qui va transmettre une onde de compression à l'échantillon, lequel est en appui simple sur les deux barres "sortantes" à ses deux extrémités. Les barres sont en nylon pour que leur impédance mécanique soit en accord avec celle de l'échantillon. L'analyse de l'essai et l'obtention des grandeurs intéressantes (forces aux interfaces, vitesses de déformations,...) sont basées sur la mesure des ondes de déformations élastiques sur les barres.

Au total, 20 essais ont été analysés. A partir des historiques des forces aux interfaces entrantes et sortantes, trois catégories de réponses ont été identifiées : (i) essais sans rupture, (ii) essais avec rupture pendant l'équilibre dynamique entre la force entrante et les forces sortantes [1]*, et (iii) essais de rupture hors équilibre. Nous pouvons observer que la vitesse relative de l'interface joue un rôle très important dans le type de réponse avec fracture. Si cette vitesse augmente, la fracture tend à se produire avant que l'équilibre dynamique ne soit établi. De plus, une diminution du temps de rupture et du déplacement à la rupture sont observées. Un seuil critique est détecté en termes d'énergie à la rupture, de temps à la rupture et de déplace-*

---

[1] L'équilibre dynamique est établi lorsque $F_{in} \approx F_{out1} + F_{out2}$

ment à la rupture. Si l'échantillon est suffisamment rigide pour dépasser ce seuil, il s'établit un équilibre entre la force entrante et les forces sortantes, ce qui correspond à un plateau dans la réponse. La rupture complète de l'échantillon est due à une fissure apparaissant dans la zone sollicitée en traction et qui se propage vers la zone comprimée (située au voisinage du point d'impact). La force maximale appliquée sur l'échantillon n'influence pas la rupture. On observe plutôt que la rupture dépend du déplacement local de la côte. french

Abstract:

This chapter presents the mechanical characterization of porcine ribs subjected to dynamic three-point bending loads. The raw experimental data base was obtained prviously by Aubert (2012) and the results were analyzed in the present thesis work.

The experimental setup is based on Hopkinson pressure bars, which permits us to study the response of sample in three point bending. It consists of three bars, an input bar and two output bars. The sample is in fact placed between input and output bars. The input bar subjects the sample to mechanical loads by transmitting a compression wave to the sample. The bars are made of nylon in order to have mechanical impedance of similar orders of magnitude as that of the sample. The analysis of the sample response is done through dynamic variables such as force at interfaces and strain rate etc.,. These dynamic variables are based on the elastic strain waves measured in the input and output bars.

A total of 20 test were analyzed. Three categories of responses were identified based on the force at interfaces: (i) tests without fracture, (ii) tests with fracture during dynamic equilibrium between input and output forces and (iii) fracture before dynamic equilibrium. We had noticed that the relative interface velocity, plays an important role in determining the type of rupture observed. As the relative velocity increases, the fracture tend to occur before dynamic equilibrium. Moreover, we had also noticed a decrease in time at rupture and displacement at rupture. This permitted us to establish a threshold in terms of energy at rupture, time at rupture and displacement rupture. If the sample is rigid enough to overcome this threshold, it shall establish the aforementioned dynamic equilibrium, which is characterized by a plateau kind response in the forces at interface. The complete rupture of the sample is characterized by a rapid decrease in input and output forces, and is due to the propagation of a crack from tensile surface towards the impact point (the zone in compression). The maximum values of force does not have an influence on the rupture. The ruptures observed are controlled by the local displacement of the sample.

2.1 Introduction to Hopkinson Bar

The Hopkinson pressure is one of the common methods to study the dynamic behavior of materials. It was first studied by John Hopkinson in the year 1872, when he investigated propagation of stress waves in iron wire. Later, (Hopkinson, 1914) introduced a methodology to save pressure vs time graphs. The accuracy of this methodology was then improved by Davies (1948). The Split Hopkinson pressure bar known as of today, was introduced by Kolsky (1949), he placed the specimen of interest in between an input bar and an output bar. The original SHPB setup is used for comprehension of material behavior subjected to dynamic compression. The SHPB setup had been modified for tests in tension and three-point bending. In general, the compression and tension test bench are used to test materials, whilst, the three-point bending test bench is used to understand the dynamic behavior of structures.

2.1.1 Principle of SHPB

The modified three bar SHPB setup used in dynamic testing is based on the Kolsky bar technique. The sample is placed in between input and output bar(s). A striker is launched at the input bar through a pressurized air cannon. Once the striker impacts the input bar, longitudinal compression waves travel though out the test bench. The waves involved in SHPB are as follows (see Fig. 2.1):

1 Waves in striker
   (a) a compression wave propagating towards the free end of the striker
   (b) a traction wave reflected from the free end, that cancels the stress imposed by the compression wave.

2 Waves in input bar
   (a) Incident Wave (ε_{inc}): A wave traveling in the input bar towards the input bar - sample interface. The difference in the mechanical impedance of the sample and bars gives rise to the separation of (ε_{inc}) into two waves. (represented in solid red line in Fig. 2.1).
   (b) Reflected Wave (ε_{ref}): A part of the incident wave, that propagates in the opposite direction to the incident wave. (represented in dotted red line in Fig. 2.1).

3 Waves in output bar(s)

(a) Transmitted wave (ε_{tr}): The other part of incident wave that passes through the sample into the output bar (represented in solid green line in Fig. 2.1).

The bars in SHPB are characterized by their density (ρ_b), Young's modulus (E_b) and cross-sectional area (A_b). All these variables together, influence the mechanical impedance (Z_b).

$$Z_b = A_b \sqrt{E_b \rho_b} \tag{2.1}$$

The characterization of tests carried out on the SHPB is based on the propagation of elastic waves within the input bar and output bar(s) (Zhao and Gary, 1995), (Zhao et al., 1997). Another important characteristic that is mandatory to obtain decent results with SHPB is the slenderness ratio of the bars. This slenderness ratio helps us to approximate 1D wave propagation in bars, thereby avoiding the non plane wave effects.

To understand the physics involved in SHPB, let us consider a volume element in the bar. The dynamic equilibrium of this volume element is

$$\frac{\partial \sigma(x,t)}{\partial x} = \rho_b \frac{\partial^2 u(x,t)}{\partial t^2} \tag{2.2}$$

where $\sigma(x,t)$ is the stress in the volume element, that is represented as

$$\sigma(x,t) = E_b \, \varepsilon(x,t) = E_b \frac{\partial u(x,t)}{\partial x} \tag{2.3}$$

where, $\varepsilon(x,t)$ represents the strain in the element and $u(x,t)$ represents the displacement along x direction in the element. Substituting Eq. 2.3 in Eq. 2.2, we get the '*D'Alembert Equation*' (Eq. 2.4)

$$\frac{\rho_b}{E_b} \frac{\partial^2 u(x,t)}{\partial t^2} = \frac{\partial^2 u(x,t)}{\partial x^2} \tag{2.4}$$

the expression ρ_b/E_b in Eq. 2.4 is the inverse square of celerity of longitudinal waves (see Eq. 2.5) in the bar *i.e.* $1/c_b^2 = \rho_b/E_b$

$$c_b = \sqrt{\frac{E_b}{\rho_b}} \tag{2.5}$$

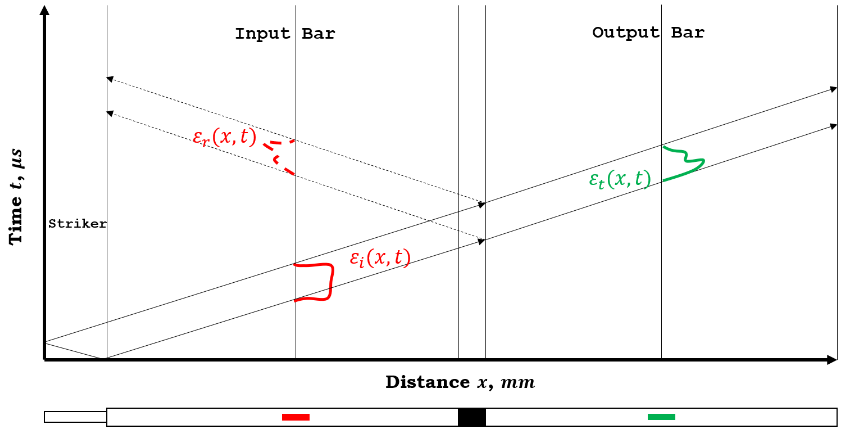

Figure 2.1 – The Lagrange diagram for a typical SHPB setup

A general solution can be written to the D'Alembert equation (Eq. 2.4) using the principle of superposition as follows:

$$u(x,t) = f\,(x - c_b t) + g\,(x + c_b t) \tag{2.6}$$

where, $f\,(x - c_b t)$ represents a wave propagating in positive x direction and $g\,(x + c_b t)$ represents a wave propagating in the opposite direction. In fact the strain $\varepsilon(x,t)$, the stress $\sigma(x,t)$ and the particle velocity $v(x,t)$ in the element can be expressed in terms of first order spatial derivative of $f\,(x - c_b t)$ and $g\,(x + c_b t)$ in spatial domain.

The expression of $\varepsilon(x,t)$ shows that the strain is a linear combination of spatial derivative of the two waves (f and g) that propagate in opposite direction. Thus the strain in a section of the bar can be expressed in terms of incident wave ε_{inc} and reflected wave ε_{ref} as

$$\varepsilon(x,t) = \varepsilon_{inc} + \varepsilon_{ref} \tag{2.7}$$

Similarly, we can write the input and output forces in terms of ε_{inc} and ε_{ref} as in Eq. 2.8 and Eq. 2.9 respectively.

$$F_{in} = A_b E_b \left[\varepsilon_{inc} + \varepsilon_{ref}\right] \tag{2.8}$$

$$F_{out} = A_b E_b \left[\varepsilon_{tr}\right] \tag{2.9}$$

On the other hand, the velocities of the input and output bar interfaces can be written in terms of c_b, ε_{inc} and ε_{ref} as in Eq. 2.10 and Eq. 2.11 respectively.

$$v_{in} = -c_b \left[\varepsilon_{inc} - \varepsilon_{ref}\right] \tag{2.10}$$

$$v_{out} = -c_b \left[\varepsilon_{tr}\right] \tag{2.11}$$

2.1.2 Experimental Difficulties

Impedance adaptation

The characterization of the material response using SHPB is based on evaluation of force and displacement imposed on the sample at input and output interfaces at every time. Since the forces (Eq. 2.8, Eq. 2.9) and velocities (Eq. 2.10, Eq. 2.11) can be calculated though the strain signals, for an acceptable characterization, the mechanical impedance must be adapted between the bars and the sample. The mechanical impedance of the bar material (Z_b) and that of sample (Z_s) , controls the amplitude of reflected wave ε_{ref} through Eq. 2.12 and transmitted wave ε_{tr} through Eq. 2.13 respectively.

$$R = \frac{Z_b - Z_s}{Z_b + Z_s} \tag{2.12}$$

$$T = \frac{2Z_s}{Z_b + Z_s} \tag{2.13}$$

where, Z_b is the mechanical impedance of bar material and Z_s is the mechanical impedance of sample.

Therefore, there is a strong influence of material used as bars in the characterization of sample response. Since, the testing material is bone and it not a uniform material *i.e.* some areas of bone are made of soft tissue whilst other are of hard tissue. Moreover, the mechanical impedance of bone is feeble. Thus the use of bars with high mechanical impedance such as steel or aluminum leads to incomprehension of different waves involved in SHPB tests and also high noise-to-signal ratio. Several authors had investigated the use of polymeric bars such as PMMA (Zhao et al., 1997), (Sawas et al., 1998) and (Chen et al., 1999). Therefore, we'd chosen bars of Nylon to characterize the dynamic response of bone.

Shifting of waves in spatial and temporal domain

As said above, the forces and velocities are calculated at the interface, this poses another difficulty. The reason is, it is impossible to differentiate between the incident and reflected wave at any given instant at the interface due to complex wave interaction phenomena and the change in sign of these both waves. Therefore in practice, we capture the signal at a certain distance from the interface as in Fig. 2.2. Later these waves are shifted in such a way that they were captured at the interface. This methodology is perfect for bars made of elastic materials.

For example, let us consider that the strain signals acquired are in terms of absolute time frame ($t^{'}$). The shifting procedure consists of defining an origin time $t_0^{'}$ which is the time of arrival for the incident pulse at the input bar sample interface. Then a relative time t is defined in such a way that the strain signals were acquired at the interfaces of bars and sample.

In case of polymeric bars, wave attenuation and wave dispersion phenomena due to the viscous property of these bars. According to (Bacon, 1998), in order to shift these signals in time, it is necessary to reconstruct these signal by taking the dispersion and attenuation into consideration. Moreover, Gary et al. (1991) had proposed to introduce a viscoelastic correction factor based on the Pochammer-Chree model for an infinite cylinder. He had considered the polymeric bar as a linear isotropic visco-elastic material, that lead to an equation in frequency domain with a complex solution. Zhao et al. (1997) put forth two keen relations that were used in the reconstruction of these waves, (i) a relation between the frequency and phase velocity and (ii) a relation between frequency and damping of waves. We follow the same procedure of Zhao et al. (1997) *i.e.* firstly the measured signal is decomposed into a Fourier series, then the phases in the fourier series is modified by taking the dephasing in the wave due to transport into consideration. Lastly, the amplitude of the wave is modifies by taking damping into account.

Non-plane wave

Another well known issue in a SHPB setup is *non plane wave* effect. A non plane wave effect is nothing but a non uniform distribution of strain through out the cross section normal to the direction of propagation of waves. In other words, it is the possibility of having zero strain at the outer surfaces and a non-zero strain within the cross-section.

This issue of critical importance was studied by several authors and one of the note works was proposed by Merle and Zhao (2006). They have presented a detailed discussions on the non plane wave effects by taking the radius of the bar, the spectrum of pulse wave and the material of bar into consideration. According to them, the assumptions of uniform strain distribution in the bar for the experimental conditions in this thesis, leads to a maximum error of less than 5%. Therefore, the corrections applied in this study are only for dispersion but not for three dimensional effects.

2.2 Experimental Setup at our Laboratory

The setup used in this thesis is shown in Fig. 2.2.

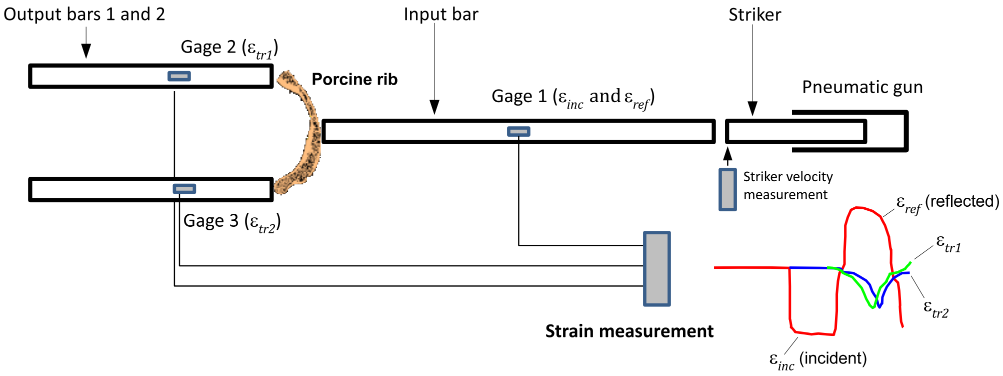

Figure 2.2 – The modified three-point bending SHPB setup

Striker:

It consists of a nylon striker of $15\,mm$ in diameter and either $500\,mm$ or $1300\,mm$ long. The striker is launched at the input bar through an air cannon. The pressure in the air cannon varies between 1 bar and 5 bar. The velocity of the striker is measured using an optical method through reflective bands that are placed at regular intervals on the striker (silver bands on striker in Fig. 2.3).

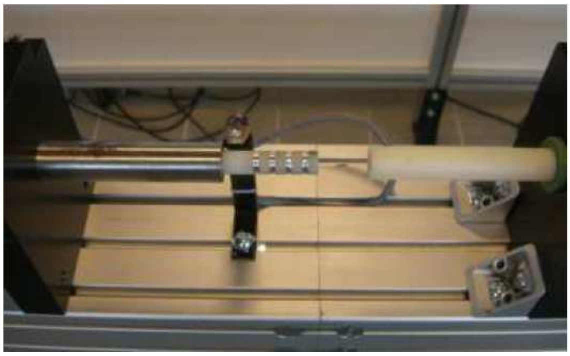

Figure 2.3 – Reflective bands placed on striker and optical sensors

Once the striker is released from the canon, a photosensitive sensor placed in the vicinity of canon exit, captures the passage of these reflective bands. The signals are acquired at a time interval $dt = 1 \times 10^{-6}$. The striker velocity v_{str} can be related to air canon pressure P_{can} as in Fig. 2.4.

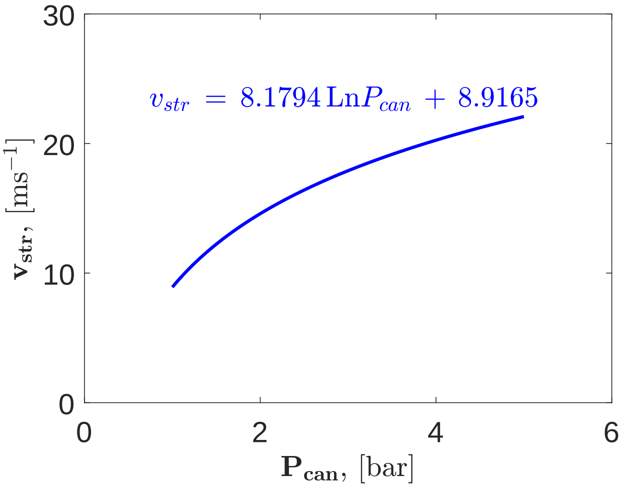

Figure 2.4 – P_{can} *vs* v_{str} for long striker (Pavier, 2013)

Bars The input bar is also made of nylon, and is $20\,mm$ in diameter and $3000\,mm$ long. On the other hand, the output bars are also of nylon, $20\,mm$ in diameter and $1750\,mm$ long. All the bars are supported by friction less supports, attached to the test bench. The output bars are backed up by a damping system at other extremity.

2.2.1 Measurement of signals

It is established that the striker has reflective bands placed at certain intervals to reflect the laser so that the striker velocity can be measured. Once the striker passes the optical sensors, it triggers the measurement chain used for strain signals. The time is set to $t' = 0$, which is an absolute quantity. The strain gage on the input bar measures the incident and reflected strains vs time t': $\varepsilon_{inc}(t')$ and $\varepsilon_{ref}(t')$ respectively. On the other hand, the two strain gages on the two output bars, measure the transmitted waves in absolute time t': $\varepsilon_{tr1}(t')$ and $\varepsilon_{tr2}(t')$ respectively.

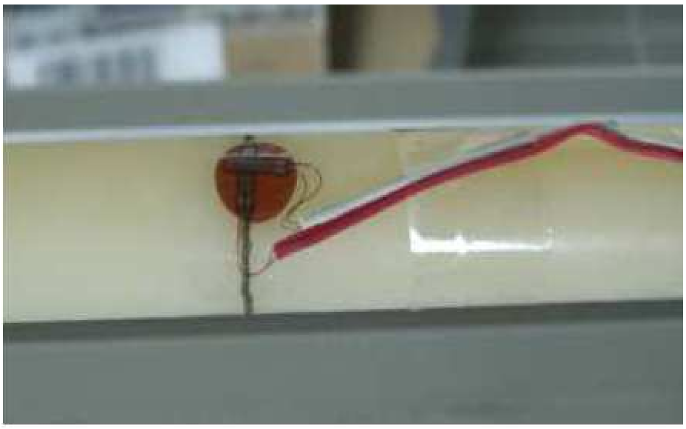

Figure 2.5 – Strain gage for signal measures

These gages are in a Wheatstone bridge arrangement so that one gage measures the longitudinal strain (ε) whilst the other measures the transverse strain signals ($-\nu\varepsilon$). Another advantage of Wheatstone bridge arrangements is that it is sensible and it eventually eliminates the effects of bending in bar. Once the bridge is at equilibrium, we modify the gain of the system using an oscilloscope. This is done be calibrating the variation in resistance and the variation in the measured tension through:

$$\Delta Em = \frac{1}{4}\left(\frac{\Delta R_1}{R_1} - \frac{\Delta R_2}{R_2} + \frac{\Delta R_3}{R_3} - \frac{\Delta R_4}{R_4}\right) \times V \tag{2.14}$$

We know that the strain and the variation in resistance are related as

$$\frac{\Delta R_4}{R_4} = k \times (\varepsilon) \tag{2.15}$$

where k is strain gage factor and for strain gages used in testing, $k \approx 2$.

The signals are saved using National Instrument PXI-5105 (as in Fig. 2.6), with an acquisition memory of 12 bits and 8 ports. This helps us to save input strain signal, output strain signal and striker velocity data simultaneously. All these signals are saved with a sampling time interval of 1×10^{-6}s and are triggered when the optical sensor capture any motion of striker.

The acquired signals are then treated using a software DAVID, developed at the "*Laboratoire de Mécanique des Solides de Palaiseau*" (LMS). The DAVID software, permits us to reconstruct the strain signals (shifting procedure) by taking the dispersion correlation and attenuation of the bars used in the SHPB. The user must execute a supplementary test with the bars (*i.e.* without sample) in order to calibrate the dispersive and dissipative behavior of SHPB bars.

Figure 2.6 – Signal acquisition setup

A part from this, a mirror and a high speed camera are placed on either side of the sample during the tests. A pattern is placed below the rib with horizontal lines at every 5 mm. The high speed camera has an acquisition frequency of 11500 img/s. The ensemble of test equipment, helps us to understand the behavior of porcine ribs under dynamic mechanical environment.

2.2.2 Preparation of rib

Porcine ribs were used as human surrogates for the tests carried out, it is quite common to use porcine ribs for studies in thoracic response as it shares geometrical and anatomical similarities with human ribs.

Fresh porcine ribs brought from a local butcher. The muscles and membranes surrounding the rib were removed. The extremities of the rib were then sanded to a planar surface in order to establish a good contact surface. Every rib specimen were then numbered and their characteristics such as mass, global dimensions were then noted. All the ribs were stored in ambient temperature before testing. The ribs were placed in between input and output bar(s) with zero initial stress condition and the distance between these interfaces was always 120 mm so that we have uniform results.

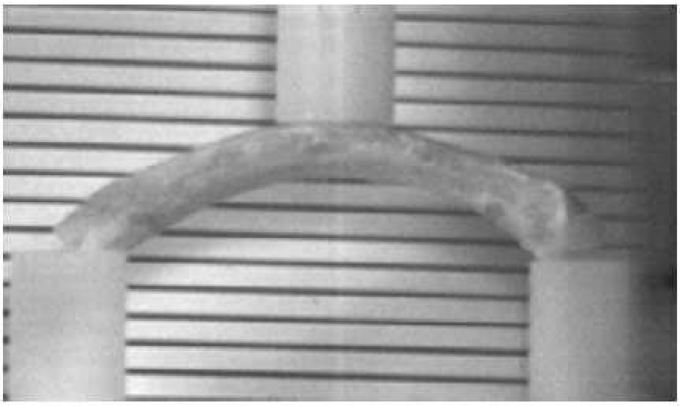

Figure 2.7 – Initial Position of the sample

2.3 Geometrical statistics of bone sample

A rib in general can be approximated to a curved beam. The most simple way to do this is to assume that the rib has a constant cross-section as shown in Fig. 2.8.

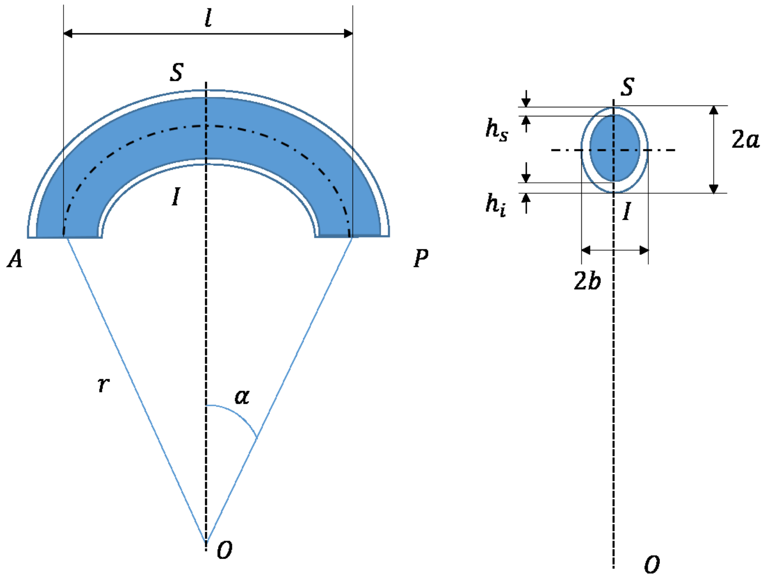

Figure 2.8 – Curved beam approximation of a rib

In such case, we can have the physical, global geometrical and local geometrical characteristics of rib prior to tests. These characteristics are presented below.

- Physical : Mass of the rib sample (m) in grams.
- Global geometry :
    - anterior-posterior length l [mm]
    - global curve radius r [mm]
    - curvature angle α [deg]
- Local geometry :
    - Major axis $2a$
    - Minor axis $2b$
    - superior layer thickness h_s
    - interior layer thickness h_i

Out of 27 ribs tested, only 19 were considered to be worth for further analysis. A general normal distribution with 95% confidential bounds is used for calculating mean μ and standard deviation s.d. for each variable is given in tab. 2.1 and is also represented graphically with corresponding probability density function in Fig. 2.9.

Property	mean μ	standard deviation s.d.
Mass m	15.6316 g	2.6918
Length l	113.594 mm	10.5015
Radius r	63.3105 mm	17.0245
Angle α	55.7716 deg	14.66
Major axis $2a$	10.0789 mm	3.941
Minor axis $2b$	9.7842 mm	3.6823
Superior layer thickness h_s	1.0789 mm	0.44669
Inferior layer thickness h_i	1.9632 mm	0.80499

Table 2.1 – Mean and standard deviation values for all properties

Let us say that we have a set of data and we know is mean μ and its standard deviation σ, then the variance is σ^2. Knowing these values, the probability density function pdf of normal distribution is expressed as

$$\text{pdf} = \frac{1}{\sqrt{2\pi\sigma^2}} e^{-(x-\mu)^2/2\sigma^2} \tag{2.16}$$

This pdf signifies the relative likely hood when the value of a sample equals to that of the sample in a given space.

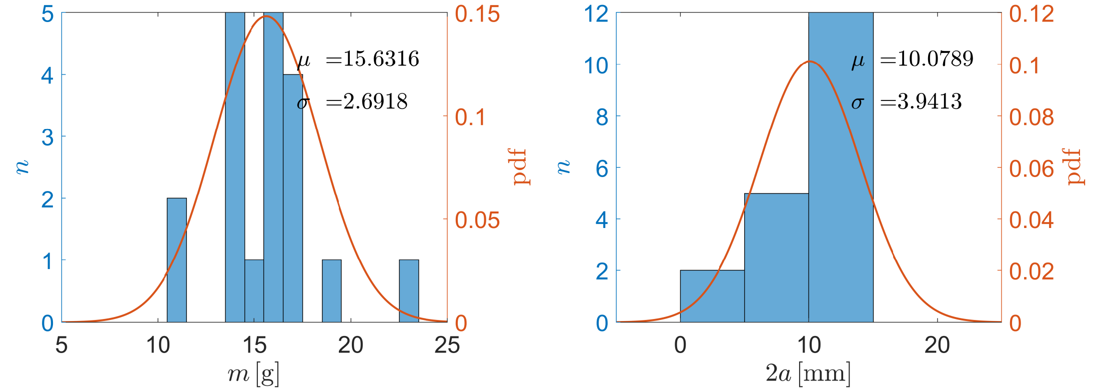

(a) mass (b) major axis

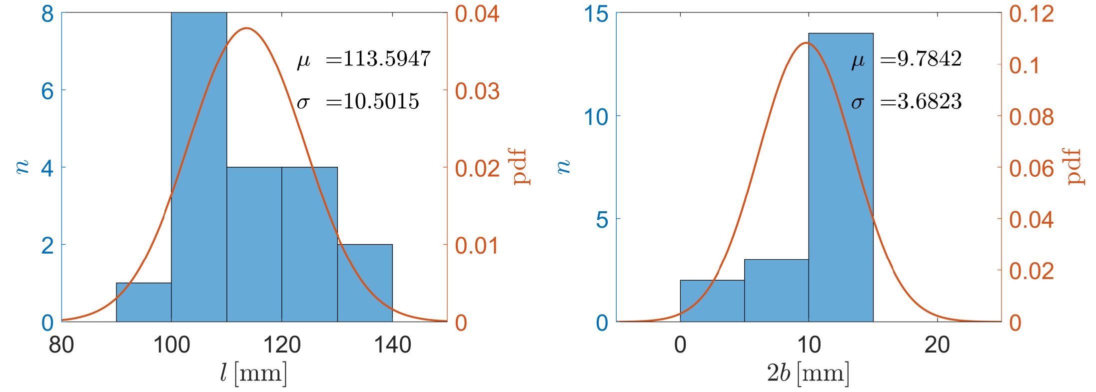

(c) length (d) minor axis

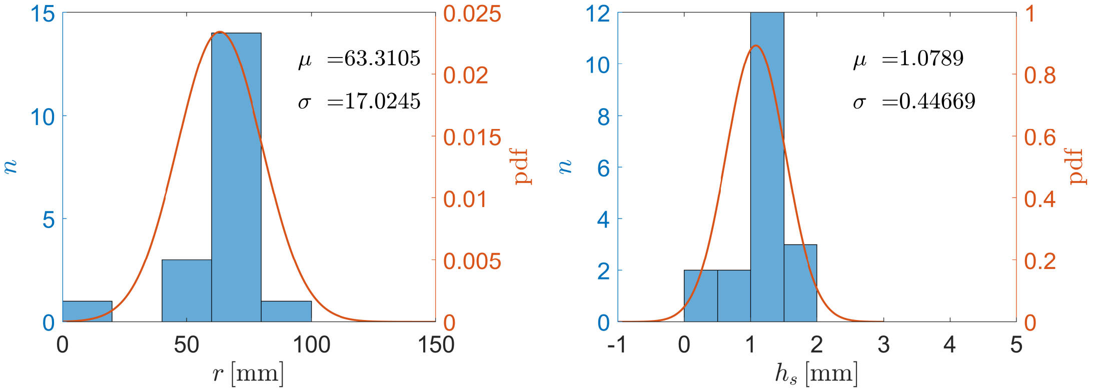

(e) radius (f) superior thickness

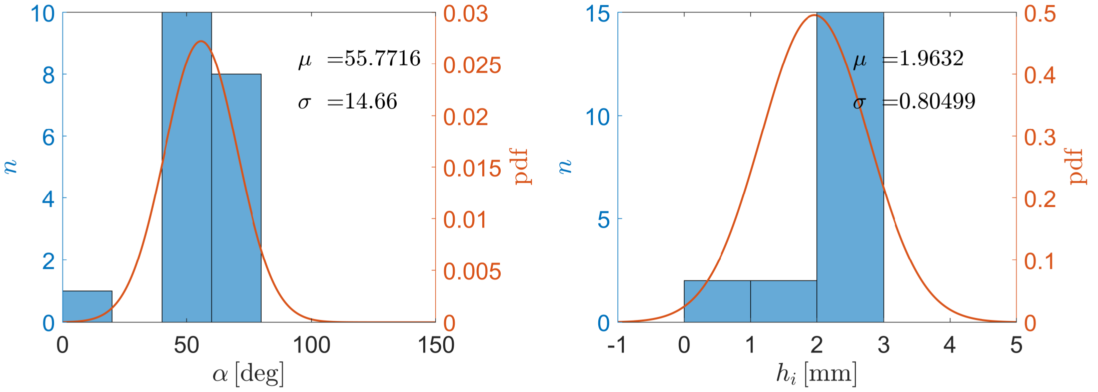

(g) angle (h) inferior thickness

Figure 2.9 – Normal distribution of all samples tested

2.4 Experimental Results

The experimental results presented in this section are based on the waves shifted in time and space *i.e.* $\varepsilon_{inc}(t)$, $\varepsilon_{ref}(t)$, $\varepsilon_{tr1}(t)$, and $\varepsilon_{tr2}(t)$. We have two transmitted waves as the setup consists of two transmitted bars. If the stress distribution is below the yield limits of the bar material, the dynamic variables used for characterization of material / structure could be calculated as in Eq. 2.17a to Eq. 2.17f through the plane wave propagation.

$$F_{in} = A_b E_b \left[\varepsilon_{inc} + \varepsilon_{ref}\right] \tag{2.17a}$$

$$F_{out1} = A_b E_b \left[\varepsilon_{tr1}\right] \tag{2.17b}$$

$$F_{out2} = A_b E_b \left[\varepsilon_{tr2}\right] \tag{2.17c}$$

$$v_{in} = -c_b \left[\varepsilon_{inc} - \varepsilon_{ref}\right] \tag{2.17d}$$

$$v_{out1} = -c_b \left[\varepsilon_{tr1}\right] \tag{2.17e}$$

$$v_{out2} = -c_b \left[\varepsilon_{tr2}\right] \tag{2.17f}$$

Apart form the equations Eq. 2.17a to Eq. 2.17f, two supplementary equations were also used to characterize the response of rib, they are the relative interface velocity V and relative interface displacement U and are expressed as follows

$$V = v_{in} - \left(\frac{v_{out1} + v_{out2}}{2}\right) \tag{2.18}$$

$$U = \int_0^t V dt \tag{2.19}$$

The tests carried out had permitted us to identify an ensemble of 20 treatable tests, with and without fracture of the specimen. With the help of air canon, we were capable of subjecting the specimens to relative velocities V between $5\,\mathrm{m.s^{-1}}$ and $13\,\mathrm{m.s^{-1}}$. The ensemble of data had led us to the identification of transition phenomenon in the dynamic response of rib structure. The results are presented below.

2.4.1 Tests without fracture

The name itself says that no visible fracture was observed in this test. Screen shots of high speed camera are shown in figure below. (*Note: The red mark indicates the initial position of the input bar-sample interface*). This peculiar case represents the response of rib at $V = 6\,\mathrm{m.s^{-1}}$, $v_{str} = 9.27\,\mathrm{m.s^{-1}}$.

Through Fig. 2.10, we can quantitatively say that the input bar imposes a displacement of $7.5\,mm$ during 1.5×10^{-3}s from the point time of impact. We do see negligible displacement of output bars. Even though Fig. 2.10 provides us with some quantitative information, the analysis of forces involved is important for a better comprehension.

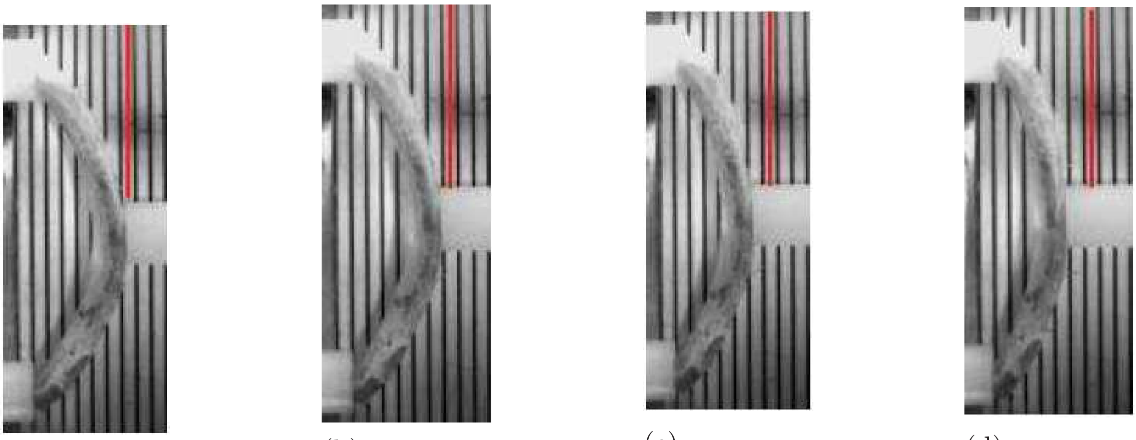

(a) $t = 0\mu$s (b) $t = 500\mu$s (c) $t = 1000\mu$s (d) $t = 1500\mu$s

Figure 2.10 – Test without fracture

Force vs. time response The forces involved in the test are presented in Fig. 2.11a. These forces permits us to identify and analyze the equilibrium state involved in this test. We were able to identify three different phases in the response of rib:

- ***Phase A***, which is seen during the first 200×10^{-6}s of the response. In this phase, we observe a drastic increase in the F_{in}, followed by a sharp shoot. On the other hand, the ΣF_{out} is zero during 150×10^{-6}s. This proves that the waves generated at the point of impact in the sample, propagate in the sample and are yet to reach the output bar-sample interface. At 200×10^{-6}s, the waves start to agitate the output bars, they start to exert reaction force on the sample.

- ***Phase B***, this phase seems to exist between 200×10^{-6}s and 600×10^{-6}s. It is during this phase, we observe the reflection of waves from the output bar-sample interface towards the input bar-sample interface. This phenomenon is characterized by the oscillation of ΣF_{out} around F_{in}.

- ***Phase C***, this phase seems to come into existence beyond 600×10^{-6}s. The equilibrium is established between F_{in} and ΣF_{out} during this phase and the sample it subjected three-point bending.

Force vs. Displacement response The F_{in} vs. U aids in the comprehension of rib structural response. The U is calculated from Eq. 2.19.

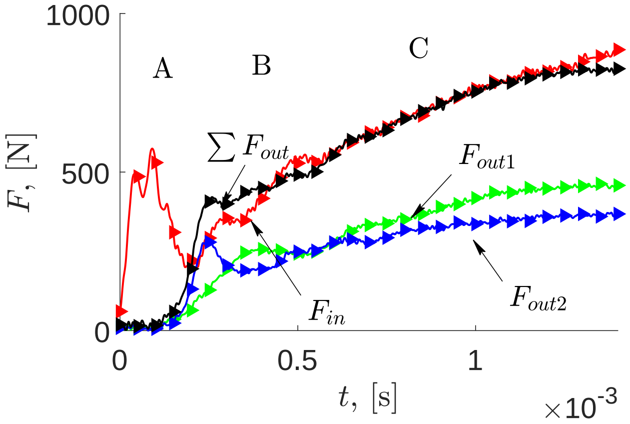

(a) Force vs. Time response

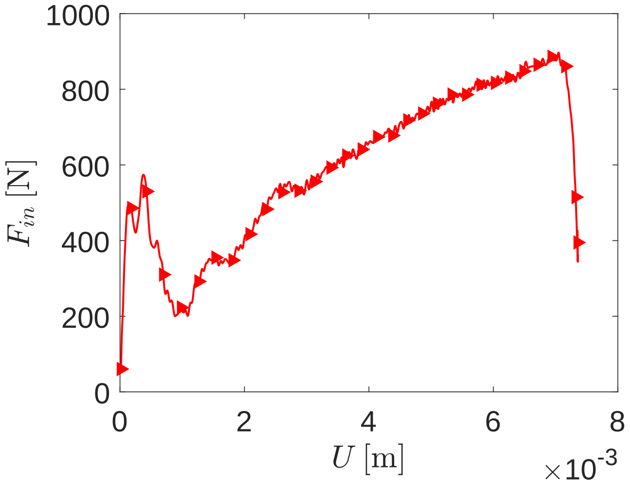

(b) Force vs. Displacement response

Figure 2.11 – Experimental data for $v_{str} = 9.27\,\mathrm{m.s^{-1}}$

2.4.2 Tests with Fracture

During Dynamic Equilibrium

The Fig. 2.12, represents a case of fracture during the dynamic equilibrium phase, corresponding to an experimental case with $V = 9\,ms^{-1}$ and $v_{str} = 17.39\,ms^{-1}$.


(a) $t = 0\mu$s
(b) $t = 1090\mu$s
(c) $t = 1450\mu$s

Figure 2.12 – Test with fracture during dynamic equilibrium

Force vs. time response The force vs. time response for this concerned experimental case can be seen in Fig. 2.13a. The shape of F_{in}, F_{out1} and F_{out2} are relatively symmetrical. We do observe a peak in the F_{in} and the oscillations in the curve(s) can be explained through two different phenomena, (i) the perturbations during the contact between the striker and the input bar and (ii) the queuing error.

Similar to the response in the case 2.4.2, we can differentiate three phases of response. Firstly, a transition zone during first 100×10^{-6}s, followed by a zone with increase in output forces between 100×10^{-6}s and 600×10^{-6}s. Beyond this point, the F_{in} and ΣF_{out} are almost equal, which helps us to identify the equilibrium is established at $\approx 625 \times 10^{-6}$s. In addition to this, the Fig. 2.13a alongside Fig. 2.12, also helps us to identify that a macro crack stats to develop at 985×10^{-6}s and leads to total rupture of the specimen at around 1100×10^{-6}s from the time of impact.

Force vs. displacement response The F_{in} vs u_{rib} for this case is presented in Fig. 2.13b. Based on the data, we can identify that the rib was subjected to a displacement of 9 mm, the debut of crack noted at $u_{rib} = 7.9$ mm leading to rupture at $u_{rib} = 8.75$ mm.

The analysis of all the experiments showing evidences of the presence of equilibrium phase, leads us to a conclusion that "*the dynamic equilibrium is established between* 600×10^{-6}s *and* 800×10^{-6}s". The time at which equilibrium is established, depends on properties of rib such as celerity of waves and geometry.

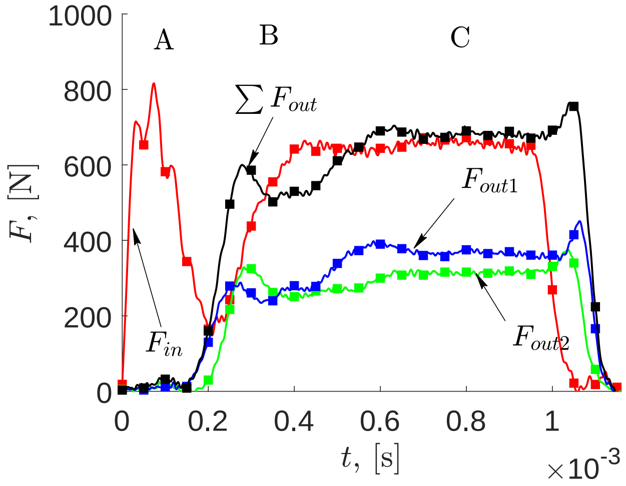

(a) Force vs. Time response

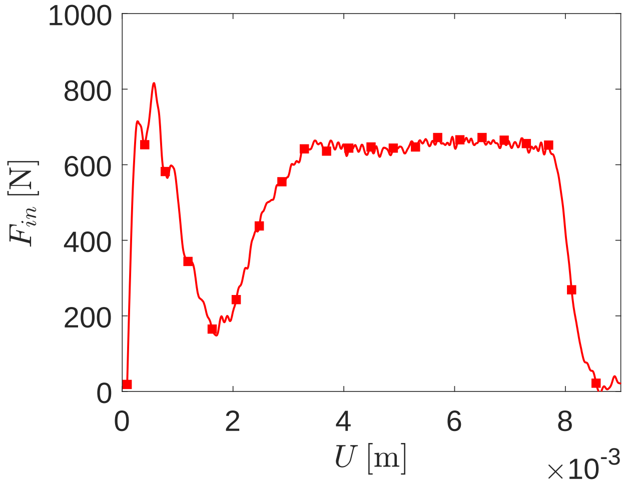

(b) Force vs. Displacement response

Figure 2.13 – Experimental data for $v_{str} = 17.39\,\mathrm{m.s^{-1}}$

Before Dynamic Equilibrium

The Fig. 2.14, represents a case of fracture before the dynamic equilibrium phase, corresponding to an experimental case with $V = 11.5\,\mathrm{m.s^{-1}}$ and $v_{str} = 19.21\,\mathrm{m.s^{-1}}$.

(a) $t = 0\mu$s (b) $t = 545\mu$s (c) $t = 1000\mu$s

Figure 2.14 – Test with fracture before dynamic equilibrium

Force vs. time response The time history of Force(s) is presented in Fig. 2.15a. In fact, in this case, we seen only the first two phases *i.e.* Phase A and Phase B. Moreover, this case does show evidence of a time difference between F_{out1} and F_{out2}, which is assumed to appear since the tested rib sample had some geometrical asymmetry.

The reason why, this experimental case is presented in this section is that we do not observe the Phase-C in force *vs* time response. A keen observation to Fig. 2.15a, shows that the rupture occurs at 520×10^{-6}s, which is $< 600 \times 10^{-6}$s. Thereby proving that equilibrium is never achieved.

Force vs. displacement response The F_{in} *vs* U for this case is presented in Fig. 2.15b. Based on the data, we can identify that the rib was subjected to a displacement of 6 mm, the debut of crack noted at $U \approx 4$ mm leading to rupture at $U \approx 5.6$ mm.

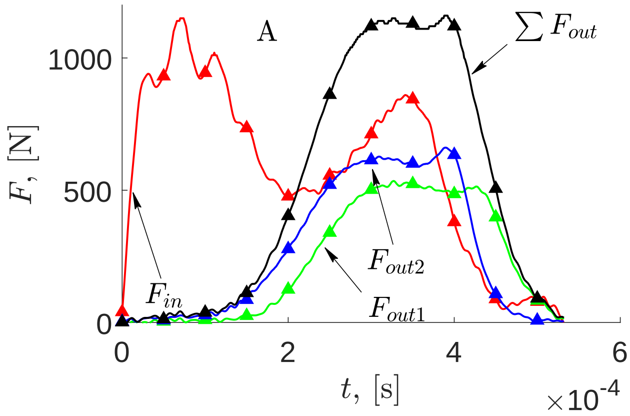

(a) Force *vs* Time response

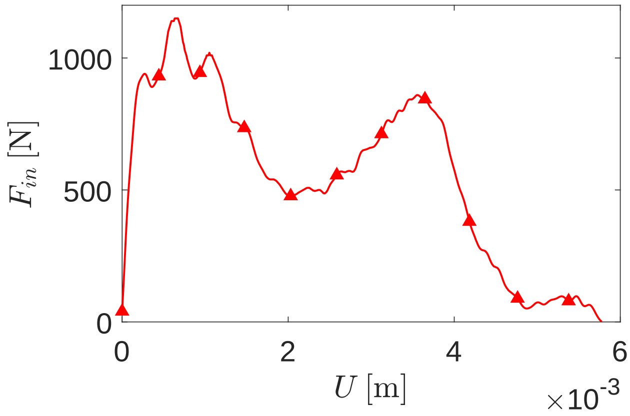

(b) Force *vs* Displacement response

Figure 2.15 – Experimental data for $v_{str} = 19.21\,\mathrm{m.s^{-1}}$

2.5 Analysis of Experimental Results

2.5.1 Effect of striker velocity on time for fracture

The variation of time at fracture t_{frac} from the instance $t_0^{'}$ is presented in Fig. 2.16. The o points signify cases with fracture during equilibrium whilst the stars represent fracture before equilibrium. We can notice that as the striker is launched at velocities greater than 15 $[\mathrm{m.s^{-1}}]$, t_{frac} decreases to below 0.8×10^{-3} [s]. Another interesting point to notice is that the experimental cases with fracture before equilibrium occur for $t \leq 0.8 \times 10^{-3}$ [s]. To be precise, out of 5 such experimental cases, 4 of them are around 0.5×10^{-3} [s]. Thus, we can deduce that the characteristic time for fracture t_{frac} to have a fracture before the dynamic equilibrium is established is around 0.5×10^{-3} [s].

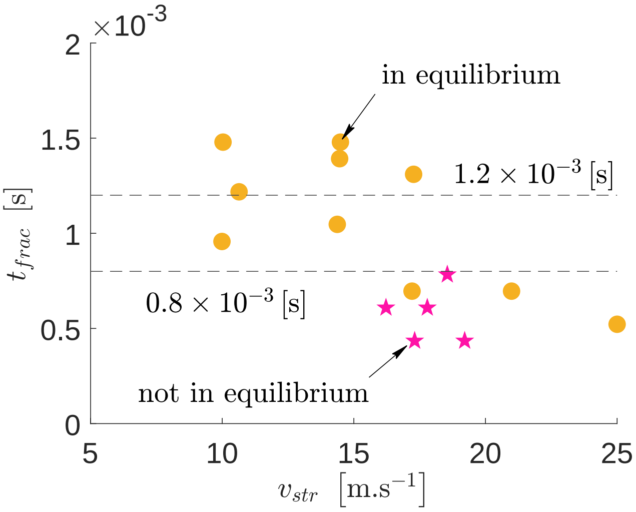

Figure 2.16 – t_{frac} *vs* v_{str}

2.5.2 Energy at fracture

Similar to t_{frac}, the energy at rupture W_{r} as a function of relative interface displacement at rupture U_r is presented in Fig. 2.17. We notice that around 75% of the experimental results are grouped in displacements between 0.005 [m] and 0.01 [m] whose corresponding energies at rupture vary between 2 [J] and 6 [J]. The black markers present the mean of each category.

Comparing W_{r} with t_{frac}, we can notice this dispersion of energy with respect to fracture before and during equilibrium in a more significant manner (see Fig. 2.18).

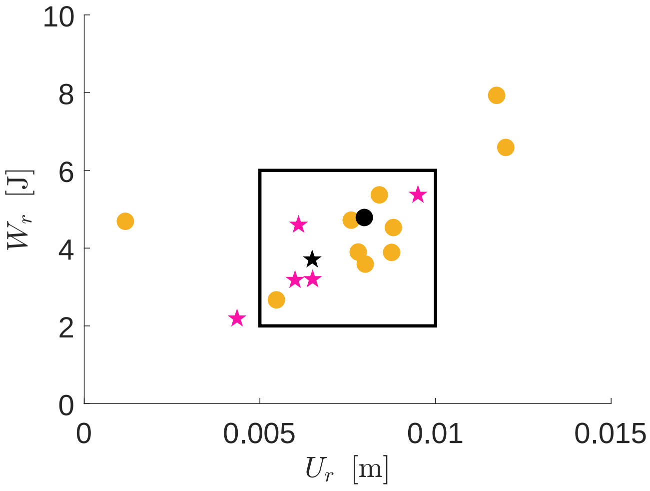

Figure 2.17 – Energy at fracture W_{r} *vs* displacement U_r

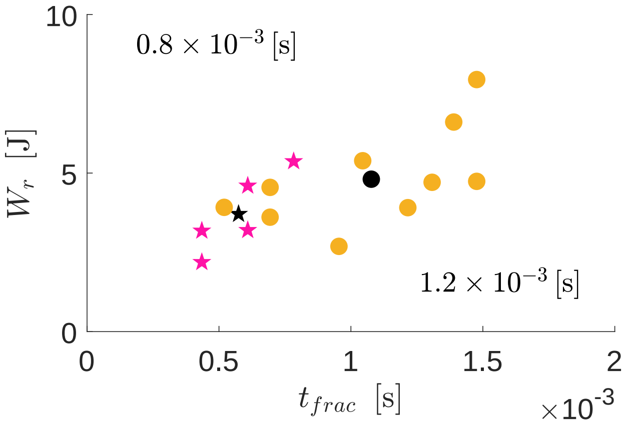

Figure 2.18 – Energy at fracture W_{r} *vs* t_{frac}

All out together, we can deduce that higher the striker velocity, less is the time and energy required for fracture. Thus, we can establish a barrier for transition between fracture before equilibrium and fracture during equilibrium in terms of $t_{frac} \approx 0.5 \times 10^{-3}\,[\mathrm{s}]$ and $W_{\mathrm{r}} \approx 4.2\,[\mathrm{J}]$. If the sample is rigid enough to surpass this barrier, it shall be capable of establishing an equilibrium thereby producing a plateau kind response in the force response.

2.5.3 Fracture Mode in ribs subjected to dynamic impacts

The question posed quite often in three-point bending tests, is the mode of fracture observed in the sample whilst subjected to dynamic impact loads. In this case, we find three possible modes of fracture:

1. A rupture controlled by shear stress without global bending of the sample.
2. A rupture due to crack originating from the tensile surface due to global bending of the sample.
3. A combination of two preceding modes.

The ensemble of 20 treatable experimental tests carried out had permitted us to conclude that

- The rupture of the sample is due to a crack originating from the tensile surface of the sample.
- This so called rupture was observed to occur either during the dynamic equilibrium or before the equilibrium was established.
- The maximum force imposed on the sample by the input bar *i.e.* F_{in} does not influence the rupture. Since, the maximum peak in F_{in} is seen during the

transition phase (Phase A) but neither in Phase B nor in Phase C, where the rupture is supposed to occur.

- Rather, the rupture is dependent on the local displacement of the rib. We had observed that the displacement attained by the sample during rupture was in between $4\,mm$ and $12\,mm$, whose lengths varied in between $100\,mm$ and $135\,mm$.

2.5.4 Characterization of Structural response

On the other hand, the experimental protocol presented in this thesis had provided us the useful data insights for understanding the structural response of porcine rib. The insights in this concern are given through the impedance adaptation between the bars and different samples tested, there by helping us to identify the parameters influencing the mechanical behavior of bone subjected to dynamic loads.

Since the geometry of rib plays an important role in its mechanical behavior, it is therefore impossible to characterize the structural response using fixed geometry of rib. To avoid these difficulties, we had decided to characterize the response in terms of F_{in} vs. U curves and the corridors obtained from maxima and minima of these curves. The F_{in} vs. U curves were analyzed with respect to rate of displacement V at the input bar - sample interface. This led us to identify three different corridors:

1 Corridor 1, $5\,\mathrm{m.s}^{-1} \leq V \leq 7\,\mathrm{m.s}^{-1}$. (see Fig. 2.19a)

2 Corridor 2, $8\,\mathrm{m.s}^{-1} \leq V \leq 10\,\mathrm{m.s}^{-1}$. (see Fig. 2.19b)

3 Corridor 3, $11\,\mathrm{m.s}^{-1} \leq V \leq 13\,\mathrm{m.s}^{-1}$. (see Fig.2.19c)

This methodology of presenting the results in form of experimental corridors, helps us to understand the influence of V on F_{in} and the bending displacement of ribs. We were able to identify the following:

- On the peak of F_{in} seen during Phase A (of sec.2.4.1 and sec.2.4.2). At low rates of displacement (*i.e.* $V \leq 7$), the peak of F_{in} varies between 400 N and 800 N. On the other hand, for high rates of displacement (*i.e.* $V \geq 8$), the peak of F_{in} varies between 800 N and 1400 N.

- As V increases, the fracture of rib tends to occur before dynamic equilibrium. The time at which the rupture occurs, depends on boundary conditions imposed on the specimen and also on the rate of loading. In other words, more the rate of displacement, less time for fracture to occur.

- Finally, we do remark an influence of V on the shape of F_{in} vs. U. We can see that at low rates of displacement, the force tends to increase continuously till rupture (see Fig. 2.19a). Whereas, at relatively high rates of displacement, the force decreases from its peak, followed by a subtle increase and stays constant (plateau like response) as in Fig. 2.19b and Fig. 2.19c. This plateau like response corresponds either to plastification or damage of structure.

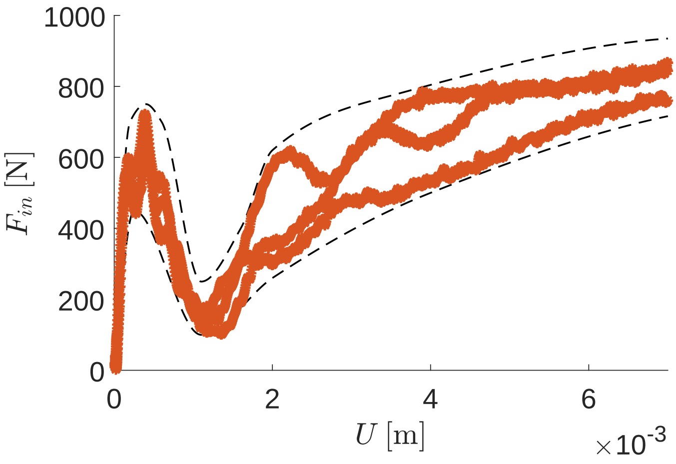

(a) Corridor 1, $5\,\mathrm{m.s^{-1}} \leq V \leq 7\,\mathrm{m.s^{-1}}$

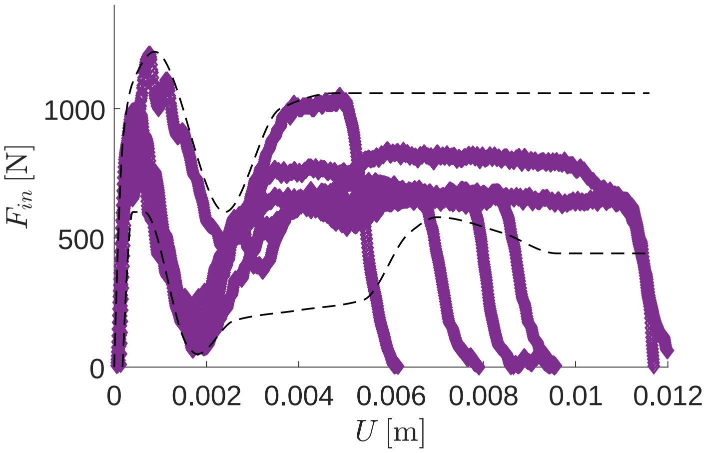

(b) Corridor 2, $8\,\mathrm{m.s^{-1}} \leq V \leq 10\,\mathrm{m.s^{-1}}$

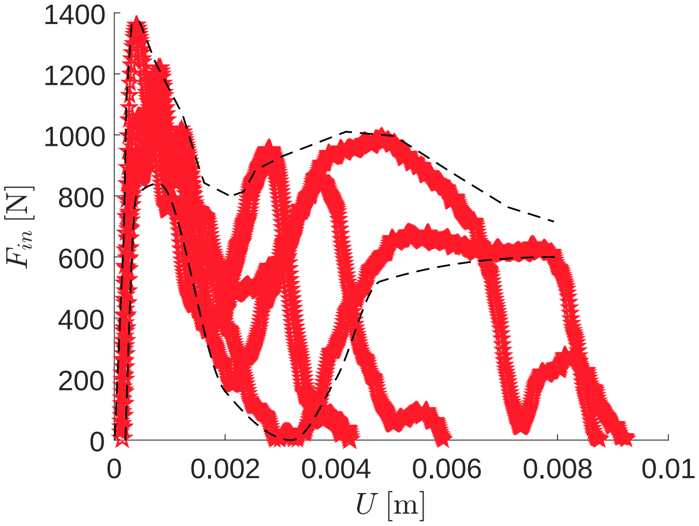

(c) Corridor 3, $11\,\mathrm{m.s^{-1}} \leq V \leq 13\,\mathrm{m.s^{-1}}$

Figure 2.19 – Experimental corridors

Note that the experimental response case of fracture before dynamic equilibrium is an interesting case as the energies and displacements are high enough that the bone fractures too early. Moreover, in reality, we cannot assume the establishment of equilibrium all the time. Therefore, we have decided to try to replicate two experimental cases in the numerical simulations at experimental scale namely case 1 and case 2. Case 1 represents to an experimental case with a striker velocity $v_{str} = 17$ [m.s^{-1}] and Case 2 represents to the experimental case with a striker velocity $v_{str} = 19.21$ [m.s^{-1}], that is an average of striker velocities corresponding to all experimental cases with fracture before dynamic equilibrium. The experimental force displacement responses in corridor 3 are presented below

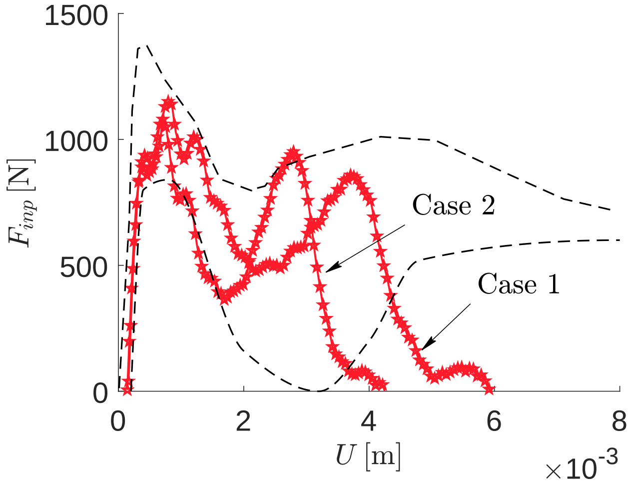

Figure 2.20 – Experimental force displacement for Case 1 and Case

2.5.5 Influence of geometry on structural response

In order to understand the effect of geometry on the type of response seen *i.e.* corridor type, we had grouped the corresponding samples with respect to corridors (see Fig. 2.21). We do see that the sample corresponding to corridor 2 (C-2) are concentrated near the global mean of all samples. Whereas, the samples corresponding to that of corridor 1 and corridor 3 have means less than that of the global mean. For example, let us consider the property l of the samples. The global mean presented in 2.3 μ_l is 113.59 mm, the means of lengths corresponding to corridors 1,2 and 3 are 109.68, 113.59 and 111.78 respectively.

A similar tendency is noticed among all other parameters. Unfortunately, we are unable to express the distinct nature of geometrical effects. In fact, to clearly understand the effects of geometry, it is advisable to carry out tests on a much larger sample size with considerable variations in their geometries.

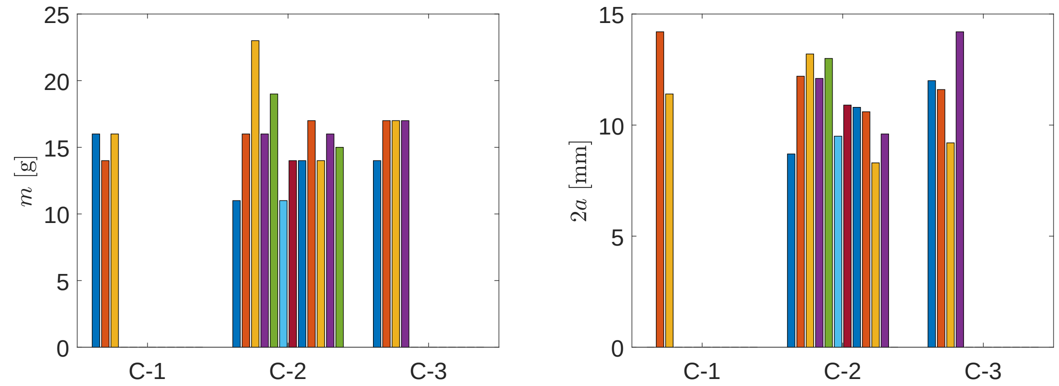

(a) mass (b) major axis

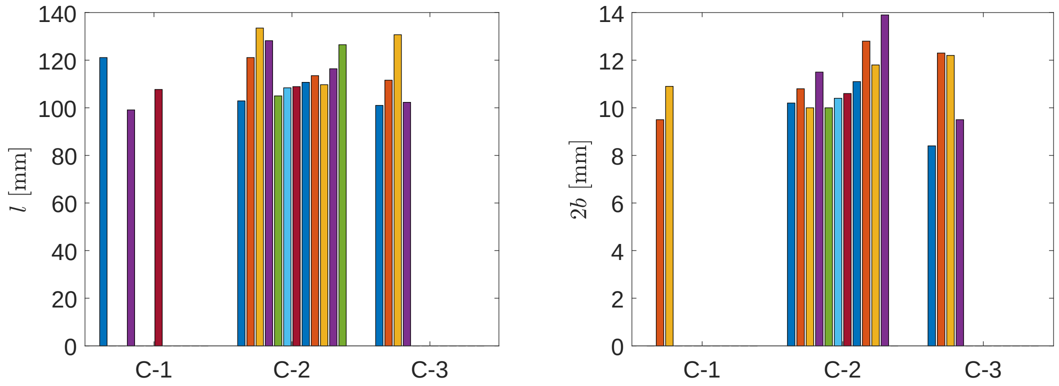

(c) length (d) minor axis

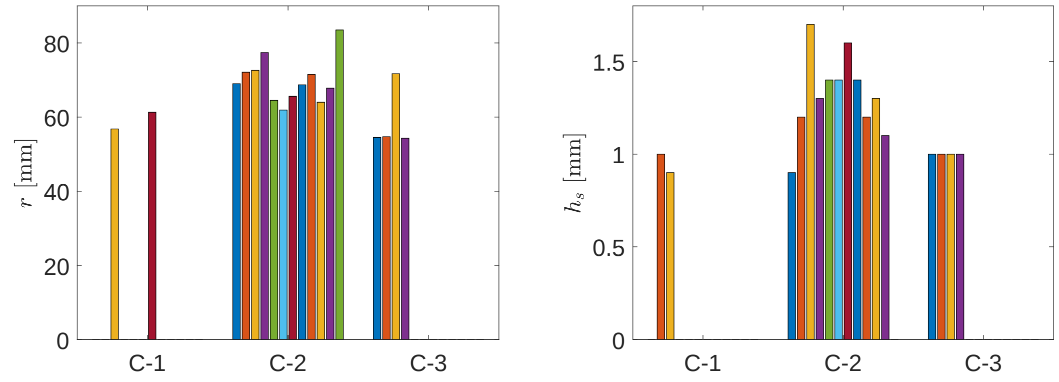

(e) radius (f) superior thickness

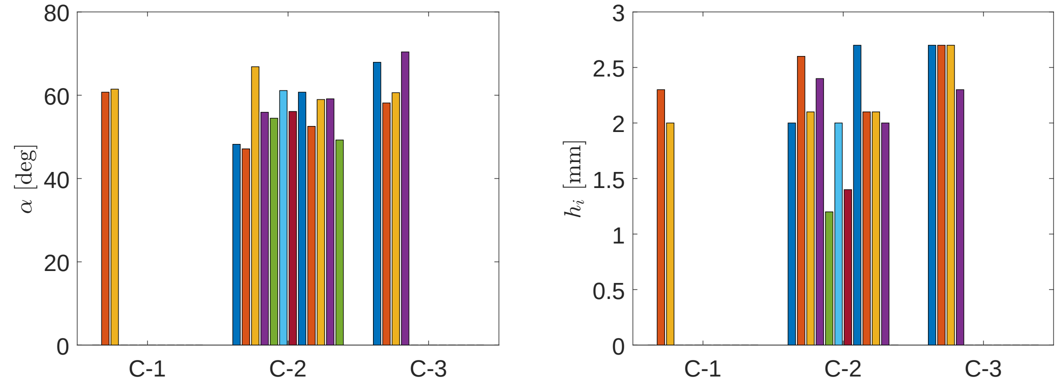

(g) angle (h) inferior thickness

Figure 2.21 – Samples grouped with respect to experimental corridors

2.6 Summary

The difficulties involved in a typical Split Hopkinson Pressure Bar system were over come by choosing nylon bars. Since these bars have a mechanical impedance similar to bone material, we were able to differentiate and shift the different waves of SHPB. Moreover, the sanding of porcine rib anterior and posterior extremities had ensured the establishment of decent contact with output bars.

These altogether, led to the comprehension of rib's response to dynamic three-point bending loads. It was found that the geometry of the specimen plays an important role similar to the human rib.

In the cases of fracture during dynamic equilibrium and fracture before dynamic equilibrium, the rupture of rib was due to a crack originating at the tensile surface of the rib. On the other hand, the maximum force imposed on the sample did not influence the rupture, since the rupture was observed during plastification phase of the response. Rather, the rupture was highly influenced by the displacement of rib, which varied between 4mm and 12mm. This variation in displacement was once again due the difference in geometry of the sample.

It was also noted that the velocity at the sample and bar(s) interfaces influenced rib displacement. Which in turn influenced the response of rib in terms of increase in peak force, time for fracture and shape of the response. As the interface displacement rate increased,

1. there was an increase in the magnitude of peak force.
2. the fracture tends to occur before the dynamic equilibrium is established.
3. the force tend to decrease from its peak, followed by a subtle increase and a plateau response.

These results show that the rib as a whole structure is sensible to strain rate.

Part III

Development of Finite Element model for dynamic fracture simulation of ribs

Chapter 3

Generation of numerical rib sample

Résumé :

L'échantillon numérique a été généré à partir des images DICOM obtenus par imagerie tomographique à haute résolution (HR-pQCT). La géométrie 3D a été ensuite reconstituée à partir des contours des images DICOM en utilisant le module de numérisation IP du logiciel Simpleware.

Les propriétés mécaniques (module d'Young, contraintes limites,...) sont reliées à la masse volumique, laquelle est elle même corrélée au niveaux de gris (échelle HU). Comme il y a plusieurs définitions de la masse volumique, nous en avons testé deux : la masse volumique apparente ρ_{app} et la masse volumique apparente de contenus de cendre ρ_{α}. Dans un premier temps la densité est corrélée avec la variable HU des images tomographiques. Ensuite il est possible de connaître les propriétés mécaniques associées à chaque zone de niveaux de gris par l'intermédiaire de la relation ρ_{app}(HU) ou ρ_{α}(HU). Nous avons utilisé les relations entre les propriétés et la densité publiées dans la littérature.

Nous constatons que les propriétés mécaniques en fonction de ρ_{app} sont les plus pertinentes dans le cadre de cette thèse.

Comme ρ_{app} nous permet de connaître la fraction volumique et la porosité Po de chaque constituant de la côte numérique. Connaissant la porosité, nous pourrions utiliser les équations de loi de puissance pour connaitre les propriétés mécaniques de ces constituants.
french

Abstract:

The numerical sample was generated from the DICOM images obtained through high resolution peripheral computed tomography (HR-pQCT). The 3D geometry and mesh were constructed from the contours of DICOM images using the Scan IP module of Simpleware.

The mechanical properties of bone constituents are linked to density values. We have tested two different mass density definitions in order to ensure which density definition is a reliable measure for mechanical properties for predicting the rib response observed experimentally. First of all, the apparent density ρ_{app} *was correlated with grey scale values expressed in* HU *through a linear equation. Secondly, the apparent ash density* ρ_{α} *was tested. The mechanical properties of each rib constituent were then found through power law regression equations available in literature.*

It is found that the mechanical properties from ρ_{app} *are the most reliable for this thesis. As* ρ_{app}*, gives us access to corresponding volume fraction* V_f *and porosity* Po *values, respective power law equations were used to differentiate between cortical and trabecular bone.*

3.1 HR-pQCT Scan procedure

A batch of porcine ribs were bought from a local meat processing plant in order to ensure homogeneity of samples. These samples were wrapped in a damp cloth, soaked in saline (9% NaCl) to avoid dehydration. The damp samples were then stored at stored in refrigerator at 4° C whilst not in use. They were defatted in an aqueous solution of Sodium Hypochlorite (NaClO) and Salt (NaCl) prior to the CT scan. Later, they were scanned using High Resolution peripheral Quantitative Computed Tomography (**HR-pQCT**)(XtremeCT,Scanco,Switzerland). The DICOM image slices were obtained using a multi-sclice device at 120 kVp, 160 mAs with an 512 × 512 image matrix and 150 × 150 mm field view. Each image sclice was 7 mm thick with a spatial resolution of 0.25 mm × 25 mm as in Fig. 3.1.

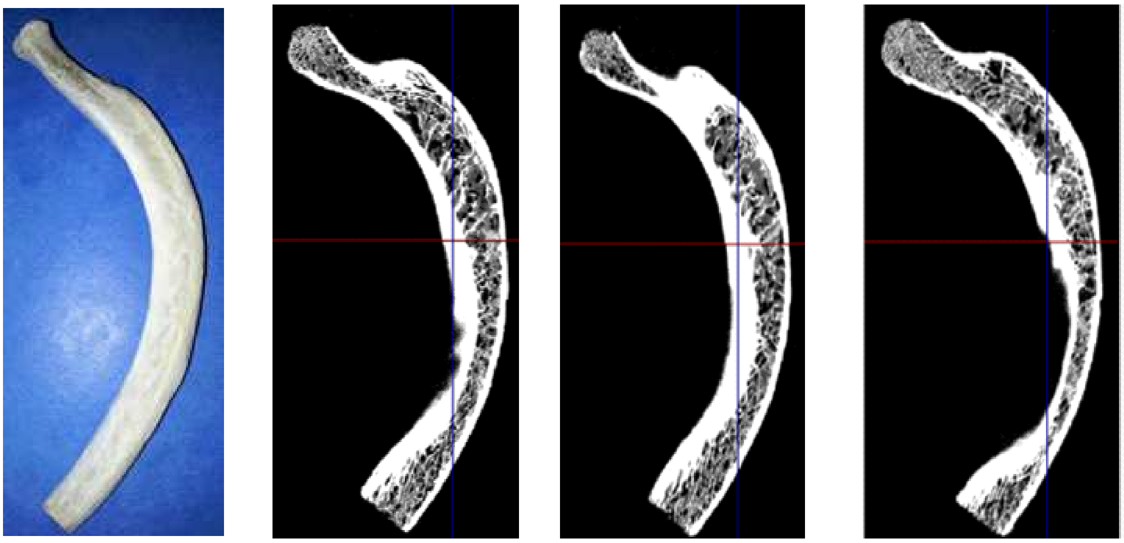

Figure 3.1 – Treated porcine rib and CT scan images

A 3D geometry was then created from the contours of the DICOM images in order to generate a hexahedral mesh for numerical simulations. ScanIP module of Simpleware® code Trial version, (Simpleware®, 2014), was used to import the DICOM raw data, perform image processing, visualization and segmentation of the rib geometry. A distribution of 8 grey scale intensities (see Tab. 3.1) was chosen to determine the heterogeneous mechanical properties of eight parts within the rib. A grey intensity (or level) is associated with a particular value of the linear attenuation coefficient μ. Five-sample calibration phantoms (Mindways®) with known equivalent K_2HPO_4 and H_2O densities were placed below the rib during the scan. Using an algorithm implemented into Simpleware® code, we obtained the linear calibration coefficients μ to convert the raw data into normalized data (GS), expressed in Hounsfield Units (HU) using the following linear expression (Taylor

2002, Teo et al. 2006):

$$GS = 1000\,\frac{(\mu_b - \mu_w)}{(\mu_w - \mu_a)};\ \mu_w = 0;\ \mu_a = -1000. \tag{3.1}$$

where: μ_b, μ_w, and μ_a are the values for bone, water and air respectively. This was done by calculating the average GS within each of the five calibration samples along the length of the scan and calculating the slope and intercept *vs* the known equivalent K_2HPO_4 and H_2O densities.

Part Number	Greyscale Intensity
1	184.314
2	364.706
3	552.941
4	741.176
5	921.569
6	1109.800
7	1298.040
8	1400.000

Table 3.1 – Grey scale values for porcine rib

3.2 Interpolation of Apparent Density

To quantify the mechanical properties of the constituents of porcine rib, the apparent density was first interpolated using the hypothesis put forth by Taylor (2002). The hypothesis is as follows

1. Having verified the units of CT values, first we calculate the effective density ρ_{eff} based on the relation proposed by Taylor (2002). According to them, ρ_{eff} includes the mass of bone, bone marrow and bone fluids. In other words it is equivalent to ρ_{wet}

$$\rho_{eff}[\mathrm{kg.m^{-3}}] = 0.523GS + 1000 \tag{3.2}$$

2. As we know that the dry density of water is zero and the apparent density of the hard bone segment in the rib corresponds to $\max(\rho_{eff})$. Using this hypothesis, the apparent density is correlated to HU with a line of slope a and zero intercept. This leads to the following relation

$$\rho_{app}[\mathrm{kg.m^{-3}}] = 1.2097GS \tag{3.3}$$

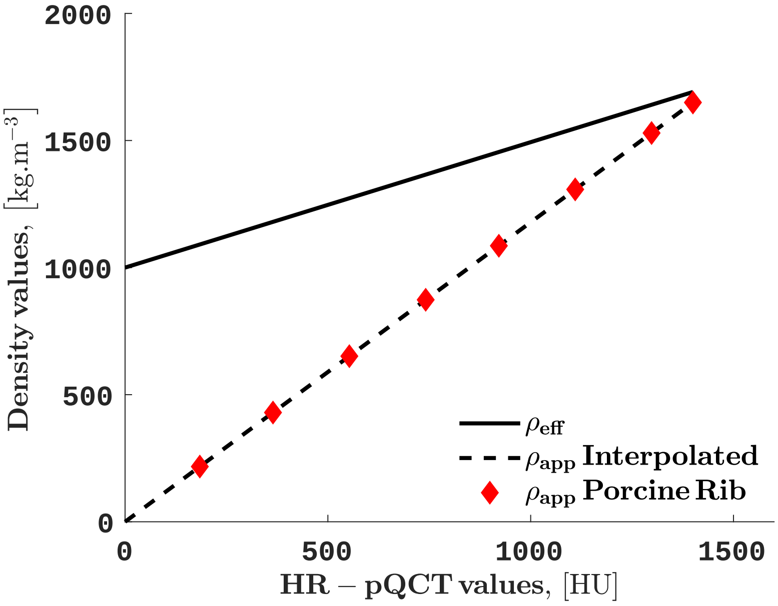

Figure 3.2 – Correlation of ρ_{app} with respect to CT$_{PR}$

The distribution of apparent density of the FE sample *i.e.* the ρ_{app} values represented by red markers in Fig. 3.2, are shown in Fig. 3.3. The Fig: 3.3 shows both longitudinal and transverse cross-sections. Two planes longitudinal section planes were chosen as examples for having an optimized view on the distribution of elements corresponding to different densities.

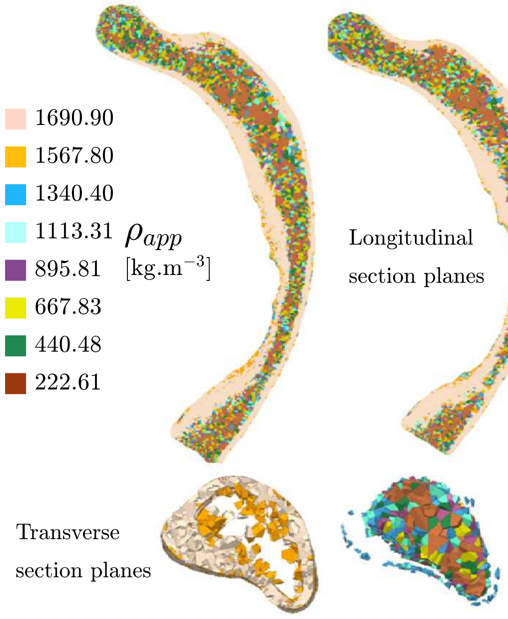

Figure 3.3 – Cross-sectional views of the rib FE model showing the density distribution.

A close look to the posterior end of the rib in Fig. 3.3 shall reveal that there is almost zero distribution of high density value elements at the posterior end. This is due to the defatting process carried out before CT scans. The corresponding region of the real porcine rib shall also be noted in Fig. 3.1. This shows that the defatting process does modify the structure a little bit. Unfortunately, this was the best and optimized result that we could obtain for this thesis.

3.3 Mechanical properties for numerical rib sample

As said in Sec. 1.3, two different regression models were tested *i.e.* one variable model (either ρ_{app} or ρ_{α}) as control variable and two variables model with volume fraction and ash fraction (V_f and α) as control variables.

3.3.1 One variable model

Three different models were tested for mechanical properties based on single variable power law regression. Out of which, one model considered ρ_{app} as control variable (referred as Model-1a) and two models considered ρ_{α} as control variable (referred as Model-1b and Model-1c)

Apparent density ρ_{app}

Model-1a: As said above, this model considers only apparent density in Fig. 3.2. The constituents of porcine rib were then identified by porosity $\mathrm{Po_{app}}$ from volume faction $\mathrm{V_{f_{app}}}$ through the Eq.

$$\mathrm{V_{f_{app}}} = \frac{\rho_{app}}{\rho_{tissue}} \tag{3.4}$$

$$\mathrm{Po_{app}} = \left(1 - \mathrm{V_{f_{app}}}\right) \times 100 \tag{3.5}$$

Based on the hypothesis proposed by Keaveny et al. (2003), cortical and trabecular bone constituents were identified as in Tab. 3.2. Based on the porosity values, corresponding power law regression equations were used. The equations for cortical and trabecular bone are given in tab. 3.3 respectively.

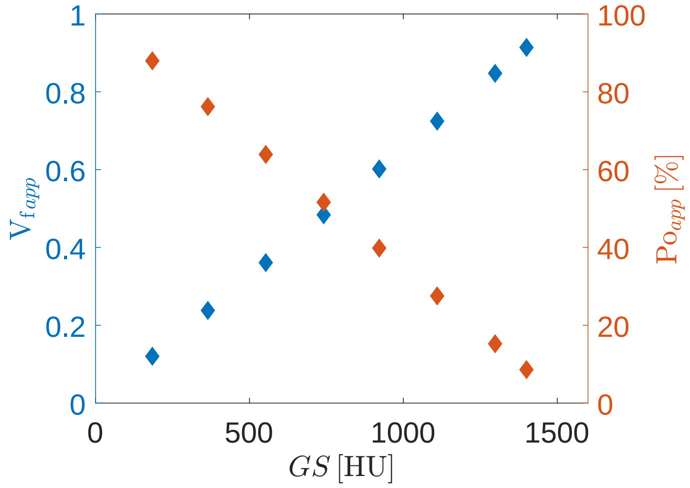

Figure 3.4 – V_{fapp} and Po_{app} *vs* CT_{PR}

Part Number	CT_{PR}	ρ_{app} [kg.m^{-3}]	V_{fapp}	Po_{app}[%]	Classification
1	181.31	222.61	0.1203	87.96	Trabecular
2	374.70	440.48	0.2381	76.18	Trabecular
3	552.90	667.83	0.3610	63.90	Trabecular
4	741.17	895.18	0.4839	51.51	Trabecular
5	921.56	1113.10	0.6017	39.83	Trabecular
6	1109.80	1340.40	0.7245	27.54	Trabecular
7	1298.00	1567.80	0.8474	15.26	Cortical
8	1400.00	1690.90	0.9140	8.60	Cortical

Table 3.2 – Different constituents of Porcine rib based on ρ_{app}

Property	Cortical	Trabecular
Young's Modulus E	$1.109 \times 10^{-6}\,\rho_{app}^{3.09}$	$0.5903\,\rho_{app}^{1.20}$
Compressive Strength σ_{uC}	$1.659 \times 10^{-4}\,\rho_{app}^{1.88}$	$8.534 \times 10^{-4}\,\rho_{app}^{1.53}$
Tensile Strength σ_{uT}	$1.61 \times 10^{-4}\,\rho_{app}^{1.88}$	$8.201 \times 10^{-4}\,\rho_{app}^{1.07}$
Compressive Yield σ_{yC}	$1.422 \times 10^{-4}\,\rho_{app}^{1.85}$	$5.167 \times 10^{-4}\,\rho_{app}^{1.60}$
Tensile Yield σ_{yT}	$3.064 \times 10^{-4}\,\rho_{app}^{1.67}$	$7.5686 \times 10^{-3}\,\rho_{app}^{1.04}$

Table 3.3 – Power law regression equations used for mechanical properties (unit for stresses is here MPa)

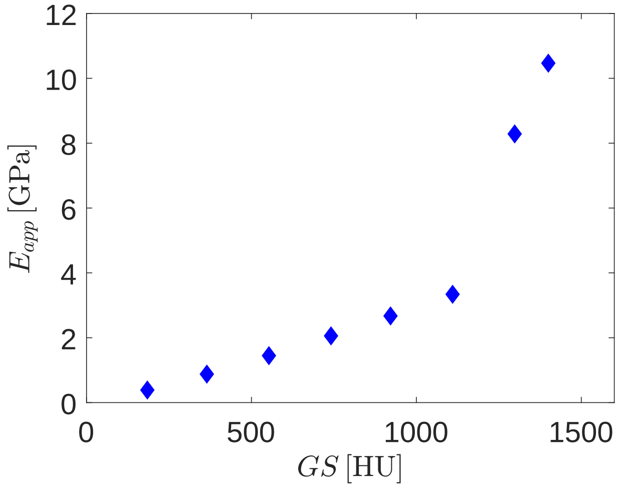

(a) CT$_{PR}$ *vs* E_{app}

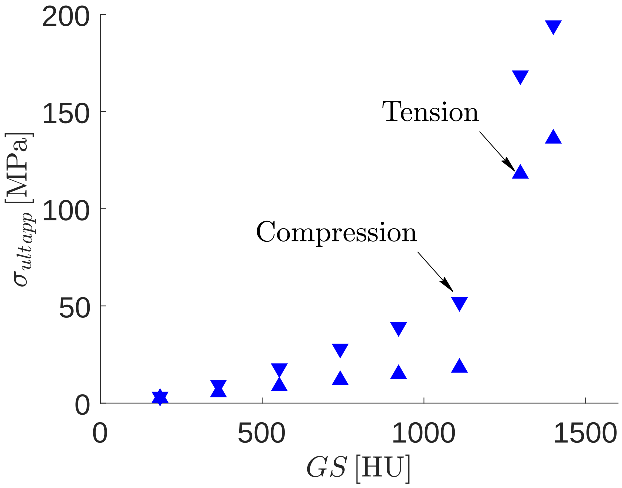

(b) CT$_{PR}$ *vs* σ_{ultapp}

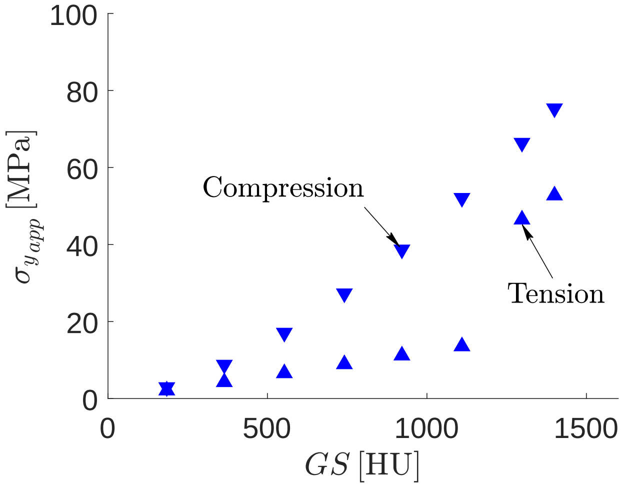

(c) CT$_{PR}$ *vs* σ_{yapp}

Figure 3.5 – Mechanical properties of porcine rib with ρ_{app}

Apparent ash density ρ_α

As said above, two different models were tested for ash fraction (α) and apparent ash density (ρ_α). Model 1b is based on the study proposed by Keller (1994) whilst the ρ_α in Model 1c was interpolated through Equivalent Mineral Density (ρ_{EQM}) from CT$_{PR}$.

Model 1b: The ρ_α in this model was interpolated to ρ_{app} of porcine rib data using the following relation proposed by Keller (1994)

$$\rho_\alpha = 0.522\rho_{app} + 0.007; \; for \; \rho_{app} < 1000 \text{ kg.m}^{-3} \tag{3.6}$$

$$\rho_\alpha = 0.779\rho_{app} - 0.250; \; for \; \rho_{app} \geq 1000 \text{ kg.m}^{-3} \tag{3.7}$$

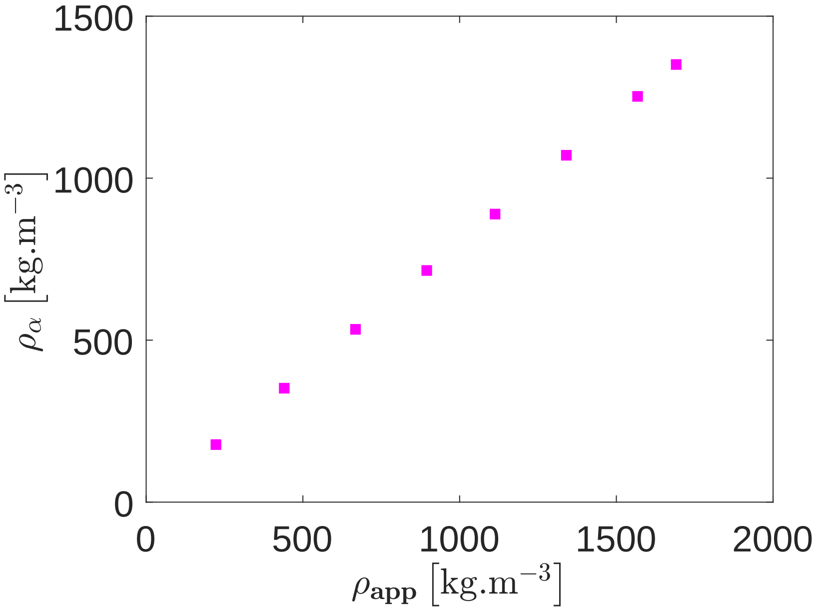

Figure 3.6 – ρ_α vs ρ_{app} of porcine rib based on Keller (1994)

Since the power law regression presented by Keller (1994) is based on pooled data from human femur and vertebrae, the equations relating to the later were considered for interpolation of mechanical properties and are given below.

$$E \text{ [GPa]} = 3.284 \times 10^{-6}\rho_\alpha^{1.92} \tag{3.8}$$

$$\sigma_{ult,Com}\text{[MPa]} = 4.399 \times 10^{-5}\rho_\alpha^{2.27} \tag{3.9}$$

$$\sigma_{ult,Ten}\text{[MPa]} = 3.079 \times 10^{-5}\rho_\alpha^{2.27} \tag{3.10}$$

Model 1c: Similar to Model 1b, this model also considers ρ_α as control variable. The only difference is that the ρ_α is interpolated from the Equivalent Mineral density of porcine rib, which is determined from CT_{PR}.

$$\rho_{EQM}\ [\mathrm{kg.m^{-3}}] = 0.6452\mathrm{CT}_{PR} + 0.487 \tag{3.11}$$

$$\rho_{\alpha EQM}\ [\mathrm{kg.m^{-3}}] = 1.27\rho_{EQM} + 0.0452 \tag{3.12}$$

In order to compare the two models (1b and 1c), the ash fractions (from Eq.3.13) and the mechanical properties through Eq. 3.8, Eq. 3.9 and Eq. 3.10 were considered.

$$\alpha = \frac{\rho_\alpha}{\rho_{app}} \tag{3.13}$$

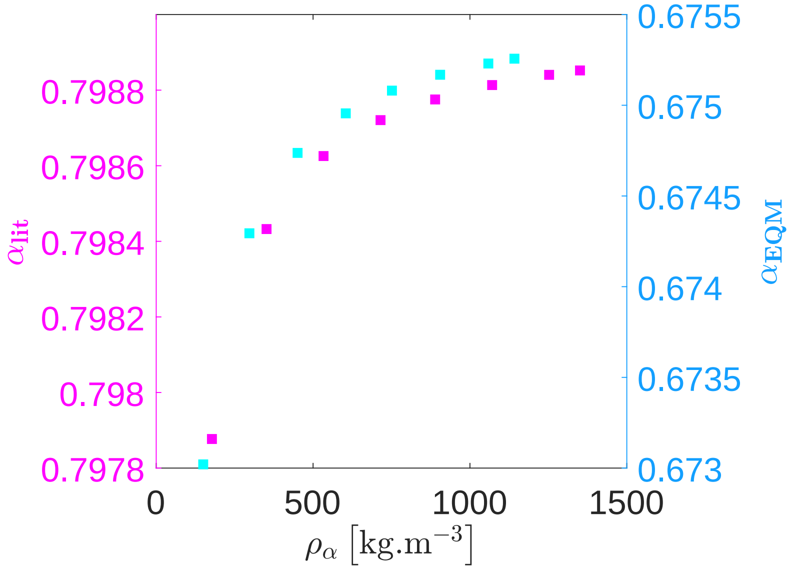

Figure 3.7 – Comparison of α from model 1b and 1c

The range of α from Eq. 3.6 and Eq. 3.7 is $0.795 < \alpha_{lit} < 0.8$ whilst the range of α from ρ_{EQM} was $0.672 < \alpha_{EQM} < 0.676$. According to Martin (1984), the ash fraction of a fully mineralized bone is ≈ 0.7 and that of an osteon is 0.0. Based on this hypothesis and comparing the α values from model 1b and model 1c, suggest that α_{EQM} is more reliable for porcine rib than that of α_{lit}.

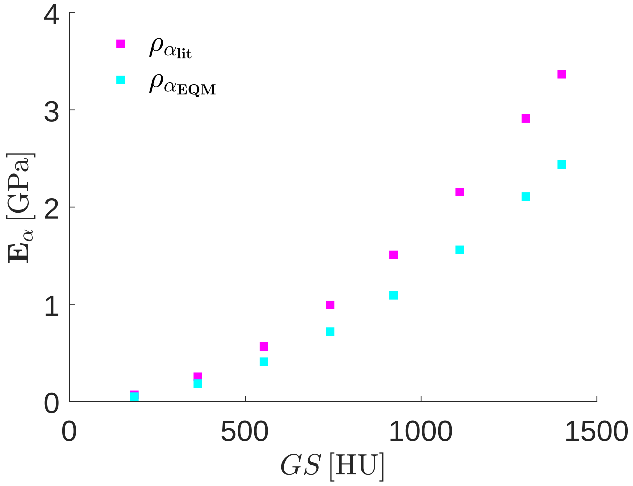

(a) CT$_{PR}$ vs E_α

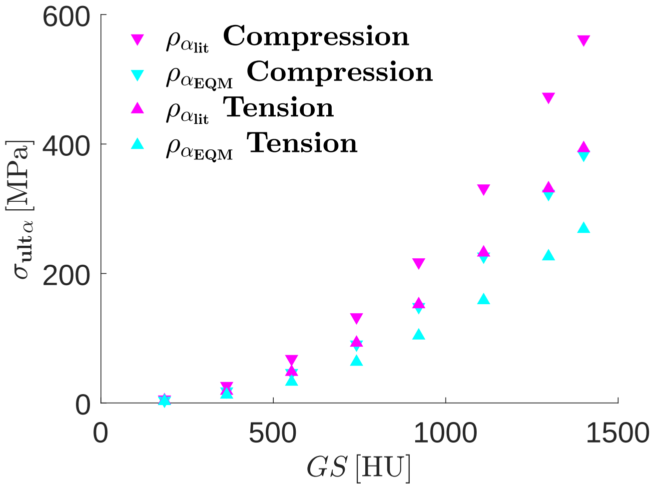

(b) CT$_{PR}$ vs σ_{ult}

Figure 3.8 – Mechanical properties of porcine rib with ρ_α

It is clearly seen that the variation in strength of bone is more pronounce due to change in ash content rather than in apparent density or volume fraction. On the other hand, models based on ash content seem to under estimate the elastic property of bone.

3.3.2 Two variables model

In order to have a better understanding of the influence of volume fraction and ash fraction, Hernandez et al. (2001) had put forth two variables based models that were supposed to give a better insight. They had considered both V_f and α as control variable for the pooled data produced by Keller (1994). The application of this model to numerical porcine rib is referred as model 2 in this thesis.

Model 2: the tissue density ρ_{tissue} is considered as a function of α as in Eq. 3.14, which is based on the the data of Martin (1984).

$$\rho_{tissue} = \frac{\rho_{app}}{1.41 + 1.29\alpha} \tag{3.14}$$

Since the range of α_{EQM} is more relevant to data produced by Hernandez et al. (2001), it was considered as reference for two variables model. The interpolated V_f and ρ_{tissue} are presented in Fig. 3.9

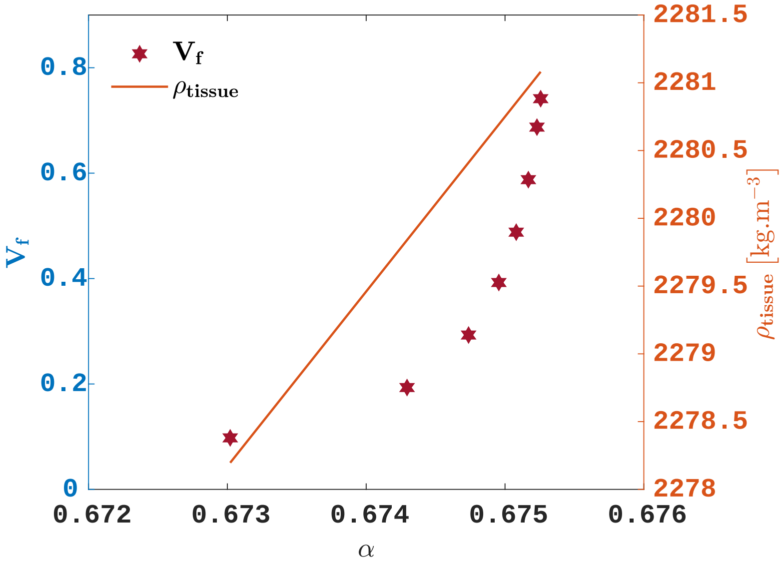

Figure 3.9 – variation of V_f and ρ_{tissue} with α

It is clearly seen that the ρ_{tissue} density determined from this hypothesis is surely over estimated and is much higher than that considered in Sec. 3.3.1. Thereby the V_f is under estimated, thus suggesting that the porcine rib consists of only one cortical bone constituent in contrast to Tab. 3.2.

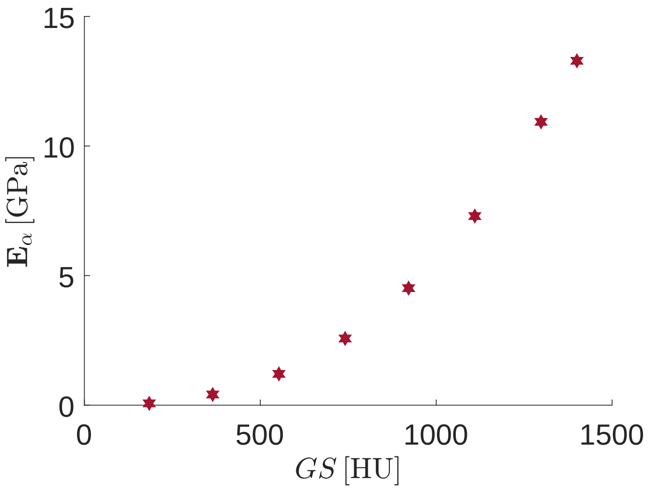

(a) CT$_{PR}$ vs E_α

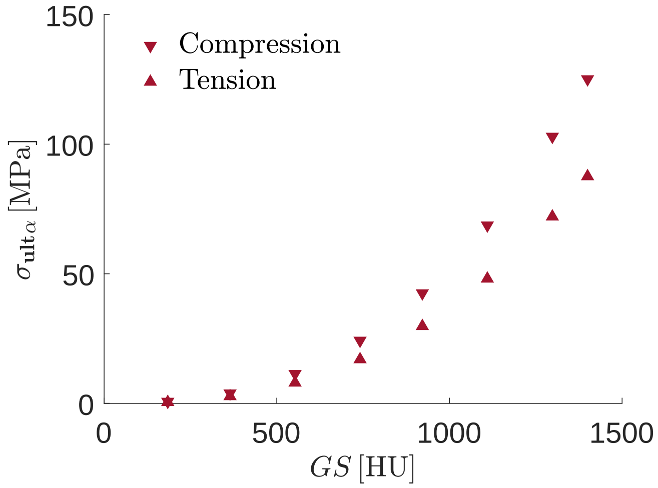

(b) CT$_{PR}$ vs σ_{ult}

Figure 3.10 – Mechanical properties of porcine rib with two variable model

On the other hand, the range of E and σ_{ult} (in Fig. 3.10a and Fig. 3.10b) determined from two variable model is similar to that of determined though ρ_{app}. Yet this proves that there is an influence of V_f but is less comparing to that of α.

3.3.3 Comparison of mechanical properties

In order to make sure which hypothesis shall be considered for the material properties of bone, the results of single variable model and two variable model were compared and verified with the element distribution in the numerical rib sample.

Firstly, the different density measures are compared and are presented in the Fig. 3.11.

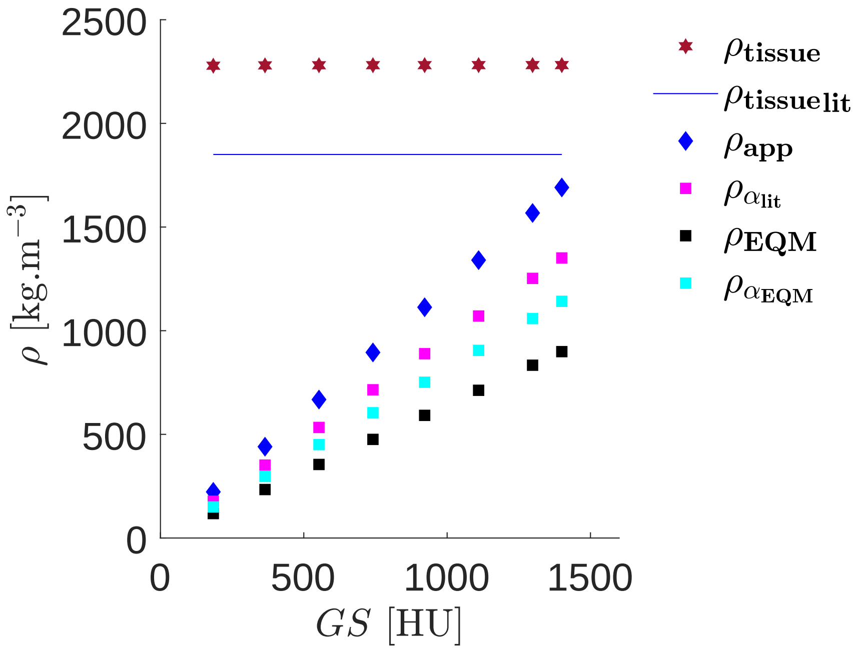

Figure 3.11 – Different density measures for porcine rib

Two striking conclusions can be drawn from Fig. 3.11

- The ρ_α from model 1b is slightly higher than that determined from model 1c. This difference in ash density can be explained by the origin of sample. For example, the relations proposed by Keller (1994) were based on pooled from human vertebrae and femur. Thus showing a difference in mineralization for different species.
- On the other hand, the ρ_{tissue} density from model 2 is also higher than that used in model 1a. which can be explained due to the consideration of α in Eq. 3.14.

The ash fraction does not only influence density measures, it rather has an effect on almost all the mechanical and architectural properties. For example, let us consider the $\mathrm{V_f}$ and Po depicted by blue and orange colored markers respectively in Fig. 3.12. Regarding the mechanical properties, following conclusions can be drawn

- The young's modulus obtained thorough apparent density and two variable model are of similar range and are largely high to those obtained from apparent ash density based models (see Fig. 3.13a).
- The ultimate properties are highly influenced by α or ρ_α as it can be seen in Fig. 3.13b. Even though the model 2 considers α, it does produce results similar to those obtained from apparent density.

We can conclude that the ash content in bone has a strong positive correlation on strength of bone and a negative correlation on the initial elastic behavior of bone. The reason for this influence in particular for human ribs or its biological surrogates is yet to be explained.

Unfortunately, there is a lack of data on the influence of α, ρ_α or two variable models on σ_y.

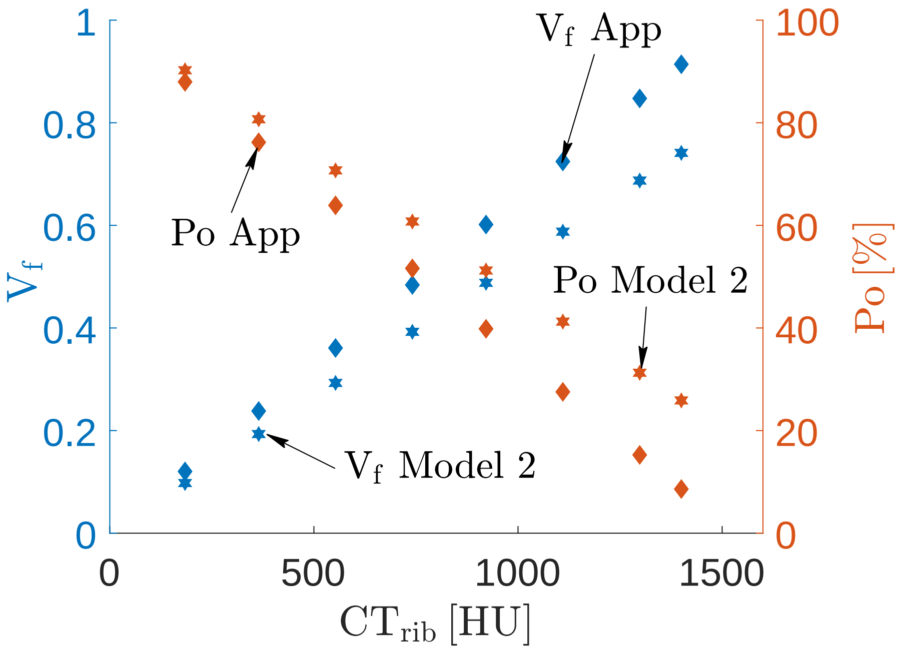

Figure 3.12 – Comparison of architectural properties

Again, this difference in $\mathrm{V_f}$ is due to the consideration of α in model 2.

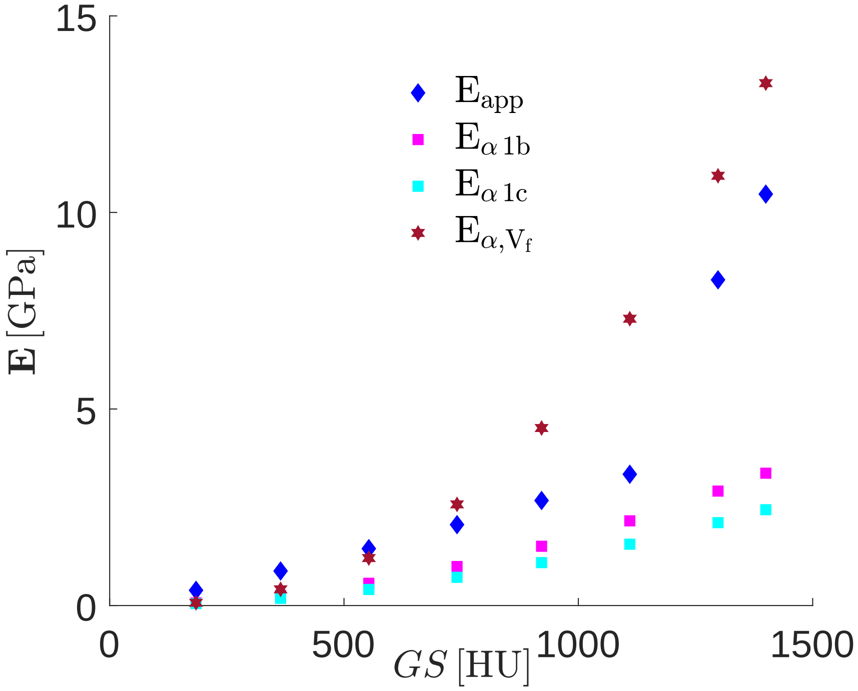

(a) Young's Moduli

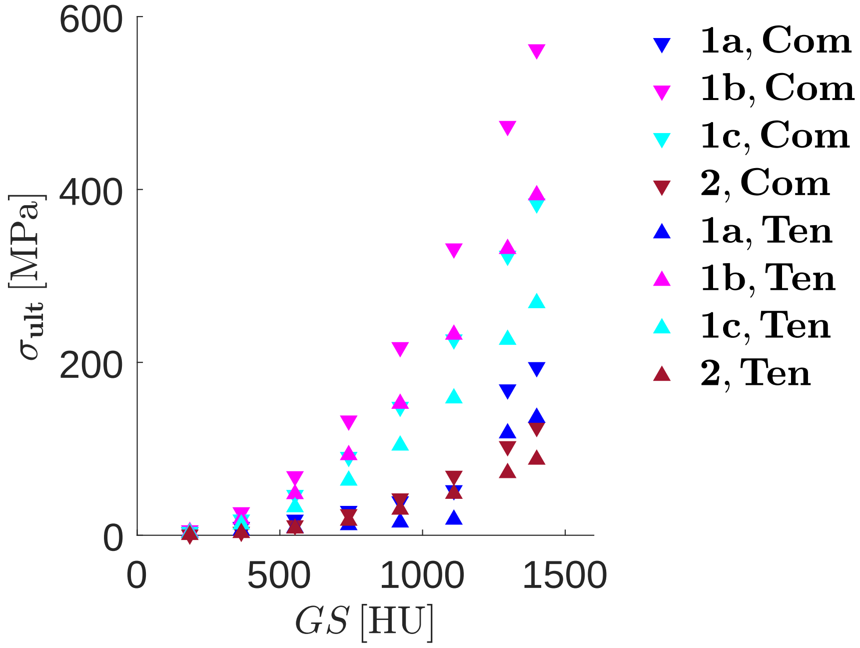

(b) Ultimate Strength

Figure 3.13 – Comparison of mechanical properties for porcine rib

The constituents of porcine rib, obtained from model 1a and model 2 were compared with the element distribution of numerical rib sample based on porosity values. It is clearly seen that $\mathrm{Po}_{\mathrm{app}}$ (represented as orange diamonds in Fig. 3.9) is in strict accordance with the element distribution in contradiction to those obtained by $\mathrm{Po}_{\alpha,\mathrm{V_f}}$ of model 2 (represented by orange stars in Fig. 3.9). This element distribution is shown in figure below and corresponding density and porosity values are given in Tab. 3.2

(a) Cortical bone

(b) Trabecular bone

Figure 3.14 – Element distribution in porcine rib sample

The properties obtained from apparent density are in accordance with that used by previous authors for human rib. The comparison in presented below

Author	Origin	Bone	ρ, kg.m^{-3}	E, GPa	σ_y, MPa
Charpail (2006)	Human	Cortical	2000	13	150
	Human	Trabecular	1000	2.4	2
Li et al. (2010)	Human	Cortical	2000	11.5	88
	Human	Trabecular	1000	0.04	2.2
Yates and Untaroiu (2018) a	Human	Cortical	2000	11.03	98.98
	Human	Trabecular	1000	0.04	1.8
Yates and Untaroiu (2018) b	Human	Cortical	2000	12.38	82.36
	Human	Trabecular	1000	0.04	1.8
This study	Porcine	Cortical	1630.00	9.37	70.876
	Porcine	Trabecular	779.92	1.80	24.48

Table 3.4 – Comparison of average porcine rib apparent properties with human rib

These data prove that either V_f or ρ_{app} based regression models are efficient and reliable for having a decent insight on mechanical properties of a numerical model.

3.4 Summary

The apparent density ρ_{app} follows a linear relationship with grey scale intensity of porcine rib CT_{PR}. Regarding the interpolation of mechanical properties, two one variable models and one two variable models were tested. Results show that the considering either apparent ash density ρ_{α} or ash fraction α as independent variable, overestimates the ultimate and post yield properties. Therefore, mechanical properties based on ρ_{app} are in good correlation and also are in the same range of properties used in previous numerical studies of human ribs (see Tab. 3.4). Yet this proves that porcine ribs are biologically reliable as human surrogates.

Chapter 4

Definition of numerical model

Résumé :

Dans ce chapitre, nous présentons les choix principaux concernant : la loi de comportement et la loi d'endommagement, le maillage, l'algorithme numérique du contact.

Les résultats expérimentaux nous montrent que la vitesse relative des interfaces n'influence pas la partie linéaire de la réponse de la côte. Par contre, elle a une forte influence sur la partie plastique. Donc, une loi de comportement élasto-viscoplastique a été retenue. Trois formulations de lois de comportement élasto-viscoplastique ont été testées.

Une loi d'endommagement incrémentale et dépendante de l'état de contrainte a été couplée avec les lois de comportement testées. Cette loi d'endommagement est capable de tenir compte de l'accumulation non-linéaire de l'endommagement et ses conséquences (perte de rigidité...). De plus, l'influence de la vitesse de déformation ($\dot{\varepsilon}$) *sur la déformation à la rupture* (ε_f) *a été prise en compte.*

Un algorithme de contact entre les surfaces, basé sur la méthode des pénalités a été choisi pour les interfaces entre les barres et l'échantillon. Pour tenir compte de la cohésion entre les éléments internes de la côte (zones dotées de propriétés mécaniques différentes), un contact intérieur a été défini. Ainsi, le solveur numérique considère la côte comme une structure composite.
french

Abstract:

This chapter presents the important choices considered for simulation of porcine rib at experimental case, such as the constitutive law, the damage law, mesh, and

contact between the sample and bar interfaces.

It is well known that the bone is strain rate sensitive, thus use of constitutive laws such as viscoelastic-viscoplastic or elasticviscoplastic could be noted in the literature available today. The experimental results obtained in this thesis proves that the relative interface velocity does not affect the initial linear response of the sample, rather it has a pronounced effect on the post yield behavior. Therefore, an elasticviscoplastic constitutive law is the suitable law in this thesis. A total of three elasticviscoplastic constitutive laws were tested.

As all three constitutive laws do not offer coupled damage law, an incremental and stress-state dependent damage law was chosen. This damage law is dependent on stress-state of the sample with a capacity to consider non-linear damage accumulation and reduction in force carrying capacity with increase in damage. Moreover, the effects of strain rate $\dot{\varepsilon}$ *on fracture strain* ε_f *was taken into consideration through a logarithmic equation.*

A penalty based surface-to-surface contact was chosen for contact at bar-sample interfaces. As the numerical sample is a distribution of different densities, thus different mechanical properties, a contact ("Contact Interior") was defined internally between each elements of the sample in order to represent the internal cohesion of the structure. By doing so, the solver is capable to apprehend that these constituents form a single structure.

The bibliographical research and experimental results have shown that the numerical sample must have a decent geometrical representation, the material model for bone must consider the effects of strain rate both in mechanical behavior and damage. Therefore, we present a numerical model generated through CT scan images of porcine rib for a good geometrical representation and an elastic-viscoplastic constitutive law, coupled with an external damage law that takes the effects of strain rate on damage accumulation.

Apart from these considerations, the numerical model does involve one dimensional wave propagation in bars and contact between each constituent of the numerical model. The numerical constraints addressed are:

- Wave propagation in bars
- Constitutive and damage law for rib and its constituents
- Contact algorithm for bar and sample.

4.1 Wave propagation in a bar

First of all, the choice of constitutive law for bars is important. The bars of SHPB experimental setup are made of nylon in order to have mechanical impedance of same order of magnitude as bones. Even though nylon is a viscoelastic material, the viscosity of nylon induces only small variations to the local linear relations between particle velocity, stress and strain (Zhao et al., 1997). This led to the use of classic elastic constitutive law for nylon bars in our simulations.

Property	value
Density (ρ_b kg.m^{-3})	1200
Young's Modulus (E_b GPa)	3.3
Poisson's ratio (ν_b)	0.3

Table 4.1 – Elastic properties of Nylon for bars in SHPB

Another classical problem encountered in a numerical model with wave propagation in a non-uniform mesh is that it produces wave reflection and there is a difference in wave celerity. Thus, the accuracy of a numerical simulation depends on the mesh size and mesh density (Roth, 2009). Moreover, the mesh size and its variation does affect the uniform propagation of waves in a numerical simulation (Bazant, 1978). The main assumption considered in SHPB setup is one dimensional propagation of waves. Therefore, in order to avoid spurious wave reflection, we had adapted the principle put forth by Roth (2009). This relation is used to determine the mesh density (Γ) and mesh size (Δx) for a desired wave length (λ) so that the celerity of numerical wave (c_{FEM}) is almost equal to theoretical celerity of waves (c_{th}) as in Eq. 2.5.

According to Bazant (1978), the relation between c_{FEM} and c_{th} is given as

$$\frac{c_{FEM}}{c_{th}} = \frac{2}{\Phi}\left[(\sin\frac{\Phi}{2})^{-2} - \frac{2}{3}m\right]^{-\frac{1}{2}} \tag{4.1}$$

$$\text{where, } \Phi = \frac{2\pi\Delta x}{\lambda} \tag{4.2}$$

$$\Gamma = \frac{\lambda}{\Delta x} \tag{4.3}$$

$$\therefore \ \Phi = \frac{2\pi}{\Gamma} \tag{4.4}$$

where, m in Eq. 4.1 represents type of mass distribution $m = 0$ for lumped mass matrix, $m = 1.0$ for consistent mass matrix and $m = 1.5$ for hybrid mass matrix. The variation of celerity ratio for respective mass matrices is presented in Fig. 4.1

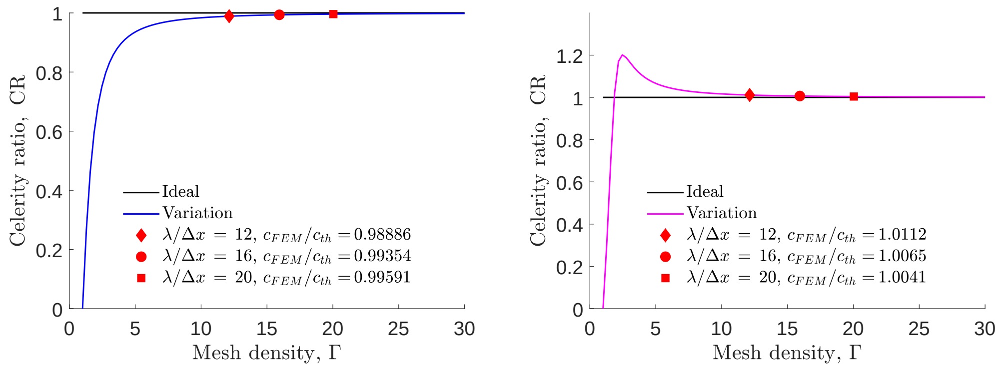

(a) lumped mass matrix ($m = 0.0$) (b) consistent mass matrix ($m = 1.0$)

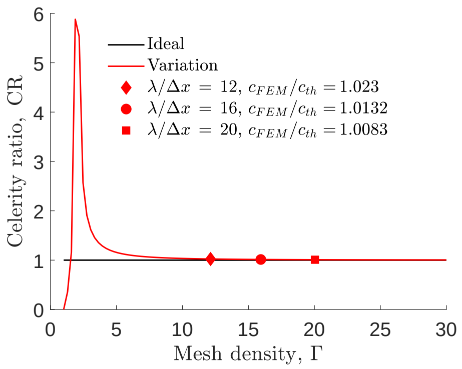

(c) hybrid mass matrix ($m = 1.5$)

Figure 4.1 – Variation of celerity ratio with mass matrices

As the bar is considered a deformable body and deformable solid elements in LS-Dyna are made of consistent mass matrix *i.e.* *'the mass of a element is distributed evenly at all the eight nodes of the element'*. Therefore, the variation of CR , resembles to that of Fig. 4.1b.

In order to test the desired mesh size for a uniform wave propagation in bars, a samll scaled model was used as reference. This model consists a striker 0.1 m long and 3×10^{-3} m in diameter and a bar 0.6 m long and 4×10^{-3} m in diameter. Three different values of mesh density were tested for a specific wavelength ($\Gamma = 12, 16$ and 20). Three elements at $l_b'/4$, $l_b'/2$ and $3l_b'/4$ respectively were used to record the strain signal to verify c_{FEM}.

Γ	c_{FEM}, m.s^{-1}	Number of cycles	Time (min s)
12	1635.98	15200	3 min 33 s
16	1648.26	15200	4 min 48 s
20	1659.50	15200	6 min 56 s

Table 4.2 – Effect of Γ on accuracy and calculation time

The change in mesh size did show a negligible affect on the strain signal response (see Fig. 4.2). On the other hand, the contact force was not affected.

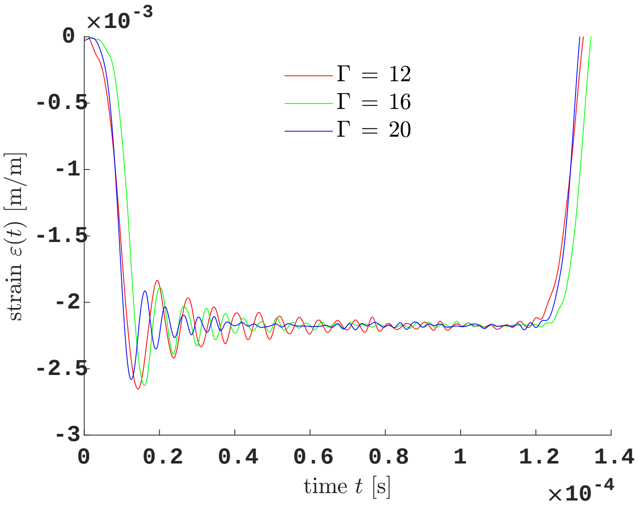

Figure 4.2 – Incident strain signals at mid point of the bar

Even though $\Gamma = 20$ takes more time per cycle of the calculation, it is more accurate in terms of wave celerity. Thus, the corresponding mesh size was considered for bars. Another common problem encountered in numerical simulation of wave propagation is the element formulation with respect to number of Gaussian integral points. Previous studies that investigated the model convergence recommended using an element of size less than 3 mm to accurately capture the heterogeneous variations in the mechanical properties (Keyak et al. 1994, Bessho et al. 2007) and to ensure accurate prediction of the fracture path growth (Hambli, 2013). Therefore, an element size of about 0.15 mm was retained to mesh the ribs leading to a total of 226520 eight nodes hexahedral (solid brick) elements.

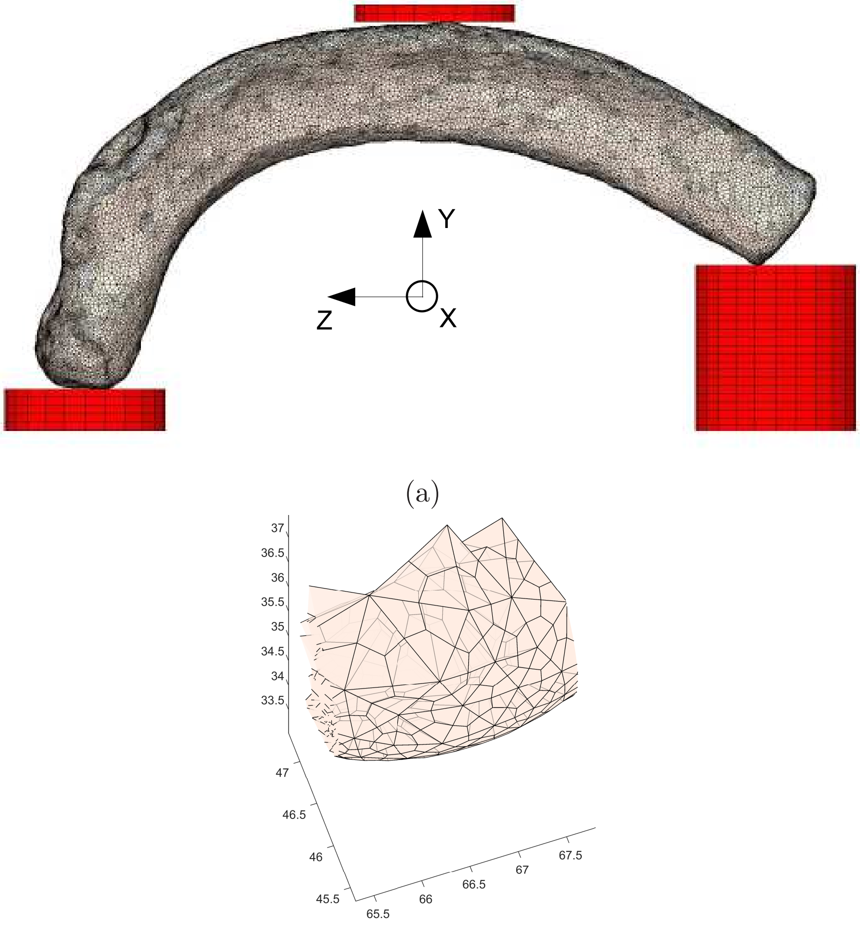

(a)

(b)

Figure 4.3 – Finite element mesh of porcine rib and bars (a) and zoom of the left rib extremity showing the hexahedral elements (b) – dimensions in mm

4.2 Constitutive and Damage Law for bone

Several authors have presented different constitutive laws for cortical bone tissue. However, the damage accumulation and the considerations its accumulation into numerical models have been a point of arguments among these authors. We can find many articles using an elastic-plastic constitutive law, for example Garcia (2006), Pavier (2013). A realistic constitutive law for bone must consider the effects of strain rate. Regarding the effects of strain rates, quite a few authors have suggested either *viscoelastic-viscoplastic* constitutive model (Johnson et al., 2010) or elastic-viscoplastic constitutive model (Li et al., 2010).

Similar to cortical bone tissue, several constitutive laws were proposed for trabecular bone. The main difference is the architecture of trabecular bone, which makes it anisotropic. Moreover, the high porosity of trabecular bone leads to a foam like behavior. Some constitutive laws considering the trabecular bone architecture can be seen in Cowin (1986), Pietruszczak et al. (1999) and so on. On the other hand, Gibson (2005), Karkar (2017) have considered foam like models for trabecular bone.

For simulations concerning the fracture of bone tissue, damage accumulation and evolution plays and important role. Numerous studies have pointed out the limitations of basic fracture criteria models such as von-Mises equivalent stress criteria, Hill's criteria to model the damage of bone. For example Malik et al. (2003), Taylor and Lee (2003), Vashishth et al. (2003), Ural and Vashishth (2007) and Abdel-Wahab and Silberschmidt (2011) had used Fracture mechanics approach but failed to predict the complete fracture patterns since these models are restricted to single dominant idealized planar crack. Whilst, Hambli (2011a), Hambli (2011b) and Dall'Ara et al. (2013) have proposed damage models based on continuum damage mechanics (CDM).

Note that the porcine rib model presented in this thesis is a homogenized model *i.e.* it does not consider the architecture of trabecular bone. Therefore, considering of foam like constitutive law for trabecular bone components may not be the priority here. Thus, we concentrate on considering rate effects in constitutive law and coupling it to a credible damage law.

Before choosing a reliable constitutive law, let us take a keen look at the experimental corridors presented in Fig. 2.19a, Fig. 2.19b and Fig. 2.19c. We notice that the slope of initial elastic response stays almost unaffected by the change in strain rate $\dot{\varepsilon}$. This lays the foundation for an *elastic-viscoplastic* behavior of rib. The difference in behavior of cortical and trabecular bone is considered through hardening. Cortical bone was assumed to show isotropic hardening behavior in contrast to trabecular bone, which shows kinematic hardening behavior.

On the other hand, the experimental results have proved that the crack initiation occurred in the tensile surface and propagated towards compressive surface in the vicinity of impact load. Moreover, we could see some material erosion at the point of contact with input bar. Therefore, a credible damage law must consider this phenomenon.

4.2.1 Constitutive laws in LS-Dyna

As the experimental results prove that an elastic-viscoplastic constitutive law is suitable for the porcine rib, we must now choose a good candidate based on the data in our possession. In this case, we can narrow down to three possible candidates that are capable of considering elastic-viscoplastic behavior:

1. Elastic-viscoplastic constitutive law with internally coupled damage law (*MAT-105)
2. Modified elastic-viscoplastic constitutive law with kinematic and isotropic hardening (*MAT-003)
3. Modified elastic-viscoplastic constitutive law with isotropic hardening only (*MAT-024)

Elastic-Viscoplastic with Continuum Damage Mechanics (*MAT-105)

This material model, offers elastic-viscoplastic behavior through Cowper-Symmonds model (*i.e.* post yield stress scaling) and is internally coupled with a damage law based on the hypothesis of effective stress proposed by Lemaitre (1996). The yield function (ϕ)

$$\phi \;=\; \frac{1}{2}S_{ij}S_{ij} \;-\; \frac{\sigma_y^2}{3} \;\leq\; 0 \tag{4.5}$$

The yield function in Eq. 4.5, is expressed in terms of Deviatoric stress components (S_{ij}) and the dynamic yield stress (σ_y) . The effects of $\dot{\varepsilon}$ on post yield stress are considered through the Eq. 4.6.

$$\sigma_y \;=\; \left[1 \;+\; \left(\frac{\dot{\varepsilon}}{C}\right)^{\frac{1}{p}}\right]\left[\sigma_{y_0} \;+\; f_h(\varepsilon^P_{eff})\right] \tag{4.6}$$

Here, C and p are Cowper-Symmonds parameters, σ_{y_0} is the initial yield stress and $f_h(\varepsilon^P_{eff})$ is the hardening function .

The hardening function is treated in two different ways:

1. The user can give different curves in a tabular form for $f_h(\varepsilon^P_{eff})$ and LS-Dyna interpolates the hardening with respect to the curves provided in the table.
2. A default linear treatment, that is expressed as

$$f_h(\varepsilon^P_{eff}) \;=\; E_P(\varepsilon^P_{eff}) \tag{4.7}$$

where, E_P is the plastic hardening modulus, expressed in terms of tangent modulus (E_{TAN}) and Young's modulus (E) as in Eq. 4.8 and ε^P_{eff} is the effective plastic strain, as in Eq. 4.9.

$$E_P = \frac{E_{TAN}E}{E_{TAN} + E} \tag{4.8}$$

$$\varepsilon^P_{eff} = \int_0^t \left(\frac{2}{3}\dot{\varepsilon}^P_{ij}\,\dot{\varepsilon_{ij}}^P\right)^{1/2} dt \tag{4.9}$$

The damage law is a continuum damage mechanics model, that considers effective stress concept. The effective stress for a damaging material is expressed as

$$\tilde{\boldsymbol{\sigma}} = \frac{\boldsymbol{\sigma}}{(1 - D)} \tag{4.10}$$

here, D is the damage variable. The evolution of D with time is considered as below

$$\dot{D} = \begin{cases} \frac{\Upsilon}{\varsigma(1-D)}\dot{r} & \text{for } r > r_D \text{ and } \boldsymbol{\sigma_I} > 0 \\ 0 & \text{otherwise} \end{cases} \tag{4.11}$$

where, Υ is the strain energy density release rate, ς is the strain energy release rate, r is the damage effective plastic strain, r_D is the damage threshold and $\boldsymbol{\sigma_I}$ is the maximal principal stress. The strain energy density release rate in Eq. 4.11 is expressed in terms of triaxiality function $R_v(\eta)$ as below

$$\Upsilon = \frac{\sigma^2_{vm}R_v(\eta)}{2E(1-D)^2} \tag{4.12}$$

$$R_v = \frac{2}{3}(1+\nu) + 3(1-2\nu)\eta^2 \tag{4.13}$$

where η is the stress triaxiality expressed in terms of hydrostatic stress ($1/3\mathrm{tr}\,\boldsymbol{\sigma}$) and von-Mises stress ($\sigma_{vm}$) as

$$\eta = \left(\frac{\frac{1}{3}\mathrm{tr}\,\boldsymbol{\sigma}}{\sigma_{vm}}\right) \tag{4.14}$$

The rate of damage accumulated plastic strain $\dot{r}$ is expressed in terms of effective plastic strain rate ($\dot{\varepsilon}^P_{eff}$) and damage ($D$) as in Eq. 4.11 is represented as

$$\dot{r} = \dot{\varepsilon}^P_{eff}(1-D) \tag{4.15}$$

Modified elastic-viscoplastic material model (*MAT-003)

This material model has the ability to consider either kinematic hardening or isotropic hardening or even a combination of both kinematic and isotropic hardening. This can be achieved by varying a parameter β_h between 0.0 and 1.0. If $\beta_h = 0.0$, the material is considered as kinematic hardening and for $\beta_h = 1.0$, the material is isotropic hardening. As we know that the center of the yield surface shifts according to the behavior for kinematic hardening, the yield condition can be expressed as

$$\phi = \frac{1}{2}\xi_{ij}\xi_{ij} - \frac{\sigma_y^2}{3} = 0 \tag{4.16}$$

$$\xi_{ij} = S_{ij} - \alpha_{ij} \tag{4.17}$$

$$\sigma_y = \left[1 + \left(\frac{\dot{\varepsilon}}{C}\right)^{\frac{1}{p}}\right]\left(\sigma_{y_0} + \beta_h E_P \varepsilon_{eff}^p\right) \tag{4.18}$$

S_{ij} and α_{ij} of Eq. 4.17 are deviatoric stress and the center of yield surface respectively. The variable σ_y of Eq. 4.18 is the rate dependent yield stress, σ_{y_0} is the initial yield stress defined in the material parameters and the variables C and p are Cowper-Symmonds parameters. The other variables of Eq. 4.18 are calculated as follows:

$$\dot{\varepsilon} = \sqrt{\dot{\varepsilon}_{ij}\dot{\varepsilon}_{ij}} \tag{4.19}$$

$$E_P = \frac{E_{TAN}E}{E_{TAN} + E} \tag{4.20}$$

$$\varepsilon_{eff}^P = \int_0^t \left(\frac{2}{3}\dot{\varepsilon}_{ij}^P \, \dot{\varepsilon_{ij}}^P\right)^{1/2} dt \tag{4.21}$$

The plastic strain rate $\dot{\varepsilon}_{ij}^P$ in Eq. 4.21 is difference between total strain rate $\dot{\varepsilon}_{ij}$ and elastic strain rate $\dot{\varepsilon}_{ij}^e$

$$\dot{\varepsilon}_{ij}^P = \dot{\varepsilon}_{ij} - \dot{\varepsilon}_{ij}^e \tag{4.22}$$

Numerical implementation of *MAT-003:

- First the stress are updated elastically through the Eq. 4.23

  $$\sigma_{ij}^* = \sigma_{ij}^n + C_{ijkl}\Delta\varepsilon_{kl} \tag{4.23}$$

  here, $\boldsymbol{\sigma_{ij}^*}$ is the trial stress tensor, $\boldsymbol{\sigma_{ij}^n}$ is the stress tensor from previous iteration, C_{ijkl} is the elastic tangent modulus matrix and $\Delta\varepsilon_{kl}$ is the increment in strain.

- The yield function is checked.

  (a) If the yield function of Eq. 4.16 is satisfied, the solution advances to next iteration.

  (b) If the yield function is violated, an increment in plastic strain is calculated, the stresses are scaled back to yield surface and the yield surface center is updated.

Let us assume the trial deviatoric stress S_{ij}^* and it's trial invariant ξ_{ij}^* as of the state $n+1$ as in Eq. 4.24 and Eq. 4.25 respectively

$$S_{ij}^* \;=\; \sigma_{ij}^* \;-\; \frac{1}{2}\sigma_{kk}^* \tag{4.24}$$

$$\xi_{ij}^* \;=\; S_{ij}^* \;-\; \alpha_{ij} \tag{4.25}$$

Then the yield function is defined as follows

$$\phi \;=\; \frac{3}{2}\xi_{ij}^*\xi_{ij}^* \;-\; \sigma_y^2 \;=\; \Lambda^2 \;-\; \sigma_y^2 \begin{cases} \geq\; 0 & \text{for elastic response} \\ <\; 0 & \text{for plastic hardening} \end{cases} \tag{4.26}$$

where,

$$\Lambda \;=\; \sqrt{\frac{3}{2}\xi_{ij}^*\xi_{ij}^*}$$

In the case of plastic hardening (*i.e.* for $\phi \;<\; 0$), the following steps are executed

- updating of plastic strains

$$\varepsilon_{eff}^{P^{n+1}} \;=\; \varepsilon_{eff}^{P^n} \;+\; \frac{\Lambda - \sigma_y}{3G + E_P} \tag{4.27}$$

- scaling back of stress deviators

$$\sigma_{ij}^{n+1} \;=\; \sigma_{ij}^n \;-\; \frac{3G\Delta\varepsilon_{eff}^P}{\Lambda}\xi_{ij}^* \tag{4.28}$$

  here, $G \;=\; E/[2(1+\nu)]$

- updating the center of yield surface

$$\alpha_{ij}^{n+1} \;=\; \alpha_{ij}^n \;+\; \frac{(1-\beta_h)\,E_P\Delta\varepsilon_{eff}^P}{\Lambda}\xi_{ij}^* \tag{4.29}$$

Piecewise Linear Plasticity model (*MAT-024)

This model is a basic elastic-plastic constitutive law, that gives the user to choose yield stress scaling with respect to strain rate $\dot{\varepsilon}$, thereby producing an elastic-viscoplastic law. The yield function in this model is

$$\phi = \frac{1}{2} S_{ij} S_{ij} - \frac{\sigma_y^2}{3} \leq 0 \tag{4.30}$$

$$\sigma_y = \left[1 + \left(\frac{\dot{\varepsilon}}{C} \right)^{\frac{1}{p}} \right] \left(\sigma_{y_0} + f_h(\varepsilon^p_{eff}) \right) \tag{4.31}$$

The yield function in Eq. 4.30 is expressed in terms of deviatoric stress tensor S_{ij} and dynamic yield σ_y as opposed to that in Eq. 4.16, which considers the invariant of deviatoric stress component ξ_{ij}. Moreover, the difference between *MAT-003 and this model is that it considers isotropic hardening only and the hardening function $f_h(\varepsilon^p_{eff})$ is treated differently. The *MAT-024 offers two different ways of treatment for the hardening function:

1. The user can give different curves in a tabular form for $f_h(\varepsilon^P_{eff})$ and LS-Dyna interpolates the hardening with respect to the curves provided in the table.
2. A default linear treatment, that is expressed as

$$f_h(\varepsilon^P_{eff}) = E_P(\varepsilon^p_{eff}) \tag{4.32}$$

   where, E_P and ε^P_{eff} are expressed in similar manner as in Eq. 4.20 and Eq. 4.21 respectively.

This material model has another advantage over *MAT-003. The rate effects can be considered either through a user defined table consisting the stress-strain curves of the material for different strain rates or by the for the variable VP. The later is considered in LS-Dyna as follows:

$$\text{VP} = \begin{cases} \text{Cowper} - \text{Symmonds} & \text{if VP} = -1.0 \\ \text{Yield stress scaling} & \text{if VP} = 0.0 \\ \text{Entirely Viscoplastic} & \text{if VP} = 1.0 \end{cases}$$

Therefore, this material model has an upper hand to *MAT-003 when it comes to consideration of strain rate effects.

Numerical implementation of *MAT-024:

- the stress are updated in similar fashion to *MAT-003.
- the yield function in Eq. 4.30 is checked.
  - If satisfied, the deviatoric stresses are accepted.

- if the yield function is not satisfied, an increment in plastic strain is computed through

$$\Delta\varepsilon^{P}_{eff} \;=\; \frac{\left(\frac{3}{2}S^{*}_{ij}S^{*}_{ij}\right)^{1/2} \;-\; \sigma_y}{3G \;+\; E_P} \tag{4.33}$$

  then the trial deviatoric stresses S^{*}_{ij} are scaled back to the yield surface

$$S^{n+1}_{ij} \;=\; \frac{\sigma_y}{\left(\frac{3}{2}S^{*}_{ij}S^{*}_{ij}\right)^{1/2}}S^{*}_{ij} \tag{4.34}$$

Summary of feature available in all three constitutive laws is presented in Tab. 4.3.

Model	yield function ϕ	strain rate effects $\sigma_y(\dot{\varepsilon})$	Damage Law
MAT-105	$\frac{1}{2}S_{ij}S_{ij} \;-\; \frac{\sigma_y^2}{3} \;\leq\; 0$	$\left[1 \;+\; \left(\frac{\dot{\varepsilon}}{C}\right)^{\frac{1}{p}}\right]\left(\sigma_{y0} \;+\; f_h(\varepsilon^{P}_{eff})\right)$	coupled (CDM)
MAT-003	$\xi_{ij}\xi_{ij} \;-\; \frac{\sigma_y^2}{3} \;=\; 0$	$\left[1 \;+\; \left(\frac{\dot{\varepsilon}}{C}\right)^{\frac{1}{p}}\right]\left(\sigma_{y0} \;+\; \beta_h E_P\varepsilon^{P}_{eff}\right)$	none
MAT-024	$\frac{1}{2}S_{ij}S_{ij} \;-\; \frac{\sigma_y^2}{3} \;\leq\; 0$	$\left[1 \;+\; \left(\frac{\dot{\varepsilon}}{C}\right)^{\frac{1}{p}}\right]\left(\sigma_{y0} \;+\; f_h(\varepsilon^{P}_{eff})\right)$	none

Table 4.3 – Key factors of elastic-vicoplastic models in LS-Dyna

Note that S in Tab. 4.3, denotes the devitoric stress components whereas ξ denotes the invariant of deviatoric stress components and in expressed as in terms of deviatoric stress components and center of the hardening curves. The material models MAT-105 and MAT-024 are the same in terms of numerical formulations of the constitutive law, whereas the MAT-003 approaches the problem in a different manner as it includes an additional parameter β_h for taking the effects of kinematic hardening into consideration.

In contrast to similarities in constitutive behavior of these models, the material models MAT-003 and MAT-024 need an external damage law for an effective simulation of fracture and damage propagation. This makes them less efficient in terms of calculation time.

Understanding the constitutive laws

Elastic-viscoplastic formulation

Since the material model MAT-024 the only providing two different types of yield stress scaling for considering the effects of strain rate on plastic part, simulations were carried out on single element model as in Fig. 4.4a.

To understand the difference between VP $=$ 0 and VP $=$ -1.0, a force boundary condition at different loading rates (as in Fig. 4.4b) was imposed. The parameters of Cowper-Symmonds model $C = 2.5$ and $P = 7.0$ were adapted from Li et al. (2010). The stress strain response corresponding to each loading rate for VP $=$ 0 (solid curves) and VP $=$ -1.0 (dashed curves) is presented in Fig. 4.4c.

It is clear that the MAT-024 model with VP $=$ -1.0 is the one more effective and does consider the effects of strain rate as it is supposed to. The yield stress scaling behavior of MAT-003 is also executed in a similar fashion. Moreover, as MAT-105 is just an extension of MAT-024 for constitutive law, it does behave similar to that of MAT-024 and MAT-003. Therefore, we can say that the Cowper-Symmonds model is the suitable candidate.

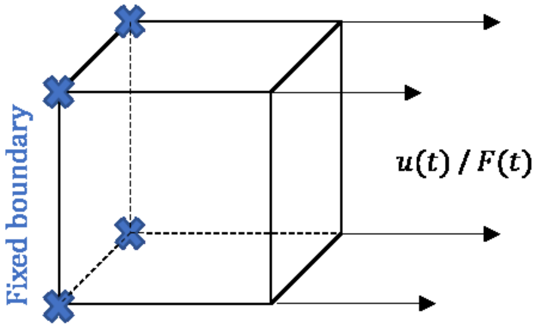

(a) One element model

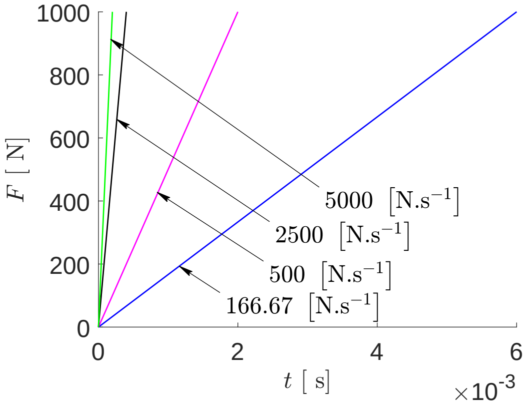

(b) Force boundary condition

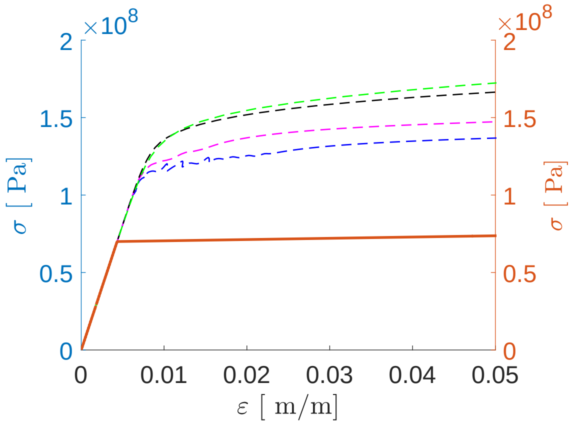

(c) Response with VP = 0.0 and VP = −1.0

Figure 4.4 – Yield stress scaling MAT-024

Consideration of hardening

The parameter β_h is the one responsible for hardening in MAT-003. In order to understand its influence, a random cyclic displacement imposed on 4 nodes of one extremity whilst the other 4 nodes were constrained with 0 displacement in all directions as in Fig. 4.5.

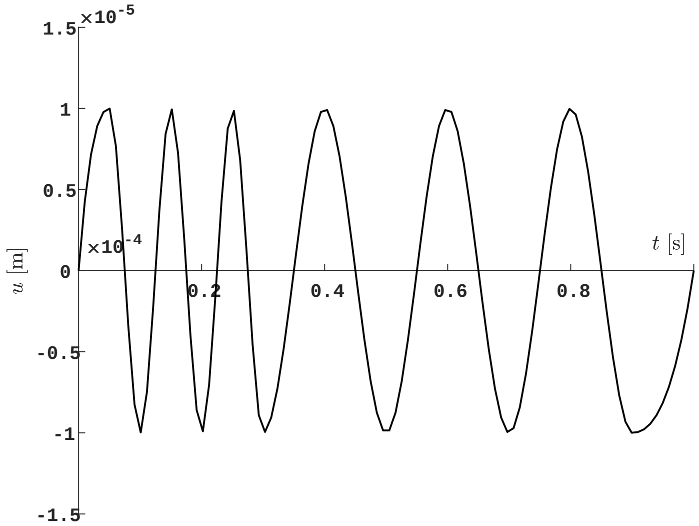

Figure 4.5 – Displacement boundary condition

The response of material for the displacement curve is shown in Fig. 4.6 and Fig. 4.7. The effect of β_h is shown in Fig. 4.6. We can notice that for $\beta_h < 0.5$, the material response is similar to that of kinematic hardening. Whereas for $\beta_h > 0.5$, it tends to be more isotropic.

The Fig. 4.7 shows the difference between the material response for kinematic hardening ($\beta_h = 0.0$ in red) and isotropic hardening ($\beta_h = 1.0$ in blue). We can notice that the material response depicted by red curve shows a shift in the stress strain curve, yet stress of similar order of magnitude to that of initial loading. This is characterized by a shift in α_{ij} of the yield surface and almost constant radius. On the other hand, the response for isotropic hardening, depicted by blue curve shows an increase in magnitude and a negligible shift in α_{ij}.

To understand, the difference between the formulation of isotropic hardening of *MAT-024 and that of *MAT-003, the same one element model was carried out but this time with *MAT-024 for the same load as in Fig. 4.5. The comparison of response for *MAT-003 with $\beta_h = 1.0$ and *MAT-024 is shown in figure below. We can notice that the response with *MAT-024 almost superimposes that of *MAT-003 with $\beta_h = 1.0$.

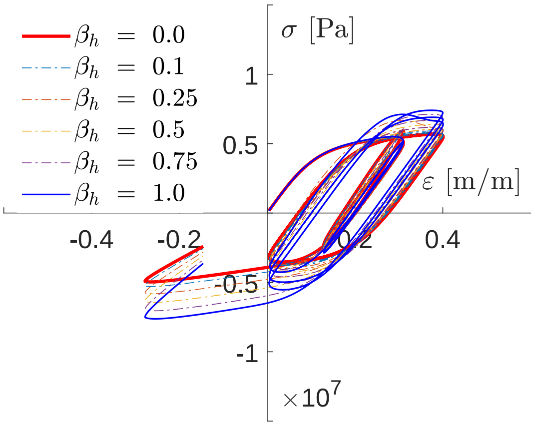

Figure 4.6 – Effect of β_h *MAT-003

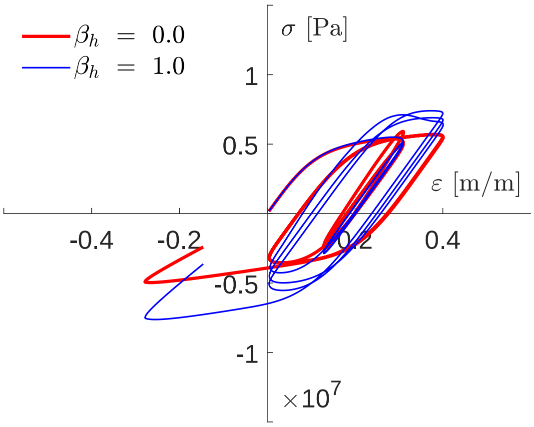

Figure 4.7 – Kinematic and Isotropic hardening *MAT-003

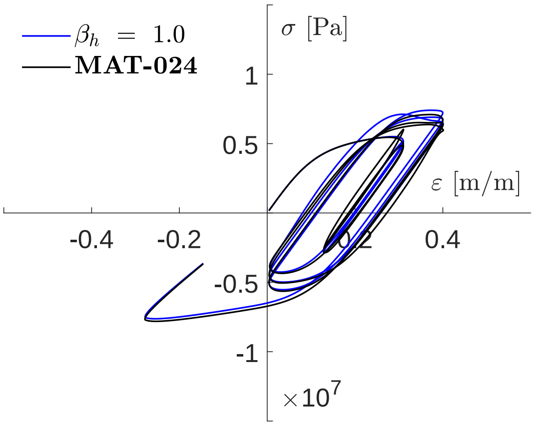

Figure 4.8 – Comparison of *MAT-003 and *MAT-024

4.2.2 External damage law for bone tissue

As said above, a credible damage law must be able to differentiate the tensile and compression surfaces in the rib sample and also consider the effects of strain rate in the reduction of strain at fracture.

Even though material models *MAT-003 and *MAT-024 provide failure option with strain at failure though element erosion, they are not sufficient enough to consider the progressive nature of fracture and strain rate effects, thus they must be coupled with an external damage law. In this case, the only external damage law satisfying our needs is *MAT-Add-Erosion of LS Dyna material library. This law is based on element deletion / erosion criteria. The *MAT-Add-Erosion, offers three different approaches for damage evolution:

1. Erosion
2. **GISSMO** (Generalized Incremental Stress-State dependent damage MOdel)
3. **DIEM** (Damage Initiation and Evolution Model).

Erosion is a general approach, that considers the failure strain and elements are removed through erosion once this criteria is satisfied. On the other hand GISSMO and DIEM are more sophisticated damage models that work on the basis of element deletion depending on the criteria chosen by the user. For example, GISSMO is a phenomenological model that considers incremental damage accumulation, softening and failure as opposed to DIEM which relies on criteria given by user for damage initiation and evolution. A total of 5 criteria can be chosen for DIEM model. As we know that the stiffness and rigidity of bone decreases with increase in damage and the objective of this thesis is to capture progressive fracture process, we had chosen GISSMO as a potential candidate for an external damage law.

*MAT-Add-Erosion with GISSMO

The GISSMO model offers an incremental and stress-state dependent criteria, moreover it considers progressive evolution of damage, reduction in stiffness and strain rate effects as well. It was proposed by Neukamm et al. (2009) and Haufe et al. (2010). The stress-state of the material is considered in terms of triaxiality η as follows

$$\eta = \frac{\frac{1}{3}\mathrm{tr}\,\boldsymbol{\sigma}}{\sigma_{vm}} \tag{4.35}$$

here, $\frac{1}{3}\mathrm{tr}\,\boldsymbol{\sigma}$ represents the hydrostatic stress or mean stresses and σ_{vm} represents the von-Mises / equivalent stress.

Damage Evolution

The damage evolution is in fact a generalization of Johnson-Cook model. The path dependent criteria is taken into consideration through a user defined curve of static fracture strain as a function of $\varepsilon_f(\eta)$. Moreover, it also offers non linear damage evolution through the variable n. The damage evolution is expressed as follows

$$\Delta D \;=\; \frac{n}{\varepsilon_f(\eta)} D^{\left(1\,-\,\frac{1}{n}\right)} \Delta\varepsilon_p \tag{4.36}$$

Post Critical Behavior

Post critical behavior signifies the effects of damage on the behavior of a material such as softening, reduction in stiffness and rigidity until entire rupture. There are three different ways to invoke the post critical behavior, which is controlled by ECRIT variable in the LS-Dyna Add Erosion card.

1. By giving a constant value for ε_{crit}. Once ε_p reaches this value, the current damage value is noted as critical damage value *i.e.* $D\,|_{(\varepsilon_p\,=\,\varepsilon_{crit})} =\, D_{crit}$. This point is considered as the onset of reduction in stress carrying capacity and the damage is coupled to stress through a modified equation of Lemaitre's effective stress concept:

   $$\boldsymbol{\sigma} \;=\; \tilde{\boldsymbol{\sigma}} \left[1 \,-\, \left(\frac{D\,-\,D_{crit}}{1\,-\,D_{crit}}\right)^{m}\right] \tag{4.37}$$

   where $\tilde{\sigma}$ is the effective stress (as in Lemaitre concept), m is the fading exponent. The Eq. 4.37 continues to be couple until the D value reaches 1 and the element is removed from the calculation.

2. Second way is to provide a curve for ε_{crit} with respect to η. In this case, an incremental instability measure is calculated in the similar manner to ΔD as in Eq. 4.36.

   $$\Delta F \;=\; \frac{n}{\varepsilon_{crit}(\eta)} F^{\left(1-\frac{1}{n}\right)} \Delta\varepsilon_p \tag{4.38}$$

   the variable F represents the instability and is supposed to vary as $0 \;\leq\; F \;\leq\; 1$. Once ΔF reaches unity, the damage is coupled to stress with Eq. 4.37.

3. By declaring ECRIT $=$ 0 and giving D_{crit} values. In this case, coupling of stress with damage starts as soon as D reaches D_{crit}. This method gives us flexibility to enter any arbitrary value. If the value for D_{crit} is unknown and

the value of the fading exponent m is unity, the Eq. 4.37 is rewritten as follows

$$\boldsymbol{\sigma} = \tilde{\boldsymbol{\sigma}} (1 - D) \tag{4.39}$$

The Eq. 4.39 is the same as that proposed by Lemaitre, found in MAT-105

In our case, the third method was chosen with values of D_{crit} taken from literature and the fading exponent is unity.

Effects of strain rate

Since we deal with ribs subjected to dynamic impacts, literature proves that $\dot{\varepsilon}$ effects the damage behavior of bones (McElhaney, 1966), (Wood, 1971) and (Johnson et al., 2010). Thus, we had provided *MAT-Add-EROSION with an additional curve for the effects of $\dot{\varepsilon}$, which is controlled by the variable LCSRS. The curves were based on the equation given by Wood (1971) and the static ε_f values were changed in order to study its effects on the response of rib. The ratio of dynamic strain dependent fracture strain ε_{fd} to that of static fracture strain ε_{fs} varies with respect to strain rate $\dot{\varepsilon}$ as follows

$$\varepsilon_{fd}/\varepsilon_{fs} = A - B\mathrm{Ln}\dot{\varepsilon} \tag{4.40}$$

The difference in damage law considered in MAT-105 and that of GISSMO model is presented below

Features	MAT-105 CDM	GISSMO
Pros	coupled internally simple implementation	stress-state dependent strain rate effects for ε_f more user friendly
Cons	requires tests data for parameters not stress-state dependent no strain rate effects of ε_f	external coupling additional test data for advanced parameters

Table 4.4 – Summary of simulations with single part porcine rib and rigid walls

4.2.3 Working principle of damage law

The damage law is incremental, stress state dependent and is capable of considering non-linear damage accumulation, and reduction in force carrying capacity with increase in strain rate. In order to have coherent results, this damage model needs a curve for considering the variation of fracture strain ε_f with respect to stress state η, which is presented in Fig. 4.9a.

The lack of data for the variation of ε_{crit} with respect to triaxiality η, forced us to use a critical damage value D_{crit} was specified in the damage law. When the yield specified in the material card of the sample is reached, the damage D starts to couple with the stress field. Meanwhile, the fading exponent data is also unavailable for porcine rib, thus forcing us to set it to unity. The parameters required for post yield behavior such as critical damage D_{crit}, damage exponent for non linear damage n and fading exponent m for coupling with effective stress were adapted from literature and are presented in Tab. 4.5.

Property	Cortical Bone	Trabecular Bone
Damage Exponent n	1.25	2.0
Critical Damage D_{crit}	0.2	0.5
Fading Exponent m	1.0	1.0

Table 4.5 – Damage law parameters of porcine rib

For positive triaxiality values, the damage law scales the corresponding strain values (*i.e.* strain values of $\eta \in [0.0, 1.0]$ in Fig. 4.9a) with respect to strain rate through curves presented in Fig. 4.9b. The scale factor curves in Fig. 4.9b were obtained by varying the variable B in the Eq. 4.40.

Curve number	$\varepsilon_{fd}/\varepsilon_{fs}$
1	$0.63 - 1.00 \times 10^{-2}\,\mathrm{Ln}\dot{\varepsilon}$
2	$0.63 - 1.25 \times 10^{-2}\,\mathrm{Ln}\dot{\varepsilon}$
3	$0.63 - 1.60 \times 10^{-2}\,\mathrm{Ln}\dot{\varepsilon}$
4	$0.63 - 2.00 \times 10^{-2}\,\mathrm{Ln}\dot{\varepsilon}$
5	$0.63 - 4.00 \times 10^{-2}\,\mathrm{Ln}\dot{\varepsilon}$

Table 4.6 – List of different $\varepsilon_{fd}/\varepsilon_{fs}$ vs $\dot{\varepsilon}$ relations tested

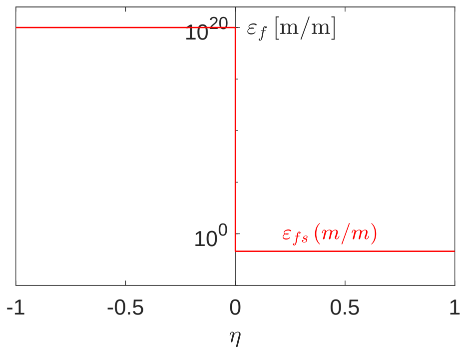

(a) Example of fracture strain with stress-state

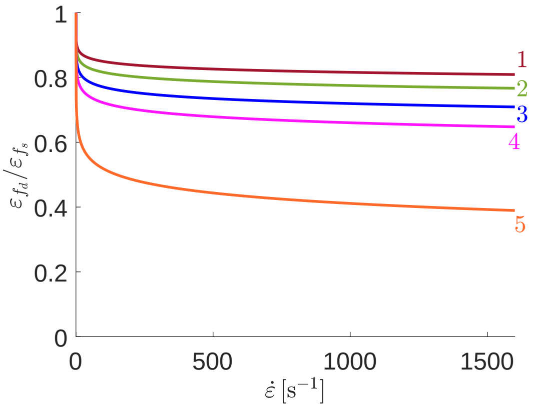

(b) $\varepsilon_{fd}/\varepsilon_{fs}\, vs\, \dot{\varepsilon}$

Figure 4.9 – Input curves of damage law

Note that the static fracture strain provided by Wood (1971) is 0.86×10^{-2} m/m, which corresponds to a quasi-static strain-rate of 3.18×10^{-3} s^{-1}. Similarly, in the present study Eq. 4.40 is not applicable for $\dot{\varepsilon}$ lower than 3.00×10^{-3} s^{-1}, which are quasi static. For all values $0\ \mathrm{s}^{-1} \leq \dot{\varepsilon} \leq 3.00 \times 10^{-3}\ \mathrm{s}^{-1}$, a linear approximation is applied so that $\varepsilon_{fd}/\varepsilon_{fs} = 1$ at $\dot{\varepsilon} = 0\ \mathrm{s}^{-1}$.

To understand the effects of damage law parameters on the behavior of sample, a simple three-point bending tests was carried out using rigid walls and a rectangular sample of 80 mm long and 100 mm^2 square cross-section Fig. 4.10a. The rigid walls were provided with velocities from one of the experimental cases (see Fig. 4.10b). The velocities are negative since they are in the opposite Y direction. A total of three simulations were carried out, (i) with no *MAT-Add-Erosion *i.e.* the failure criteria was provided as a constant value in the material model card $\varepsilon_{fs} = 2.0 \times 10^{-2}$ [m/m], (ii) with *MAT-Add-Erosion but no effects of strain rate *i.e.* $\varepsilon_f(\eta)$, and (iii) with *MAT-Add-Erosion with effects of strain rate $\varepsilon_{fd}(\eta, \dot{\varepsilon})$.

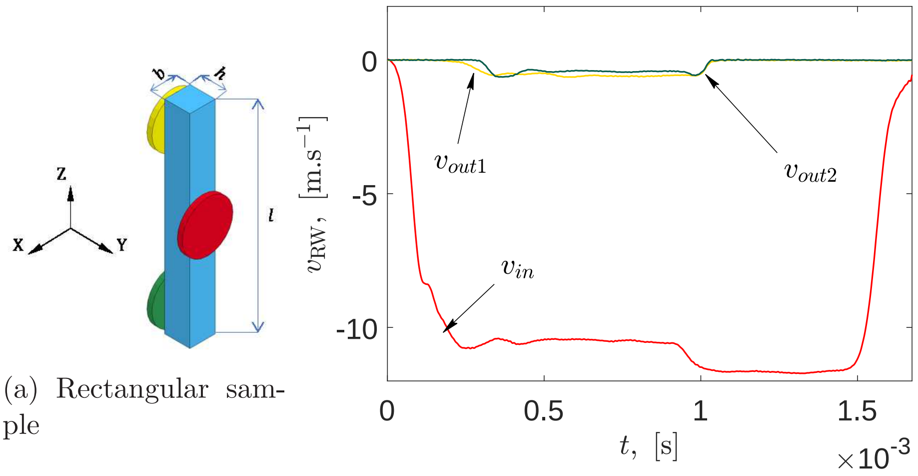

(a) Rectangular sample

(b) Rigid wall velocities

Figure 4.10 – Model for damage law validation

In order to compare the three cases, Force vs displacement (Fig. 4.11a), impulse (Fig. 4.11b), energy (Fig. 4.11c) and integral of energy (Fig. 4.11d) were compared.

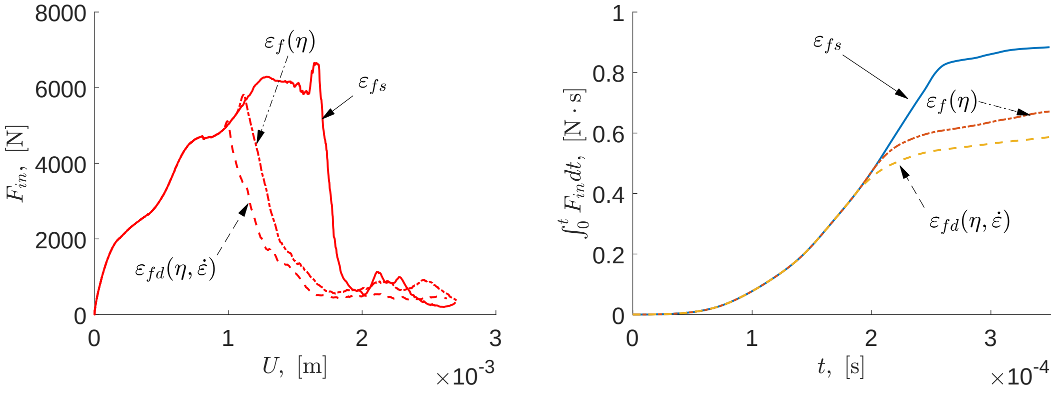

(a) F_{in} vs U

(b) Impulse

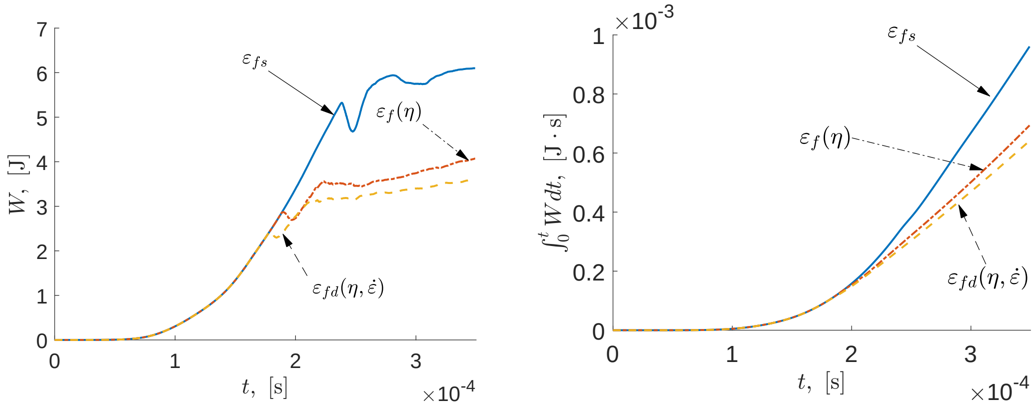

(c) Energy

(d) Integral of energy

Figure 4.11 – Effects of damage law parameters

The input force F_{in} is obtained from the contact algorithm between input rigid wall and the sample, where as the relative displacement U is calculated through the formula in Eq. 2.19. The impulse was calculated through the integral of F_{in} with respect to time. The energy data presented was obtained through part energy history in LS Dyna.

We can notice that the sample without damage law (represented by solid lines in Fig. 4.11) is subjected to more displacement and more energy before entire rupture. This is due to the absence of coupling between the damage D and flow stresses. On the other hand, the sample under the influence of damage law ($\varepsilon_f(\eta)$ in dash-dot line and $\varepsilon_{fd}(\eta, \dot{\varepsilon})$ in dashed line) do eventually rupture way before their counterpart. For example, let us consider the energy absorbed by the sample before rupture (Fig. 4.11c). The curves corresponding to the cases $\varepsilon_f\eta$ and $\varepsilon_{fd}(\eta, \dot{\varepsilon})$ have values much less than that of ε_{fs}. This could be explained by the coupling of damage with flow stresses as soon as the stresses in the sample exceed its static yield limit σ_{yT}. Another peculiar response is that of the sample with $\varepsilon_{fd}(\eta, \dot{\varepsilon})$ passes into plateau region for an energy of ≈ 2.8[J]. This is due to the reduction in fracture strain with increasing strain rate.

4.3 Numerical Model Considerations

The numerical considerations such as decisions for which constitutive law to use, coupling of constitutive law with an external damage law if required and contact parameters were done using a single constituent porcine rib model (Fig. 4.12a) with rigid walls instead of bars to economize time as in Fig. 4.12b

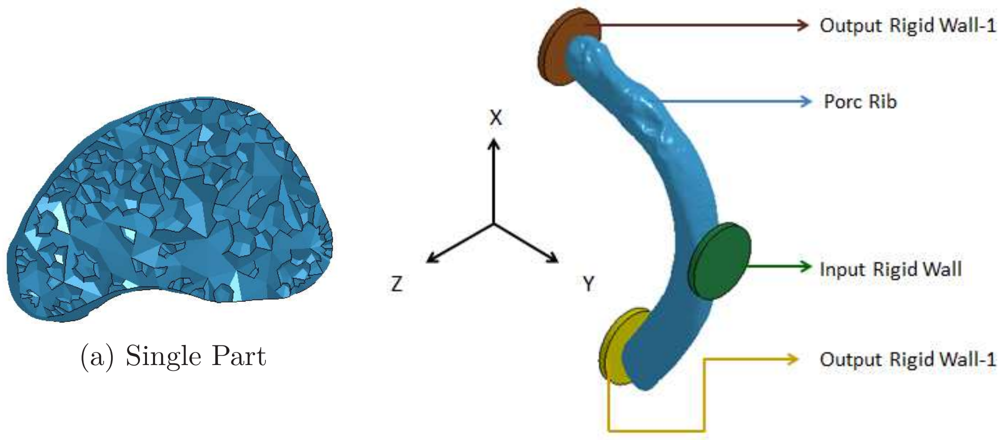

(a) Single Part

(b) Numerical model

Figure 4.12 – Numerical Porcine Rib Sample used for model considerations

The difference between the real porcine rib sample and single part sample is that, the later is made of only one bone constituent instead of 8.

The rigid walls were modeled using the *MAT-020-Rigid of LS-Dyna material library. This material model furnishes the ability to convert any geometrical mesh of either shell or solid elements to convert into a rigid body. As the elements of "rigid body" are bypassed to store history variables, this model is cost effective. In order to replicate the sample behavior as close as possible to the original SHPB model, input and output interface velocities of one of the experimental cases were given to respective input and output rigid walls (see Fig. 4.10b). Since thee definition of contact between porcine rib sample and rigid walls is mandatory, the rigid wall were attributed with same properties of nylon as in Tab. 4.1.

To finalize the constitutive law, damage law and contact algorithm, all three constitutive laws (Sec. 4.2.1), coupled with damage law if necessary were tested with the contact algorithm of Sec. 4.4. The different models tested are presented below.

Material Law	Model	Strain rate effects	data source
MAT 105	Model-105	Yes	Pavier (2013)
MAT-24	Model-24a	No	Pavier (2013)
	Model-24b	Yes	Pavier (2013)
	Model-24c	Yes	Li et al. (2010)
MAT-3	Model-3a	Yes	Li et al. (2010)
	Model-3b	Yes	Pavier (2013)

Table 4.7 – Summary of simulations with single part porcine rib and rigid walls

4.3.1 Single Part Model-105

Since the material model *MAT-105 has damage law readily coupled to constitutive law, it would be interesting to test it. Therefore, we had embarked with this model. The material properties of cortical bone were considered from ρ_{app} and are shown in Tab. 4.8.

In addition to these mechanical properties, three additional damage parameters are required for complete implementation of *MAT-105.

1 Damage threshold(r_D): The value of effective plastic strain, at which material softening begins.

2 Damage Material constant ς

3 Critical Damage parameter D_c : That signifies the damage variable value at which element(s) are deleted from the calculation.

Some researchers have studied the type of fracture in bones and have found that there is a ductile to brittle transition in bones (Hasson and Armstrong, 1974) and in case of dynamics, Kirchner (2006) reported that this transition (not sharp) from ductile to brittle but occurs when the strain rate is around 10 s^{-1}. Thus the fracture we are supposed to see in our simulations is either brittle fracture or quasi-brittle fracture. This lead to the decision to approximate the damage law parameters for cortical bone as in Tab. 4.9.

Property	Value
Density (ρ, kg.m^{-3})	1630.00
Young's Modulus (E, GPa)	9.37
Poisson's ratio (ν)	0.3
Tensile yield (σ_y, MPa)	86.876
C, GPa	2.5
p,	7.0

Table 4.8 – Properties of cortical bone for Model-105

Property	**Value (Units)**
Damage Threshold,(r_D)	0.0 mm/mm
Damage Material Constant,ς	250 Pa
Critical damage parameter,(D_c)	0.2

Table 4.9 – Damage parameters of Cortical Bone

NOTE: The damage parameter ς is an approximation based on that for concrete. Concrete was chosen since, it shows quasi-brittle fracture.

The simulation seemed to be credible at initial stages till the penetration was encountered between the elements of input rigid wall (Master segment) and single part rib sample (Slave segment). It seemed that the penetration was due to parameters chosen in contact algorithm. The problem still persisted upon changing the contact parameters. Upon further investigation, we noticed that the elements were eroded and removed from the calculation at the compression surface of rib.

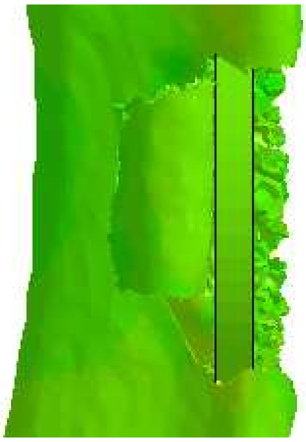

Figure 4.13 – Penetration of Input wall into the sample

Even though this material model is complex and efficient, it is unable to differentiate between the compression and tension surfaces when applied to three point bending. Moreover, the erosion of element are not only due to this reason, yet they might occur due to the choice of damage parameters. Nevertheless we have no choice to let go off this constitutive law.

4.3.2 Single Part Model-24

A total of 3 different models were carried out *i.e.* Model-24a (Pavier, 2013), Model-24b (Pavier, 2013) plus VP $= -1.0$ and Model-24c (Li et al., 2010). The corresponding material properties are presented in Tab

Model	ρ, kg.m^{-3}	E, GPa	σ_y, MPa	C, GPa	p
Model-24a	6000	14	70	-	-
Model-24b	6000	14	70	2.5	7.0
Model-24c	2000	11	88	2.5	7.0

Table 4.10 – Mechanical properties for single part model-24

This model has erosion option for element based on fracture strain, which is not reliable for progressive crack propagation. Therefore, it was coupled to the external damage law *MAT-Add-Erosion with GISSMO option. The damage law parameters are presented in

Model	ε_f, m/m
Model-24a	7.6×10^{-2}
Model-24b	7.6×10^{-2}
Model-24c	2.0×10^{-2}

Table 4.11 – Tensile fracture strain for single part model-24

As explained in Sec. 4.2.2, this damage law Every model was compared in terms of fracture propagation and contact force response. These contact force responses were then compared with experimental results.

Model-24a Results

Crack Propagation (Model-24a)

On applying the phenomena specified of dynamic crack propagation (Miannay, 2001) to the results of this simulation, we see that the damage is still at the microscopic level till 0.46 ms. At 0.48 ms, we have a crack that surfaces at macroscopic scale and is initiated in the sample. At 0.8 ms, we see the arrest of the crack. Apart from this, we also notice along-branching or kincking. (see figure:4.14)

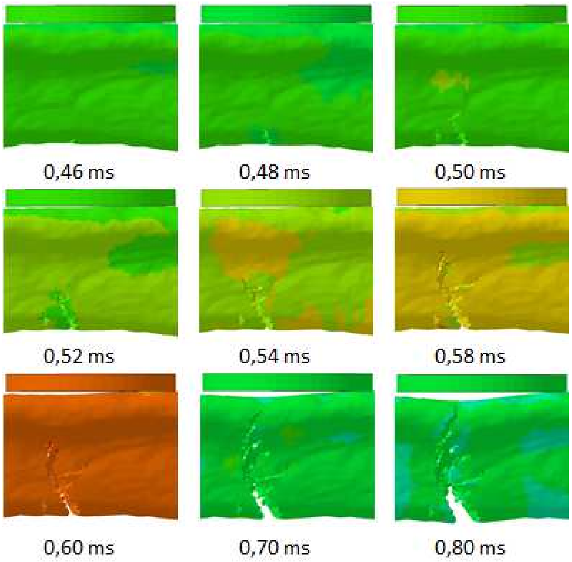

Figure 4.14 – Crack growth in Model-24a

Force Analysis (Model-24a)

The forces were recovered at the contact interface of Rigid walls and Sample. Initially, we see a great amount of increase in Input Contact force till it reaches its maximum value of 4.15kN and starts to decrease. The decrease in contact force signifies the increase in microscopic damage and reduction in force carrying capacity between $t = 0.132\,\text{ms}$ and $t = 0.46\,\text{ms}$. Once the microscopic voids/cracks surface at macroscopic level, we see the crack initiation at $t = 0.48\,\text{ms}$ and propagation between $t = 0.48\,\text{ms}$ and $t = 0.80\,\text{ms}$. After which, the sample breaks entirely. (see figure:4.15)

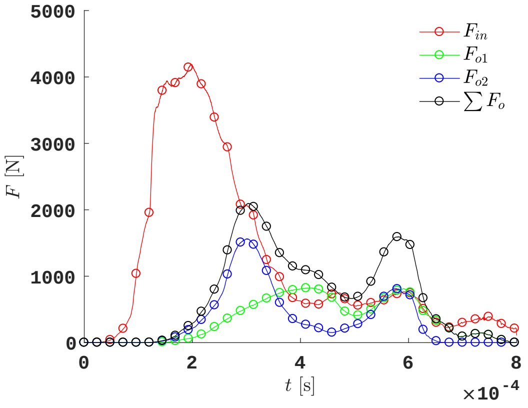

Figure 4.15 – Contact Forces in Model-24a

Model-24b Results

In Model-24b, the numerical rib was give the same properties an in table:4.10. In addition to that, this model also take into account the strain rate effects through Cowper-Symmonds model *i.e.* $\text{VP} = -1.0$. The Cowper-Symmonds parameters were adapted from Li et al. (2010), $C = 2.5$ and $P = 7.0$.

Crack Propagation (Model-24b)

Whereas, on including the strain rate formulation through Cowper-Symmonds model, we see that the crack initiation is delayed by 0.04 ms, which is not a significant difference. The crack is initiated at 0.5 ms and at 0.8 ms we see the arrest of the crack. In contrast to model-2a, we do not see knicking.(see figure:4.16)

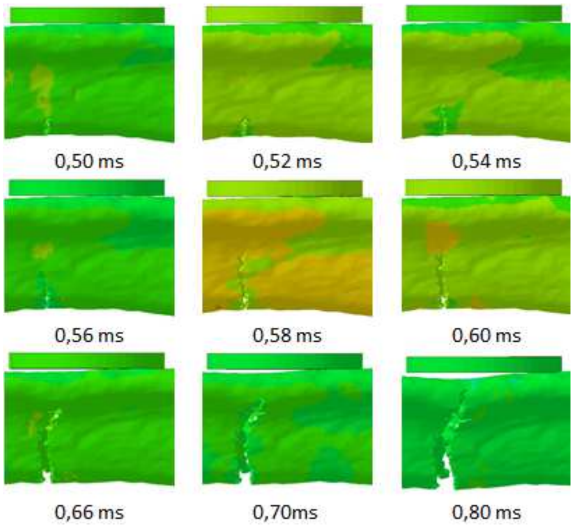

Figure 4.16 – Crack growth in Model-24b

Force Analysis (Model-24b)

Initially, we see a great amount of increase in Input Contact force till it reaches its maximum value of 4.95kN and starts to decrease. The decrease in contact force signifies the increase in microscopic damage and reduction in force carrying capacity between $t = 0.132\,ms$ and $t = 0.50\,\text{ms}$. Once the microscopic voids/cracks surface at macroscopic level, we see the crack initiation at $t = 0.50\,\text{ms}$ and propagation between $t = 0.50\,\text{ms}$ and$t = 0.80\,\text{ms}$. After which, the sample breaks entirely.(see figure:4.17)

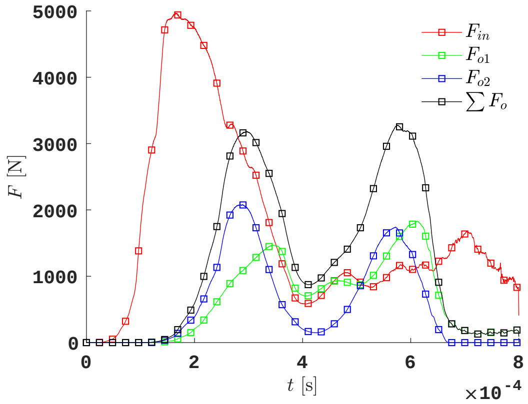

Figure 4.17 – Contact Forces in Model-24b

Model-24c Results

Model-24c, is based on the properties adapted from Li et al. (2010) and it does consider the strain rate effects through Cowper-Symmonds model with same values of C and P. In contrast to Li et al. (2010), we have also added a damage law based on GISSMO model with triaxiality curve.

Crack Propagation (Model-24c)

On applying the phenomena specified above to the results of this simulation, we see that the crack is initiated at time between $\text{t} = 0.32\,\text{ms}$ and $\text{t} = 0.36\,\text{ms}$. At $\text{t} = 0.36\,\text{ms}$, we have a crack that is already initiated and propagating in the sample. At $\text{t} = 0.40\,\text{ms}$, we see the arrest of the crack. Apart from this, we also notice that there is no along-branching or kincking. (see figure:4.18). Once the crack comes to arrest (in this case the sample is completely broken), the fragments start rotating. Apparently, the Input rigid wall re-establishes contact and we see Contact force signals again.

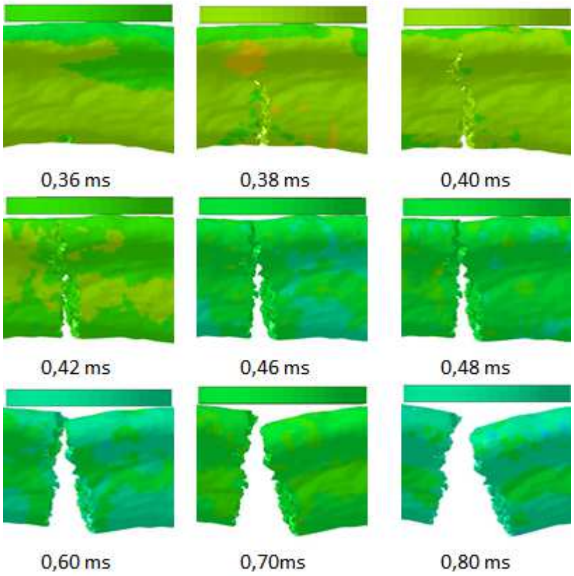

Figure 4.18 – Crack propagation in Model-24c

Force Analysis (Model-24c)

Initially we see increase in contact force till t = 0.1179 ms, at this point Microscopic damage is in progress till we have a crack that surfaces at macroscopic level (t = 0.36 ms). This crack then propagates till the sample is entirely broken t = 0.545 ms. But we do not see any kinking. Alongside, we do notice that the sum of output forces is greater than Input force for most of the simulation *i.e.* the system is not in equilibrium. The contact force at the Input wall-sample interface does not drop down to zero as the wall reestablishes contact with the broken sample and the elements stay in contact.

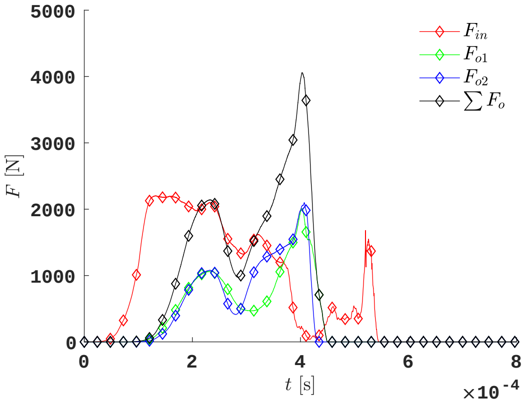

Figure 4.19 – Contact Forces in Model-24c

4.3.3 Single Part Model-3

Two different models were tested using the material model *MAT-003 *i.e.* Model-3a, with properties from Li et al. (2010) and Model-3b, with properties from Pavier

(2013).

Model-3a Results

Crack Propagation in Model-3a

On applying the phenomena specified above to the results of this simulation, we see that the crack is initiated at time between 0.32 ms and 0.34 ms. At 0.34 ms, we have a crack that is already initiated and propagating in the sample. At 0.4 ms, we see the arrest of the crack. Apart from this, we also notice that there is no along-branching or kincking. (see figure:4.20)

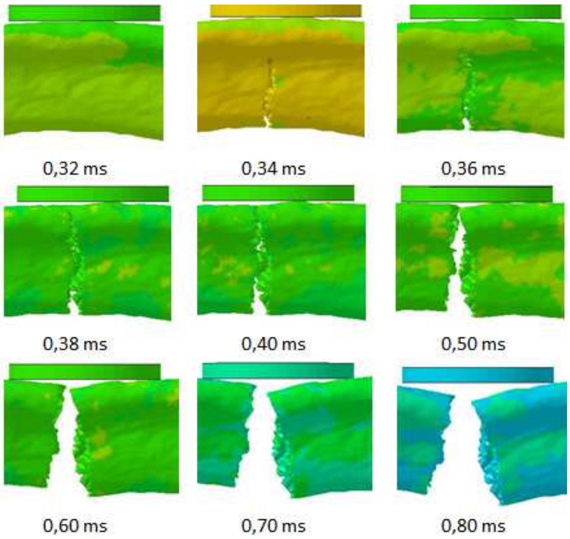

Figure 4.20 – Crack propagation Model-3a

Force Analysis in Model-3a

Initially, we see a great amount of increase in Input Contact force till it reaches its maximum value of 2.15kN and starts to decrease. The decrease in contact force signifies the increase in microscopic damage and reduction in force carrying capacity between $t = 0.121\,\mathrm{ms}$and $t = 0.33\,\mathrm{ms}$. Once the microscopic voids/cracks surface at macroscopic level, we see the crack initiation at $t = 0.33\,\mathrm{ms}$ and propagation between $t = 0.33\,\mathrm{ms}$ and $t = 0.4\,\mathrm{ms}$. After which, the sample breaks entirely. (see figure:4.21)

Moreover, we also notice that the sum of contact forces between Output wall and the sample is greater than force between input wall and sample, this signifies that the system is not in equilibrium. This phenomenon coincides with the experimental results of Pavier (2013) as the experimental velocity were taken from a case that was not in equilibrium.

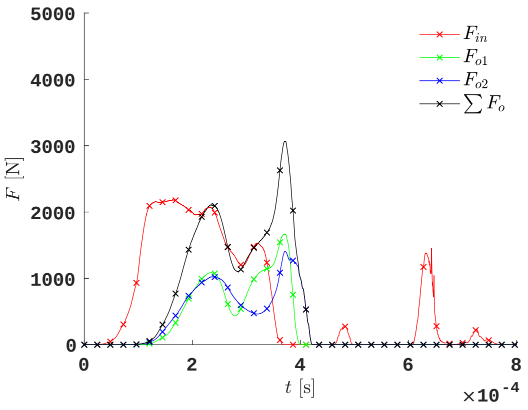

Figure 4.21 – Contact forces Model-3a

Model-3b Results

Crack Propagation (Model-3b)

In contrast to model-24b (*MAT-024), this model behaves a bit differently. We see a huge delay in crack initiation *i.e.* instead of initiation at t = 0.5 ms, the crack in model-3b is initiated in between t = 0.66 ms and t = 0.68 ms. Moreover, two cracks are initiated instead of one but only one crack propagates from t = 0.68 ms and the crack is arrested at t = 0.8 ms.

Force Analysis (Model-3b)

Like all other models, initially the input force increases till t = 0.1635 ms but has the same magnitude as in Model-24b. The decrease in input force is backed-up by increasing microdamage thereby a decrease in Force Carrying capacity. The Input force does not descend to zero as the Input wall always see some elements of the rib.

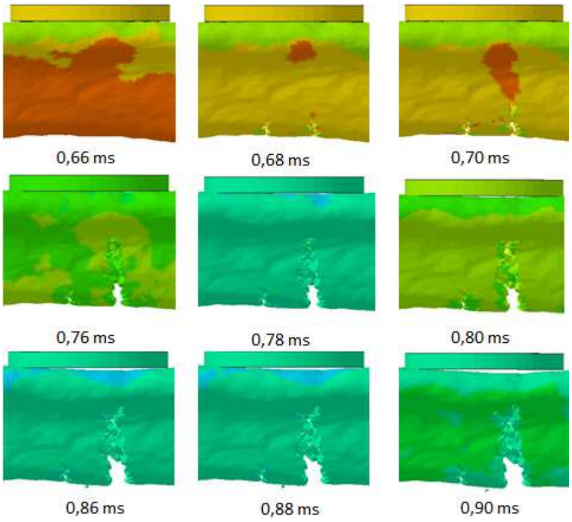

Figure 4.22 – Crack propagation Model-3b

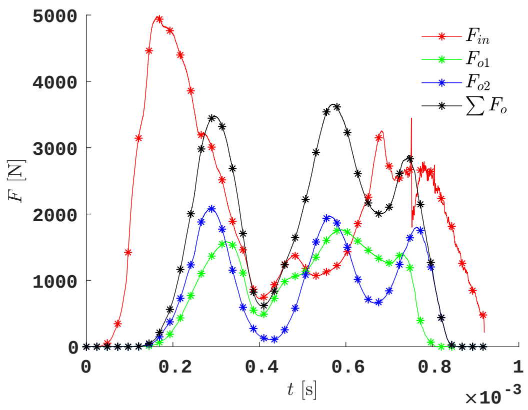

Figure 4.23 – Contact forces Model-3b

4.4 Contact Algorithm

An automatic surface to surface contact was used for contact between bars and porcine rib. This contact algorithm uses a segment based penalty approach. On the other hand, an interior contact was defined between elements of each constituents of porcine rib in order to assist transmission of forces and to avoid negative elements.

The segment based automatic surface to surface contact is not dependent on segment orientation *i.e.* the algorithm looks on both salve and master segments, thereby producing a symmetric contact. Thanks to the algorithm, we can obtain the forces involved in the contact. In fact the contact force depends on the shape of the geometry. The contact algorithms and their differences are presented in AppendixB

For example, let us consider porcine rib in three point bending (to your left in Fig. 4.24) and an assumed cylindrical bone sample in pure compression (to your right in Fig. 4.24)

Figure 4.24 – Influence of contact surface on force

The two geometrical configurations were modeled using the same contact algorithm and material properties. The resultant forces at the input bar-sample interface are presented in Fig. 4.25. “3PB” represents three-point bending and “PC” represents pure compression.

Analysis of forces with respect to geometrical configuration

Three-point bending (3PB)

1. As the sample starts to bend under load, the contact forces are written. Since, only a set of nodes are supposed to be in contact with the bars at corresponding interfaces, we see a difference between F_{in} and $\sum F_{out}$.
2. In this case, both F_{in} and $\sum F_{out}$ drop down to zero, which signifies the rupture and loss of contact at the sample-bar(s) interface.

Pure compression (PC)

1. As opposed to rib sample, the input and output bars are in contact with all salve nodes in the salve segment throughout the simulation. Thus F_{in} and F_{out} superimpose.
2. In contrast to 3PB sample, the F_{in} and F_{out} do not drop to zero as the sample is always in contact even though it is subjected to damage and elements being eroded.

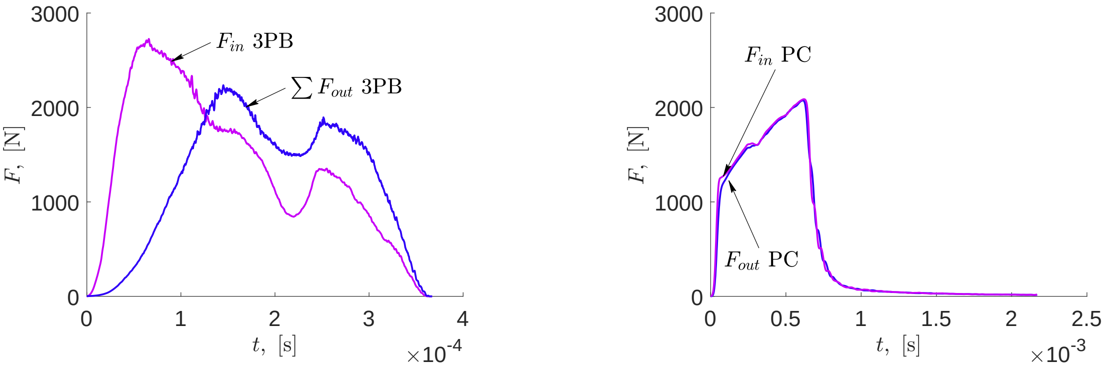

(a) Three-point bending (b) Pure compression

Figure 4.25 – F vs t form contact force data

4.5 Discussions

The mesh density and mesh size have an influence on the numerical propagation of longitudinal waves and wave celerity c_{FEM}. A mesh density of $\Gamma = 20$ per wavelength gives the best possible results yet not cost efficient in terms of calculation time. Therefore, for a better propagation of longitudinal waves, the element size in the direction of wave propagation was considered to be 1 mm.

The choice of constitutive law and damage law plays an important role in the results. We had pointed out some hurdles in experiments regarding behavior of porcine rib cortical and trabecular bone sample under dynamic environment. For example, due to miniature geometrical nature of porcine ribs, it is difficult to extract uniform rectangular or dog-bone samples for dynamic tension or compression tests. On the other hand, cylindrical samples of trabecular bone extracted from porcine rib might not capable of producing comprehensible experimental results. Moreover, as said in Sec. 4.2, the numerical porcine rib model used in this thesis is homogenized *i.e.* we do not consider the trabecular bone architecture. Therefore, we had no other choice rather to let go off using foam like behavior for trabecular bone constituents of porcine rib.

These all together , have led us to use a elastic-viscoplastic constitutive law coupled with an external damage law in order to simulate the time and path dependent progressive crack propagation until entire fracture. In this case, three material models were tested (*MAT-105,*MAT-024 and *MAT-003).

1. Out of which the first model was ruled out as there were penetrations of the Input rigid wall into the sample. It seems that the damage material parameter ς of material model *MAT-105 was the reason.
2. The response of ribs with properties from Pavier (2013) (Models-24a,24b and 3b) seem to respond well even though there is a significant amount of difference in the force magnitudes.
    a Model-24a is a replication of its first version but the numerical sample is solid bone instead of a hallow tube as in Aubert (2012). We strongly believe that the rigidity of the solid bone increases the force alongside a decrease in displacement.
    b Model-24b considers the strain rate effects through Cowper-Symmonds formulation. The values considered for Cowper-Symmonds parameters C and P do not correspond to bone material. As a reason, this has a strong influence in further increase in contact forces.
    c Model-3b was executed in first place for comparing the material model *MAT-024 and *MAT-003. Similar to Model-24b, we have effects of strain rate in this model. Moreover, this model is based on Kinematic Hardening principle instead of Isotropic. The Kinematic Hardening parameter β_h delays the time of crack initiation.

In all the three cases *i.e.* (Models-24a,24b and 3b), the magnitude of Input force is consistent.

3. The response of ribs with properties from Li et al. (2010) (Models-24c and 3a) too correspond well qualitatively with experimental responses.

    a Model-3a is an upgrade to its first version through a damage law that helps to differentiate between tensile and compressive failure instead of a simple Failure strain criteria as in Li et al. (2010). The force magnitudes are less than that of Models-24a,24b and 3c due to the difference in material properties of (Pavier, 2013) and (Li et al., 2010).

    b Model-24c was executed to compare the material models *MAT-003 and *MAT-024. The crack propagation in this model is an evidence for the influence of kinematic hardening parameter β_h of *MAT-003.

Part IV

Simulations

Chapter 5

Simulation at experimental scale

Résumé:

Ce chapitre présente l'application du modèle numérique mis en place dans le chapitre (4) aux cas expérimentaux. Les signaux de déformation numériques ont été enregistrés aux même points (sur les barres) que les signaux expérimentaux mesurés sur les barres de Hopkinson.

Dans un premier temps, nous avons testé un échantillon numérique fictif en le supposant uniquement formé d'os cortical. Les résultats numériques montrent que cet échantillon est trop rigide par rapport aux résultats expérimentaux. Ceci prouve que l'os trabéculaire joue un rôle très important dans l'absorption des forces d'impacts.

Deuxièmement, l'échantillon numérique "composite" (cortical + trabéculaire) a été testé avec les conditions expérimentales correspondant à la fracture hors équilibre. Les résultats de ces simulations sont conformes aux gabarits expérimentaux définis dans le chapitre 2.

Les résultats numériques prouvent que le temps, l'énergie et le déplacement à la rupture diminuent avec l'augmentation de la vitesse donnée à l'impacteur.

Si on le compare au cas expérimental retenu, le modèle numérique proposé montre une grande efficacité dans la prévision du déplacement, des forces aux interfaces, des seuils d'énergie et des fractures.

Abstract:

This chapter presents an application of the numerical model established in the preceding chapter at experimental scale. In order to ensure similar conditions of experimental setup, numerical strain signals were extracted from elements at same distances from the sample interfaces.

First of all, a numerical sample was assumed to be made of only cortical bone was tested (namely single part). The results show that the single part sample is too rigid with respect to experimental cases. This proved that the trabecular bone plays a crucial role in absorbing the impact forces of a rib.

Secondly, a numerical sample with both cortical and trabecular was tested (namely multi part sample). Experimental cases corresponding to fracture before dynamic equilibrium were the center of interest. Therefore, striker velocities of corresponding cases were simulated. The results of multi part sample are in accordance with the established experimental corridors.

The numerical results show that as striker velocity increases, the time , energy and displacement at fracture decreases. The numerical threshold values of time, energy and displacement at fractures are similar to that of experimental threshold values.

The proposed FE model shows high efficiency in predicting force-displacement, energy thresholds and similar fracture patters to that of experimental cases.

Even though the rigid wall model produces results resembling to experimental cases, it is always better to carry simulations at experimental scale to have reliable and accurate comparisons. Thus the simulations at experimental scale were carried out with exact dimensions. Two numerical samples were considered, (i) single part porcine rib, and (ii) multi-part porcine rib. In both cases, the rib sample was meshed with under-integrated eight node solid elements of 0.15 mm in size and were provided with a stiffness based Flanagan-Belytschko hourglass was provided to avoid hourglass modes.

As concluded in §4.5, the bars and striker were meshed with under-integrated eight node solid brick elements of 1 mm in size along the direction of propagation of longitudinal waves. A stiffness based Flanagan-Belytschko hourglass formulation was used to avoid hourglassing modes.

An automatic-surface-to-surface contact with segment based penalty formulation was considered between every master and slave surface in the model. In addition to this, an interior contact algorithm was specified between each constituent of porcine rib if required.

This chapter presents the different numerical tests carried out on single and multi part porcine rib samples as well as a generalized 5th human rib of 80 mm in length.

5.1 Single-part porcine rib sample

The numerical model consists of single part porcine rib sample, a short striker, an input bar and two out put bars as shown in Fig. 5.1.

The striker was given an initial velocity of $v_{str} = 17$ m.s^{-1}. The numerical strain signals were recorded at element at 1.5 m on the input bar and from elements at 0.4 m on out bars.

The strain signals recorded at respective elements have to be transported in such a way that they were recorded at the bar-sample interface for calculation of forces at interfaces and interface velocity. The raw numerical strain signals acquired at the aforementioned strain gauge locations in absolute time t' are shown in Fig. 5.2

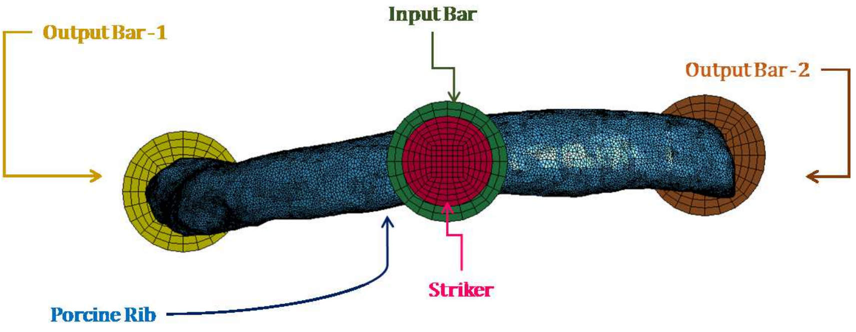

Figure 5.1 – Single part porcine rib with SHPB at experimental scale

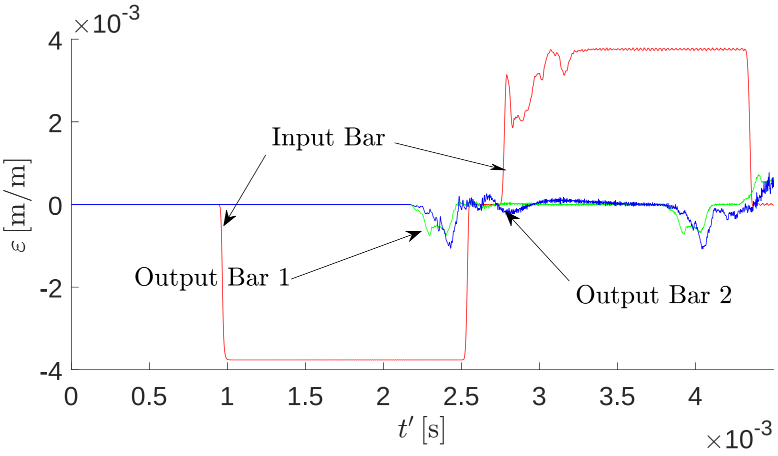

Figure 5.2 – Raw numerical strain signals

Once the raw strain signals were acquired, they were shifted in both time and space so that the each and every part of these signals were recorded separately at the interfaces. Therefore, we have ε_{inc}, ε_{ref}, ε_{tr1}, and ε_{tr2} as presented in Fig. 5.3a and Fig. 5.3b. In this case, the arrival time t_0' of the incident wave pulse at input bar-sample interface was $\approx\ 1.8 \times 10^{-3}$ [s].

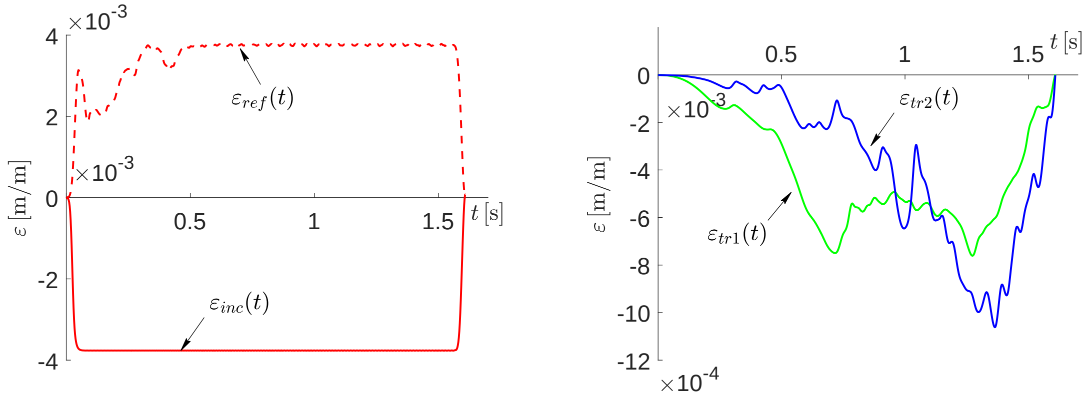

(a) ε_{inc} and ε_{ref}

(b) ε_{tr1} and ε_{tr2}

Figure 5.3 – Shifted strain signals of single part porcine rib

The next step is to calculate the dynamic variables involved at the interface for characterization of the sample. This is done using Eq. 2.17a to Eq. 2.17f, Eq. 2.18, and Eq. 2.19. Note that the curves presented in red, green and blue represent the variables at input bar-sample interface, output bar -sample interface 1, and output bar-sample interface 2 respectively. The curves in black represent either the sum or relative variables.

On the other hand, the energy absorbed by the sample was calculated through the methodology proposed by Lundberg (1976). The energy absorbed by the sample during fracture in three point bending can be expressed in terms of the energy of incident, reflected and transmitted stress pulses as follows

$$W_{PR} \;=\; \frac{A_b c_b}{E_b} \int_0^t \left(\sigma_{inc}^2 \;-\sigma_{ref}^2 \;-\; \sigma_{tr1}^2 \;-\; \sigma_{tr2}^2\right) dt \tag{5.1}$$

The Eq. 5.1 is modified to calculate the energy in three bars SHPB test.

Let us consider the time history of W_{PR} and in Fig. 5.4d for further analysis. Initially, W_{PR} exhibits a linear evolution till $t \;=\; 0.298 \times 10^{-3}$ [s], which corresponds to the energy for crack initiation W_{ci}. From this point of time, we see fluctuation till entire rupture of the sample at $t \;=\; 0.4998 \times 10^{-3}$ [s], corresponding to the energy for entire rupture W_{r}.

The relative interface velocity V for this corresponding case is $\approx\; 12.5\; [m.s^{-1}]$, thus it is logic to compare the F_{in} vs U curve to the established experimental corridor-3.

Even though the energy and displacement values correspond to that of experimental values, we can see that the force amplitude is more than that of experimental. This proves that the trabecular bone plays an important role in determining the overall response and flexural strength of the rib. This is in opposition with that Granik and Stein (1973) had proposed.

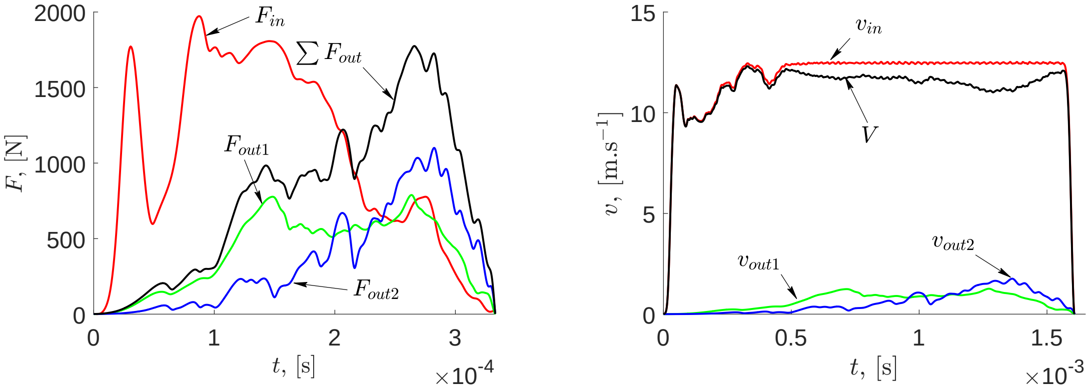

(a) F vs. t (b) v vs t

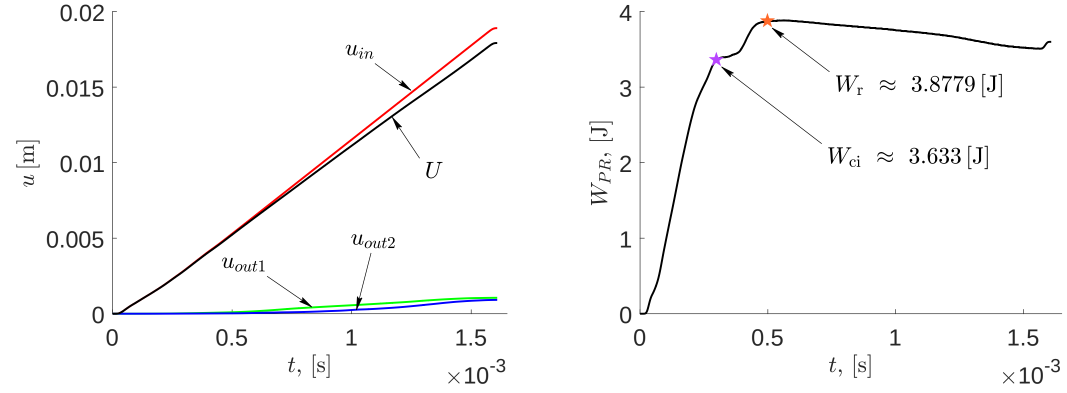

(c) u vs t (d) $W_{PR}(t)$

Figure 5.4 – Dynamic variables and energy for single part porcine rib

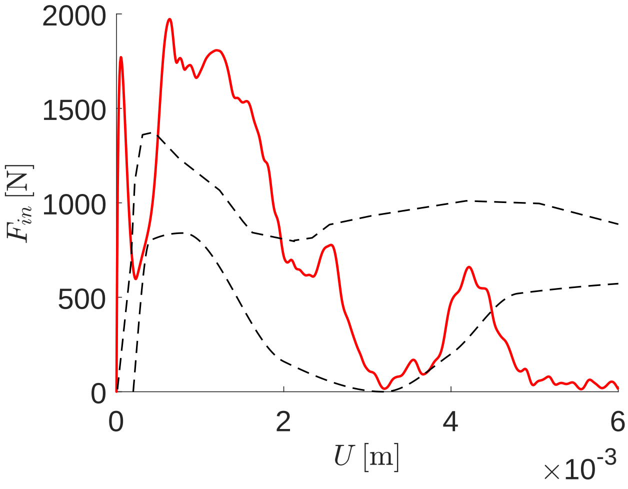

Figure 5.5 – Comparison of single part to experimental corridor-3

5.2 Multi-part porcine rib sample

As seen above, a singe part porcine rib (*i.e.* with only cortical bone) is more rigid when compared to tested real porcine ribs. Therefore, a multi part porcine rib was tested. The trabecular bone elements were modeled using elastic-viscoplastic with kinematic hardening and cortical bone using elastic-viscoplastic with isotropic hardening. Since a model with different mechanical constants would be complicated to understand at this stage, the cortical and trabecular bone elements were provided with average material properties an in Tab. 3.4. The numerical setup with multi part rib resembles that as shown in Fig. 5.6.

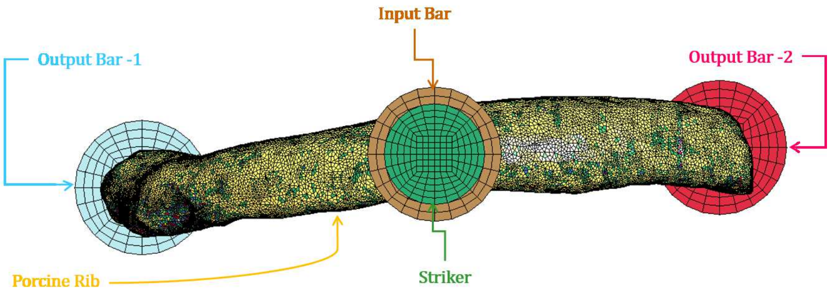

Figure 5.6 – Multi-part porcine rib with SHPB at experimental scale

The multi-part numerical model is different from that of single part, as the definition of contact surfaces (slave and master) is not based on part ID but is rather through Part Set ID for contact at sample-bar interfaces. Moreover, an interior contact is added for different parts of porcine rib so that the solver can recognize that these parts form a single structure.

5.2.1 Case 1

The case 1 is with $v_{str} = 17$ [m.s^{-1}], so that the effect of trabecular bone can be pointed out. The raw strain signals in terms of absolute time t' for this case are presented in Fig. 5.7.

The same methodology was followed for post processing of strain signals and the respective results are presented below. As the bar dimensions and material are the same, the arrival time t'_0 for multi-part sample is also 1.80×10^{-3} [s].

Comparing the shifted strain signals of multi-part and single part porcine rib samples, we can notice that the reflected wave signal of multi-part (Fig. 5.8a) has changed a bit whilst the overall shape remains similar. On the other hand, the force responses at the interface show a pronounced change. For example, the Max(F_{in}) of single part was around 2000 [N] whereas, the Max(F_{in}) of multi-part is around 1200 [N]. This proves that the single part sample more rigid and takes less time for fracture ($t_{frc} \approx 3.46 \times 10^{-4}$ [s]) when compared to multi-part whose t_{frc} is prolonged to $\approx 5.80 \times 10^{-4}$ [s], thus proving that the trabecular bone has an effect on fracture of the structure.

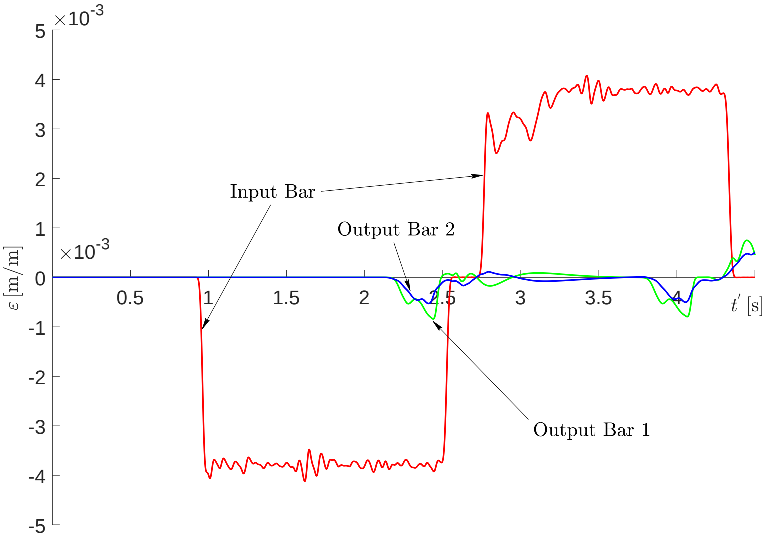

Figure 5.7 – Raw numerical strain signals for case 1

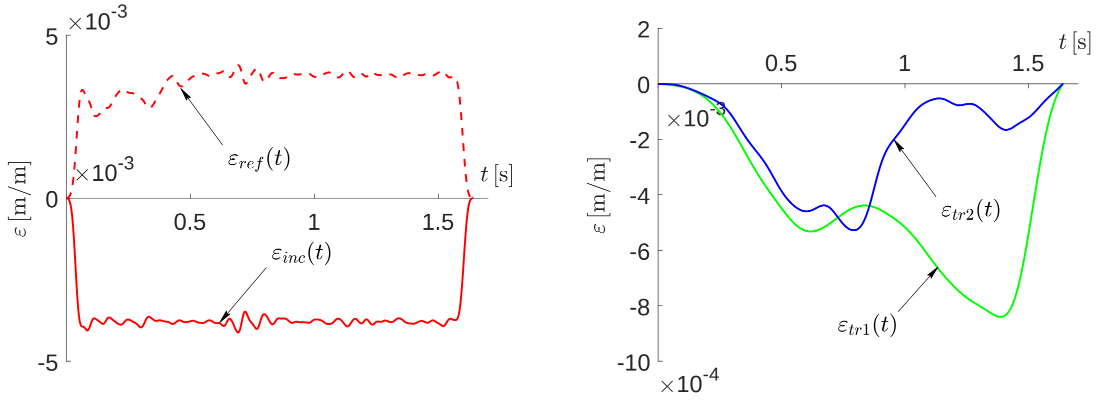

(a) ε_{inc} and ε_{ref}

(b) ε_{tr1} and ε_{tr2}

Figure 5.8 – Shifted strain signals of multi-part porcine rib case 1

Since the striker velocity (v_{str}) is the same for both single part and multi-part case 1, the evolution of energy in incident wave $W_{inc}(t)$ is the same. Where as the evolution of energy in reflected wave $W_{ref}(t)$ is slightly different. The Fig. 5.9d shows the energies required for crack initiation and rupture W_{ci} and W_{r} respectively. The values are lower than that absorbed by single part porcine rib. This is due the rapid accumulation of damage in trabecular bone. Remind that the damage accumulation parameter n of trabecular bone is 2.0 whilst that for cortical bone is 1.25. Eventually the damage accumulates faster in trabecular bone thereby, the elements reach the required criteria for erosion faster. This justifies the decrease in energies W_{ci} and W_{r}.

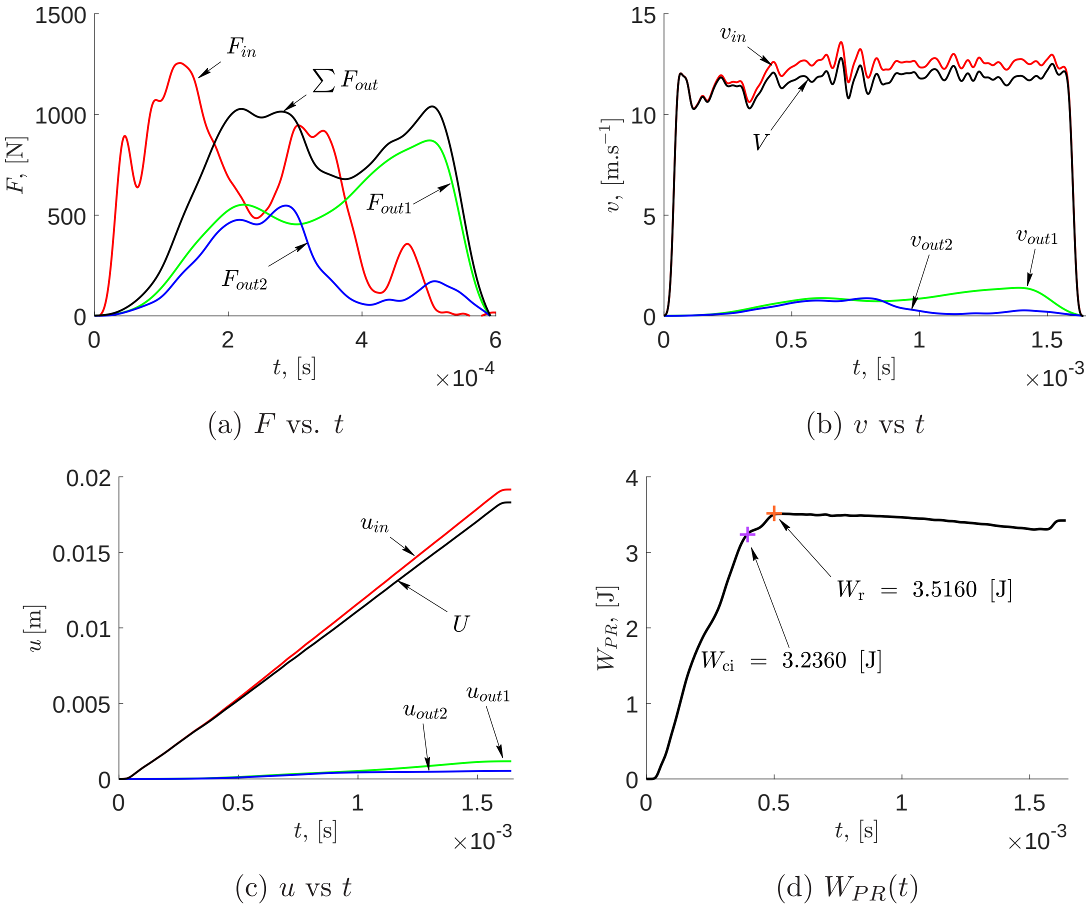

(a) F vs. t (b) v vs t

(c) u vs t (d) $W_{PR}(t)$

Figure 5.9 – Dynamic variables and energy at interfaces for case 1

5.2.2 Case 2

This case corresponds to a numerical striker velocity of 19.21 $[\mathrm{m.s}^{-1}]$, which is the average velocity of all experimental cases in corridor 3 with fracture before dynamic equilibrium.

It is logic that the increase in striker velocity v_{str} must increase the amplitude of strain in the bar. As the difference in v_{str} is not huge, the increase in strain must not be large. This increase in v_{str} will in turn increase the interface velocities. Comparing Fig. 5.9b and Fig. 5.10b, we can observe that the mean value of V for case 1 is $\approx$ 11.41 $[\mathrm{m.s}^{-1}]$ where as that for case 2 is $\approx$ 12.45 $[\mathrm{m.s}^{-1}]$. Thus, the sample has further less time to establish an equilibrium with input and output forces. This is justified by a decrease in time for fracture t_{frac} (see Fig. 5.10a).

Similarly, the energy of incident wave $W_{inc}(t)$ is also increased due to the increase in v_{str}. Whereas, the energies required for crack initiation and rupture (W_{ci} and W_{r}) have a negative correlation with striker velocity. The values presented in Fig. 5.9d and Fig. 5.10d for cases 1 and 2 respectively, speak for themselves.

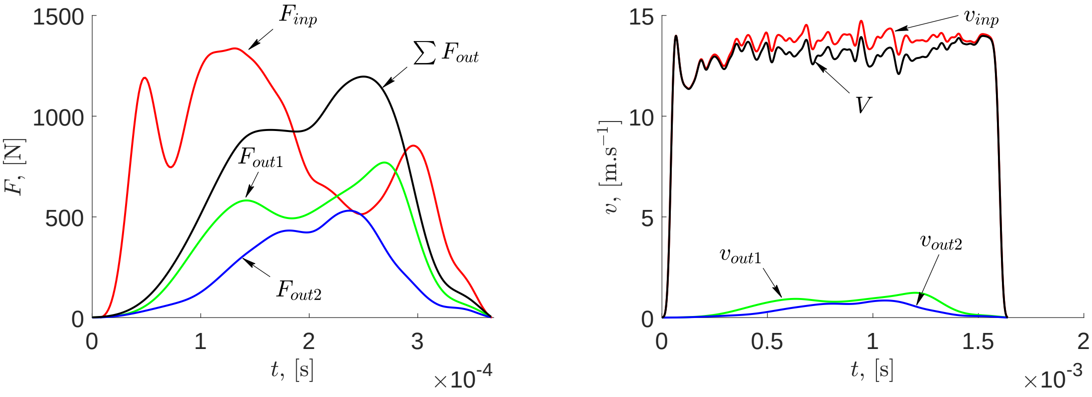

(a) F vs. t

(b) v vs t

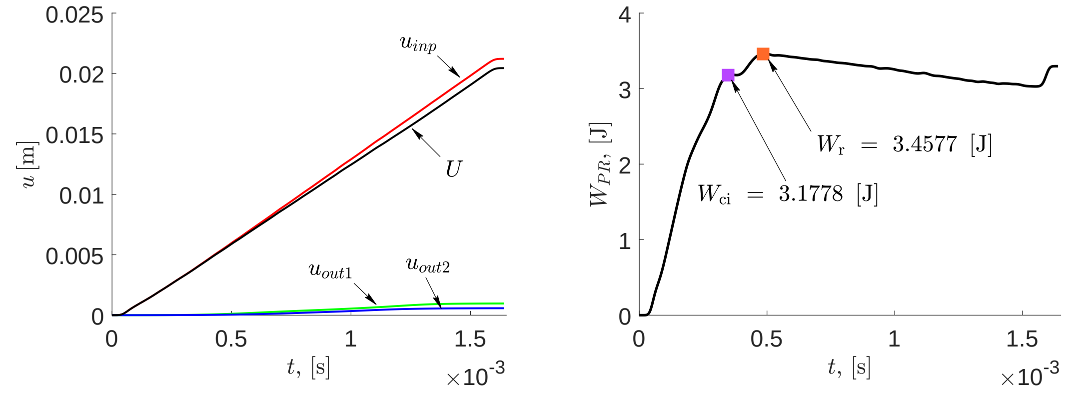

(c) u vs t

(d) $W_{PR}(t)$

Figure 5.10 – Dynamic variables and energy at interfaces for case 2

Comparison with experimental data

The relative interface velocity V for this case varies around 11.14 $[\mathrm{m.s}^{-1}]$. Therefore, the results were compared to the experimental corridor 3.

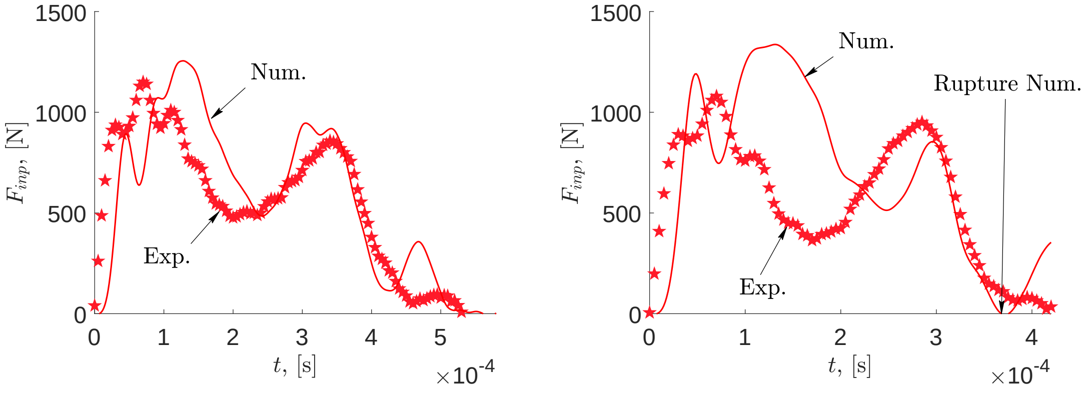

(a) F_{inp} vs. t (b) F_{inp} vs. t

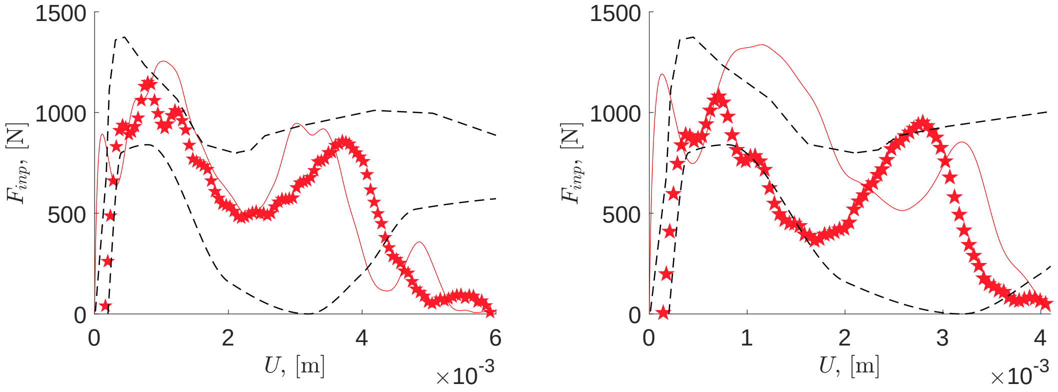

(c) F_{inp} vs U (d) F_{inp} vs U

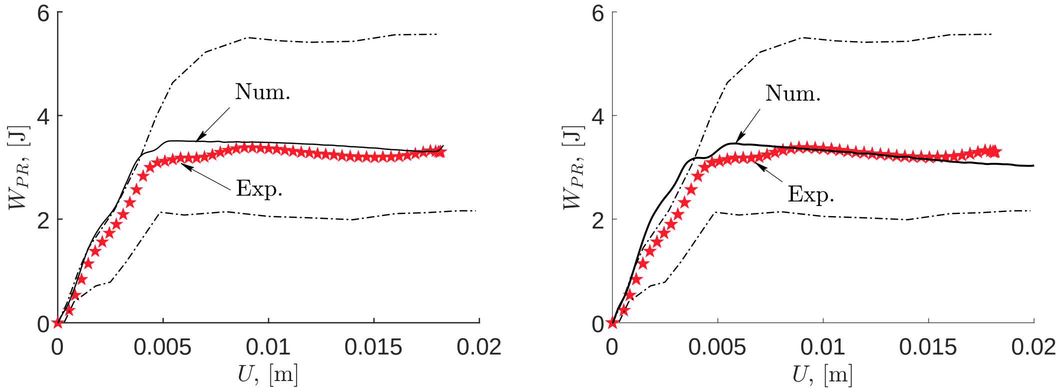

(e) W_{PR} vs U (f) W_{PR} vs U

Figure 5.11 – Comparison of case 1 (left) and case 2 (right) with experimental data

5.3 Analysis of numerical response

5.3.1 Consistency of force response

As said in sec. 4.4, the contact algorithm does provide us the ability to have force at the interface. The forces obtained from shifted strain signal and contact force shall be similar, given that the contact algorithm has a significant representation of its physical counterpart. The Fig. 5.12a shows $F_{inp}(t)$ from contact algorithm of LS-Dyna and $F_{inp}(t)$ obtained from shifted strain signals through Eq.2.17a.

We can see that the initial linear response is the same for force obtained through both methods. After a certain time limit, fluctuations are observed in F_{inp} from strain signals (as pointed by an arrow in Fig. 5.12a). This fluctuation is due to the accuracy of selection of starting point of incident and reflected waves of raw strain signal in shifting process. This accuracy issue is in fact a well known problem of SHPB experiments.

Moreover, we do notice a time lag of $\approx \ 0.19 \times 10^{-3}$ [s] in the force obtained from strain signals. It is important to recall that the forces obtained from strain signals of SHPB is based on the assumption: “*there is total contact between sample and bars at corresponding interfaces*”. Rather in reality, only a certain area of the sample is in contact and the area of contact is not constant throughout the test. In simple terms, the difference between contact force and force from strain signals depends on the geometry of sample. A more detailed explication is given in sec. 4.4 and the results are presented in Fig. 4.25.

To make sure that the contact force is accurate than that from strain signals, the F_{inp} vs U curves were compared to corresponding experimental results as in Fig. 5.12b.

As we can see that the linear elastic response of contact force superimposes with that of experimental case, this proves that the contact force is more physical than that of force from strain signals. Yet it is always better to compare the later with experimental response in order to have similar post processing methods.

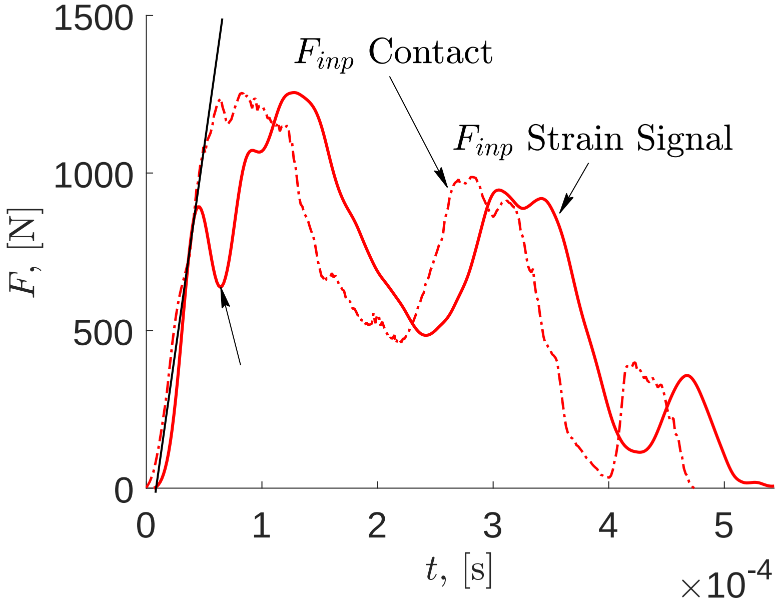

(a) Consistency of force response

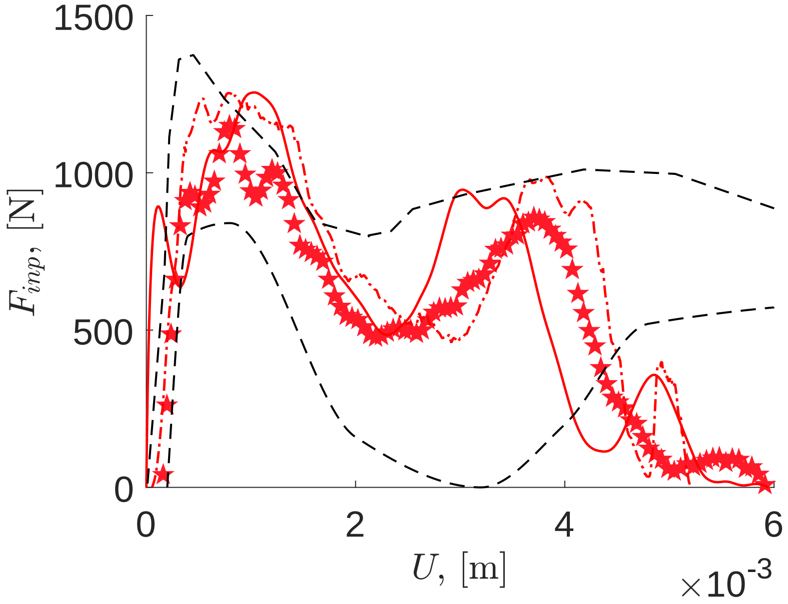

(b) Consistency with experimental corridor

Figure 5.12 – Consistency of force response

5.3.2 Effect of scale factor curves

As said in sec. 4.2.2, the external damage law is provided with different curves to consider the effects of strain rate on post yield behavior of the sample. Five different curves were tested, based on the equation proposed by Wood (1971) (see Fig. 5.13a) repeated here for clarity. The rate of decrease of ε_f is controlled by the variable B of the equation.

Before seeing the influence of scale factor curves on force response, we need to first understand the trend seen in all numerical and experimental responses corresponding to fracture before equilibrium. the Fig. 5.13b, shows F_{inp} vs t response with all five scale factor curves.

The structure initially behaves as an elastic body (response to the left of the vertical dotted line) in Fig. 5.13b and continues to increase till it reaches maximum value of F_{inp}. Till this point of time, the response obtained with each scale factor curve is almost similar. A second peak is observed, as the structure tries to establish an equilibrium with the output forces. This is where the damage starts to couple with flow stresses. As the interface velocity is high when compared to other experimental cases, the structure does not have sufficient time to establish the equilibrium. Thus, we see a rapid decrease in F_{inp} till rupture of the sample. Therefore, a good candidate for the scale factor curve must produce the above characteristics (*i.e.* two peaks).

The curve 5 of Fig. 5.13a is unable to reproduce the second peak, which means that the rate of decrease in scale factor with strain rate is so brutal that the flow stresses couple to damage before hand and the rupture occurs way before the output forces come back to the impact point. Hence, the suitable curve for porcine rib is among curves 1 to 4.

Response obtained from each scale factor curve was then compared to corresponding experimental results to choose the suitable curve. The curve capable of reproducing similar results to experimental case was chosen see. The Fig. 5.13c shows F_{inp} vs U numerical response (solid lines with corresponding colors to scale factor curves used) and experimental result (represented with red pentagons).

It is clear that the curves 5,4 and 3 could be ruled out as either they failed to produced the second peak or a second peak of less magnitude. In contrast to curves 4 and 3, the curve 1 had a tendency to overestimate the second peak magnitude. The best response is obtained with scale factor curve 2. Even though the magnitude of peak is overestimated, the displacement and time at fracture U_{frac} and t_{frac} is almost similar to that observed in experimental case.

Similar to force, a decreasing response can also be noted in the energy at fracture W_{r}. The energy at rupture for the sample with curve 5 is very low that it is not in the established energy corridor. On the other hand, the energy with curve 3 and curve 4 could be barely accepted. Rather, it is curve 2 that gives acceptable response with respect to experimental corridor.

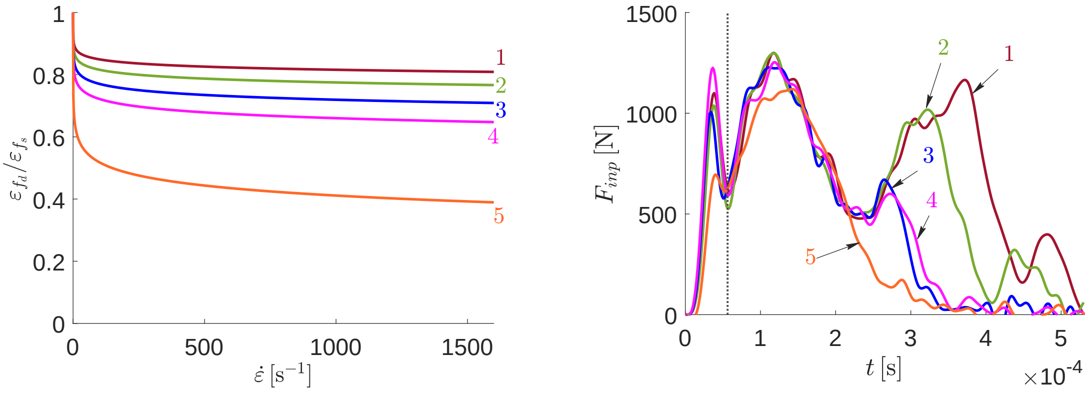

(a) Scale factor curves (b) Effect of scale factor on F_{inp}

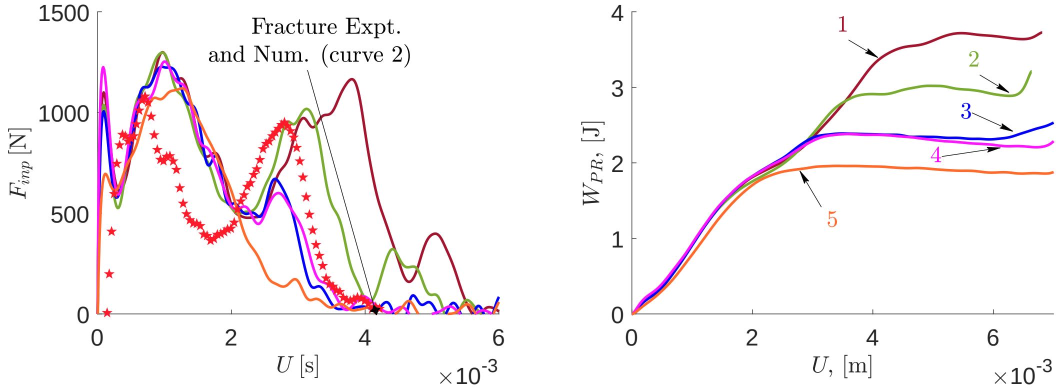

(c) Best scale factor curve (d) Effect of scale factor on W_{r}

Figure 5.13 – Effect of scale factor curves

NOTE: All numerical responses presented in sec. 5.1 and sec. 5.2 were obtained through curve 2.

5.3.3 Comparison of numerical and experimental energies

As we have already established the experimental energy at rupture W_r in sec. 2.5.2, we can now compare the consistency of numerical data. Since the aim of numerical simulations is to have insights on fracture before equilibrium, The numerical data were compared to corresponding experimental values.

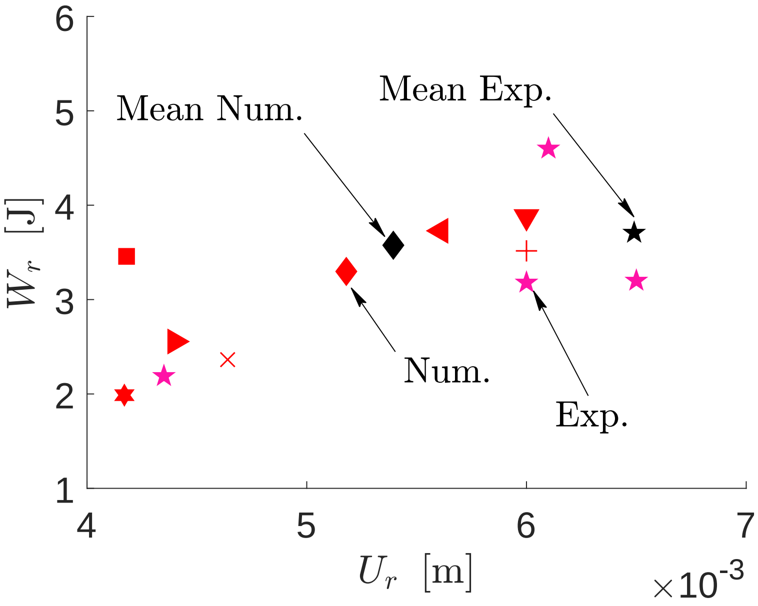

(a) W_r vs. U

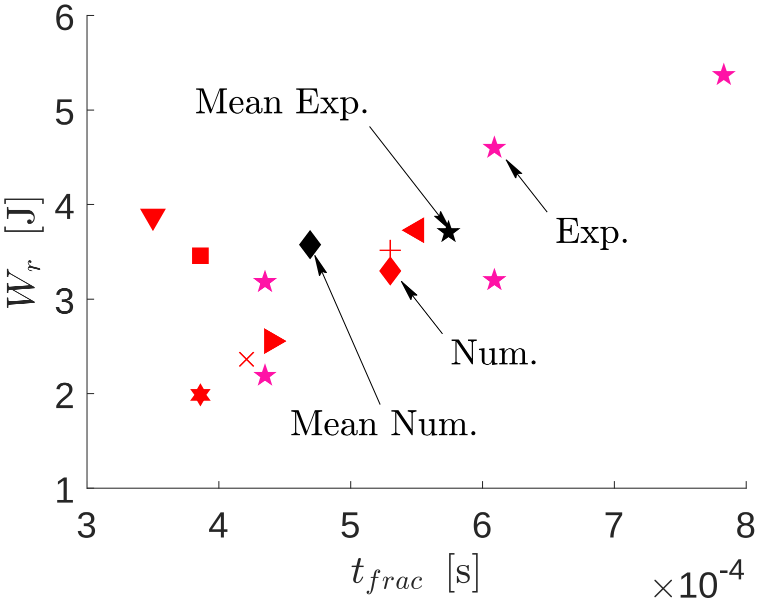

(b) W_r vs t_{frac}

Figure 5.14 – Consistency with experimental data

The experimental data are represented by solid makers whilst, the numerical data are represented by red markers with no fill. We do notice that the numerical energy at rupture clusters alongside that of experimental case. Moreover, the numerical values are close to that of experimental mean (diamond and star black markers respectively).

We can notice two distinctive responses corresponding to single part porcine rib sample (inverted triangle red marker) and multi-part porcine rib sample case

2 (square red marker) in Fig. 5.14b. We see that these two samples needed less t_{frac} with respect to samples with similar W_r. This proves that the composition and striker velocity play an important role in determining the time at fracture.

We had already established that more the relative interface velocity V, the more fracture tends to down shift towards transition phase or the more it tends to occur before dynamic equilibrium. Moreover, the neither of the samples are of similar geometries. Therefore, it would be better to compare the correlation coefficient ($r_{X,Y}$) of displacement at rupture U_r and energy at rupture W_r for both experiments and numerical values. The correlation coefficient for experimental values ($r_{U,W}$ Exp.) is 0.8608 where as that of numerical values ($r_{U,W}$ Num.) is 0.7689.

5.4 Summary

The single part porcine rib results show that the sample is too rigid with respect to experimental results. Therefore, trabecular bone does play an important role in absorbing impact forces under these mechanical conditions.

The ensemble of mutli part simulations proves that the structure behaves in an elastic manner initially till it reaches the peak force and it depends on the distribution of mechanical properties and stiffness in the vicinity of impact. Later, the force starts to decrease till the point where the reaction forces arrive at the point of impact. This is the reason why we see an increase in input force. The second peak represents the maximum deflection the sample can sustain before crack initiation. The decrease in force after this point represents the propagation of crack and loss of structural rigidity.

The numerical simulation was carried out with a striker velocity of 17.39m/s, leading to a numerical interface velocity V of 10.46m/s. The numerical results are compared to an experimental case of similar conditions i.e. Corridor-3. The best numerical result corresponds to that obtained with input curve 2 of the damage law and is shown in Fig. 5.13a.

The differences between experimental and numerical response arise due to the difference in the geometry of samples tested.

Chapter 6

Discussions

The mechanical properties of porcine rib obtained through one variable and two variable models were compared. It is clear that the properties obtained from ρ_{app} as independent variable are more representative than that obtained from either ash fraction α or properties as a function of ash fraction and volume fraction (α, V_f). Moreover, the constituents of porcine rib from apparent porosity values match to that of element distribution obtained through grey scale finite element mesh. It is rather interesting to see that the average mechanical apparent properties of rib constituents is of similar order of magnitudes to that used in past for human rib. This shows that the apparent mechanical properties for porcine rib are biologically reliable, given that the apparent density is correctly correlated with grey scale intensities. Yet proving that the porcine rib as human surrogate is an adequate choice.

The experimental set up used in this thesis had given important insights on the behavior of rib under dynamic loads at intermediate strain rates. The rupture of sample occurred either post equilibrium or pre equilibrium. In fact the rupture of the sample is dependent on rate of displacement V and so is the peak input force F_{inp}. At low rates of displacement (*i.e.*) $V \leq 7$ [m.s^{-1}], the sample was capable to resist the force for large displacements. Yet as the rate of displacement increased, the peak of input force F_{inp} increased and the displacement before fracture decreased. Another interesting point is that as V increases, the sample ruptured before establishing a dynamic equilibrium. Moreover, for high rates of displacements (*i.e.*) $V \geq 8$ [m.s^{-1}], the sample attains its peak, followed by a subtle increase in force and a constant plateau like response. This plateau response corresponds either to plastification or damage of the structure or both. Upon further increasing the rate of displacement (*i.e.*) $V \geq 11$ [m.s^{-1}], the sample attains its peak, followed by a subtle increase in force and a drastic decrease in force. This proves that the response of rib depends on rate of displacement V and therefore, strain rate $\dot{\varepsilon}$.

These results have led to establish the parameters such as time at fracture t_{frac}, energy at fracture W_r and displacement at fracture U_r. For rates of displacements between 8 [m.s^{-1}] and 10 [m.s^{-1}], the mean values of the aforementioned variables are $t_{frac} \approx 1.15 \times 10^{-3}$ [s], $W_r \approx 5.12$ [J] and $t_{frac} \approx 8 \times 10^{-3}$ [m]. On the other hand, for rates of displacements between 11 [m.s^{-1}] and 13 [m.s^{-1}], the mean values of the aforementioned variables are $t_{frac} \approx 0.55 \times 10^{-3}$ [s], $W_r \approx 4.89$ [J] and $t_{frac} \approx 6 \times 10^{-3}$ [m]. The fracture modes observed in experimental tests is due to a crack originating from tensile surface due to global bending of the sample, which tend to propagate towards the compression surface. The rupture is not influenced by the maximum force imposed on the sample. It rather depends on the local displacement of the rib.

A close look to the experimental data reveals that the rate of loading has a more pronounced influence on post yield behavior than on the linear elastic part. This suggests that the rib exhibits an elastic-viscoplastic behavior. Three different material models with elastic-viscoplastic capability were chosen initially. The material model MAT-105, which has damage law coupled internally is more efficient in calculation time than the other two. Unfortunately, this model was dropped as it could not consider the effects of strain rate on fracture strain.

Meanwhile, the literature suggests that the trabecular bone exhibits kinematic hardening behavior that is more pronounced than that exhibited by its counterpart cortical bone. Therefore, the material model *MAT-003 with kinematic hardening and MAT-024 with isotropic hardening was chose for trabecular and cortical bone respectively. These two material models were coupled to an incremental and stress-state dependent external damage law. Thanks to the curves provided by user, it can consider the variation of fracture strain with both stress-state and strain rate.

The parameters used for damage law permits to work in such a way that, when static yield stress of the material is reached, the damage D starts to accumulate. At the instance when $D = D_{crit}$, damage starts to couple with the flow stresses. The dynamic fracture strain ε_{fd}, influences the accumulation of D. The more ε_{fd} decreases with increase in $\dot{\varepsilon}$, the more drastic is the increase in damage accumulation and plastic strain. The ultimate damage value $D = 1$ is attained through the non-linear coupling between damage D, dynamic fracture strain $\varepsilon_{fd}(\eta, \dot{\varepsilon})$, the plastic strain ε_p and damage coupled flow stress. When this value is reached

($D = 1$), the element does not exist in the calculation, thereby initiating a crack. This continues until entire rupture of the sample.

Regarding numerical simulations at experimental scale, two different numerical samples were tested (i) the porcine rib with an assumption of only cortical bone, and (ii) the porcine rib was assumed to consist a distribution of only one cortical and one trabecular constituents with average of mechanical properties. In either case, the static tensile yield given in the material card of rib constituent is reached at point corresponding to the peak of the contact force at the input bar and sample interface. Yet this proves that the interface displacement rate or the velocity of the corresponding interface does not influence the initial linear response.

The fracture of samples is a pure local phenomenon. The fracture process is related to wave propagation and forces. From the point of impact till the peak, the response is elastic, which depends on the local distribution of the mechanical properties. From this instance till the second peak, we see a complex three dimensional wave propagation in the sample. The increase in F_{in} before the second peak is due to the arrival of reflected waves from the sample-output bar interfaces. This increase in force signifies the onset of coupling between damage and flow stresses. It is at this point, the waves reflected from anterior end-output bar interface travel towards the posterior end-output bar interface and *vice-versa*. These waves traveling in opposite directions are the ones responsible for subjecting the sample to further tension and fracture.

Part V

Conclusions and Perspectives

Chapter 7

Conclusions and perspectives

7.1 Conclusions

Rib fractures are important when it comes to chest trauma. The consequences of rib fracture shall lead to complex medical conditions and eventual death. The existing trauma evaluation scores do give critical insights to the condition of victim but they are not applicable prior to a radio-logical examination. Moreover, these so called evaluation scores are not applicable for single ribs. Thereby driving to a need for comprehension of rib fracture under dynamic loads.

Most of the blunt trauma are due to road accidents. Other driving factors are ballistic impacts, sport accidents and industrial accidents. The advances in computational capabilities have led to the development of several numerical models of the human thorax. Even though these models are being used quite often, there is a lack of geometrical representation, mechanical behavior and fracture prediction to be precise. The goal of this thesis was to carry numerical simulations on isolated porcine ribs with a feasible geometrical representation and realistic constitutive law coupled to damage law.

As this thesis deals with isolated porcine, it is always better to characterize the different bone tissues from anatomy point of view. Speaking of rib anatomy, a rib is composed of two different bone tissues at macroscopic level: cortical and trabecular bone. These two tissues are different in terms of mechanical behavior and properties. Therefore, care must be taken so that a reliable constitutive law. Literature says that the trabecular bone does not play a significant load in the load carrying capacity. Speaking of considering the rib as a structure has an inconvenience as we cannot differentiate the role played by two bone in precise manner. Moreover, there is a lack of experimental database for ribs subjected to dynamic loads at intermediate and high strain rates.

The experimental setup used in this study had led us some key insights on the dynamic behavior in three point bending. In order to differentiate the waves involved in split hopkinson pressure bar and for impedance adaptation, bars made of nylon were used. Even though the split hopkinson pressure bar setup is widely used in dynamic characterization of materials and structures, it imposes three main difficulties: (i) impedance adaptation, (ii) time and space shifting of waves and (iii) non-plane wave effects. Theses three issues of critical importance must be verified prior to experimental characterization, if not they lead to either poor characterization of sample of incoherent results. Since the ribs used during the experimental tests are not the same, there will be variations in the experimental results. Despite the difficulties, we were able to present three different kinds of force response.

The force displacement curves obtained from experimental characterization proved that the rate of displacement had a more pronounced influence on the post yield behavior of the sample. Therefore, an elastic-viscoplastic constitutive law was chosen. Out of the material models presented in this thesis, the models MAT-024 and MAT-003 were chosen as potential candidates. Based on the literature study, we were able to decide that the trabecular bone exhibits more kinematic hardening than that of cortical bone. Therefore, isotropic hardening was chosen for cortical bone (MAT-024) and kinematic hardening was chosen for trabecular bone (MAT-003). A yield stress scaling based on Cowper-Symmonds model was used to consider the effect of strain rate on the post yield behavior of both cortical and trabecular bone.

Even though, these material models are capable of simulating failure, they are not sufficient enough for considering crack propagation till entire rupture. Therefore, we have decided to couple these models with an external damage law. The chosen damage law is stress state dependent and does consider the effects of strain rate on the fracture strain. The lack of possibility to obtain uniform and reliable samples of cortical and trabecular bone from porcine rib is a major constrain to characterize their behavior in dynamic tensile loading. Therefore, we had chosen a relation put forth for cranial bone for the reduction in fracture strain with increase in strain rate. This choice of critical importance was made as the structure at macroscopic levels of cranial bone and rib resemble. A total of 5 variations of this curve were tested. It is evident that the reference curve of cranial bone is not suitable for rib as it drove to a much less rigid response of the rib with respect to corresponding experimental data. Therefore, a less decreasing curve was selected and the one that gave the best response was $\varepsilon_{fd} = 0.63 - 1.25 \times 10^{-2}\mathrm{Ln}\dot{\varepsilon}$.

Regarding the contact between bars and bone, a segment based penalty contact with a static friction coefficient of 0.1 was chosen. The segment based penalty contact is applicable here in order to adapt between the difference in material properties of bone and bar. The segment based contact is more precise for determining the contact force as it removes the initial penetration of each time step iteration before calculating the contact force of the current iteration. This is why it is expensive in terms of calculation time. As the porcine rib sample consists of elements with different mechanical properties and behavior (*i.e.* a composite structure), another contact is necessary to represent the internal cohesion of the structure, which helps the solve to understand that the sample is composed of different material properties. This in turn avoids a negative volume elements.

Concerning the numerical simulations at experimental scale, the proposed constitutive law coupled to damage law, with the help of contact is able to consider the effects of strain rate in both behavior and in fracture. First of all, the numerical force response are similar to that of experimental (both in terms of time and displacement). The mean fracture time, displacement at rupture and energy at rupture are approximately the same for cases with fracture before equilibrium. Thanks to the numerical simulations, we can deduce that the energy for rupture before equilibrium is around 3.8 [J]. Given that the rate of displacement imposed on the sample at the bar interfaces is not brutal enough, the sample might need more energy , time and displacement for rupture. Therefore, the rate of displacement or velocity of impact do play an important role.

Therefore, the current study indicates successful FE implementation of complicated constitutive and damage law with the consideration of strain rate effects and non-linear damage accumulation.

7.1.1 Limitations of the proposed methodology

Despite the consistent performance of the mode presented in this thesis, there are quite a few limitations. For example,

- It is isotropic *i.e.* it does not consider the effects along other axis even though it is three dimensional.

- It does not consider the difference of behavior in compression and tension.
- The parameters used of material properties and constitutive laws are optimized form of existing mathematical models.

In order to overcome these limitations, I suppose that the following experimental steps could give us important insights

- Tests on cortical and trabecular samples in different stress state modes and directions
- Implementation of a user defined model based on triaxiality both in constitutive law and damage law *i.e.* damage variable shall be considered as a vector rather than scalar.
- Dynamic tensile and compression tests on porcine bone coupons for the effects of $\varepsilon_f(\dot{\varepsilon})$.

7.2 Perspectives

Even though the correlation between the experimental and numerical fracture pattern is adequate, an accurate representation of a more realistic fracture behavior requires model improvements such as: bone heterogeneity, transmission of forces between the different constituents of the rib. Moreover, optimization of the damage law parameters through respective experimental data, will further improve the efficiency of the proposed FE model.

The improved porcine rib model shall be tested on a numerical human rib so that we could understand the critical parameters for human ribs under similar mechanical environments. Once this is done, it could be implements to numerical thorax models to give insights on injury severity, thereby contributing to betterment of passenger safety or to a link between prediction of critical condition and treatment to be provided at trauma centers.

Appendices

Appendix A

Solid Element Formulation

Preliminary

Let us consider a body denoted by κ in a Cartesian coordinate system initially at a point represented by X_α, $(\alpha = 1,2,3)$ which displaces to a point x_i, $(i = 1,2,3)$ that is denoted by $\varkappa$ in the same coordinate system with time t as in Fig. A.1.

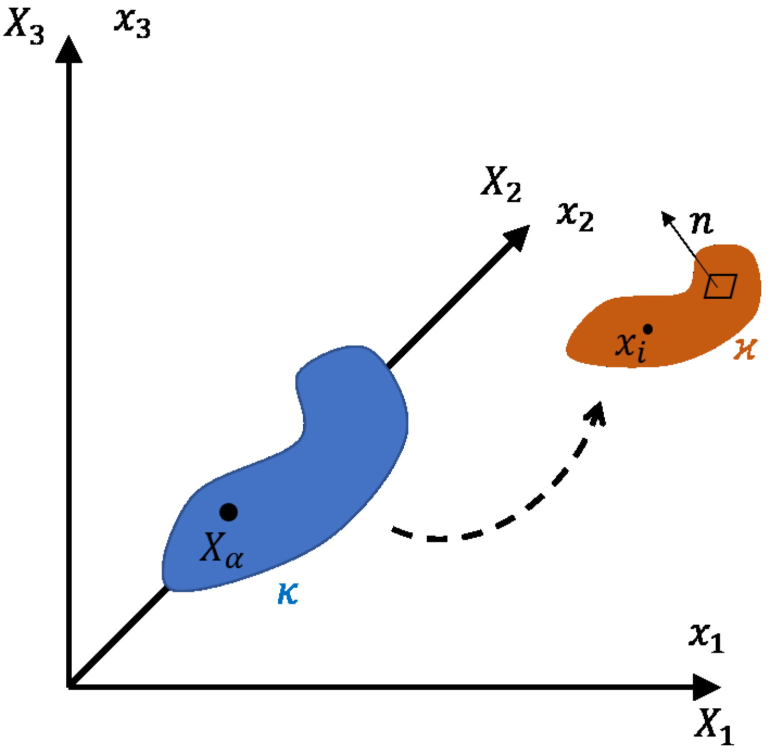

Figure A.1 – Body in a Cartesian system

The time dependent displacement of this body using the Lagrangian approach can be written in terms of its initial coordinates as follows:

$$x_i = x_i(\mathrm{X}_\alpha, t) \tag{A.1}$$

Thus, the initial condition at time $t = 0$ can be expressed as

$$x_i(\mathrm{X}_\alpha, 0) = \mathrm{X}_\alpha \tag{A.2}$$

$$\dot{x}_i(\mathrm{X}_\alpha, 0) = v_i(\mathrm{X}_\alpha) \tag{A.3}$$

where, v_i is the initial velocity.

Similar to the initial conditions, the boundary condition on the bodies, such as traction boundary condition of the system, displacement boundary condition on the boundary κ and the contact discontinuity boundary condition on the boundary $\varkappa$ can be expressed as in Eq. A.4, Eq. A.5 and Eq. A.6 respectively.

$$\sigma_{ij}\mathrm{n}_{ij} = t_i(t) \tag{A.4}$$

$$x_i(\mathrm{X}_\alpha, t) = D_i(t) \tag{A.5}$$

$$({\sigma_{ij}}^+ - {\sigma_{ij}}^-)\mathrm{n}_{ij} = 0 \tag{A.6}$$

here, σ_{ij} is the Cauchy's stress tensor, $\mathrm{n_{ij}}$ is unit normal of an element on the boundary of body configuration $\varkappa$ and D_i is the displacement matrix of the body $\varkappa$. The notations $^+$ and $^-$ represent the quantities exterior and interior to the boundary of $\varkappa$.

Having established the initial and boundary conditions, the governing equations for the system in Fig. A.1 are written as follows:

Conservation of mass:

$$\rho V \ = \rho_0 \tag{A.7}$$

where, ρ_0 is the reference or initial density and V is the relative volume and is expressed in terms of determinant of deformation gradient matrix F_{ij}.

Conservation of momentum:

$$\sigma_{ij,\ j} \ + \ \rho f_i \ = \ \rho \ddot{x}_i \tag{A.8}$$

where $\sigma_{ij,\ j}$ represents the co-variant differential of stress tensor and $\ddot{x}_i$ represents the acceleration. The solution of momentum equation Eq. A.8 in its weak form must satisfy the boundary conditions in Eq. A.4, Eq. A.5 of κ and Eq. A.6 on $\varkappa$ respectively.

Conservation of energy:

$$\dot{E} \ = \ V S_{ij} \dot{\varepsilon}_{ij} \ - \ (p \ + \ q) \dot{V} \tag{A.9}$$

the variables s_{ij} and p represent the deviatoric stress tensor and pressure respectively and are expressed as follows

$$S_{ij} \ = \ \sigma_{ij} \ + \ (p \ + \ q)\delta_{ij} \tag{A.10}$$

$$p \ = \ -\frac{1}{3}\sigma_{ij}\delta_{ij} \ - \ q \tag{A.11}$$

here, δ_{ij} represents the Kronecker delta and q represents the bulk viscosity.

The displacement δx_i, that satisfies all the boundary conditions on $\varkappa$ can be written using the divergence theorem as:

$$\int_V (\rho\ddot{x}_i \;-\; \sigma_{ij,j} \;-\; \rho f)\delta x_i dV \;\int_{\partial\kappa} (\sigma_{ij}\mathrm{n}_j \;-\; t_i)\delta x_i ds \;+\; \int_{\partial\varkappa} ({\sigma_{ij}}^{+} \;-\; {\sigma_{ij}}^{-})\mathrm{n}_j \delta x_i ds \;=\; 0 \tag{A.12}$$

as we know that

$$(\sigma_{ij}\delta x_i)_{,j} \;-\; \sigma_{ij,j}\delta x_i \;=\; \sigma_{ij}\delta x_{i,j} \tag{A.13}$$

The Eq. A.12 can be rewritten as

$$\int_V (\sigma_{ij}\delta x_i)_{,j})dV \;=\; \int_{\partial\kappa} \sigma_{ij}\mathrm{n}_j \delta x_i ds \;+\; \int_{\partial\varkappa} ({\sigma_{ij}}^{+} \;-\; {\sigma_{ij}}^{-})\mathrm{n}_j \delta x_i ds \tag{A.14}$$

This leads to the statement of virtual work in its weak form as in Eq. A.15

Principle of virtual work Using the principle of virtual work, the change in external work done in a system can be expressed in an integral form as follows:

$$\delta\pi \;= \int_V \rho\ddot{x}_i \delta x_i dV \;+\; \int_V \sigma_{ij}\delta x_{i,\,j} dV \;-\; \int_V \rho f_i \delta x_i dV \;-\; \int_\kappa t_i \delta x_i dS \;=\; 0 \tag{A.15}$$

Having established the principle of virtual work for our system, let us consider that the system is discretized into $\boldsymbol{n}$ elements with k nodal points. Then, the relation representing the displacement of these nodal point is written as

$$x_i(\mathrm{X}_\alpha, t) \;= x_i(\mathrm{X}_\alpha(\xi, \eta, \zeta), t) \;=\; \sum_{j=1}^{k} \phi_j(\xi, \eta, \zeta){x_i}^j(t) \tag{A.16}$$

here, ϕ_j represents the shape or interpolation functions in natural coordinate system (ξ, η, ζ) and ${x_i}^j$ represents the nodal coordinate of j^{th} node in i^{th} direction.

Thus, the virtual work over n elements can be written as follows

$$\delta\pi \;=\; \sum_{m=1}^{n} \delta\pi_m \;=\; 0 \tag{A.17}$$

here, $\delta\pi_m$ is the contribution of each element and is expressed as

$$\delta\pi_m \;= \int_{v_m} \rho \ddot{x}_i \delta x_i d\boldsymbol{v}_m + \int_{v_m} \sigma_{ij} \delta x_{i,\,j} d\boldsymbol{v}_m - \int_{v_m} \rho f_i \delta x_i d\boldsymbol{v}_m - \int_{\partial\kappa \cap \partial v_m} t_i \delta x_i ds \;=\; 0 \tag{A.18}$$

Similar to virtual work, the dependent variables can also be written over the mesh as follows

$$\sum_{m=1}^{n} \left\{ \int_{v_m} \rho \mathbf{N}_m^{\mathbf{T}} \mathbf{N}_m \mathbf{a} dv_m \;+\; \int_{v_m} \mathbf{B}_m^{\mathbf{T}} \sigma dv_m \;-\; \int_{v_m} \rho \mathbf{N}_m^{\mathbf{T}} \mathbf{b} dv_m \;-\; \int_{\partial\kappa} \mathbf{N}_m^{\mathbf{T}} \mathbf{t} ds \right\} \;=\; 0 \tag{A.19}$$

where, $\mathbf{N}$ is the interpolation matrix, $\mathbf{B}$ is the strain displacement matrix, σ is the stress tensor, $\mathbf{a}$ is the acceleration vector, $\mathbf{b}$ is the body force vector and $\mathbf{t}$ is the applied traction load.

8 node hexahedral element

Let us consider an eight node solid hexahedral element as in Fig. A.2. The Eq. A.16 can be written as

$$x_i(\mathrm{X}_\alpha, t) \;= x_i(\mathrm{X}_\alpha(\xi, \eta, \zeta), t) \;=\; \sum_{j=1}^{8} \phi_j(\xi, \eta, \zeta) x_i{}^j(t) \tag{A.20}$$

and the shape function of corresponding element would be

$$\phi_j \;=\; \frac{1}{8} (1 \;+\; \xi\xi_j) (1 \;+\; \eta\eta_j) (1 \;+\; \zeta\zeta_j) \tag{A.21}$$

The interpolation matrix $\mathbf{N}$ is of 3×24 (Eq. A.22) whilst the strain displacement matrix $\mathbf{B}$ is of 6×24 (Eq. A.23).

$$\mathbf{N}(\xi,\eta,\zeta) = \begin{bmatrix} \phi_1 & 0 & 0 & \phi_2 & 0 & \cdots & 0 & 0 \\ 0 & \phi_1 & 0 & 0 & \phi_2 & \cdots & \phi_8 & 0 \\ 0 & 0 & \phi_1 & 0 & 0 & \cdots & 0 & \phi_8 \end{bmatrix} \tag{A.22}$$

$$\mathbf{B} = \begin{bmatrix} \frac{\partial}{\partial x} & 0 & 0 \\ 0 & \frac{\partial}{\partial y} & 0 \\ 0 & 0 & \frac{\partial}{\partial z} \\ \frac{\partial}{\partial y} & \frac{\partial}{\partial x} & 0 \\ 0 & \frac{\partial}{\partial z} & \frac{\partial}{\partial y} \\ \frac{\partial}{\partial z} & 0 & \frac{\partial}{\partial x} \end{bmatrix} \mathbf{N} \tag{A.23}$$

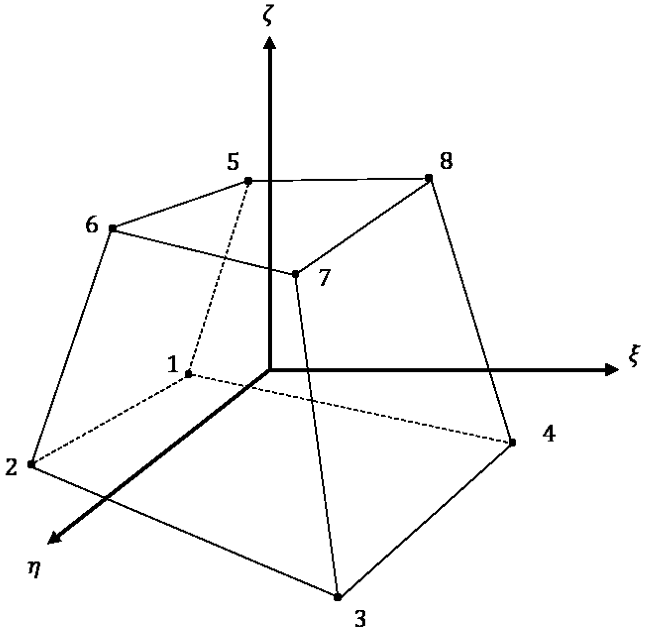

Figure A.2 – 8 node hexahedral element

The diagonal mass matrix for the k^{th} term of an eight node solid element is written as

$$m_{kk} = \int_V \rho\phi_k \sum_{i=1}^{8} \phi_i dV = \int_V \rho\phi_k dV \tag{A.24}$$

since the $\sum_{i=1}^{8} \phi_i$ leads to unity.

Thus, all the terms of strain displacement matrix can be calculated by the Jacobian **J**

Volume integration

The volume integration in LS-Dyna is executed through Gaussian quadrature method. For this case, let us assume a function 'g' defined over a volume with $\mathscr{N}$ number of integral points, then the integral of g over the volume is:

$$\int_V \mathsf{g} dV = \int_{-1}^{1}\int_{-1}^{1}\int_{-1}^{1} \mathsf{g}|\mathbf{J}| d\xi d\eta d\zeta \tag{A.25}$$

The integrals in Eq. A.26, can be approximated as summation over integral points in terms of weighting functions $w_j,\ w_k,\ w_l$ as follows

$$\sum_{j=1}^{\mathscr{N}}\sum_{k=1}^{\mathscr{N}}\sum_{l=1}^{\mathscr{N}} \mathsf{g}_{jkl}|\mathbf{J_{jkl}}| w_j w_k w_l \tag{A.26}$$

These fully integral elements have the following disadvantages:

- The computation effort required to compute the matrices is huge and is expensive in time. For example,
  (a) time required for computing the strain matrix is around 25 times more than that required for a one point integration.
  (b) the number of multiplies for strain and nodal force matrices is 16 times more than that for one point integration.
  (c) even the constitutive evaluation needed for a fully integrated element is substantially more.
- in addition to cost, the other common inconvenience with fully integrated elements is element locking whist used in plasticity problems or problems involving failure.

These disadvantages of fully integrated elements can be overcome using one point integration solid elements. Moreover, it is not new to use one point integration elements with an explicit solver for dynamic applications or applications involving large deformations. Yet the use of under integrated elements requires use of hourglass properties in order to avoid the Hourglass modes.

Hourglass

The use of under integrated elements such as one point integration, leads to the presence of zero energy modes commonly known as "*Hourglassing Modes*". These modes are oscillatory and tend to have periods less than that of the structure's response. On the other hand, the hourglass modes with time periods similar to structural response are known to have negligible effects on the response. Thus, the hourglassing modes with less time periods have to be omitted. This could be either achieved by adding additional stiffness or additional viscosity, yet having no effects on the global stiffness in the mean time. LS Dyna offers 5 different formulation of Hourglass for solid elements, as enumerated below

Type 1 Standard Viscous form

Type 2 Flanagan-Belytschko integration in viscous from

Type 3 Flanagan-Belytschko with exact volume integration in viscous from

Type 4 Flanagan-Belytschko integration in stiffness from

Type 5 Flanagan-Belytschko with exact volume integration in stiffness from

Type I

In order to understand the difference between these formulations and why hourglassing modes exist, let us consider a 8 node hexahedral element with only one Gaussian integral point. This element can be related to its spatial coordinates in terms of nodal coordinates using the isoparametric shape functions as follows (Flanagan and

Belytschko, 1981)

$$x_i \;=\; x_{ik}\phi_k(\xi, \eta, \zeta) \tag{A.27}$$

Similarly, the displacement field and velocity fields can be expressed for a hexahedral element with one point integration can be expressed as follows

$$u_i \;=\; u_{ik}\phi_k \tag{A.28}$$

$$\dot{u}_i \;=\; \dot{u}_{ik}\phi_k \tag{A.29}$$

The velocity gradient with respect to the direction and nodal coordinate can be expressed as

$$\dot{u}_{i,j} \;=\; \dot{u}_{ik}\phi_{k,j} \tag{A.30}$$

$$\mathscr{D}_{ij} \;=\; (\dot{u}_{i,j} \;+\; \dot{u}_{j,i}) \tag{A.31}$$

$$\mathscr{W}_{ij} \;=\; (\dot{u}_{i,j} \;-\; \dot{u}_{j,i}) \tag{A.32}$$

where $\mathscr{D}_{ij}$ is the velocity strain tensor that is symmetric and $\mathscr{W}_{ij}$ is the instantaneous rotation tensor that is anti-symmetric. On the other hand, the subscript (i, j), represents the differentiation of the quantity with respect to nodal coordinate.

The principle of virtual work can be expressed in terms of nodal force as :

$$\dot{u}_{ik}f_{ik} \;=\; \int_V \sigma_{ij}\mathscr{D}_{ij}dV \tag{A.33}$$

In fact the one point Gaussian integral neglects the nonlinear terms, thereby considering a uniform stress-strain state through out the element. Thereby, leading to the velocity gradient in the following form

$$\dot{u}_{ik}f_{ik} \;=\; V\bar{\sigma}_{ij}\dot{\bar{u}}_{ij} \tag{A.34}$$

In other words, the one point integration is based on the assumption that the mean stress depend only on mean strain but not the nonlinear terms. The mean kinematic terms $\dot{\bar{u}}_{ij}$ in Eq. A.34 are expressed in terms of the displacement field over the element as

$$\dot{\bar{u}}_{ij} = \frac{1}{V}\int_V \dot{u}_{i,j} dV \tag{A.35}$$

This leads to the definition of **B** matrix as follows:

$$\mathbf{B}_{ik} = \int_V \phi_{ik} dV \tag{A.36}$$

Thorough mathematical manipulations, Flanagan and Belytschko (1981) had concluded that in a one point integral framework, only the base vectors lead to stresses or nodal forces. These base vectors are given in Tab. A.1.

Node	$\Pi = 1$	$\Pi = 2$	$\Pi = 3$	$\Pi = 4$
$\Gamma_{\Pi 1}$	1	1	1	1
$\Gamma_{\Pi 2}$	1	-1	-1	-1
$\Gamma_{\Pi 3}$	-1	-1	1	1
$\Gamma_{\Pi 4}$	-1	1	-1	-1
$\Gamma_{\Pi 5}$	-1	-1	1	-1
$\Gamma_{\Pi 6}$	-1	1	-1	1
$\Gamma_{\Pi 7}$	1	1	1	-1
$\Gamma_{\Pi 8}$	1	-1	-1	1

Table A.1 – Hourglass base vectors and modes for an eight node hexahedral element (Flanagan and Belytschko, 1981)

For a solid element with one point integration, when the opposite nodes have identical velocities, the strain rate $\dot{\varepsilon}_{ij} = 0$ due to the anti-symmetric property of strain matrix. The shape functions of a hexahedral solid element with one point integration in terms of hourglassing modes can be expressed as

$$\sum_{k=1}^{8} \frac{\partial \phi_k}{\partial x_i}\Gamma_{\Pi k} \;=\; 0; i = 1, 2, 3;\ \Pi = 1, 2, 3, 4 \tag{A.37}$$

where i denotes the directions and Π denotes the hourglassing modes. When the nodal velocities have no hourglass modes, the product of base vectors is zero. Therefore, the hourglass component can be written as

$$h_{i\Pi} \;=\; \sum_{k=1}^{8} \dot{x}_i^k \Gamma_{\Pi k} \;=\; 0 \tag{A.38}$$

Hence, the hourglass resisting forces $f_{i\Pi}^k$ can be expressed as

$$f_{i\Pi}^k \;=\; \mathrm{Q}_{\mathrm{HG}} \rho v_e^{2/3} \frac{c}{4} h_{i\Pi} \Gamma_{\Pi k} \tag{A.39}$$

here, v_e represents the volume of the element, c represents the celerity of waves in the solid and Q_{HG} represents the Hourglass coefficient either for stiffness or viscosity formulation defined by the user. In general, the values given for the hourglass coefficient are in the range of $0.05 \leq \mathrm{Q}_{\mathrm{HG}} \leq 0.15$. The equations A.37, A.38 and A.39 form the basis for the Type I hourglass formulation in LS-Dyna.

It is evident that the base vectors of Type I are not orthogonal to the linear velocity fields. Therefore, LS Dyna offers another formulation, in which the base vectors $\Gamma_{\Pi k}$ are orthogonal to the linear vector filed by adapting an other manipulation proposed by Flanagan and Belytschko (1981), which is referred to as Type II.

Types II and III

The hourglass type II is based on the hypothesis of isolating the linear modes from the total velocity or displacement field gives rise to hourglass fields. This is mathematically expressed as

$$\dot{x}_i^{k^{\text{HG}}} \;=\; \dot{x}_i^k \;-\; \dot{x}_i^{k^{\text{LIN}}} \tag{A.40}$$

where, the linear velocity field is expressed as

$$\dot{x}_i^{k^{\text{LIN}}} \;=\; \frac{1}{8}\sum_{k=1}^{8} \dot{x}_i^k \;+ \dot{\bar{x}}_{i,j}(x_j^k \;-\; \frac{1}{8}\sum_{k=1}^{8} x_i^k) \tag{A.41}$$

This adds to the definition of another vector in terms of base vectors, that is known as hourglass shape vectors $\gamma_{\Pi k}$ as follows

$$\gamma_{\Pi k} \;=\; \Gamma_{\Pi k} \;-\; \phi_{k,i}\sum_{k=1}^{8} x_i^k \Gamma_{\Pi k} \tag{A.42}$$

therefore, the analogue for the hourglass components of Eq. A.38 and hourglass resisting forces are rewritten as

$$g_{i\Pi} \;=\; \sum_{k=1}^{8} \dot{x}_i^k \gamma_{\Pi k} \;=\; 0 \tag{A.43}$$

$$f_{i\Pi}^k \;=\; \text{Q}_{\text{HG}} \rho v_e^{2/3} \frac{c}{4} g_{i\Pi} \gamma_{\Pi k} \tag{A.44}$$

The equations A.42, A.43 and A.44 are the basis for both types II and III. The only difference between type II and type III is that the shape function derivatives are evaluated at the centroid of the element for type III instead of calculating them at origin of nodal coordinate system. By doing so the anti-symmetry property of strain displacement tensor vanishes, thereby the tyep III requires few more number of evaluations for each time step. Yet the advantage of a type III hourglass formulation is that it produces an exact volume integration.

Types IV and V

The types II and III are executed by adding certain viscosity to the elements. This unfortunately absorb more energies thereby, leading to discrepancies in the total energy involved in the model. This can be avoided by replacing the additional viscosity with springs of certain stiffness. Therefore, we have the hourglass types IV and V that are mathematically identical to types II and III represented by equations A.42, A.43 and A.44.

In general, a hourglass with stiffness form is used in problems involving large deformations (automotive crash environments for example) where as, a viscous from hourglass is chosen in problems involving deformations at high velocities. Thus, the a hourglass of stiffness from was chosen for both bone and bar materials in this thesis.

Appendix B

Contact Algorithms

To understand the function of contact algorithms, let us consider two bodies $\mathscr{B}^1$ and $\mathscr{B}^2$ with boundaries $\delta\mathscr{B}^1$ and $\delta\mathscr{B}^2$ respectively in a region $\mathbb{R}^3$ as in Fig. B.1. Let us assume that the bodies are separated at a certain distance initially (at $t_0 = 0$) and are in motion. Assuming that impact occurs at $t = t_i$, the bodies $\mathscr{b}^1$ and $\mathscr{b}^2$ establish a contact $(\mathscr{C})$ certain points on their respective boundaries $\delta\mathscr{b}^1$ and $\delta\mathscr{b}^2$

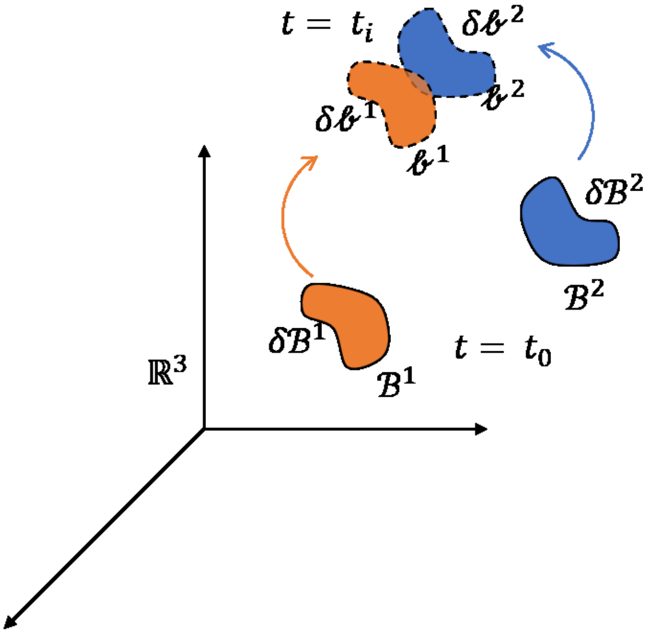

Figure B.1 – Two bodies in $\mathbb{R}^3$

(Hughes et al., 1976)

According to Hughes et al. (1976), "Contact $(\mathscr{C})$ is either a *boundary-value problem* or an *initial-boundary-value-problem* in which two bodies $\mathscr{B}^1$ and $\mathscr{B}^2$ interact according to the principles of mechanics of continuous media".

Thus, we can write the intersection of boundaries at t_0 and their intersection at t_i as in Eq. B.1 and Eq. B.2 respectively.

$$\delta\mathscr{B}^1 \cap \delta\mathscr{B}^2 = \emptyset \tag{B.1}$$

$$\delta\mathscr{b}^1 \cap \delta\mathscr{b}^1 \neq \emptyset \tag{B.2}$$

$$\tag{B.3}$$

Therefore, the expression of $\mathscr{C}$ at t_i becomes

$$\mathscr{C} = \delta\mathscr{b}^1 \cap \delta\mathscr{b}^2 \tag{B.4}$$

A general rule of thumb for slave and master surfaces involved in contact is that a coarse mesh surface is always declared as master (say the $\mathscr{B}^1$) and the other as salve surface ($\mathscr{B}^2$). Therefore, all the nodes on the discretized boundary $\delta\mathscr{b}^1$ are treated as master nodes and the others as slave nodes (on the boundary $\delta\mathscr{b}^2$). This is the basis of contact algorithms available on LS-Dyna.

Contact between sliding or impacting interfaces can be implemented by three different methods in LS-Dyna :

1. Kinematic Constraint Method (KCM): The constraints are imposed on the global equations of the system through transformation of nodal displacement of slave surface on the contact interface. This transformation, eliminates the normal degrees of freedom on the slave nodes. In order to retain the efficiency of the explicit time integration, the mass is lumped in such a way that only nodes of master surface are coupled. The disadvantage of this method is lack of accuracy when the master surface has a mesh finer than slave surface. This leads to unnecessary penetration of master nodes into the slave surface (represented by X in Fig. B.2).

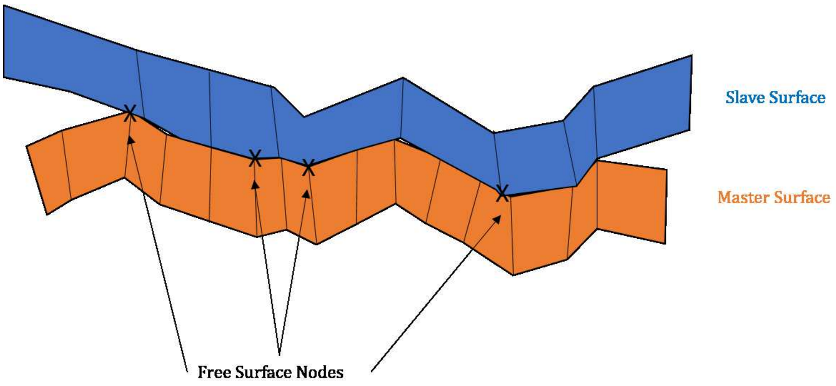

Figure B.2 – Surface treatment in kinematic constraint method

2. Penalty Constraint Method (PCM): In contrast to KCM, this method adds springs of certain stiffness between all penetrating nodes. In fact when applied to under integrated elements, the PCM does not excite mesh houglassing thereby avoiding unnecessary oscillation. As opposed to KCM, the momentum is exactly conserved in this method therefore, there is no need of external condition for its conservation. Currently, three different penalty contact methods are available in LS-Dyna:
    (a) Standard Penalty Formulation
    (b) Soft Constraint Penalty Formulations and
    (c) Segment based Penalty Formulation.
3. Distributed Constraint Method (DCM): This method has a peculiar way of function. Firstly, the one half mass of each slave element in contact is distributed over the covered master elements in contact. The pressure distribution to the master surface area is determined by the internal stress in each element. Once the mass and pressure are distributed, the acceleration is updated. Lastly, constraints are applied on the slave node accelerations and velocities in order to insure the movement of slave surface along the master surface. The major drawback is that this methodology does not allow for penetration of elements between slave and master surfaces.

This comparison of different contact algorithms have led us to the conclusion that the Penalty Constraint Method (PCM), has an upper hand over all three and is chosen as potential candidate for the contact analysis in this thesis.

Slave Search

The most common and classic slave search is by searching for nodes in the proximity of master nodes. For this, let us consider a salve node n_s that is sliding on a master surface as in Fig. B.3a. Lets assume that the search algorithm had determined the nearest master node m_s. If m_s and n_s coincide, the search is terminated and a line perpendicular to m_s is drawn from n_s.

In case these two nodes do not coincide, then n_s is assumed to be in any of the segments (for example say S_1). This can be verified by using the following equations

$$(\mathbf{c}_i \times \mathbf{s}) \cdot (\mathbf{c}_i \times \mathbf{c}_{i+1}) > 0 \tag{B.5}$$

$$(\mathbf{c}_i \times \mathbf{s}) \cdot (\mathbf{s} \times \mathbf{c}_{i+1}) > 0 \tag{B.6}$$

here, $\mathbf{c}_i$ and $\mathbf{c}_{i+1}$ are vectors along the adjacent edges of S_1 pointing outward from m_s. $\mathbf{s}$ is the projection of vector $\mathbf{g}$ on the segment S_1 (see Fig. B.3b), that is expressed as

$$\mathbf{s} = \mathbf{g} - (\mathbf{g} \cdot \mathbf{m})\mathbf{m}; \tag{B.7}$$

$$\mathbf{m} = \frac{\mathbf{c}_i \times \mathbf{c}_{i+1}}{|\mathbf{c}_i \times \mathbf{c}_{i+1}|} \text{ for } S_1 \tag{B.8}$$

Logically speaking, the contact surfaces are not always uniformly meshed. In case the contact surfaces contain badly shaped elements, it is not easy to locate the slave nodes as there is a probability that the salve node n_s is not located in the identified master segment (as in Fig. B.3c). The identification of this point on the segment near to m_s becomes nontrivial. This problem is confronted in LS-Dyna by allocating a parametric function ($\mathbf{r}$) of the following form to the segment S_1 in terms of natural coordinate system.

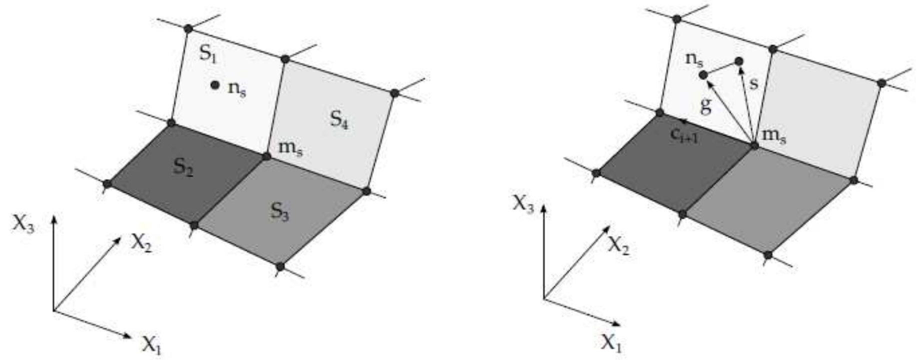

(a) Initial Search (b) Projection of $\mathbf{g}$

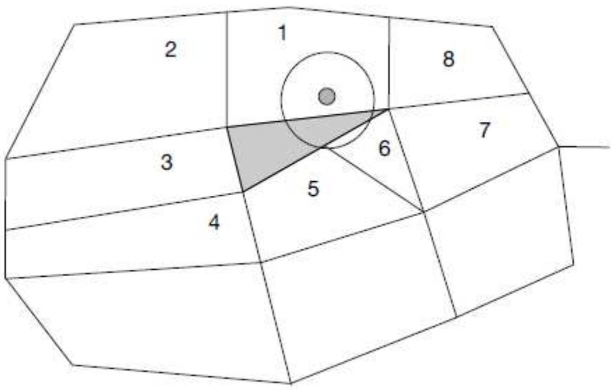

(c) Slave search for badly shaped elements

Figure B.3 – Slave and Master nodes for slave search

(John.O, Halloquist, 2006)

In fact $\mathbf{r}$ is differentiable atleast once in the iterative process satisfying the following condition

$$\frac{\partial \mathbf{r}}{\partial \xi} \times \frac{\partial \mathbf{r}}{\partial \eta} \neq 0 \tag{B.9}$$

This proves that $\mathbf{r}$ of a segment has a unique normal, whose direction depends on S_1 (see Fig. B.4). Solving all these equations gives the location of n_s. For more information on slave search, see §26.6 of John.O, Halloquist (2006)

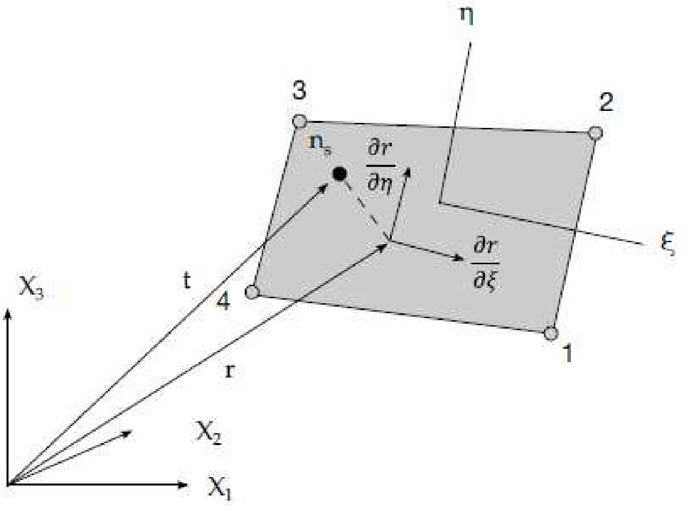

Figure B.4 – Unique normal of a master segment S_1

Penalty Formulations

Standard Penalty Formulation

This is most commonly used penalty contact formulation. On implementation, each and every slave node n_s in contact is searched for penetration through master surfaces. Once identified, two cases can show up

1. In the case of no penetration of n_s, nothing is done and the calculation is advanced to next iteration

2. If penetration occurs, an interface force between n_s and contact point is applied which is proportional to the amount of penetration as follows.

    - the penetration is identified mathematically as

    $$\mathbb{P} \;=\; \mathbf{n}_i \times [\mathbf{t} \;-\; \mathbf{r}(\xi_c, \eta_c)] \;<\; 0 \tag{B.10}$$

    here, $\mathbf{n}_i$ is normal to the master segment at contact point.

    - an interface force $\mathbf{f}_s$ is added to n_s and a force $\mathbf{f}_m^i$ to each node of the corresponding master segment S_i. These forces are expressed in equations below

$$\mathbf{f}_s = -\mathbb{P}k_i\mathbf{n}_i \text{ if } \mathbb{P} < 0 \tag{B.11}$$

$$\mathbf{f}_m^i = \phi_i((\xi_c, \eta_c))\mathbf{f}_s \text{ if } \mathbb{P} < 0 \tag{B.12}$$

here, k_i is the stiffness factor for master segment and is expressed as

$$k_i = \frac{f_{si}K_iA_i^2}{V_i} \tag{B.13}$$

where, f_{si} is the stiffness factor for the interface (0.01 by default). K_i, A_i and V_i are the bulk modulus, area and volume of the corresponding master segment respectively.

Whist used for contact between material with different bulk modulus, the contact stiffness f_{si} can be under estimated thereby making a weak contact. Therefore, the standard penalty formulation might require manual adjustments in order to avoid instabilities.

Soft Constraint Penalty Formulation

The soft based penalty formulation was developed as a counter action to standard penalty formulation. This formulation is well suited for application to materials with huge difference in bulk modulus.

An additional stiffness based on Courant's stability criterion of the local masses (master and slave) connected by a spring is used. This additional stiffness is expressed as

$$k_{cs}(t) = 0.5 \cdot \mathrm{SOFCL} \cdot m\left(\frac{1}{\Delta t_c(t)}\right)^2 \tag{B.14}$$

here, SOFCL is the scale factor used to constrain forces in Soft based contact, m is a function of masses of slave and master nodes and Δt_c is time step for contact, that is updated at every iteration to avoid unstable contact behavior. The final contact stiffness used for contact is expressed as follows

$$k_{\text{soft}} \;=\; max\left(k_{cs}, k_i\right) \tag{B.15}$$

NOTE the Δt_c is always set to the current solution time step value and is updated every time step increment.

Segment based Penalty Formulation

The contact stiffness in this approach is calculated similar to that of Soft constraint. The only difference is that the mass function m is the mass of master and slave segments as opposed to mass of master and slave nodes.

$$k_{cs}(t) \;=\; 0.5 \cdot \text{SLSFAC} \begin{pmatrix} \text{SFS} \\ \text{or} \\ \text{SMS} \end{pmatrix} \cdot \frac{m_1 m_2}{m_1 + m_2}\left(\frac{1}{\Delta t_c(t)}\right)^2 \tag{B.16}$$

where,m_1 and m_2 are masses of master and slave segments in contact. In case of solid elements, the segment masses are one half of element mass. SFS and SMS are penalty scale factors for slave and master segments respectively, SLSFAC is the scale factor for sliding interfaces in contact.

Another difference is that Δt_c is updated only when the time step of solution is greater than $5\%\Delta t_c$.

Bibliography

Abdel-Wahab, A. A. and V. V. Silberschmidt (2011). Numerical modelling of impact fracture of cortical bone tissue using X-FEM. *Journal of Theoretical and Applied Mechanics Vol. 49 nr 3*, 599–619.

Amine, M. (2017). Modélisation des côtes humaines en flexion antériopostérieur. Master's thesis, Chalmers University and Institut scientifiqe et polytecnique de Galilée.

Andriacchi, T., A. Schultz, T. Belytschko, and J. Galante (1974, November). A model for studies of mechanical interactions between the human spine and rib cage. *Journal of Biomechanics 7*(6), 497–507.

Arnoux, P., S. Jooneknidt, L. Tholon, and K. Kayvantash (2003, January). Radioss finite element model of the Thor dummy. *International Journal of Crashworthiness 8*(6), 529–541.

Arunan, Y. and B. Roodenburg (2017). Chest trauma. *Anaesthesia & Intensive Care Medicine 18*(8), 390–394.

Aubert, R. (2012). Étude du comportement des côtes sous sollicitations dynamiques. Master's thesis, École Nationale Supérieur d'Ingénieurs de Bourges - Université de Poitiers, Bourges.

Aubert, R., J. Pavier, N. Eches, A. Langlet, and P. Bailly (2012, September). On the use of Hopkinson bar-bending apparatus to study soft impact on porcine ribs. *Computer Methods in Biomechanics and Biomedical Engineering 15*(sup1), 311–312.

Aukema, T. S., L. F. Beenen, F. Hietbrink, and L. P. Leenen (2011, August). Validation of the Thorax Trauma Severity Score for mortality and its value for the development of acute respiratory distress syndrome. *Open Access Emergency Medicine : OAEM 3*, 49–53.

Bacon, C. (1998, December). An experimental method for considering dispersion and attenuation in a viscoelastic Hopkinson bar. *Experimental Mechanics 38*(4), 242–249.

Baker, S. P., B. O'Neill, W. Haddon, and W. B. Long (1974, March). The injury severity score: a method for describing patients with multiple injuries and evaluating emergency care. *The Journal of Trauma 14*(3), 187–196.

Barlow, P. (2012, April). A practical review of the Glasgow Coma Scale and Score. *The Surgeon 10*(2), 114–119.

Bazant, Z. P. (1978, October). Spurious reflection of elastic waves in nonuniform finite element grids. *Computer Methods in Applied Mechanics and Engineering 16*(1), 91–100.

Behrens, J. C., P. S. Walker, and H. Shoji (1974, May). Variations in strength and structure of cancellous bone at the knee. *Journal of Biomechanics 7*(3), 201–207.

Bensusan.J.S and Verdin.D.J (1983). Tensile, Compressive and torsional testing of Cancellous bone. *Transaction of the annual meeting of the Orthopaedic Research Society 8*.

Bessho, M., I. Ohnishi, J. Matsuyama, T. Matsumoto, K. Imai, and K. Nakamura (2007). Prediction of strength and strain of the proximal femur by a CT-based finite element method. *Journal of Biomechanics 40*(8), 1745–1753.

Blau, S., D. Ranson, and C. O'Donnell (2018, January). 4 - High-Energy, Blunt-Force Trauma: Motor Vehicle (MV) Incidents. In S. Blau, D. Ranson, and C. O'Donnell (Eds.), *An Atlas of Skeletal Trauma in Medico-Legal Contexts*, pp. 275–394. Academic Press.

Brown.T.D and Ferguson.A.B (1980). Mechanical property distribution in the cancellous bone of Human Proxima Femur. *Acta Orthopaedica Scandinavica 51*, 429–437.

Bull, J. P. (1975, December). The injury severity score of road traffic casualties in relation to mortality, time of death, hospital treatment time and disability. *Accident Analysis & Prevention 7*(4), 249–255.

Burnside, N. and K. McManus (2014, May). Blunt thoracic trauma. *Surgery (Oxford) 32*(5), 254–260.

Carter, D. R. and W. C. Hayes (1977, October). The compressive behavior of bone as a two-phase porous structure. *The Journal of Bone and Joint Surgery. American Volume 59*(7), 954–962.

Carter, D. R., G. H. Schwab, and D. M. Spengler (1980, January). Tensile Fracture of Cancellous Bone. *Acta Orthopaedica Scandinavica 51*(1-6), 733–741.

Carter.D.R and Hayes.W.C (1977). The compressive behavior of bone as a two-phase porous material. *Journal of Bone Joint Surgery 59*(A), 954–962.

Cavanaugh, J. M., Y. Zhu, Y. Huang, and A. I. King (1993, November). Injury and Response of the Thorax in Side Impact Cadaveric Tests. SAE Technical Paper 933127, SAE International, Warrendale, PA.

Champion, H. R., W. J. Sacco, A. J. Carnazzo, W. Copes, and W. J. Fouty (1981, September). Trauma score. *Critical Care Medicine 9*(9), 672–676.

Champion, H. R., W. J. Sacco, W. S. Copes, D. S. Gann, T. A. Gennarelli, and M. E. Flanagan (1989, May). A revision of the Trauma Score. *The Journal of Trauma 29*(5), 623–629.

Charpail, E. (2006, January). *Analyse du comportement mécanique des côtes humaines en dynamique.* thesis, Paris, ENSAM.

Chaurasia, B. (2006). *Human Anatomy: Regional & Applied : Upper Limb & Thorax* (4 ed.), Volume 1 of *B D Chaurasia's Human Anatomy: Regional and Applied Dissection Ans Clinical.* CBS Publishers & Distributors.

Chawda, M. N., F. Hildebrand, H. C. Pape, and P. V. Giannoudis (2004, April). Predicting outcome after multiple trauma: which scoring system? *Injury 35*(4), 347–358.

Chen, W., B. Zhang, and M. J. Forrestal (1999, June). A split Hopkinson bar technique for low-impedance materials. *Experimental Mechanics 39*(2), 81–85.

Cowin, S. C. (1985, July). The relationship between the elasticity tensor and the fabric tensor. *Mechanics of Materials 4*(2), 137–147.

Cowin, S. C. (1986, September). Fabric dependence of an anisotropic strength criterion. *Mechanics of Materials 5*(3), 251–260.

Crowninshield, R. D. and M. H. Pope (1974, June). The response of compact bone in tension at various strain rates. *Annals of Biomedical Engineering 2*(2), 217–225.

Currey, J. D. (1975, January). The effects of strain rate, reconstruction and mineral content on some mechanical properties of bovine bone. *Journal of Biomechanics 8*(1), 81–86.

Currey, J. D. (1979, January). Changes in the impact energy absorption of bone with age. *Journal of Biomechanics 12*(6), 459–469.

Currey, J. D. (1988, January). The effect of porosity and mineral content on the Young's modulus of elasticity of compact bone. *Journal of Biomechanics 21*(2), 131–139.

Currey, J. D., K. Brear, and P. Zioupos (1996, February). The effects of ageing and changes in mineral content in degrading the toughness of human femora. *Journal of Biomechanics 29*(2), 257–260.

Currey J.D (1969). The mechanical consequences of variation in the mineral content of bone. *Journal of Biomechanics 2*, 1–11.

Dall'Ara, E., B. Luisier, R. Schmidt, F. Kainberger, P. Zysset, and D. Pahr (2013, January). A nonlinear QCT-based finite element model validation study for the human femur tested in two configurations in vitro. *Bone 52*(1), 27–38.

Davies, R. M. (1948, January). A critical study of the Hopkinson pressure bar. *Phil. Trans. R. Soc. Lond. A 240*(821), 375–457.

Dewar, D. C., S. M. Tarrant, K. L. King, and Z. J. Balogh (2013, March). Changes in the epidemiology and prediction of multiple-organ failure after injury. *The Journal of Trauma and Acute Care Surgery 74*(3), 774–779.

Fallouh, H., R. Dattani-Patel, and S. Rathinam (2017). Blunt thoracic trauma. *Surgery (Oxford) 35*(5), 262 – 268.

Ferreira, F., M. A. Vaz, and J. A. Simões (2006). Mechanical properties of bovine cortical bone at high strain rate. *Materials Characterization 2*(57), 71–79.

Flanagan, D. P. and T. Belytschko (1981). A uniform strain hexahedron and quadrilateral with orthogonal hourglass control. *International Journal for Numerical Methods in Engineering 17*(5), 679–706.

Galante, J., W. Rostoker, and R. D. Ray (1970, December). Physical properties of trabecular bone. *Calcified Tissue Research 5*(1), 236–246.

Garcia, D. (2006). *Elastic plastic damage laws for cortical bone.* Ph. D. thesis, Ecole Polytechnique Fédérale de Laussane, Laussane, Switzerland.

Gary, G., J. Klepaczko, and H. Zhao (1991). Correction de dispersion pour l'analyse des petites déformation aux barres d'Hopkinson. *Journal de Physique IV Colloque 01*(C3), C3–403–C3–410.

Gennarelli, T. A. and E. Wodzin (2006). AIS 2005: A contemporary injury scale. *Injury 37*(12), 1083 – 1091.

Gibson, L. J. (1985). The mechanical behaviour of cancellous bone. *Journal of Biomechanics 18*(5), 317 – 328.

Gibson, L. J. (2005, March). Biomechanics of cellular solids. *Journal of Biomechanics 38*(3), 377–399.

Got, c., G. Walfish, A. Fayon, and C. Faverjon (1975). Les Caractéristiques Morphologiques, Chimiques et Physiques des côtes et leurs relations avec la déflexion provoquée du thorax. In *IRCOBI Conference proceedings*, Birmingham,UK, pp. 220–228.

Granik, G. and I. Stein (1973, May). Human ribs: Static testing as a promising medical application. *Journal of Biomechanics 6*(3), 237–240.

Gray, H. and W. H. Lewis (1918). *Anatomy of the human body.* Philadelphia : Lea & Febiger.

Griffith, J. F. and H. K. Genant (2008). Bone mass and architecture determination: state of the art. *Best Practice & Research Clinical Endocrinology & Metabolism 22*(5), 737 – 764.

Guedes, R. M., J. A. Simões, and J. L. Morais (2006). Viscoelastic behaviour and failure of bovine cancellous bone under constant strain rate. *Journal of Biomechanics 39*(1), 49–60.

Hambli, R. (2011a, August). Apparent damage accumulation in cancellous bone using neural networks. *Journal of the Mechanical Behavior of Biomedical Materials 4*(6), 868–878.

Hambli, R. (2011b). Multiscale prediction of crack density and crack length accumulation in trabecular bone based on neural networks and finite element simulation. *International Journal for Numerical Methods in Biomedical Engineering 27*(4), 461–475.

Hambli, R. (2013, October). Micro-CT finite element model and experimental validation of trabecular bone damage and fracture. *Bone 56*(2), 363–374.

Hamid, U. I. and K. McManus (2011, May). Blunt thoracic trauma. *Surgery (Oxford) 29*(5), 231–236.

Hansen, U., P. Zioupos, R. Simpson, J. D. Currey, and D. Hynd (2008, February). The Effect of Strain Rate on the Mechanical Properties of Human Cortical Bone. *Journal of Biomechanical Engineering 130*(1), 011011–011011–8.

Hasson, D. F. and R. W. Armstrong (1974, July). A ductile-to-brittle transition in bone? *Journal of Materials Science 9*(7), 1165–1170.

Haufe, A., F. Neukamm, M. Feucht, and T. Borvall (2010). A Comparison of recent Damage and Failure Models for Steel Materials in Crashworthiness Application in LS-DYNA. In *11th Internaltional LS-DYNA Users Conference*, Dearborn,MI,USA.

Haug, E., H.-Y. Choi, S. Robin, and M. Beaugonin (2004, January). Human Models for Crash and Impact Simulation. In *Handbook of Numerical Analysis*, Volume 12 of *Computational Models for the Human Body*, pp. 231–452. Elsevier.

Hernandez, C. J., G. S. Beaupré, T. S. Keller, and D. R. Carter (2001, July). The influence of bone volume fraction and ash fraction on bone strength and modulus. *Bone 29*(1), 74–78.

Hopkinson, B. (1914, January). A method of measuring the pressure produced in the detonation of high, explosives or by the impact of bullets. *Phil. Trans. R. Soc. Lond. A 213*(497-508), 437–456.

Horst, K., H. Andruszkow, C. D. Weber, M. Pishnamaz, C. Herren, Q. Zhi, M. Knobe, R. Lefering, F. Hildebrand, and H.-C. Pape (2017, October). Thoracic trauma now and then: A 10 year experience from 16,773 severely injured patients. *PLOS ONE 12*(10), e0186712.

Hughes, T. J., R. L. Taylor, J. L. Sackman, A. Curnier, and W. Kanoknukulchai (1976, July). A finite element method for a class of contact-impact problems. *Computer Methods in Applied Mechanics and Engineering 8*(3), 249–276.

Irogi, N. D., K. Maruca, G. Patti, and S. Mora (2018). Update on bone density measurements and their interpretation in childrens and adolescents. *Best Practice & Research Clinical Endocrinology & Metabolism 32*(4), 477 – 498.

John.O, Halloquist (2006). *LS-Dyna Theory Manual.* LSTC.

Johnson, T., S. Socrate, and M. Boyce (2010, October). A viscoelastic, viscoplastic model of cortical bone valid at low and high strain rates. *Acta Biomaterialia 6*(10), 4073–4080.

Kallieris, D., R. Mattern, G. Schmidt, and R. H. Eppinger (1981, October). Quantification of Side Impact Responses and Injuries. SAE Technical Paper 811009, SAE International, Warrendale, PA.

Kallieris, D. and H. Reidl (2000). Mechanical tests on bone and cartilage. Final report on the european project HUMOS.

Kaplan, S. J., W. C. Hayes, J. L. Stone, and G. S. Beaupré (1985, January). Tensile strength of bovine trabecular bone. *Journal of Biomechanics 18*(9), 723–727.

Karkar, M. (2017, November). *Personnalisation morpho-mécanique de la voûte crânienne humaine à différentes vitesses de sollicitations.* PhD Thesis, Valenciennes.

Keaveny, T. (2001). Strength of Trabecular Bone. In *Bone Mechanics Handbook* (2 ed.)., Engineering & Technology, Medicine, Dentistry, Nursing & Allied Health. CRC Press.

Keaveny, T. M., E. F. Wachtel, C. M. Ford, and W. C. Hayes (1994, September). Differences between the tensile and compressive strengths of bovine tibial trabecular bone depend on modulus. *Journal of Biomechanics 27*(9), 1137–1146.

Keaveny, T. S., E. F. Morgan, and O. C. Yeh (2003). Bone Mechanics. In *Standard Hand Book of Biomedical Engiennering and Design* (1 ed.)., pp. 8.1–8.24. McGraw Hill Professional.

Keller, T. S. (1994, September). Predicting the compressive mechanical behavior of bone. *Journal of Biomechanics 27*(9), 1159–1168.

Kemper, A. R., C. McNally, C. A. Pullins, L. J. Freeman, S. M. Duma, and S. M. Rouhana (2007, October). The biomechanics of human ribs: material and structural properties from dynamic tension and bending tests. *Stapp Car Crash Journal 51*, 235–273.

Keyak, J. H., I. Y. Lee, and H. B. Skinner (1994, November). Correlations between orthogonal mechanical properties and density of trabecular bone: use of different densitometric measures. *Journal of Biomedical Materials Research 28*(11), 1329–1336.

Keyak, J. H. and S. A. Rossi (2000, February). Prediction of femoral fracture load using finite element models: an examination of stress- and strain-based failure theories. *Journal of Biomechanics 33*(2), 209–214.

Kimpara, H., M. Iwamoto, K. Miki, J. B. Lee, P. C. Begeman, K. H. Yang, and A. I. King (2003). Biomechanical properties of the Male and Female Chest Subjected to Frontal and Lateral Impacts. pp. 13.

Kirchner, H. (2006, June). Ductility and brittleness of bone. *International Journal of Fracture 139*(3), 509–516.

Knaus, W. A., D. P. Wagner, E. A. Draper, J. E. Zimmerman, M. Bergner, P. G. Bastos, C. A. Sirio, D. J. Murphy, T. Lotring, A. Damiano, and F. E. Harrell (1991, December). The APACHE III Prognostic System: Risk Prediction of Hospital Mortality for Critically Ill Hospitalized Adults. *Chest 100*(6), 1619–1636.

Knaus, W. A., J. E. Zimmerman, D. P. Wagner, E. A. Draper, and D. E. Lawrence (1981, August). APACHE-acute physiology and chronic health evaluation: a physiologically based classification system. *Critical Care Medicine 9*(8), 591–597.

Kolsky, H. (1949). An Investigation of the Mechanical Properties of Materials at very High Rates of Loading. *Proceedings of the Physical Society. Section B 62*(11), 676.

Lemaitre, J. (1996). *A course on damage mechanics* (2., rev. and enl. ed ed.). Berlin: Springer. OCLC: 845149226.

Leng, H., M. J. Reyes, N. X. Dong, and X. Wang (2013, August). Effect of age on mechanical properties of Collagen phase in different orientations of human cortical bone. *Bone 55*(2), 288–291.

Li, Z., M. W. Kindig, J. R. Kerrigan, C. D. Untaroiu, D. Subit, J. R. Crandall, and R. W. Kent (2010, January). Rib fractures under anterior–posterior dynamic loads: Experimental and finite-element study. *Journal of Biomechanics 43*(2), 228–234.

Lotz, J. C., T. N. Gerhart, and W. C. Hayes (1991, January). Mechanical properties of metaphyseal bone in the proximal femur. *Journal of Biomechanics 24*(5), 317–329.

Lowenstam, H. A. and S. Weiner (1989). *On biomineralization.* New York: Oxford University Press. OCLC: 17916751.

Ludwig, C. and A. Koryllos (2017, April). Management of chest trauma. *Journal of Thoracic Disease 9*(Suppl 3), S172–S177.

Lundberg, B. (1976). A split hopkinson bar study of energy absorption in dynamic rock fragmentation. *European Journal of Cardio-Thoracic Surgery 13*, 187–197.

Lundin, L. and S. Storm (2018). Detailed FE rib modelling for fracture prediction. Master's thesis, Chalmers University, Sweeden.

Maeno, T. and J. Hasegawa (2001, June). Development of a Finite Element Model of the Total Human Model for Safety (thums) and Application to Car-Pedestrian Impacts. SAE Technical Paper 2001-06-0054, SAE International, Warrendale, PA.

Malik, C. L., S. M. Stover, R. B. Martin, and J. C. Gibeling (2003, February). Equine cortical bone exhibits rising R-curve fracture mechanics. *Journal of Biomechanics 36*(2), 191–198.

Martin, R. B. (1984). Porosity and specific surface of bone. *Critical Reviews in Biomedical Engineering 10*(3), 179–222.

Mayeur, O. (2013, December). *Personnalisation géométrique et mécanique multi-échelles du thorax humain.* thesis, Valenciennes.

McCalden, R. W., J. A. McGeough, M. B. Barker, and C. M. Court-Brown (1993, August). Age-related changes in the tensile properties of cortical bone. The relative importance of changes in porosity, mineralization, and microstructure. *The Journal of Bone and Joint Surgery. American Volume 75*(8), 1193–1205.

McElhaney, J. H. (1966, July). Dynamic response of bone and muscle tissue. *Journal of Applied Physiology 21*(4), 1231–1236.

Merle, R. and H. Zhao (2006). On the errors associated with the use of large diameter shpb, corrections for radially non-uniform distribution of stress and particle velocity in shpb testing. *International Journal of Impact Engineeringy 32*, 1964–1980.

Miannay, D. P. (2001). *Time-Dependent Fracture Mechanics*. Mechanical Engineering Series. New York: Springer-Verlag.

Mommsen, P., T. Barkhausen, M. Frink, C. Zeckey, C. Probst, C. Krettek, and F. Hildebrand (2011, January). Productive capacity of alveolar macrophages and pulmonary organ damage after femoral fracture and hemorrhage in IL-6 knockout mice. *Cytokine 53*(1), 60–65.

Moylan, J. A., D. E. Detmer, J. Rose, and R. Schulz (1976, July). Evaluation of the quality of hospital care for major trauma. *The Journal of trauma 16*(7), 517–523.

Neil, J., T. Demos, J. Stone, and W. Hayes (1983). Tensile and compressive properties of vertebral trabecular bone. In *Transactions of the annual meeting of the Orthopaedic Research Society*, Volume 8, pp. 344.

Neukamm, F., M. Feucht, and A. Haufe (2009). Considering damage history in crashworthiness simulations. pp. 10.

Osler, T., S. P. Baker, and W. Long (1997, December). A Modification of the Injury Severity Score That Both Improves Accuracy and Simplifies Scoring. *Journal of Trauma and Acute Care Surgery 43*(6), 922.

Pape, H. C., D. Remmers, J. Rice, M. Ebisch, C. Krettek, and H. Tscherne (2000, September). Appraisal of early evaluation of blunt chest trauma: development of a standardized scoring system for initial clinical decision making. *The Journal of Trauma 49*(3), 496–504.

Pavier, J. (2013, June). *Contribution à la compréhension des phénomènes physiques lors de l'impact d'un corps sur un modèle de structure biologique*. Ph. D. thesis, Orléans. RESTRICTED CIRCULATION.

Pavier, J., A. Langlet, N. Eches, N. Prat, P. Bailly, and J.-F. Jacquet (2015, July). Experimental study of the coupling parameters influencing the terminal effects of thoracic blunt ballistic impacts. *Forensic Science International 252*, 39–51.

Petrucelli, E., J. D. States, and L. N. Hames (1981, March). The abbreviated injury scale: Evolution, usage and future adaptability. *Accident Analysis & Prevention 13*(1), 29–35.

Pietruszczak, S., D. Inglis, and G. N. Pande (1999, October). A fabric-dependent fracture criterion for bone. *Journal of Biomechanics 32*(10), 1071–1079.

Pithioux, M., D. Subit, and P. Chabrand (2004). Comparison of compact bone failure under two different loadings rates: experimental and modelling approaches. *Medical Engineering and Physics 26*, 647–653.

Rai, A., D. K. Srivastava, and S. S. Rajput (2018, January). Validation of Thorax Trauma Severity Score Using Early Emergency Department Computed Tomography (MDCT 64 Slice/Multirow Detector). *Heart, Lung and Circulation 27*, S531.

Reilly, D. T. and A. H. Burstein (1975, January). The elastic and ultimate properties of compact bone tissue. *Journal of Biomechanics 8*(6), 393–405.

Reznikov, N., R. Shahar, and S. Weiner (2014, September). Bone hierarchical structure in three dimensions. *Acta Biomaterialia 10*(9), 3815–3826.

Røhl, L., E. Larsen, F. Linde, A. Odgaard, and J. Jørgensen (1991, January). Tensile and compressive properties of cancellous bone. *Journal of Biomechanics 24*(12), 1143–1149.

Rice, J. C., S. C. Cowin, and J. A. Bowman (1988, January). On the dependence of the elasticity and strength of cancellous bone on apparent density. *Journal of Biomechanics 21*(2), 155–168.

Roberts, S. B. and P. Chen (1971). On Some Geometric Properties of Human Ribs. Technical, Airforce Aerospace Medical Research Lab, Wright Patterson AFB,Ohio.

Roberts, S. B. and P. H. Chen (1972, March). Global geometric characteristics of typical human ribs. *Journal of Biomechanics 5*(2), 191–201.

Robin, S. (2001). HUMOS: HUman MOdel for Safety - A joint effort towards the development of refined human like car occupant models.

Roth, S. (2009). Influence of mesh density on a finite element model under dynamic loading.

Roux, P. and R. M. Fisher (1992, May). Chest injuries in children: An analysis of 100 cases of blunt chest trauma from motor vehicle accidents. *Journal of Pediatric Surgery 27*(5), 551–555.

Sawas, O., N. S. Brar, and R. A. Brockman (1998, September). Dynamic characterization of compliant materials using an all-polymeric split Hopkinson bar. *Experimental Mechanics 38*(3), 204–210.

S.C.Cowin (1999). Bone Poroelasticity. *Journal of Biomechanics 32*(3), 217–38.

Schoell, S. L., A. A. Weaver, N. A. Vavalle, and J. D. Stitzel (2015). Age- and sex-specific thorax finite element model development and simulation. *Traffic Injury Prevention 16 Suppl 1*, S57–65.

Shen, F., T. E. Tay, J. Z. Li, S. Nigen, P. V. Lee, and H. K. Chan (2006, October). Modified Bilston nonlinear viscoelastic model for finite element head injury studies. *Journal of biomechanical engineering 128*(5), 797–801.

Stein, I. D. and G. Granik (1976, December). Rib structure and bending strength: An autopsy study. *Calcified Tissue Research 20*(1), 61–73.

Stone, J. L., G. S. Beaupre, and W. C. Hayes (1983, January). Multiaxial strength characteristics of trabecular bone. *Journal of Biomechanics 16*(9), 743–752.

Sundaram, S. H. and C. C. Feng (1977, January). Finite element analysis of the human thorax. *Journal of Biomechanics 10*(8), 505–516.

Taylor, D. and T. Lee (2003, August). Microdamage and mechanical behaviour: predicting failure and remodelling in compact bone. *Journal of Anatomy 203*(2), 203–211.

Taylor, W. R. (2002). Determination of orthotropic bone elastic constants using FEA and modal analysis. *Journal of Biomechanics 35*, 767–773.

Teasdale, G. and B. Jennett (1974, July). ASSESSMENT OF COMA AND IMPAIRED CONSCIOUSNESS: A Practical Scale. *The Lancet 304*(7872), 81–84.

Teo, J. C., K. M. Si-Hoe, J. E. Keh, and S. H. Teoh (2006). Relationship between ct intensity, micro-architecture and mechanical properties of porcine vertebral cancellous bone. *Clinical Biomechanics 21*(3), 235 – 244.

Tortora, G. J. and M. T. Nielsen (1983). *Principles of human anatomy* (1st ed ed.). Hoboken, NJ John Wiley & Sons.

Turner, C. H., S. C. Cowin, J. Y. Rho, R. B. Ashman, and J. C. Rice (1990, January). The fabric dependence of the orthotropic elastic constants of cancellous bone. *Journal of Biomechanics 23*(6), 549–561.

Ural, A. and D. Vashishth (2007, October). Effects of intracortical porosity on fracture toughness in aging human bone: a microCT-based cohesive finite element study. *Journal of Biomechanical Engineering 129*(5), 625–631.

Vashishth, D., K. E. Tanner, and W. Bonfield (2003, January). Experimental validation of a microcracking-based toughening mechanism for cortical bone. *Journal of Biomechanics 36*(1), 121–124.

Vose, G. P. and A. L. Kubala (1959). Bone strength-its relationship to X-ray-determined ash content. *Human Biology 31*, 261–270.

Wagner, D. P. and E. A. Draper (1984, November). Acute physiology and chronic health evaluation (APACHE II) and Medicare reimbursement. *Health Care Financing Review 1984*(Suppl), 91.

Wang, X., X. Shen, X. Li, and C. M. Agrawal (2002, July). Age-related changes in the collagen network and toughness of bone. *Bone 31*(1), 1–7.

Whitehouse, W. J. (1974, July). A stereological method for calculating internal surface areas in structures which have become anisotropic as the result of linear expansions or contractions. *Journal of Microscopy 101*(Pt 2), 169–176.

Williams, J. L. and J. L. Lewis (1982, February). Properties and an anisotropic model of cancellous bone from the proximal tibial epiphysis. *Journal of Biomechanical Engineering 104*(1), 50–56.

Wong, A. K. O. (2016). A comparison of peripheral imaging technologies for bone and muscle quantification: a technical review of image acquisition. *Journal of Musculoskeletal and Neuronal Interactions 16*(4), 265 – 282.

Wood, J. L. (1971, January). Dynamic response of human cranial bone. *Journal of Biomechanics 4*(1), 1–12.

Wright, T. M. and W. C. Hayes (1976, November). Tensile testing of bone over a wide range of strain rates: effects of strain rate, microstructure and density. *Medical & Biological Engineering 14*(6), 671–680.

Yates, K. and C. Untaroiu (2018). Subject-Specific Modeling of Human Ribs: Finite Element Simulations of Rib Bending Tests, Mesh Sensitivity, Model Prediction with Data Derived From Coupon Tests. pp. 7.

Yoganandan, N. and F. A. Pintar (1998, February). Biomechanics of human thoracic ribs. *Journal of Biomechanical Engineering 120*(1), 100–104.

Zhao, H. and G. Gary (1995, August). A three dimensional analytical solution of the longitudinal wave propagation in an infinite linear viscoelastic cylindrical bar. Application to experimental techniques. *Journal of the Mechanics and Physics of Solids 43*(8), 1335–1348.

Zhao, H. and G. Gary (1996, September). On the use of SHPB techniques to determine the dynamic behavior of materials in the range of small strains. *International Journal of Solids and Structures 33*(23), 3363–3375.

Zhao, H., G. Gary, and J. R. Klepaczko (1997, April). On the use of a viscoelastic split hopkinson pressure bar. *International Journal of Impact Engineering 19*(4), 319–330.

Aravind Rajan AYAGARA

Caractérisation de la fracturation dynamique des os de la cage thoracique: simulations numériques et validation expériementale

Résumé :

L'objectif de cette thèse est de caractériser le comportement mécanique des côtes isolées sous impact en dynamique rapide par l'expérimentation et les calculs EF. Dans le cadre de cette étude, les côtes de porc on été choisies comme substituts de la côte humaine. Les essais de flexion trois points en dynamique rapide on été réalisés avec les barres de Hopkinson. Les résultats de campagne expérimentale ont mis en évidence l'influence de la vitesse de déformation sur le temps de fracture, le faciès de rupture et également, sur l'amplitude des forces d'impact. Un modèle numérique 3D d'une côte de porc a été développé, grâce aux images obtenues par micro-CT en Haute Résolution (HR-pQCT). Ensuite, les propriétés élastiques des constituants on été attribués à partir des niveaux de gris des images de HR-pQCT. Une loi de comportement élastique-viscoplastique, modifiée pour prendre en compte les effets de la vitesse de déformation couplée avec une loi d'endommagement a été élaborée. La loi d'endommagement présentée, nous permet de prendre en compte l'endommagement non-linaire, la réduction de la rigidité de la structure et les effets de la vitesse de déformation. Le modèle EF présenté dans cette thèse est capable de prédire la fracture des côtes sous impact en dynamique rapide.

Mots clés : Chocs, Impactes, Réponse dynamique, côte de porc, HR-pQCT, simulations EF, LS-Dyna, SHPB

Characterization of rib fractures subjected to impact loads: numerical simulations and experimental validation

Abstract :

The objective of this study is to characterize the mechanical behavior of isolated porcine ribs subjected to dynamic impact through experiments and numerical simulations. The porcine rib was used as a human surrogate rib in order to develop an adapted methodology for the human rib. A three Split Hopkinson Pressure Bar (SHPB) setup for three-point bending tests was used. An ensemble of 20 tests data was considered to be comprehensible for experimental characterization, thereby, showing an influence of strain rate on both time for fracture and amplitudes of force response. A three-dimensional porcine rib model was generated from the DICOM images of High-Resolution peripheral Quantitative Computed Tomography (HR-pQCT) scans. Material properties interpolated using power law regression equations based on apparent density were assigned to the numerical rib. A modified elastic-viscoplastic constitutive law, capable of considering the effects of strain rate was elaborated. An incremental and stress-state dependent damage law, capable of considering effects of strain rate on fracture propagation, non-linear damage accumulation and instabilities was coupled to the constitutive law. The proposed Finite Element model is able to predict satisfactory force-displacement curve and fracture patterns of the tested ribs indicating that the developed numerical model may be used to investigate the fracture behavior of human ribs under dynamic loads.

Keywords : Blunt impact, Dynamic response, porcine ribs, HR-pQCT, Finite Element simulations, LS-Dyna, Split Hopkinson Pressure Bar

Région Centre-Val de Loire

Laboratoire LaMé - Université d'Orléans
63 Av de Lattre de Tassigny, 18000 Bourges.

LaMé Laboratoire de Mécanique Gabriel Lamé